Long-range Functional Connectomics

Towards a functional connectome underlying the generation of stimulus selectivity in mouse visual cortex

David Laubender

Dissertation zur Erlangung des Doktorgrades der Naturwissenschaften

an der Fakultät für Biologie

der Ludwig-Maximilians-Universität München

12. Januar 2022

Supervisors:

Prof. Tobias Bonhoeffer	Max Planck Institute of Neurobiology
Prof. Mark Hübener	Max Planck Institute of Neurobiology
Prof. Tobias Rose	University of Bonn
Prof. Moritz Helmstaedter	Max Planck Institute for Brain Research

Referees:

1st referee: Prof. Tobias Bonhoeffer

2nd referee: Prof. Laura Busse

Date of submission:

12.01.2022

Date of defense:

09.05.2022

Table of contents

Table of contents 4
Abstract 9
1 Introduction 11
1.1.1 From What to How 11
1.1.2 Functional connectivity 11
1.2 Organization of the visual system 12
1.2.1 Retina 12
1.2.2 Retinal projections 14
1.2.3 Superior colliculus 14
1.2.4 Dorsolateral geniculate nucleus 14
1.2.5 Limited functional retino-geniculate convergence 15
1.2.6 Non-retinal inputs to dLGN 15
1.2.7 Topographic organization of dLGN 16
1.2.8 Geniculo-cortical projections 16
1.2.9 Topographic organization of V1 17
1.2.10 Mouse as a model organism for visual neuroscience 18
1.3 Coding in the geniculo-cortical circuit 19
1.3.1 Ocular Dominance 19
1.3.2 Receptive Fields 19
1.3.3 Orientation- and Direction Tuning 20
1.4 Geniculo-cortical convergence: Hubel & Wiesel 21
1.4.1 Support for the Hubel & Wiesel model 21
1.4.2 Arguments against the Hubel & Wiesel model 22
1.4.3 Alternative and complementary models 22
1.4.4 Need for a comprehensive dataset 23
1.5 Technological advances towards 2P-EM functional connectomics 24
1.5.1 From electrodes to optics 24
1.5.2 How to see neuronal function 24
1.5.3 Calcium indicators 24
1.5.4 Two-photon microscopy 25
1.5.5 Roads to connectivity 26
1.5.6 3D electron microscopy 27
1.5.7 Towards automated data processing of petabyte-scale EM datasets 29
1.5.8 Towards long-range functional connectomes – bridging photons and electrons 30
1.6 Aim of this study 31
2 Materials and Methods 33
2.1 Materials 33

2.1.1 Desoxyribonucleic acids 33
2.1.2 Enzymes 33
2.1.3 Viruses 34
2.1.4 Antibodies 34
2.1.5 Pharmaceuticals 34
2.1.6 Chemicals 35
2.1.7 Solutions 36
2.1.8 Media 38
2.1.9 Glues, cements, paints & gels 39
2.1.10 Materials and Instruments 39
2.1.11 Software 44
2.2 Ethics 45
2.3 Molecular Cloning 45
2.3.1 Cloning of Cre-dependent FlpO-recombinase 45
2.3.2 Cloning of FlpO-dependent jGCaMP7b 46
2.4 Organotypic rat hippocampal slice cultures 46
2.5 Biolistic transfection and viral transduction in organotypic slice cultures 47
2.6 Epifluorescence imaging of organotypic slice cultures 48
2.7 *In vivo* virus injection and chronic window implantation 48
2.8 Intrinsic optical signal imaging 50
2.9 *In vivo* two-photon calcium imaging 50
2.10 Visual stimulation 52
2.10.1 Visual stimulation for intrinsic optical signal imaging 52
2.10.2 Visual stimulation for two-photon Calcium-imaging 52
2.11 Histology and Immunohistochemistry 55
2.12 EM-grade transcardial perfusion 56
2.13 Stereotaxic biopsy extraction 56
2.14 En bloc heavy metal staining 57
2.15 En bloc embedding 57
2.16 Micro Computed Tomography 58
2.17 Sample trimming & smoothing 58
2.17.1 Trimming 58
2.17.2 Smoothing 59
2.18 Automated tape-collecting ultra-microtome 59
2.18.1 ATUM experiments 60
2.19 Multibeam Scanning Electron Microscopy 61
2.19.1 Mounting on silicon wafers 61
2.19.2 Mounting on wafer holder 62

2.19.3 Wafer light microscopy and section definition 62
2.19.4 Multibeam Scanning Electron Microscopy 63
2.20 Image and data analysis 64
2.20.1 Intrinsic optical signal imaging – data analysis 64
2.20.2 Two-photon imaging – pre processing 64
2.20.3 Two-photon imaging – baseline normalization and responsiveness 65
2.20.4 Two-photon imaging – Preferred Orientation and Direction 65
2.20.5 Two-photon imaging – Ocular Dominance 65
2.20.6 Two-photon imaging – Orientation & Direction Selectivity 66
2.20.7 Two-photon imaging – Receptive fields 66
2.20.8 mSEM Image Alignment 69
2.21 Statistics 70
3 Results 72
3.1 Deep, dual-color *in vivo* two-photon imaging 73
3.1.1 Deep, *in vivo* two-photon axon imaging 73
3.1.2 Deep, simultaneous, dual-color *in vivo* two-photon calcium imaging of overlapping cells and axons 77
3.1.3 Deep *in vivo* two-photon calcium imaging of OS, DS and OD for functional connectomics 79
3.1.4 Deep *in vivo* two-photon calcium imaging for mapping of RFs for functional connectomics 84
3.1.5 Alignment of RF orientation and PO in L4 cells 89
3.1.6 Linking neuronal function to structure in L4 cells and dLGN axons *in vivo* 90
3.2 Large-scale 3D multibeam electron microscopy 91
3.2.1 Homogeneous heavy metal staining for 3D-EM 91
3.2.2 Targeted biopsy extraction via vascular triangulation for functional connectomics 93
3.2.3 Optimizing ATUM for single-shot experiments 95
3.2.4 ATUM sectioning for functional connectomics 96
3.2.5 3D mSEM for functional connectomics 97
3.2.6 Alignment of mSEM raw-data in 3D 99
3.3 Summary 102
4 Discussion 105
4.1 Alternative approaches to functional connectivity? 105
4.1.1 Paired/multi patch-clamp recordings 105
4.1.2 *In vivo* dendritic spine imaging 106
4.1.3 *In vivo* dendritic spine imaging and 3D-EM 107
4.1.4 *In vivo* two-photon microscopy and GRASPs 108
4.1.5 *In vivo* two-photon microscopy and monosynaptic rabies virus tracing 109
4.1.6 *In vivo* two-photon microscopy and 3D-EM 110
4.2 Towards a functional connectome underlying stimulus selectivity in bV1 111
4.2.1 Choice of GECIs 111

4.2.2 A system to titrate transduction sparsity in genetically modified, Cre-recombinase expressing mice 112
4.2.3 Intra-axonal bouton response similarity 113
4.2.4 Extraction of functional responses in vivo in co-labeled dLGN axons and L4 cells in bV1 114
4.2.5 Ocular dominance, orientation and direction tuning of dLGN axons and cells in L4 of bV1 115
4.2.6 Receptive Fields of dLGN axons and cells in L4 of bV1 117
4.2.7 Correlation of RF- and preferred orientation 119
4.2.8 Matching functional to structural imaging *in vivo* 120
4.2.9 Single shot in vivo data acquisition and perfusion 121
4.2.10 Biopsy preparation and re-finding via vascular triangulation 121
4.2.11 Long-range ATUM ultra-sectioning for functional connectomics 122
4.2.12 Multibeam Scanning Electron Microscopy 123
4.2.13 3D-EM image alignment and neurite continuity 125
4.3 Future directions 126
4.3.1 3D segmentation 126
4.3.2 LM-EM re-finding 127
4.3.3 Connectome extraction 129
4.3.4 Deciphering functional connectivity logic 129
4.4 Conclusion 130
5 Bibliography 133
6 Supplement 167
List of figures 176
List of tables 177
List of abbreviations 178
Acknowledgements 181
Affidavit 183

Abstract

Ever since Hubel and Wiesel proposed their famous model on how circular receptive fields in the visual thalamus are transformed into the elongated and oriented receptive fields of simple cells in layer 4 of primary visual cortex (Hubel and Wiesel, 1962), this circuit has become a classic example of how stimulus selectivity emerges in the neocortex. They suggested that this transformation is implemented by a simple feedforward connectivity scheme, by which sets of geniculate neurons with their circular receptive fields aligned in visual space specifically converge onto individual cortical simple cells. Consequently, postsynaptic simple cells obtain their elongated receptive fields by simple linear summation, thereby becoming selective to orientations in space. However, despite being reproduced in almost every neuroscience textbook, direct evidence in favor or against this circuit model is still lacking today, more than half a century later.

During my PhD, I aimed to obtain a comprehensive dataset for determining the role of the circuit logic underlying the generation of orientation selectivity in simple cells of the mouse primary visual cortex. To decipher the functional logic of connectivity, two components are necessary: the neurons' function and their inter-connectivity, which coalesce in an approach called functional connectomics (Reid, 2012). In order to yield the necessary single cell resolution for functional connectivity, a functional readout of *in vivo* two-photon calcium imaging should ideally be combined with subsequent high-resolution 3D electron microscopy-based connectomics. So far, each of these have been studied in isolation due to technological limitations, or have been confined to local functional connectomics (Bock et al., 2011; Briggman et al., 2011; Lee et al., 2016b; MICrONS Consortium et al., 2021).

In this thesis, I developed a novel long-range functional connectomics pipeline. I tailored and deployed this experimental pipeline to acquire a comprehensive, multimodal dataset. Specifically, I mapped functional receptive field properties, like ocular dominance, spatial receptive fields, orientation and direction selectivity, in layer 4 cells and dLGN axons in thalamo-recipient layer 4 of binocular primary visual cortex of mice using dual-color, deep *in vivo* two-photon calcium imaging. I found that functional response properties differed significantly between both populations, with cortical layer 4 cells being more binocular, having larger, more elongated and retinotopically confined receptive fields, sharper orientation and direction tuning compared to dLGN axons, in line with the circuit proposed by Hubel and Wiesel. The respective neurite morphologies of both layer 4 cells and dLGN axons were imaged in 3D, the mouse subsequently transcardially perfused, and a biopsy containing the imaged tissue extracted.

For determining the underlying connectome, the biopsy was stained for electron microscopy with heavy metals, resin infiltrated and embedded. I re-identified vascular landmarks using micro computed tomography and tracked the position of the functionally imaged field-of-view using vascular triangulation. Next, I ultra-sectioned the biopsy from upper layer 5 to middle of layer 2/3 into > 10000 consecutive 35-40 nm thin sections without a single section loss. Lastly, I imaged the neuronal ultrastructure of a 1 x 1 x 0.33 mm^3 volume centered on the functional field-of-view using 3D multi-beam scanning electron microscopy, and aligned the resulting petabyte-sized rawdata into a coherent 3D volume. Although the connectomic analysis is still ongoing, I am convinced that this dataset provides the data quality and richness required for providing comprehensive evidence on the functional logic of geniculo-cortical connectivity in mouse binocular primary visual cortex. Such a functional connectome will finally allow us to make conclusive statements on the generation of orientation selectivity in cortical simple cells.

1 Introduction

*"The human brain is the most complicated biological structure in the known universe. We've only just scratched the surface in understanding **how** it works"* – Francis S. Collins

1.1.1 From What to How

Understanding the brain has been – and remains – one of the biggest scientific frontiers. More than 100 years after Santiago Rámon y Cajal ushered the era of modern neuroscience, the sheer complexity of the brain continues to amaze. While neuroscience has made substantial leaps in deciphering "what" the brain, certain brain areas or even individual cells are coding for, our understanding of "how" the brain computes information lags behind. This disparity originates mostly from limitations in neurotechnology. Here, I take a first step towards bridging this gap. So far, neuronal function and connectivity have mostly been studied in isolation. In this work, I combine both, by reading out functional information via *in vivo* two-photon calcium imaging paired with subsequent reconstruction of the connectome with three-dimensional electron microscopy (3D-EM). This approach is known as "functional connectomics" (Reid, 2012). In this thesis, I describe how I overcame previous technical limitations to develop an experimental pipeline for long-range functional connectomics. I specifically tailored and applied this pipeline for interrogating how stimulus selectivity is computed in a sub-circuit of the visual system of mice, which I introduce in the following paragraphs.

1.1.2 Functional connectivity

Analogous to the rest of our body, the brain is made up of individual cells: nerve cells and glia. These cells, thought to be the main actors for processing information, are called neurons. In stark contrast to cells from other organs, however, neurons have very complex, tree-like morphologies, allowing them to connect to 1000s of other neurons (DeWeerdt, 2019; Wildenberg et al., 2020) even outside the direct vicinity of their cell body. Consequently, they form complex networks, through which they communicate. Their physical communication points are called synapses. Information flow at these contact sites is believed to be mostly unidirectional, from the presynaptic to the postsynaptic neuron. While within a neuron, information is then mainly propagated via electrical signals, at synapses, information is passed on to other cells by chemical molecules, the so-called neurotransmitters.

The brain is hereby not arranged in an anatomically random manner, but organized into distinct brain areas that form functional hubs for information processing. While some brain areas are morphologically distinct (Brodmann, 1909), many functional modules have only become apparent with the advent of functional imaging techniques. Today, it is not only possible to read out activity of entire brain areas, but also of individual cells. To move towards an understanding of "how" the brain processes information, it is, however, not merely sufficient to investigate the output of neurons, but also their input. In other words, one needs to understand which information is used as a basis to compute the neuron's output.

In addition, the existence of a functional logic to neuronal wiring itself bears the potential of reducing computational complexity in stereotyped circuits. Therefore, knowing both the input, connectivity and output of a neuronal circuit enables one not only to draw conclusions about the computational operations individual cells perform, but also about the role of their connectivity in reducing computation. In this study, I set out to investigate this in the context of one of the most famous circuit motifs in visual neuroscience, proposed by David Hubel and Torsten Wiesel over half a century ago

(Hubel and Wiesel, 1962): the geniculo-cortical convergence. In the following, I will introduce this circuit and convergence model in more detail.

1.2 Organization of the visual system

We perceive and interact with our environment via our senses, one of which is vision. Using our eyes, we continuously capture a two-dimensional (2D) image of the outside world. However, we can only observe a limited fraction of the spectrum of light, or electromagnetic wave-lengths. The ones we can perceive are converted in the retina into neuronal signals and propagated to diverse brain areas for further processing. These early steps in visual processing belong to the most extensively studied circuits in neuroscience to date. Most of this pioneering work was conducted in monkeys, cats and ferrets. However, in recent years the majority of the field has switched to rodents, such as mice. Their superior genetic accessibility and short generation times enable more targeted research approaches that would otherwise not be possible. Several studies have further shown the importance of vision in guiding rodent behavior (Morris, 1984; Prusky and Douglas, 2003; Prusky et al., 2004; Hoy et al., 2016), despite their low visual acuity (Wong and Brown, 2006) compared to e.g. humans (Campbell and Green, 1965). Although the more lateral eye positioning in rodents results in a reduced binocular overlap of only 30-60° of the visual scene (Drager and Hubel, 1976; Drager, 1978; Dräger and Olsen, 1980; Rice et al., 1995; Coleman et al., 2009; Sterratt et al., 2013), the first steps of visual processing are nonetheless analogously organized in hierarchical fashion.

1.2.1 Retina

While the space around us is three-dimensional (3D), our eye first collapses it into an inverted, 2D projection onto the retinal surface, where photons are converted into neuronal signals via photoreceptors (PRs). In mammals, counterintuitively, these PRs sit at the back of the retina. Hence, photons first pass through the scattering cellular tissue of the retina, before reaching the PRs, where they get absorbed by the photo-pigments for photo-transduction. Just behind those PRs lies the pigment epithelium, which absorbs residual photons to avoid backscattering into the eye. PRs can be grouped into two distinct classes based on both their morphology and pigments: rods and cones. They are arranged in a “retinal mosaic” (Wässle et al., 1978) and in mice, the cones are greatly outnumbered by rods (Carter-Dawson and Lavail, 1979; Jeon et al., 1998). Both PR types exhibit an elongated cellular morphology, with an outer segment housing pigment-containing disks (Sjöstrand, 1948), an inner segment enriched in mitochondria (Sjöstrand, 1953), the cell body, and the axon synaptic terminal (Sjöstrand, 1958). However, their outer segment morphology differentiates them. The rods have a cylindrical outer segment, with their disks stacked, but floating freely inside. Cones on the other hand have tapered outer segments and their disks are continuously integrated with the outer cell membrane (Kandel et al., 2013). Apart from their morphology, the two PR types also differ functionally. Rods are very light-sensitive. They can signal absorption of a single photon (Hecht et al., 1942; Velden, 1946), but quickly saturate with more light. Similar to rods, cones absorb specific ranges of electromagnetic wavelength. However, in contrast to rods, cones consist of several subtypes, that differ in their absorption spectra and are used for color vision. In contrast to tri-chromatic humans (S (short-wave), M (medium-wave) and L (long-wave) cones) (Kandel et al., 2013), mice are dichromats, lacking the long-wave cones and showing maximum absorption in the ultraviolet spectrum (Jacobs et al., 1991). In mouse, the M cones are strongly biased towards the dorsal retina, while the ultraviolet cones are located at the ventral half (Szél et al., 1992; Röhlich et al., 1994). In comparison to rods, cones have faster response dynamics and need more photons for photo-transduction (Fain and Dowling, 1973). Hence, they are mainly used for vision during well-lit situations such as during

daylight. During low light, mammals rely on rods for vision, resulting in inferior color vision during the night, termed the duplex theory of vision (Schultze, 1866).

Furthermore, the PR density is not equal over the retinal surface, with lower densities in the retinal periphery. Some mammals additionally exhibit a confined area of strongly increased cone density for high visual acuity called the fovea in primates (Michaelis, 1842; Müller, 1856) and *area centralis* in cats (Rapaport and Stone, 1984). The fovea is specialized to improve visual acuity such that the inner cellular layers are bent aside to directly expose the PRs and reduce the degradation of acuity caused by tissue scattering. By centering certain parts of the visual scene onto this area via eye and head movements, visual space can be inspected in greater detail. Mice, however, lack this retinal specialization. Nonetheless, their retina shows a higher number of PRs in the central part (Jeon et al., 1998; Volland et al., 2015). Notably, it has been found recently that mice have a region slightly above their head in visual space that is represented at higher resolution in visual cortex, termed the focea (van Beest et al., 2021).

The retina is also organized into distinct layers along the optical axis: 3 cellular layers, harboring the cell bodies of 5 different cell types, separated by 2 synaptic layers (Tartuferi, 1887; Cajal, 1894; Polyak, 1941). The outer nuclear layer accommodates the PRs, which synapse onto bipolar cells (Tartuferi, 1887) in the outer plexiform layer, either directly or indirectly via inhibitory horizontal cells. Together with the inhibitory amacrine cells, their cell bodies are located in the inner nuclear layer. These three cell types preprocess visual information by modulation and integration of PR outputs. Subsequently they communicate the visual information through synapses in the inner plexiform layer to the output cells of the retina, the retinal ganglion cells (RGCs). While bipolar cells provide a more direct connection from PRs to RGCs, both horizontal and amacrine cells provide lateral connectivity and inhibition (Creutzfeldt and Sakmann, 1969; Werblin and Dowling, 1969). Importantly, there are two bipolar sub-types: ON (reacting to light increments) and OFF (reacting to light decrements) bipolar cells (Werblin and Dowling, 1969), allowing the analysis of light to dark transitions and vice versa in parallel. These opposing sign responses are passed on to RGCs, and form the basis for subsequent visual processing.

The extent of lateral connectivity, and the number of PRs converging onto a single RGC, is not fixed and differs across retinal regions and species. PRs greatly outnumber RGCs, resulting in local convergence, and hence early low-level retinal pre-processing of visual information. The visual area that is covered by the PRs that are presynaptic of an RGC or their respective bipolar cell is called their receptive field (RF, (Hartline, 1938); term coined earlier by Charles Sherrington in the skin (Sherrington, 1906)). The number of PRs that RGCs pool information from differs across the retina, with RF and PR sizes as well as densities increasing with retinal eccentricity (Schultze, 1866; Osterberg, 1935; Curcio et al., 1990). Mediated by lateral inhibition, these bipolar cell and RGC RFs are made up of two subfields of opposite polarity: an ON field and an OFF field (Hartline, 1938; Granit, 1947). The subfields are concentrically arranged with a small circular central portion, surrounded by a ring of the opposite polarity (Kuffler, 1953; Hartline, 1969). This arrangement is called center-surround. Based on these basic RF properties, RGCs can be divided into two major types: ON center and OFF center. As their sign-opposing sub-fields are mutually inhibiting, the highest response can therefore be elicited when both subfield regions are covered by their respective luminance polarities. Apart from local contrast detection, RGCs show diversified responses, with some that are even selective to particular features in the visual scene like edges and direction of movement (Barlow and Hill, 1963; Barlow et

al., 1964). The role of the latter type, called direction selective RGCs, remains a topic of great debate, as this response feature is thought to be re-computed in visual cortex for further processing. Although they have been implicated in reflex behaviors in a separate visual pathway that does not target visual cortex directly, their exact role and projection pattern is still debated today. Overall, based on their diverse response patterns, RGCs can be sub-classified into a minimum of 32 functional response types (Baden et al., 2016) with diverse projection targets. All their axons, however, are bundled into the optic nerve, leaving the retina at the blind spot of the eye, due to the retina's inverted architecture.

1.2.2 Retinal projections

The optic nerves from each eye cross to the contralateral brain hemisphere at the optic chiasm. However, instead of a strict eye-segregated crossing, it is rather the axons representing each visual hemifield that are re-sorted into the posterior optic nerves. Specifically, RGC axons with retinal RFs covering the binocular visual field also project ipsilaterally (about 5-10%, (Dräger and Olsen, 1980; Coleman et al., 2009)). This holds true even in mouse, despite their strong eye lateralization. From the optic chiasm these axons then project in varying degrees to 40-50 brain regions (Morin and Studholme, 2014; Martersteck et al., 2017). For further visual processing, there are, however, two main subcortical targets: the superior colliculus (SC) and the dorsolateral geniculate nucleus (dLGN). While this study focuses on the dLGN, which is thought to be the major gate for further visual processing in cortex, the role of SC in visual processing has gained more and more attention recently and should not be disregarded.

1.2.3 Superior colliculus

Much of the early research into SC was performed in primates, in which it receives input from only about 10% of RGCs (Perry and Cowey, 1984). Hence, the SC has long been outside the major research focus of visual neuroscience, and was thought to be mainly involved in e.g. saccades or attention (for review see (Krauzlis et al., 2013)). Recently – driven by the major switch of vision research into small rodents – SC has gained more attention in its role in visual processing. In contrast to primates, in mice the SC is targeted by >85% of RGCs (Hofbauer and Dräger, 1985; Ellis et al., 2016). More specifically, about 80% of classical dLGN-innervating RGCs also project to the SC, providing the SC with a large portion of the total retinal information (Ellis et al., 2016). Furthermore, SC gets input not only from the visual, but also other sensory systems, which is why it has emerged as a popular brain region for studying multisensory integration (e.g. (Ghose et al., 2014)). In recent years, visual responses of increasing complexity have been found, from more traditional surround suppression, orientation preference, direction preference or speed preference to more complex responses such as to looming (Gale and Murphy, 2014; Ahmadlou and Heimel, 2015; Feinberg and Meister, 2015; Seabrook et al., 2017; Shi et al., 2017). Apart from individual visually driven neuronal responses, SC has further been linked to a palette of visually guided behaviors such as visual target selection, eye movements, head movements, spatial attention or even more complex predator avoidance (Douglas et al., 2005; Shang et al., 2015; Seabrook et al., 2017; Crapse et al., 2018; Evans et al., 2018) or prey capture (Furigo et al., 2010; Almada et al., 2018; Hoy et al., 2019; Shang et al., 2019; Huang et al., 2021b).

1.2.4 Dorsolateral geniculate nucleus

The main gateway of retinal information to visual cortex, however, is the dLGN, the most posterior-lateral thalamic nucleus in the brain. It has long been believed to act as a mere relay station of visual information into the brain. In recent years, increasing evidence of neuromodulation and integration has shifted this perception.

Most functional response properties of dLGN projection neurons strongly resemble those of the retina (Cleland et al., 1971; Lee et al., 1983; Grubb and Thompson, 2003), although some have been also associated with behavior (see e.g. (Erisken et al., 2014)). In mice, most dLGN neurons respond to stimulation of exclusively one eye, with only a minor fraction of these neurons exhibiting binocular responses, even in the binocular visual field ((Jaepel et al., 2017; Huh et al., 2020; Bauer et al., 2021); but see: (Howarth et al., 2014; Sommeijer et al., 2017)). About half of dLGN neurons have small, round RFs with a center-surround arrangement. The remaining half responds to other, partially more complex features, some of which are already present in the retina, such as local selectivity to orientation or direction of movement (Grubb and Thompson, 2003; Marshel et al., 2012; Piscopo et al., 2013; Sun et al., 2016).

1.2.5 Limited functional retino-geniculate convergence

While intuitively these RF features could be directly inherited from the retina (Chen and Regehr, 2000; Cruz-Martín et al., 2014; Liang et al., 2018), some might be computed via convergent integration of RGC afferents (Marshel et al., 2012; Hammer et al., 2015; Liang et al., 2018; Román Rosón et al., 2019). Interestingly, despite the functional resemblance of RF features to those in the retina, in mouse less than 10% of dLGN inputs are of retinal origin (Sherman and Guillery, 1998), with only 30-40% of RGCs projecting to the visual thalamus ((Morin and Studholme, 2014; Ellis et al., 2016); in contrast to 90% in primates, (Perry and Cowey, 1984)). Nonetheless, almost all RGC types project to the dLGN (Román Rosón et al., 2019). In mouse, retino-geniculate divergence and convergence is interwoven and does not form anatomically segregated, RGC-type dependent pathways (Morgan et al., 2016). On a single cell level, RGC-type dependent retino-geniculate convergence can be divided into three groups: “relay mode”, “combination mode” and “binocular mode” (Rompani et al., 2017). Relay mode dLGN neurons receive inputs from mostly a single RGC-type. Combination mode dLGN neurons on the other hand receive input from multiple RGC-types. However, while these cells receive on average input from 5 different RGC types (Román Rosón et al., 2019), usually only 2 have a dominant functional impact (Cleland et al., 1971; Usrey et al., 1999; Román Rosón et al., 2019). Similarly, despite synaptic ocular convergence of RGCs onto some dLGN neurons, their functional integration is limited by specific input refinement, favoring monocularity (Bauer et al., 2021). Taken together, despite structural (Rompani et al., 2017) and ultrastructural (Hammer et al., 2015; Morgan et al., 2016) evidence of strong retino-geniculate convergence, on a functional level retinal features are relayed to visual cortex with only limited convergence.

1.2.6 Non-retinal inputs to dLGN

Despite being considered the main visual nucleus of the thalamus, the majority of dLGN afferents are non-retinal. Of those, the bulk is provided by cortical feedback from L6 of visual cortex (Guillery, 1969; Bourassa and Deschenes, 1995), the thalamic reticular nucleus (Cucchiaro et al., 1991; Wang et al., 2001), the SC (Graham, 1977; Graybiel and Berson, 1980) and the brainstem (Hughes and Mullikin, 1984; Erişir et al., 1997). Knowledge about functional role of these afferents in dLGN processing is limited, but they were suggested to provide modulatory and behavioral context signals, such as locomotion (Erisken et al., 2014; Roth et al., 2016).

The second major class of input are provided by intra-geniculate afferents from local interneurons. Extra-geniculate modulatory signals are frequently transmitted via this inhibitory network. For example, RGC input is frequently arranged in so called triad synapses: direct connections to a geniculo-

cortical excitatory neuron paired with a connected inhibitory neuron (Rafols and Valverde, 1973). This feedforward inhibition is believed to regulate e.g. contrast gain (Sherman, 2004).

1.2.7 Topographic organization of dLGN

In higher mammals, the dLGN is organized into layers that anatomically segregate RGC inputs into their cell-types and ocular origin. Primates have a six-layered organization, each of which can be distinguished based on their afferents' features. The neurons of the first two layers, termed the magnocellular layers, have larger cell bodies and are innervated by RGCs with large RFs (Perry et al., 1984; Dacey and Petersen, 1992). In contrast, the last 4 layers, termed the parvocellular layers, have smaller neuronal cell bodies and receive input from RGCs with smaller RFs (Perry et al., 1984; Dacey and Petersen, 1992). These layers also segregate in their axonal projection positions in layer 4 (L4) of primary visual cortex (V1; (Hubel and Wiesel, 1972)). Furthermore, each dLGN layer receives exclusively monocular retinal input (Tigges and Tigges, 1970): layers 1, 4 and 6 – are contralateral and layers 2, 3 and 5 – are ipsilateral. While the dLGN similarly segregates into three anatomical layers in cat and ferret, rodent dLGN does not laminate (Rafols and Valverde, 1973; Reese, 1988).

Despite its fuzzy network logic (Morgan et al., 2016), mouse dLGN is structurally arranged into multiple overlaying topographic regions. In particular, analogous to higher mammals, the mouse dLGN is retinotopically organized. In rodents, RGC inputs are anatomically arranged according to their retinal position ((Reese and Jeffery, 1983; Reese, 1988); for more recent reviews see e.g. (McLaughlin and O'Leary, 2005; Huberman et al., 2008)), leading to a topographic processing of visual information in the dLGN that mimics the retina. Furthermore, RGC axons terminate in non-overlapping eye-specific zones (Reese, 1988; Coleman et al., 2009; Dhande et al., 2011). The ipsilateral termination zone lies in the dorsomedial part of the geniculate nucleus, which retinotopically represents the binocular visual field. The remaining dLGN is targeted by contralateral RGC axons. These contra afferents specifically avoid the ipsilateral projection core with some overlap at the ipsi borders, resulting in largely segregated eye-specific projection zones. Lastly, the dLGN can be subdivided into a dorsolateral shell and a core region. While, biochemically, cells in the shell are enriched in the calcium binding protein calbindin-D28k (Grubb and Thompson, 2004), the shell region also receives the majority of SC input (Grubb and Thompson, 2004; Bickford et al., 2015). Recently the shell has further been shown to receive direction selective RGC input (Huberman et al., 2009; Kim et al., 2010). In summary, the topographic arrangement of multiple features in mouse dLGN suggests organized processing of visual information, despite the absence of anatomical layers.

1.2.8 Geniculo-cortical projections

Onwards from the LGN, visual information is transferred to V1, a laminar six-layered structure (for review on the neocortical circuit see e.g. (Harris and Shepherd, 2015)), where visual information is processed and integrated in a hierarchical fashion. The geniculate signals mainly reach V1 via the thalamo-recipient L4, although dLGN axon terminals also project to a lesser degree into lower layer 2/3 (L2/3), layer 6 (L6) and layer 1 (L1) (Hubel and Wiesel, 1972; Antonini et al., 1999; Cruz-Martín et al., 2014; Harris and Shepherd, 2015; Ji et al., 2015). L1 projections have been speculated to be a primary target of direction selective neurons located in the dLGN shell (Cruz-Martín et al., 2014). In stark contrast to other sensory areas such as barrel cortex, excitatory L4 in V1 consists almost exclusively of pyramidal cells, with a negligible fraction of stellate cells (Scala et al., 2019). In the mouse, L4 is the first location of major integration of visual information, such as RF features, by geniculo-cortical convergence (see section "1.4 Geniculo-cortical convergence: Hubel & Wiesel" for

more detail). In particular, many of the L4 cells have RFs that are elongated in one axis. They typically consist of parallel, adjacent, sign opposing subfields (ON and OFF), that are arranged in a dampened 2D sine plane wave, which can be best approximated by the Gabor function ((Jones and Palmer, 1987a) see methods section "2.20.7 Two-photon imaging – Receptive fields"). They are often referred to as Gabor-like RFs, and the cells are called simple cells, as their RFs can be easily mapped with oriented bar or patch stimuli. In other words, their RF structure predicts their response to visual stimuli. In subsequent cortical layers, these RFs become increasingly more complex, to the point where their RFs cannot be easily mapped with simple stimuli anymore. These cells are termed complex cells, and their RFs are believed to be computed by directional convergence of simple cells (Hubel and Wiesel, 1962; Alonso and Martinez, 1998). However, simple and complex cells might be more of a continuum, rather than two discrete groups (Mechler and Ringach, 2002). Furthermore, most cells are sharply tuned to certain orientations or directions in visual space, and show various degrees of binocularity. These visual features are subsequently integrated into increasingly more complex visual representations by sequential convergence in a hierarchical manner. With the exception of direction selective RGCs, L4 represents the first stage of major visual integration and emerging feature selectivity along the visual pathway.

The flow of visual information through the six layers of V1 follows a canonical circuit (Douglas et al., 1989; Douglas and Martin, 1991), which is mostly stereotypical across cortical areas and between mammalian species. While the cortex of higher mammals is organized in distinct columns, in mice this columnar architecture is absent ((Mrsic-Flogel et al., 2007), but see (Ji et al., 2015; Kondo et al., 2016; Maruoka et al., 2017)). Information from thalamo-recipient L4 reaches L2/3 cells in a feedforward fashion via their basal dendrites (Thomson et al., 2002). Here, the visual information is locally processed by specific horizontal connectivity to adjacent L2/3 cells that code for similar visual features, the so called "like-to-like connectivity" (Gilbert and Wiesel, 1989; Ko et al., 2011, 2013; Lee et al., 2016b). Next, this information is passed on to higher visual areas via long-range connections (e.g. (Glickfeld et al., 2013)) and locally to layer 5 (L5) cells. From L5, this information is distributed to the opposite hemisphere, L6 and subcortical regions. These subcortical regions are also targeted by L6, providing cortical feedback signals to e.g. dLGN (Olsen et al., 2012).

1.2.9 Topographic organization of V1

Similar to dLGN, V1 is retinotopically arranged (for mice see (Dräger, 1975; Wagor et al., 1980; Schuett et al., 2002)), an organizational principle that is conserved between mammals. This retinotopic organization originates from the spatial organization of dLGN axon innervation with respect to retinotopic RF location (see (Roth et al., 2016) for retinotopic tracing). Although in V1 RF features are integrated into larger and more complex RF structures, neurons still preferentially respond to restricted regions in visual space (Hubel and Wiesel, 1959, 1968; Dräger, 1975). This representation of visual space is, however, non-uniform. Specifically, the distance between two points on the retina is not represented as a constant distant on the V1 cortical surface. Rather, the size of V1 RFs increases with eccentricity (Hubel and Wiesel, 1974a), leading to an overrepresentation of the central visual field compared to peripheral regions. The ratio between the distance of two points in visual space and their representation on the cortical surface is called cortical magnification factor (Cowey and Rolls, 1974). This non-uniform representation across the cortical surface is especially evident in higher mammals, such as primates (Talbot and Marshall, 1941; Daniel and Whitteridge, 1961; Cowey, 1964; Rolls and Cowey, 1970; Hubel and Wiesel, 1974a; Dow et al., 1981; Van Essen et al., 1984) and cats (Hubel and Wiesel, 1962; Tusa et al., 1978), where the central retinal field around the fovea or *area*

centralis is greatly overrepresented in V1. In mice, the cortical magnification factor is more constant as a function of eccentricity. Nonetheless, their binocular visual field is disproportionally overrepresented compared to the contralaterally innervated monocular region (Bleckert et al., 2014; Garrett et al., 2014). This retinotopic arrangement is vertically preserved throughout the cortical layers, due to its inherent columnar arrangement and processing.

In many higher mammals, V1 is even further arranged in multiple topographic maps of a variety of visual features. These are arranged as functional columns, spanning cortical layers, that show a continuous feature progression along the cortical surface. This organization was first famously shown by David Hubel and Torsten Wiesel, who found that neighboring cells in the cat tended to have the same preferred orientation (PO; (Hubel and Wiesel, 1962)) using electrophysiology. They later found a continuous columnar progression of PO along the cortical surface (Hubel and Wiesel, 1974b; Hubel et al., 1977). Subsequently, with the advent of optical imaging techniques, these PO maps across the cortical surface were visualized in great detail (Blasdel and Salama, 1986) and shown to be arranged around pinwheel centers (Swindale et al., 1987; Bonhoeffer and Grinvald, 1991; Ohki et al., 2006). These functional maps for PO are further complemented by topographical maps for other visual features, such as ocular dominance (OD; Hubel and Wiesel 1962, 1969; Wiesel et al. 1974; LeVay et al. 1975; Shatz et al. 1977), preferred direction (PD; Payne et al. 1981; Weliky et al. 1996) and spatial frequency (SF; Tootell et al. 1981; Bonhoeffer et al. 1995). Overall, these maps are intricately arranged across each other to provide a complete orthogonal feature coverage (Hübener et al., 1997; Swindale et al., 2000).

Rodents, in contrast, do not exhibit comparable maps for OD, PO, PD and SF (Ohki et al., 2005; Mrsic-Flogel et al., 2007; Bonin et al., 2011). Instead, with the exception of OD, these neuronal representations are randomly scattered, the so called “salt-and-pepper” organization (Dräger, 1975; Antonini et al., 1999; Schuett et al., 2002; Ohki et al., 2005; Mrsic-Flogel et al., 2007; Kondo et al., 2016; Ringach et al., 2016; Maruoka et al., 2017). Nonetheless, neurons exhibit feature tuning similar to higher mammals (Métin et al., 1988; Niell and Stryker, 2008), suggesting that topographical arrangement is not an inherent requirement for feature selectivity (Ohki and Reid, 2007; Kaschube, 2014; Weigand et al., 2017). This would, however, have impacts on achieving like-to-like connectivity. Instead of local postsynaptic pooling, a more precise functional connectivity rule would be necessary (Harris and Mrsic-Flogel, 2013). One possible explanation for the lack of arrangement is the decreased number of neurons, representing visual space. As rodent RFs are bigger, single neurons cover more of the visual scene. Therefore, a pinwheel-like arrangement of PO would lead to biased feature coverage of space. In other words, instead of investigating each part of the visual field with multiple feature filters, certain parts would only be interrogated for certain orientations in space (Kaschube, 2014). This would likely lead to detrimental biases in processing the visual environment. However, despite being widely accepted, the salt-and-pepper map might not truly be randomly arranged. Several recent studies have found hints towards possible micro and macro organizations in rodents, such as OD patches (Laing et al., 2015; Andelin et al., 2020) and a global map of orientation tuning (Fahey et al., 2019).

1.2.10 Mouse as a model organism for visual neuroscience

Mice are nocturnal animals with comparably low visual acuity compared to most higher mammals. Taken together with their lack of topographical maps in visual cortex – with the exception of

retinotopy – and decreased binocular visual overlap, their use as a model organism in vision research has been criticized. However, recent findings have started to shift this viewpoint.

Similar to higher mammals, the mouse visual system is hierarchically organized into multiple specialized visual areas (Dräger, 1975; Schuett et al., 2002; Wang and Burkhalter, 2007; Niell and Stryker, 2008) resembling the dorsal and ventral visual streams in primates (Gao et al., 2010; Wang et al., 2011, 2012). While early studies postulated the rodent visual system was mostly used in reflex-like behaviors for stabilizing the visual scene, such as the optokinetic reflex (Stahl, 2004) and optomotor response (Prusky et al., 2004), more recent work has started to implicate its role in more complex and intricate behaviors. These behaviors can be split into two groups: innate and learned behaviors. For example, to avoid aerial predators, mice show an innate fear and escape response to overhead looming visual stimuli (Yilmaz and Meister, 2013; Shang et al., 2015; Wei et al., 2015). Further, despite their small binocular visual overlap, mice may compute depth (Scholl et al., 2013; Samonds et al., 2019) from binocular disparity signals (Scholl et al., 2013; La Chioma et al., 2019, 2020; Samonds et al., 2019). Mice can further learn to use visual cues for navigation (Morris, 1984; Douglas et al., 2006; Glas et al., 2021), categorization (Reinert et al., 2021) and can be trained to discriminate between different visual stimuli (Bussey et al., 2001; Morton et al., 2006; Oomen et al., 2013). Mouse vision has also been shown to play an important role in naturalistic behaviors, such as prey capture (Hoy et al., 2016; Park et al., 2018). Overall, despite their low visual acuity and several differences in topographic arrangement, the structure and processing of the early steps in visual processing of mice resemble the hierarchical architecture of higher mammals. Taken together with their superior genetic access, mice present an attractive model organism for studying the first stages of visual processing.

1.3 Coding in the geniculo-cortical circuit

Although many of the visual properties of cells in the dLGN and L4 of V1 have been mentioned in the previous chapter, it is important to understand these properties and their relationship in more detail in the context of this study.

1.3.1 Ocular Dominance

Eye preference describes which eye-input drives the output of a visually responsive cell the most. While this metric may be sufficient to describe ocular properties of the majority of cells in the visual thalamus, it fails to fully represent the intricacies of binocular integration in later processing stages, such as visual cortices. This specifically applies to cells processing the binocular visual field. In contrast to eye preference, Ocular Dominance describes the relative contribution of each eye in driving the output of a visually responsive cell, therefore capturing ocular integration in more detail. In this context, instead of their anatomical position (left and right), eyes are referred to in relation to the hemisphere of the cell of interest: ipsilateral (same side) and contralateral (opposite side). To capture the gradient of OD in binocular cells, an ocular dominance index (ODI) is calculated, that ranges from -1 (purely ipsilateral) to 1 (purely contralateral), with 0 being perfectly binocular (see methods section “2.20.5 Two-photon imaging – Ocular Dominance” for more detail).

1.3.2 Receptive Fields

Ipsilateral, contralateral and binocular cells do not have access to the entirety of the respective eye’s retinal field, but rather only a specific region in retinal space. This confined region in visual space is called the receptive field of a cell. While RFs in early processing stages, such as the retina and dLGN, are usually rather small, their size increases along the visual pathway by hierarchical integration of visual information. They also show different shapes, such as circular in the retina and dLGN, elongated

Gabor shapes in cortical simple cells, and more complex patterns later in the visual processing hierarchy, such as in cortical complex cells. As described in the previous chapter, RFs usually consist of subfields of opposing polarity. The so called ON fields react to light increments and OFF fields react to light decrements. These opposing subfields are usually arranged in close proximity in visual space to detect local contrast. While the circular RFs in early processing stages consist of a characteristic center-surround architecture with either an ON center and OFF surround or vice versa, simple cells have their elongated subfields arranged parallel in visual space. The latter results in an alternating pattern, which can be best approximated by a dampened sinusoidal wavelet following the so called Gabor function (see methods section "2.20.7 Two-photon imaging – Receptive fields"). In later processing stages, cells react to specific and more complex features within their respective RF, similar to a filter. It is generally believed that cortical simple cells represent the first point in visual processing where cells become selective for visual features, specifically the orientation and direction of motion of edges (but see direction selective RGCs (Barlow and Hill, 1963; Barlow et al., 1964)). Therefore, to map the underlying RF shape without its filters sparse noise stimulation is used. In this stimulus, visual space is subdivided into small rectangles, which are sequentially presented in random fashion to probe visual space. This is usually combined with a criterion, excluding the subsequent presentation of adjacent squares, so as to avoid presenting any local patterns. By recording at which positions each cell responded, their RF can be approximated.

1.3.3 Orientation- and Direction Tuning

One of these local, visual filtering properties was discovered in layer 4 of cat visual cortex by Hubel and Wiesel more than 60 years ago (Hubel and Wiesel, 1959). They found that cells preferentially respond to local edges of specific orientation in visual space with a lot of activity, their so called PO (Fig. 1.1A). If Hubel and Wiesel changed the angle of these edges away from their PO, their response strength would quickly fade off as a function of angular displacement. In other words, these cells are orientation selective (OS) and therefore act as a local edge-detector. The location of the detector in visual space is hereby given by their respective RF location. In simple cells, the PO further aligns with the elongation of the RF (Hubel and Wiesel, 1959, 1962). This observation gave rise to the notion that the elongated RFs set the orientation tuning of these cells, and they do so by forming an oriented edge between their ON and OFF subfields, therefore introducing an orientation bias by eliciting the strongest responses if their RFs are covered by aligned edges of the same polarity in visual space (Hubel and Wiesel, 1959, 1962). While this is widely accepted in simple cells, this notion breaks down in complex cells, where the complex RFs cannot predict the highly tuned PO anymore (Hubel and Wiesel, 1962), arguing for separate propagation of these features. Additionally, some simple cells respond selectively to movement of edges perpendicular to their RF elongation and consequently along their subfield displacement direction, mediated by the spatial and temporal RF components (Watson and Ahumada, 1983; Adelson and Bergen, 1985; Reid et al., 1987). These cells can show diverse levels of tuning for orientation and direction. This level of tuning was classically quantified with an orientation (OSI) or direction selectivity index (DSI), reflecting the relationship between the response of the PO/PD to its opposite angle or direction. As this neglects large parts of the tuning curve, in recent years the tuning index is calculated based on the circular variance of the entire tuning curve (Mazurek et al., 2014). Both metrics are distributed from 0 to 1, with 1 being highly selective and 0 being non-selective. Interestingly, the dLGN inputs to simple cells do not only have circular RFs, but are also largely unselective to orientations in space, which raises the question on how visual stimulus selectivity is first computationally constructed.

1.4 Geniculo-cortical convergence: Hubel & Wiesel

Ever since Hubel and Wiesel discovered the discrepancy between the OS, elongated RFs of cortical simple cells and the lack of elongation and selectivity of their presynaptic geniculate neurons (Fig. 1.1B), this circuit became a classic example of studying the emergence of stimulus selectivity in the brain. While cortex could attain stimulus selectivity de-novo, such a transformation would be computationally complex. Instead, Hubel and Wiesel suggested a simple feedforward connectivity scheme by which this transformation could be computed from the geniculate inputs, thereby reducing the complexity of this transformation to a simple linear summation (Hubel and Wiesel, 1962). Specifically, based on electrophysiological data, they proposed that LGN cells converging onto individual cortical simple cells have their round RFs linearly aligned in visual space (Fig. 1.1C). Consequently, the sum of a simple cell's presynaptic LGN inputs would yield an elongated RF, resulting in OS tuning parallel to the RF elongation. Hence, the emergence of stimulus selectivity would be determined by the functional connectivity logic of geniculo-cortical convergence, rather than an intrinsic cortical de-novo computation. Ever since, many have followed in their footsteps, trying to prove or disprove their feedforward circuit prediction.

1.4.1 Support for the Hubel & Wiesel model

The strongest support in favor of their model was provided by three studies that removed spiking activity in visual cortex neurons so as to isolate the electrical activity of thalamo-cortical afferents (Chapman et al., 1991; Ferster et al., 1996; Chung and Ferster, 1998). In each experiment, the respective authors compared the orientation tuning before and after cortical inactivation. The first study recorded activity of cortical columns extracellularly while chemically inactivating cortical spiking using the gamma-Aminobutyric acid (GABA) agonist muscimol in ferrets (Chapman et al., 1991). The remaining two studies used intracellular recordings of subthreshold signals in cortical V1 cells in L4 of cat and silenced cortical activity using either cooling (Ferster et al., 1996) or electrical stimulation (Chung and Ferster, 1998). Jointly, these studies showed that orientation preference in simple cells did not change after removing cortical spiking. Although their findings do not rule out a possible involvement of cortical circuits in sharpening the orientation tuning, they were able to show that the orientation preference is set by the thalamic inputs in a feedforward fashion. Moreover, in the first study Chapman and colleagues additionally mapped RFs, and were able to show that LGN axons that project to the same cortical column in V1 have their RFs aligned in visual space, just as proposed by Hubel and Wiesel. Further support was provided by experiments using electrical recordings that cross-correlated the RF activity of LGN – simple cell pairs. They revealed that cortical simple cells not only receive functional inputs from ON- and OFF-center LGN cells, but that simple cell RF subfields are specifically driven by them (Tanaka, 1983; Alonso et al., 2001). This connectivity seemed to be further RF-polarity specific: the estimated connection probability and synaptic strength was higher in LGN – simple cell pairs with overlapping RF subfields of the same polarity than for pairs with non-overlapping or overlapping, but opposing, subfields (Reid and Alonso, 1995). Lastly, when summing up RFs of LGN cells projecting to the same cortical column, this population RF matched the PO of that respective column (Jin et al., 2011).

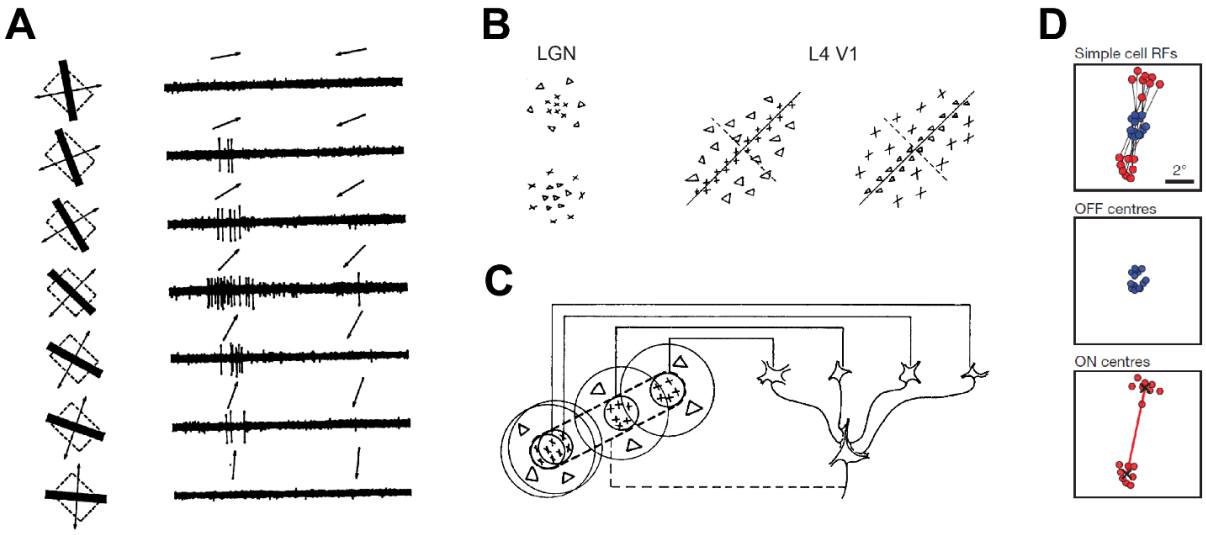

Figure 1.1: **Models on the functional logic of retino-geniculate convergence. A|** Spiking activity of a direction selective L4 cell in response to a bar moved across the cell's receptive field. Reprinted with permission from (Hubel and Wiesel, 1968). **B|** Receptive fields of two circular center surround receptive fields in the lateral geniculate nucleus (left) and two elongated simple cell receptive fields in layer 4 of primary visual cortex (middle and right). Adapted with permission from (Hubel and Wiesel, 1962). **C|** Original model by David Hubel and Torsten Wiesel on the generation of orientation selectivity via elongated simple cell receptive fields from circular geniculate receptive fields by selective feedforward functional convergence. LGN cells converging onto individual cortical simple cells have their round RFs linearly aligned in visual space, thereby reducing the geniculo-cortical transformation to a linear summation. Reprinted with permission from (Hubel and Wiesel, 1962). **D|** Alternative model for the generation of orientation and direction selectivity by ON-OFF subfield segregation. OFF subfields set the retinotopic position while the orientation of ON subfields around OFF centers sets the orientation preference. Adapted with permission from (Lee et al., 2016a).

1.4.2 Arguments against the Hubel & Wiesel model

While both RFs and PO seem to be set by LGN inputs, not all tuning intricacies are likely driven by pure feedforward geniculo-cortical convergence, but instead involve modulation by further circuit motifs. The slight broadening of orientation tuning after cortical inactivation (Ferster et al., 1996) already hinted at a possible cortical role in sharpening the LGN-inherited tuning. This sharpening of simple cell tuning over time was convincingly illustrated with electrical recordings in monkeys subsequent to very brief visual stimulation (Ringach et al., 1997). The initially broad orientation tuning sharpened after a short delay, indicating the cortical circuits kicking in to shape the broad orientation tuning inherited from LGN. In this line, optogenetic silencing experiments indicated that cortical excitatory circuits take over the thalamo-cortical inputs as early as several milliseconds after stimulus onset (Reinhold et al., 2015). The relative influence of recurrent cortico-cortical versus cortico-thalamic excitatory circuits in modulating orientation tuning is still debated. This is further complicated by the involvement of inhibitory circuits. While early studies demonstrated the disruption of OS after application of the GABA antagonist bicuculline (Sillito, 1975), more recently somatostatin expressing interneurons have been identified as inhibitory drivers (Adesnik et al., 2012).

1.4.3 Alternative and complementary models

More recently, two studies suggested an alternative hypothesis on how OS and direction selectivity (DS) emerge in simple cells (Kremkow et al., 2016; Lee et al., 2016a). Instead of geniculo-cortical convergent alignment of RFs in visual space, they propose that simple cells receive clustered, segregated ON-center and OFF-center input (Fig. 1.1D). Hence, OS is not dictated by the orientation of RF subfield elongation, but rather by the orientation of ON OFF subfield segregation in space.

Therefore, the orientation and direction tuning is set by the directional displacement of RF subfields of opposing polarity in visual space. Consequently, orientation tuning is set to be perpendicular to the ON-OFF displacement angle. More specifically, the dominant OFF pathway sets the retinotopic location, while the orientation of ON subfields around the OFF center determines the OS and DS. While this model presents an alternative circuit mechanism for the emergence of OS and DS, both models are, however, not necessarily mutually exclusive. Rather, it is possible that both can coexist in shaping orientation tuning in V1 simple cells.

1.4.4 Need for a comprehensive dataset

These studies represent the most convincing data in favor or against the circuit behind the emergence of OS, to date. However, despite being widely accepted and reproduced in almost every neuroscience textbook, conclusive proof in favor or against this model is still lacking today, almost 60 years after the original proposal by Hubel and Wiesel.

One major complication is the unification of the incremental experimental findings that are spread over a multitude of studies, conducted on a variety of species, and with an assortment of methods. While the general architecture, flow of information and computations in early visual processing are similar between species, the possible impact of differences in e.g. eye lateralization, visual acuity, dLGN layers, emergence of OS at different locations and topographic organization of visual cortex on geniculo-cortical convergence should not be neglected. Especially in the latter case, a pinwheel in contrast to salt-and-pepper arrangement could have major implications on the precision needed for achieving a distinct functional connectivity (Harris and Mrsic-Flogel, 2013). This disjunct experimental landscape highlights the need for a comprehensive and cohesive dataset in a single species in order to make conclusive statements about the functional logic behind the emergence of cortical OS.

So far, the majority of past studies have focused their efforts on population-scale investigations (e.g. a cortical column). However, to decisively test the predictions made about the functional logic of RF convergence by Hubel and Wiesel (or proposed alternative models) one needs to investigate the circuit in more fine-grained detail: at the level of individual cells and synapses. For a conclusive investigation of the functional convergence logic, one needs two components, already hidden in Hubel and Wiesel's seminal sketch: function and connectivity. More specifically, one needs to know the RF properties of both dLGN neurons and their postsynaptic simple cells as well as their interconnections. However, so far function and structure have for the most part been investigated in isolation. I am confident that by combining both, a concept termed "functional connectomics" (Reid, 2012), it would yield a dataset with all necessary components for resolving this circuit's functional convergence logic, which has remained mostly elusive for neuroscientists thus far. In this study I tackled this question by developing an experimental pipeline that combines the functional readout of *in vivo* two-photon calcium imaging with the high-resolution structural readout of the underlying circuit wiring using serial section 3D-EM. Although some early attempts of this technique have been successfully deployed previously (Bock et al., 2011; Briggman et al., 2011), their experimental use was limited to the investigation of local connectivity in small neuronal volumes. I believe that recent technological advancements have brought the development of a functional connectomics pipeline for analysis of long-range circuits (such as geniculo-cortical convergence) into the realm of possibility.

1.5 Technological advances towards 2P-EM functional connectomics

1.5.1 From electrodes to optics

Traditionally, neuronal function has been measured with electrophysiological recordings. While it remains the gold standard in terms of temporal resolution, studying the spatial arrangement of many neurons with respect to their function and tracking them over long periods of time is often not feasible. Furthermore, combining electrophysiology with specific genetic targeting remains challenging. Although the recent development of Neuropixels probes (Jun et al., 2017; Steinmetz et al., 2021) has made strides towards multi-channel electrical recordings, the concern about the invasive impact to the neuronal ultrastructure being targeted remains. Instead, in recent years, neuroscience research has pivoted to less invasive optical microscopy methods for imaging large numbers of neurons (function and structure) chronically over time with high spatio-temporal precision. This was mainly enabled by the parallel development of fluorescent indicators and two-photon microscopy.

1.5.2 How to see neuronal function

Neuronal signals propagate inside a cell via quick, transient changes in membrane potential. Ideally, one would therefore optically record these changes with voltage-dependent fluorescent molecules. While progress has been made in their development, voltage indicators have several downsides that have made them impractical thus far. These downsides comprise both optical and physiological ones. Instead, neuroscience has opted to read out activity based on a secondary molecule: calcium. Both synaptic input in dendrites and action potentials (APs) induce transient increases in intracellular calcium. These calcium transients have sharp rise kinetics and usually an elongated decay. Therefore, reading out changes in intracellular calcium concentrations can be used as an indirect proxy for neuronal activity (see e.g. (Huang et al., 2021a)). These molecules, so called calcium indicators, are fluorophores that show increased fluorescence upon binding of one or more calcium ions. While their possible impact on cellular physiology in buffering calcium should not be neglected, these effects are of more secondary nature in comparison to voltage indicators, as they e.g. do not need to be membrane-bound, but can rather be cytosolic.

1.5.3 Calcium indicators

Overall, there are two main types of calcium indicators that can be distinguished: synthetic and genetically encoded calcium indicators (GECIs). Synthetic indicators such as Oregon Green BAPTA1 are small molecules that spread by diffusion. While they come with several advantages (e.g. fast binding kinetics and more linear fluorescent representation of calcium concentrations (see e.g. (Rose et al., 2014))), their major drawback is that due to diffusion and their short half-life, they can only be imaged for a finite amount of hours (Stosiek et al., 2003), which makes them impractical for chronic functional imaging. The development of GECIs such as Chameleons (Miyawaki et al., 1997, 1999) or GCaMPs (Nakai et al., 2001) offered a workaround by letting the cells of interest themselves produce the deoxyribonucleic acid (DNA) encoded indicators, leading to a constant replenishment of the indicator pool, and allowing for chronic re-identification of cells and functional readout over months (e.g. Mank et al. 2008; Tian et al. 2009; Lütcke et al. 2010; Horikawa et al. 2010; Chen et al. 2013; Thestrup et al. 2014; Rose et al. 2016). Furthermore, they allow genetic labeling of distinct cell-types, enabling a more targeted approach to dissecting neuronal circuits. However, their mostly non-linear binding kinetics renders them unreliable for inferring the electrical spikes underlying the calcium signal (see Rose et al. 2014) for a comprehensive review). The GECI family of GCaMPs, hybrid protein fusions between a circularly permutated version of the green fluorescent protein (GFP) and the calcium binding protein calmodulin, including its myosin light chain kinase interaction domain M13, have become the major

fluorescent indicators used today. While the 6th generation of GCaMPs (Chen et al., 2013) have become widely used and accepted for routine *in vivo* imaging, several iterations of newer generations (Dana et al., 2016, 2019; Zhang et al., 2020) offer unprecedented potential for combinatorial approaches to circuit investigation.

Red-shifted calcium indicators (Dana et al., 2016; Qian et al., 2019, 2020; Dalangin et al., 2020) such as jRGECO1a – despite lacking the efficiency of their green GCaMP counterparts – have opened up the possibility for deeper optical access, due to decreased tissue scattering of longer wavelengths, as well as combinatorial approaches. Combined with their green counterparts, they could allow for spectrally separate co-labeling of distinct neuronal populations in the same tissue. Importantly, several refined indicator versions have been generated to improve both structural and functional readout of small neurites. Most notably, so called "double-constructs" encode both, green calcium indicators and red-shifted structural fluorophores such as mRuby2 (Rose et al., 2016) in the same DNA plasmid, additionally enabling ratiometric functional imaging (e.g. Rose et al. 2016). While the red activity-uncoupled fluorophore provides excellent structural detail, it cannot be used in combination with red-shifted calcium indicators, as it already uses the red channel. Although new double construct combinations using different emission spectra could be developed, new generation high baseline high signal-to-noise ratio (SNR) GCaMPs such as jGCaMP7b (Dana et al., 2019) bear the potential to not only improve functional imaging of small neurites, but also provide enough activity independent fluorescence for high resolution structural readouts.

1.5.4 Two-photon microscopy

Traditionally, confocal fluorescence microscopy is based on single-photon excitation. This technique, however, comes with several downsides, especially for imaging brain tissue chronically *in vivo*. First, many calcium indicators need to be excited with single-photon energies of wavelengths in the low-wavelength spectrum. While prolonged exposure often leads to fluorophore bleaching, ultraviolet light on its own can cause toxic intracellular photo-damage, such as inducing DNA damage. Therefore, microscopes often opt to scanning the focal plane, rather than constant illumination, to reduce these effects. As a single photon can excite a calcium indicator molecule, excitation is usually not restricted to the focal point, although excitation intensity at the focal point is usually the strongest. To block out these out of focus signals, confocal microscopes usually use a pinhole in the detection path (Denk and Svoboda, 1997). However, due to the strongly non-homogeneous and opaque nature of brain tissue, many of the photons produced at the focal plane do not pass the pinhole due to scattering, rendering the detection efficiency low (Denk and Svoboda, 1997). Due to the wavelength-dependence of tissue scattering – with scattering increasing with lower wavelengths – excitation is even more affected due to the stokes shift (Stokes, 1852). This strongly limits the imaging depths of biological tissue and hence its use *in vivo*.

Multiphoton microscopy (Denk et al., 1990), which is based on multiphoton excitation, tackles these issues (Denk and Svoboda, 1997). Fluorophores are often described as being excited by light of a certain wavelength. However, it is not the wavelength *per se*, but rather the energy the photon carries (which is inversely proportional to the wavelength) that is essential. Specifically, it needs to match the energy difference between the electrons ground-state and exited-state. Two-photon excitation states that, if two photons of half the energy hit the fluorophore within a time window of about 0.5 fs (depending on the fluorophore), their energies add up and induce excitation of the fluorophore (Göppert-Mayer, 1931; Peticolas and Rieckhoff, 1963). Consequently, longer wavelength light can be

used for excitation, reducing scattering, resulting in a more precise focal plane and opening the possibility for deeper imaging (Denk et al., 1994). Additionally, the focal plane precision improves quadratically, as a single photon cannot excite the fluorophore anymore, dramatically reducing out of focus excitation (Denk et al., 1990; Helmchen and Denk, 2005). In other words, as the probability of two photons hitting the same spot within the integration window of the given process decays quadratically as a function of distance from the focal plane, rather than linearly as is the case for a single photon, out of focus excitation is greatly reduced. The improved precision of the excitation plane makes the pinhole redundant, allowing for the collection of many more scattered emission photons, especially using scanning. Since two photons hitting the same molecule is an extremely rare event, high-intensity lasers are used to excite fluorophores in the focal plane and hence increase the probability of emitted fluorescence. Even though the increased wavelength reduces bleaching and toxicity, the required laser-intensities at the focal point for two-photon excitation would quickly heat up the brain, even with scanning. Therefore, to keep high peak intensity while simultaneously reducing average laser power, pulsed lasers are used. Instead of emitting a continuous laser beam, photons are emitted in ultra-short pulses of commonly around 100 fs at a repetition rate of around 80 MHz, allowing the tissue to cool back down in between pulses. Two-photon microscopy, especially in potent combination with calcium indicators to measure neuronal activity (Yuste and Denk, 1995; Svoboda et al., 1997; Stosiek et al., 2003) has revolutionized modern neuroscience, enabling unprecedented optical access to the brain. Recent improvements, most notably adaptive optics (Sun et al., 2016) and three-photon microscopy (Horton et al., 2013; Ouzounov et al., 2017) have pushed the optical access even deeper into the brain. However, thalamic nuclei such as the dLGN remain optically inaccessible. While there have been several invasive workarounds to gain functional optical access to deeper brain regions, such as microendoscopes (Jung and Schnitzer, 2003; Jung et al., 2004; Levene et al., 2004; Ghosh et al., 2011; Murray and Levene, 2012) or partly aspirating overhead brain tissue (e.g. (Mizrahi et al., 2004; Dombeck et al., 2010; Pilz et al., 2016)), the field has moved towards less invasive approaches. One of the most promising is imaging axonal terminals at their postsynaptic site of connectivity, instead of their cell bodies. In the context of this study, this permits access to dLGN function directly at the main thalamo-recipient layer 4 in V1. Prior to this study, dLGN axon imaging has been demonstrated *in vivo*, especially in L1 (Roth et al., 2016; Sun et al., 2016; Jaepel et al., 2017), although orientation tuning has also been mapped in L4 (Sun et al., 2016; Broussard et al., 2018). However, investigations of OD and mapping of spatial RFs with sparse noise stimulation has been lacking until recently. Using the optimizations for imaging dLGN axons in L4, described in this thesis, we were able to efficiently extract high-quality functional response properties (Bauer et al., 2021).

In conclusion, *in vivo* two-photon microscopy, especially in combination with the new generation of high-baseline, high SNR GECIs, enables high-quality readout of both function and structure for not only cell bodies, but also their fine neurites deep in cortical tissue. Furthermore, the development of red-shifted GECIs has opened the door for spectrally separate labeling and readout of two distinct neuronal populations within the same preparation.

1.5.5 Roads to connectivity

"If you want to understand causality in the brain, you need to understand the connections. Activity measurements are important, but the agents of causality are the wires connecting to the cell […]. To understand computations, you need to understand the flow of information." – Winfried Denk

While light-microscopy based techniques provide an excellent tool for visualizing both function and structure, their spatial resolution is subpar for investigation of connectivity, as small neurite segments

such as axons and spine necks are down to 50 nm thin. Despite the invention of super-resolution (Moerner and Kador, 1989; Hell and Wichmann, 1994; Betzig, 1995; Hell and Kroug, 1995; Klar et al., 2000; Betzig et al., 2006) and expansion microscopy (Chen et al., 2015), it remains impossible to verify synaptic connectivity based on sparsely labeled neuronal structure using light microscopy with high confidence. Similarly, these small neurites elude new techniques such as nano computer tomography (Kuan et al., 2020) for dense visualization of neuronal structure. While the traditional method of paired patch clamp recordings offers a reliable readout of functional connectivity, its invasive nature and low throughput prevents a scalable readout. Genetic approaches such as monosynaptic rabies tracing (Ugolini, 1995; Card and Enquist, 2001; Wickersham et al., 2007a; b; Marshel et al., 2010; Rancz et al., 2011; Vélez-Fort et al., 2014) and proximity based synapse markers (Kim et al., 2012; Macpherson et al., 2015; Talay et al., 2017; Choi et al., 2018; Perez-Alvarez et al., 2020), have reignited excitement about light-microscopy-based readouts of connectivity. However, they suffer from multiple downsides (see discussion section "4.1 Alternative approaches to functional connectivity?" for more detail) for application in mammals *in vivo*. While they can provide valuable insight into connectivity on a population level, they lack the precision for single cell resolution connectomics. Therefore, the only technique that allows for dense, precise and high-resolution investigation of neuronal connectivity to date is 3D-EM. Although tedious to both acquire and analyze, its superior resolution based on the use of electrons instead of light makes it the gold standard for visualization of dense circuit connectivity.

1.5.6 3D electron microscopy

Biological tissue is *per se* not very electron dense and would not yield a great contrast if investigated with electron microscopy (EM). Therefore, biological tissues – more specifically phospholipid membranes – are stained with heavy metals such as Osmium (Palade, 1952), Uranium (Watson, 1958) and Lead (Venable and Coggeshall, 1965) to enhance conductivity and contrast, as electron diffraction increases with the atomic number of elements (Crewe et al., 1970; Yamashita et al., 2018). Traditionally, ultra-thin sections were stained for transmission electron microscopy (TEM) after ultra microtomy. However, in the past two decades the field has shifted its focus to *en bloc* staining protocols, as staining pre-cut sections can result in deformations, damage and precipitation of electron dense clumps, deteriorating the quality of electron micrographs (Kasthuri et al., 2015; Zheng et al., 2018). While *en bloc* staining yields more homogeneous staining with less stress on the biological tissue, homogeneously staining large volumes remains challenging, as these staining protocols are based on diffusion, often resulting in staining gradients and therefore deteriorating contrast towards the tissue core. In recent years, substantial progress has been made building on top of early staining protocols (Seligman et al., 1966; Walton, 1979; Willingham and Rutherford, 1984), to both improve contrast and stainable volumes of neuronal tissue (Briggman et al. 2011; Mikula et al. 2012; Hua et al. 2015; Loomba et al. in revision, Song et al. in preparation).

While EM provides significantly superior in-plane resolution, electrons do not penetrate deep into heavy metal stained tissue without extreme scattering (Hennig and Denk, 2007). Consequently, the axial resolution is very restricted. Therefore, simply shifting the focal plane axially to result in a high-resolution 3D image is intractable. Instead, many thin 2D planes are sequentially acquired by tissue ultra-sectioning and post-hoc re-aligned in 3D. Today, there are several different approaches to 3D-EM, each having up- and downsides, which have to be carefully considered prior to experimentation and adapted to the requirements of the experimental question. Generally, two types of electron microscopes can be distinguished based on imaging modality: the traditional TEM (Knoll and Ruska, 1932) and scanning electron microscopy (SEM, (Von Ardenne, 1938)). Modern TEM uses high electron

landing energies to detect forward scattering electrons on the opposite site of the tissue (Fig. 1.2A) using charged-coupled device detectors (Bock et al., 2011). In contrast, SEM uses low electron landing energies, detecting backward scattering or secondary electrons using either solid state detectors or scintillator based photomultipliers. Due to their low energies in SEM, the electrons have less momentum and are therefore strongly affected by the electrostatic field of the positively charged heavy metals in the stained tissue, leading to backscattering. Taken together with the lack of required transmission, SEM can be employed on a tissue block directly, avoiding the necessity of cutting and maintaining stable ultrathin sections. This advantage has led to several approaches revolutionizing tissue sectioning for 3D-EM (see (Briggman and Bock, 2012) for comprehensive review of different 3D-EM techniques). While, traditionally, the tissue had to first be sliced into intact, ultrathin sections (Birch-Andersen, 1955; Bang and Bang, 1957; White and Hersch, 1982; White et al., 1986; Harris and Stevens, 1988), SEM allowed for blockface-based approaches (Fig. 1.2B-D), integrating the microtome and imaging process. This made non-destructive sectioning obsolete, greatly reducing the complexity of ultra-thin sectioning and reducing sectioning-induced tissue deformations. The first serial blockface electron microscopy (SBEM) used a diamond knife in the SEM chamber for removing ultrathin layers down to 20 nm from the tissue block in between imaging (Leighton 1981; Denk and Horstmann 2004; Fig. 1.2B). More recent iterations have opted for focused ion beams instead, to ablate even thinner tissue layers down to 4 nm using evaporation (Heymann et al. 2006; Knott et al. 2008; Fig 1.2C). While focused ion beam SEM provides the most isotropic voxel resolution, it can, however, only be applied in small in-plane field-of-views (FOVs) due to tissue-milling inconsistencies for larger FOVs. Several recent development such as gas cluster ion beam milling (Hayworth et al., 2020) in combination with hot knife sectioning has shown great promise towards bridging this gap. However, the ever-increasing volume requirements for larger-scale connectomic analyses (Briggman et al., 2011; Helmstaedter, 2013; Kasthuri et al., 2015; Morgan et al., 2016; Schmidt et al., 2017; Motta et al., 2019) beyond a cubic millimeter (Yin et al. 2020; Shapson-Coe et al. 2021; MICrONS Consortium et al. 2021; Sievers et al. in preparation) are beginning to push current-state blockface techniques beyond their limit. On these experimental scales, encountering imaging issues during an experiment becomes increasingly likely. Due to the destructive nature of blockface-sectioning in these techniques, re-imaging is not possible, causing detrimental gaps in neuronal continuity. More recently, the field has returned to the original strategy of separating the cutting and imaging processes. In support of this goal, several important advancements have been made to aid the acquisition of cubic millimeter size volumes. First, the reliability and stability of non-destructive microtome sectioning has been greatly improved by automated tape collecting ultra-microtomes (ATUM, (Hayworth et al., 2006, 2014); Fig 1.2D). Here, cut sections are automatically collected from the diamond knife via a waterbath onto a tape using a tape-reel system, eliminating tedious and error-prone manual placement of section onto EM grids traditionally used for serial section TEM (e.g. (Birch-Andersen, 1955; Bang and Bang, 1957; White et al., 1986)). Together with recently developed secondary electron detecting multibeam-SEM (mSEM, (Eberle et al., 2015)), which greatly increases the imaging speed by using 61-91 parallel electron beams, they can be combined to form a potent experimental pipeline for efficient acquisition of large EM volumes.

Taken together, recent improvements in both *en bloc* staining, ultra-microtomy and electron microscopes bear great promise for further development. This provides the field with the experimental means to investigate larger neuronal volumes on scales that will enable in depth, dense connectomic investigations of neuronal circuits.

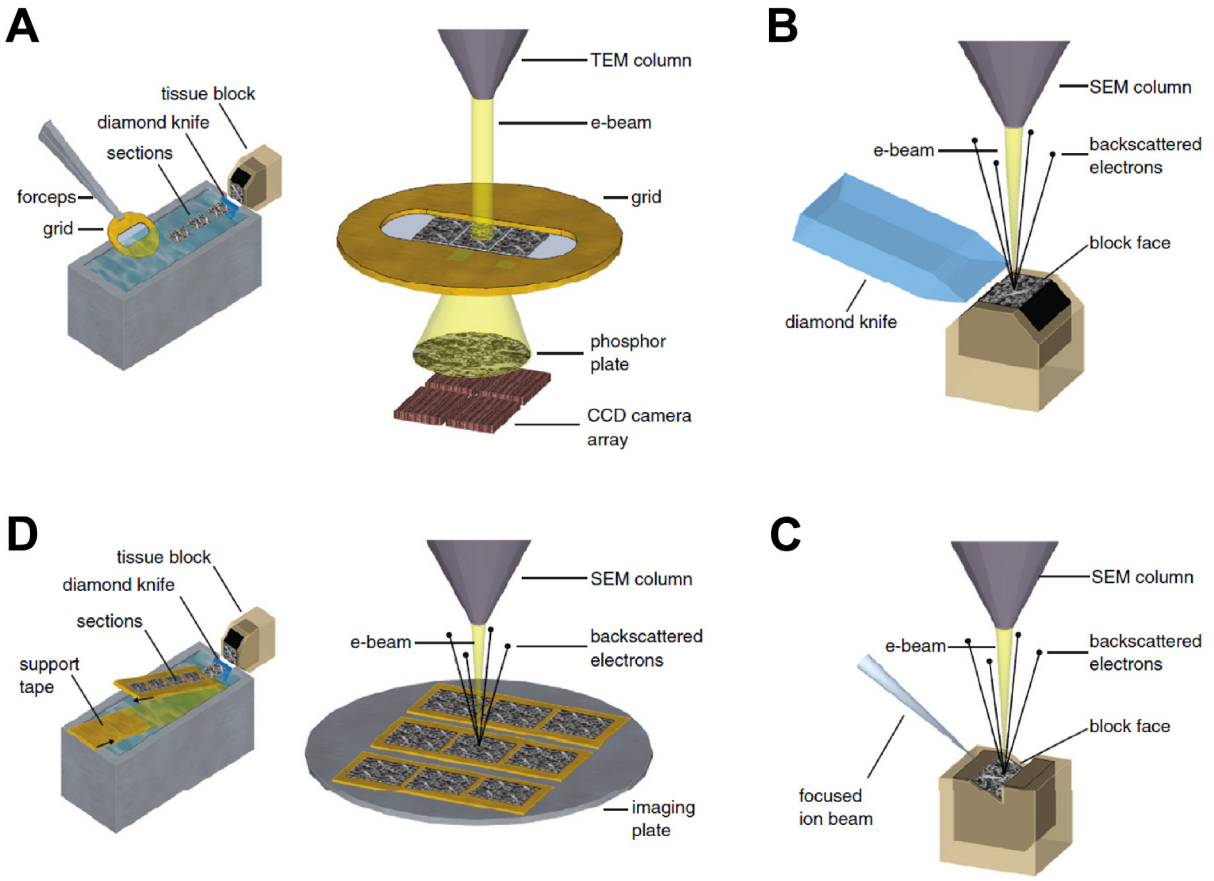

Figure 1.2: **3D Electron Microscopy techniques for reconstruction of neuronal ultrastructure. A|** Sequential diamond-knife based ultra microtomy with manual collection of serial sections on grids (left) and high speed CCD camera based serial section transmission electron microscopy (right). **B|** Interlaced ultra-sectioning and blockface scanning electron microscopy by integration of a diamond-knife based microtome into the imaging chamber. **C|** Interlaced ultra-sectioning and blockface scanning electron microscopy by integration of a focused ion beam miller into the imaging chamber. **D|** Sequential diamond-knife based ultra microtomy with automated collection of serial sections on tape (left) and scanning electron microscopy (right). Adapted with permission from (Briggman and Bock, 2012).

1.5.7 Towards automated data processing of petabyte-scale EM datasets

3D-EM results in millions of individual 2D raw data images. In a first step, these images have to be re-arranged into a coherent 3D volume to reconstruct neuronal morphologies. While early studies have relied on manual contouring of printed raw images (White et al., 1986) or later, with the introduction of computers, manual alignment of images (Fiala, 2005), this has become intractable with the exponential increase in acquired EM volumes. Ever since, the community has moved towards developing more automated routines. While in-plane alignment of image overlaps is straightforward using point-pair cross correlation, cross-plane alignment of non-blockface type datasets is non-trivial. In blockface EM methods, images across planes are inherently aligned. Therefore, e.g. stage motor positions are sufficient for finding overlapping image pairs. However, in the more recent non-blockface type datasets, images are not inherently aligned anymore as each section has a different stage motor position. Furthermore, the EM FOV is approximated based on the light microscopy (LM) section outline, leading to sufficient jitter so that image tiles are non-overlapping. Therefore, several automated alignment routines have been developed to overcome these challenges computationally,

by using a combination of global and local feature detection to find and guide alignment of overlapping images ((Preibisch et al., 2009; Scheffer et al., 2013); see methods section “2.20.8 mSEM Image Alignment” for in depth alignment logic). Recently, several approaches, including machine learning based algorithms, have been developed (Mitchell et al., 2019; Buniatyan et al., 2020) to combat error-prone local feature detection and cross correlation as well as compensate for image and sectioning artifacts (Dorkenwald et al., 2017; Lee et al., 2017; Macrina et al., 2021).

In a second step, the aligned volume has to be segmented into individual neuronal morphologies. Traditionally solved by manual contouring, the sheer density of neuronal wiring – consisting of about 7 km neurites and 1 billion synapses per cubic millimeter of brain tissue (Staffler et al., 2017) – in combination with the aforementioned exponential increase in acquired dataset volumes further substantiated the need to find more automated solutions. With human contouring speeds of 200-400 hours of human annotation per mm of neurite length (Helmstaedter et al., 2011), dense manual segmentation and synapse detection of a cubic millimeter of neuronal tissue would take several 100000 human annotation hours, highlighting the necessity for workarounds and computational advances. A first significant increase in speed was achieved by switching to skeleton-representations (Helmstaedter et al., 2011) and the possibility of tracing via 3D egocentric flight (Boergens et al., 2017). These manually annotated skeletons could be used to guide semi-automated segmentation algorithms for morphological reconstruction (Dorkenwald et al., 2017). However, there has been tremendous progress towards complete automation of neuronal segmentation (Beier et al., 2017; Wolf et al., 2017; Zung et al., 2017; Januszewski et al., 2018; Funke et al., 2019; Motta et al., 2019; Macrina et al., 2021), for example by algorithms learning neuronal morphologies (Schubert et al., 2019). On this line, advances in automated synapse detection (Kreshuk et al., 2014; Dorkenwald et al., 2017; Staffler et al., 2017; Turner et al., 2019; Buhmann et al., 2021) are closing the gap towards fully automated extraction of dense connectomes.

In conclusion, major advances of both experimental approaches and processing of petabyte scale datasets for 3D-EM now allow for routine circuit investigations on larger volume scales. Although to date dense EM volume segmentation still requires correction by human annotators (Motta et al., 2019), fully automated methods show promising potential. Together, automated detection of synapses and ultrastructural correlates of synaptic strength (Holler et al., 2021) now enable the extraction of high-dimensional, high-resolution circuit connectomes aiding in the investigation of circuit motifs at biologically relevant scales.

1.5.8 Towards long-range functional connectomes – bridging photons and electrons

In order to understand how the brain processes information, we first need to understand the underlying flow of information. While the technique of reconstructing circuit motifs with 3D-EM can provide important insights about the connectivity of the brain, such as allowing to exclude models of predicted neuronal circuit computation (Farrell et al., 2021; Klinger et al., 2021), it lacks the functional information necessary for investigations of functional connectivity. While two-photon microscopy on the other hand can provide functional insights into populations of cells on a single cell level, it lacks the spatial resolution for investigating dense connectivity. However, combining both techniques in sequence has the potential to provide all components necessary to interrogate functional connectivity (Reid, 2012). In other words, this combinatorial approach would correlate the neurons’ functional properties with their underlying wiring diagram to decipher the flow of information. Two successful studies have provided a proof of concept of functional connectomics in locally confined circuits of the

retina (Briggman et al., 2011) and V1 (Bock et al., 2011). Very recently, the Machine Intelligence from Cortical Networks consortium has launched an effort to expand functional connectomics to a cubic millimeter volume in visual cortices (MICrONS Consortium et al., 2021), a substantial step towards investigations of functional connectivity of cortical columns.

In order to achieve the true potential of functional connectomics it should not only be limited to local circuits, but allow for interrogation of any combination of inputs, including long-range connectivity. Given the current volume limitations in continuous acquisition of 3D-EM datasets, tracing connections over long distances remains infeasible. So far, re-finding functionally imaged neurons in EM relied on cell-body matching (Bock et al., 2011; Briggman et al., 2011; Lee et al., 2016b; Tsang et al., 2018). In order to scale to long-range connectivity, however, matching of neurite segments, such as long-range axons, will be key. Several recent technical developments have provided tools to bridge this gap. Advancements in commercial micro computed tomography (microCT) allow for improved 3D matching using e.g. vascular landmarks (e.g. MICrONS Consortium et al. 2021), narrowing the resolution gap between two-photon and EM. However, the resolution in microCT is not sufficient for resolving axons even with synchrotron based nano computer tomography (Kuan et al., 2020). Currently, the most clear-cut tools for re-finding axons in EM are based on electron-dense immunolabeling (Faulk and Taylor, 1971; Pallotto et al., 2015), horse-radish peroxidase (Hersch and White, 1981; Hamos et al., 1985; Horikawa and Armstrong, 1988; Anderson et al., 1994a; b; Markram et al., 1997; Costa and Martin, 2011) or convertible fluorophores (Maranto, 1982; Grabenbauer et al., 2005; Knott et al., 2009). Although the labeled neurites can be easily re-found in EM, their dark staining can mask subcellular structural features needed for e.g. synapse detection and cause ultrastructural degeneration. While more recent iterations have provided options to genetically associate sparse labeling to intracellular structures (Shu et al., 2011; Martell et al., 2012; Atasoy et al., 2014; Lam et al., 2015; Joesch et al., 2016), ultrastructural preservation remains challenging (but see (Lin et al., 2016)). Hence, more native approaches to solve matching via landmark-based co-registration of fluorescent labels with EM morphologies have been developed. Several early studies have used landmark burning as references (Bishop et al., 2011; Maco et al., 2013; Gala et al., 2017). While this is a viable method for locally confined volumes, it does not scale for bigger volumes and requires destruction of neuronal ultrastructure. These issues were recently overcome by the FluoEM protocol (Drawitsch et al., 2018) making use of the uniqueness of axonal trajectories. First, they used labeled vasculature for an initial rough matching to reduce the search space. Then, using the estimated vascular matching error, they used locally dense axonal reconstructions to find the most likely axonal match based on trajectory and bouton positioning. Despite their use of structural fluorophores for labeling long-range axons, and imaging the exact same block of tissue with both light-sheet microscopy and 3D-EM, this matching logic could be adapted to *in vivo* two-photon microscopy, therefore providing the most promising approach for the realization of long-range functional connectomics to date.

1.6 Aim of this study

Taken together, I believe that the outlined technological advances have the potential to provide the necessary building blocks for the development of long-range functional connectomics. The goal of this thesis project was to develop and realize such a pipeline experimentally, and tailor it to investigate the longstanding functional connectivity rule of geniculo-cortical convergence proposed by David Hubel and Thorsten Wiesel (Hubel and Wiesel, 1962). In particular, I aimed to produce a comprehensive dataset to resolve the circuit mechanism underlying the emergence of OS in cortical simple cells in mouse binocular visual cortex on a single cell level.

2 Materials and Methods

2.1 Materials

2.1.1 Desoxyribonucleic acids

DNA plasmid	Resistance	Supplier	Reference
pAAV-CAG-Flex-FlpO-WPRE	ampicillin	Custom made	(Bauer et al., 2021)
pAAV-EF1α-F-Flex-jGCaMP7b-WPRE	ampicillin	Custom made	(Bauer et al., 2021)
pAAV-EF1α-F-Flex-Kir2.1-T2A-tdTomato	ampicillin	Addgene (#60661)	(Xue et al., 2014)
pAAV-hSyn-axon-GCaMP6s-P2A-mRuby3-WPRE	ampicillin	Addgene (#112005)	(Broussard et al., 2018)
pCAFNF-dsRed	ampicillin	Addgene (#13771)	(Matsuda and Cepko, 2007)
pCAFNF-GFP	ampicillin	Addgene (#13772)	(Matsuda and Cepko, 2007)
pGP-AAV-syn-jGCaMP7b-WPRE	ampicillin	Addgene (#104493)	(Dana et al., 2019)
pGP-AAV-syn-jGCaMP7s-WPRE	ampicillin	Addgene (#104487)	(Dana et al., 2019)
pGP-CMV-NES-jRGECO1a	kanamycin	Addgene (#61563)	(Dana et al., 2016)
pPGK-iCre-gb	ampicillin	Custom made	/

2.1.2 Enzymes

Restriction Enzyme	Restriction type	Restriction sequence (5' → 3')	Supplier
AccI	5' Overhang	GT/MKAC	New England Biolabs GmbH (Frankfurt am Main, Germany)
AfeI	Blunt	AGC/GCT	New England Biolabs GmbH (Frankfurt am Main, Germany)
AscI	5' Overhang	GG/CGCGCC	New England Biolabs GmbH (Frankfurt am Main, Germany)
BamHI	5' Overhang	G/GATCC	New England Biolabs GmbH (Frankfurt am Main, Germany)
BsrGI	5' Overhang	T/GTACA	New England Biolabs GmbH (Frankfurt am Main, Germany)
EcoRI-HF®	5' Overhang	G/AATTC	New England Biolabs GmbH (Frankfurt am Main, Germany)
EcoRV	Blunt	GAT/ATC	New England Biolabs GmbH (Frankfurt am Main, Germany)
HindIII	5' Overhang	A/AGCTT	New England Biolabs GmbH (Frankfurt am Main, Germany)
HpaI	Blunt	GTT/AAC	New England Biolabs GmbH (Frankfurt am Main, Germany)
KpnI-HF®	3' Overhang	GGTAC/C	New England Biolabs GmbH (Frankfurt am Main, Germany)
NheI	5' Overhang	G/CTAGC	New England Biolabs GmbH (Frankfurt am Main, Germany)
NotI	5' Overhang	GC/GGCCGC	New England Biolabs GmbH (Frankfurt am Main, Germany)
SalI	5' Overhang	G/TCGAC	New England Biolabs GmbH (Frankfurt am Main, Germany)
SmaI	Blunt	CCC/GGG	New England Biolabs GmbH (Frankfurt am Main, Germany)
XhoI	5' Overhang	C/TCGAG	New England Biolabs GmbH (Frankfurt am Main, Germany)

(A = Adenine, C = Cytosine, G = Guanine, T = Thymine; [M = A or C, K = G or T])

2.1.3 Viruses

Virus	Titer (GC/ml)	Supplier	Reference
AAV1-EF1α-F-Flex-jGCaMP7b-WPRE-hGH	1.38 x 10^{13}	University of Pennsylvania Vector Core Services (Philadelphia, Pennsylvania, USA)	Custom made
AAV2/1-CAG-Flex-FlpO-WPRE-SV40	1.244 x 10^{13}	University of Pennsylvania Vector Core Services (Philadelphia, Pennsylvania, USA)	Custom made
AAV2/1-hSyn-Cre-WPRE-hGH	1.04 x 10^{13}	University of Pennsylvania Vector Core Services (Philadelphia, Pennsylvania, USA)	James M. Wilson
AAV2/1-Syn-Flex-NES-jRGECO1a-WPRE-SV40	1.08 x 10^{13}	University of Pennsylvania Vector Core Services (Philadelphia, Pennsylvania, USA)	(Dana et al., 2016)

2.1.4 Antibodies

Antibody (Identifier)	Dilution	Supplier
1° rabbit anti-GFP (AB3080)	1:1000	Merck Chemicals GmbH/Merck Millipore (Darmstadt, Germany)
2° goat anti-rabbit cy3 (111-165-045)	1:250	Dianova GmbH (Hamburg, Germany)

2.1.5 Pharmaceuticals

Name/info	Supplier
Antisedan®	Orion Pharma (Espoo, Finland)
Braunol®7.5	B. Braun Melsungen AG (Melsungen, Germany)
Dormitor®	Orion Pharma (Espoo, Finland)
Fentanyl	HEXAL AG (Holzkirchen, Germany)
Flumazenil-HEXAL	HEXAL AG (Holzkirchen, Germany)
Heparin sodium salt from porcine intestinal mucosa	Sigma-Aldrich Chemie GmbH (Taufkirchen, Germany)
Isopto-Max	Alcon Pharma GmbH (Freiburg, Germany)
Isotone Kochsalzlösung 0.9%, Infusionslösung Natriumchlorid	B. Braun Melsungen AG (Melsungen, Germany)
kodan® Tinktur forte	Schülke & Mayr GmbH (Norderstedt, Germany)
Lidocaine powder	Sigma-Aldrich Chemie GmbH (Taufkirchen, Germany)
Midazolam-ratiopharm	Ratiopharm (Ulm, Germany)
mikrozid® AF liquid	Schülke & Mayr GmbH (Norderstedt, Germany)
Naloxon-ratiopharm	Ratiopharm (Ulm, Germany)
Oculotect® fluid sine 50 mg/ml PVD Augentropfen	Novartis Pharma GmbH (Melsungen, Germany)
Rimadyl®	Zoetis (Florham Park, New Jersey, USA)
Sterofundin® VG-5 1-1 E, G-5%, Infusionslösung	B. Braun Melsungen AG (Melsungen, Germany)

Xylocain® Pumpspray	AstraZeneca GmbH (Wedel, Germany)

2.1.6 Chemicals

Name/info	**Supplier**
4-(2-Hydroxyethyl)-piperazin-1-ethansulfonsäure, N-(2-Hydroxyethyl)piperazine-N'-(2-ethanesulfonic acid); (HEPES)	Sigma-Aldrich Chemie GmbH (Taufkirchen, Germany)
Calcium ion solution for ISE 0.1 M Ca, analytical standard (for ion-selective electrodes)	Sigma-Aldrich Chemie GmbH (Taufkirchen, Germany)
Calciumchlorid-Dihydrate	Sigma-Aldrich Chemie GmbH (Taufkirchen, Germany)
Di-natriumhydrogenphosphate	Merck Chemicals GmbH/Merck Millipore (Darmstadt, Germany)
D(+)-Glucose-Monohydrat	Merck Chemicals GmbH/Merck Millipore (Darmstadt, Germany)
Gibco™ 21575 Minimum Essential Media, Hank's	Life Technologies/Thermo Fischer Scientific (Waltham, MA, USA)
Gibco™ 24020 Hank's Balanced Salt Solution	Life Technologies/Thermo Fischer Scientific (Waltham, MA, USA)
Gibco™ Horse Serum, heat inactivated	Life Technologies/Thermo Fischer Scientific (Waltham, MA, USA)
Kaliumhydrogenphosphate	Merck Chemicals GmbH/Merck Millipore (Darmstadt, Germany)
Magnesiumsulfate-heptahydrate	Merck Chemicals GmbH/Merck Millipore (Darmstadt, Germany)
Microcarrier, Gold 1.6 µm	Bio-Rad Laboratories Inc. (Hercules, CA, USA)
Normal Goat Serum (NGS)	Sigma-Aldrich Chemie GmbH (Taufkirchen, Germany)
Nuclease-Free Water	Ambion®/Thermo Fischer Scientific
Polyvinyl-Pyrrolidone	Sigma-Aldrich Chemie GmbH (Taufkirchen, Germany)
Potassium chloride, ACS reagent	Sigma-Aldrich Chemie GmbH (Taufkirchen, Germany)
Silica Gel	Sigma-Aldrich Chemie GmbH (Taufkirchen, Germany)
Sodium Chloride, ACS reagent	Sigma-Aldrich Chemie GmbH (Taufkirchen, Germany)
Spermidine	Sigma-Aldrich Chemie GmbH (Taufkirchen, Germany)
Sucrose for microbiology	Merck Chemicals GmbH/Merck Millipore (Darmstadt, Germany)
Triton X-100	Sigma-Aldrich Chemie GmbH (Taufkirchen, Germany)
1,1'-Dioctadecyl-3,3,3',3'-Tetramethylindodicarbocyanine (DiD)	Invitrogen/Thermo Fischer Scientific (Carlsbad, CA, USA)
Acetone, research grade	SERVA Electrophoresis GmbH (Heidelberg, Germany)
Calcium Chloride Dihydrate, for molecular biology, ≥99%	Sigma-Aldrich Chemie GmbH (Taufkirchen, Germany)
Epoxy Embedding Medium kit – epoxy DDSA	Sigma-Aldrich Chemie GmbH (Taufkirchen, Germany)
Epoxy Embedding Medium kit – epoxy DMP	Sigma-Aldrich Chemie GmbH (Taufkirchen, Germany)
Epoxy Embedding Medium kit – epoxy embedding medium	Sigma-Aldrich Chemie GmbH (Taufkirchen, Germany)
Epoxy Embedding Medium kit – epoxy MNA	Sigma-Aldrich Chemie GmbH (Taufkirchen, Germany)
Ethanol undenatured absolute, analytical grade	SERVA Electrophoresis GmbH (Heidelberg, Germany)
Glutaraldehyde 50% solution in water, for electron microscopy	SERVA Electrophoresis GmbH (Heidelberg, Germany)
Hydrochloric acid, c(HCl) = 1 mol/l (1 N) Titripur® Reag. Ph Eur,Reag. USP	Sigma-Aldrich Chemie GmbH (Taufkirchen, Germany)
Isopropanol, molecular biology grade	SERVA Electrophoresis GmbH (Heidelberg, Germany)
Lead(II) Nitrate, ≥99.99% trace metal basis	Sigma-Aldrich Chemie GmbH (Taufkirchen, Germany)
L-Aspartic acid, research grade, Ph. Eur.	SERVA Electrophoresis GmbH (Heidelberg, Germany)

Osmium tetroxide 4%, solution for electron microscopy	SERVA Electrophoresis GmbH (Heidelberg, Germany)
Paraformaldehyde, reagent grade, crystalline	Sigma-Aldrich Chemie GmbH (Taufkirchen, Germany)
pH-buffer solution 4.0	Carl Roth GmbH + Co. KG (Karlsruhe, Germany)
pH-buffer solution 7.0	Carl Roth GmbH + Co. KG (Karlsruhe, Germany)
pH-buffer solution 10.0	Carl Roth GmbH + Co. KG (Karlsruhe, Germany)
Potassium hexacyanoferrate(II) trihydrate, BioUltra, ≥99.5%	Sigma-Aldrich Chemie GmbH (Taufkirchen, Germany)
Potassium hydroxide solution, c(KOH) = 1 mol/l (1 N) Titripur® Reag. Ph Eur,Reag. USP	Sigma-Aldrich Chemie GmbH (Taufkirchen, Germany)
Sodium Cacodylate, research grade	SERVA Electrophoresis GmbH (Heidelberg, Germany)
Sodium hydroxide solution, c(NaOH) = 1 mol/l (1 N) Titripur® Reag. Ph Eur,Reag.	Sigma-Aldrich Chemie GmbH (Taufkirchen, Germany)
Thiocarbohydrazide, 98%	Sigma-Aldrich Chemie GmbH (Taufkirchen, Germany)
Uranyl Acetate dehydrate, research grade	SERVA Electrophoresis GmbH (Heidelberg, Germany)

2.1.7 Solutions

All solutions were prepared in water unless stated otherwise.

Solution	Components	Concentration
1° antibody solution (in PBS)	1° rabbit anti-GFP	1:1000
	NGS	10%
	TritonX	0.3%
2° antibody solution (in PBS)	2° goat anti-rabbit cy3	1:250
	NGS	5%
Antibody blocking solution (in PBS)	Normal goat serum	10%
	TritonX	0.3%
Aqueous TCH solution	Thiocarbohydrazide	1%
Artificial cerebro-spinal fluid (pH 7.4, adjusted with 1 N NaOH)	NaCl	125 mM
	KCl	5 mM
	$C_6H_{12}O_6 * H_2O$	10 mM
	$C_8H_{18}N_2O_4S$	10 mM
	$CaCl_2 * 2 H_2O$	2 mM
	$MgSO_4 * 7 H_2O$	2 mM
Buffered osmium solution	OsO_4	2%

	Cacodylate buffer	0.15 M
Cacodylate Buffer (pH 7.4, adjusted with 1 N HCl)	$(CH_3)_2AsO_2Na * 3H_2O$	0.3 M
EM fixing perfusion solution (pH 7.4 adjusted with 1 N HCl, 700-800 mosmol)	Sodium Cacodylate	0.08 M
	Paraformaldehyde	2.5%
	Glutaraldehyde	1.25%
	$CaCl_2$	0.5%
EM flushing perfusion solution (pH 7.4, adjusted with 1N HCl, 300 mosmol)	Sodium Cacodylate	0.15 M
	1,1'-Dioctadecyl-3,3,3',3'-Tetramethylindodicarbocyanine	5 µM
Ferrocyanide solution	Potassium hexacyanoferrate trihydrate	2.5%
	Cacodylate buffer	0.15 M
GBSS	$CaCl_2 * 2 H_2O$	1.5 mM
	KCl	5.0 mM
	KH_2PO_4	0.2 mM
	$MgSO_4 * 7 H_2O$	0.3 mM
	$MgCl_2 * 6 H_2O$	1.0 mM
	$NaHCO_3$	2.7 mM
	NaCl	136.9 mM
	Na_2HPO_4	0.9 mM
	D-(+) Glucose * H_2O	5.6 mM
Lead-Aspartate buffer (pH 3.8, adjusted with 1 N KOH)	L-aspartic acid	0.03 M
Lead aspartate solution (pH 5.0, adjusted with 1 N KOH)	Lead (II) nitrate	0.02 M
	Lead-aspartate buffer	0.03 M

LM fixing perfusion solution	Paraformaldehyde	4%
	Phosphate Buffer Saline	0.1 M
LM flushing perfusion solution	NaCl	0.9%
	Heparine	0.00028%
	Lidocaine	0.0005%
Phosphate buffered saline (PBS)	NaCL	137 mM
	KCl	2.7 mM
	Na_2HPO_4	5.4 mM
	KH_2PO_4	1.5 mM
Sucrose solution (in PBS)	Sucrose	30%
Unbuffered osmium solution	OsO_4	2%
Uranyl acetate solution	Uranyl acetate	1%

2.1.8 Media

Medium	Components	Component ratio
Epoxy Resin	Epoxy	5.9 g
	DDSA	2.25 g
	MNA	3.7 g
	DMP	205 µl
Organotypic Slice Culture Prep-	GBSS	98 ml
Medium	Kynurenic acid	1 ml
(adjust to pH 7.2 with HCl)	Glucose Stock solution (see above)	1 ml
Stoppini-Muller Medium	1x MEM	191 ml
(adjust to pH 7.2 with NaOH)	HBSS	100 ml

	Horse Serum	100 ml
	5M D-(+) Glucose	4 ml
	1M HEPES	5 ml

2.1.9 Glues, cements, paints & gels

Name/info	**Supplier**
Druckluftspray nicht brennbar, CRC Kontakt Chemie	CRC Industries Deutschland GmbH (Iffezheim, Germany)
Elfenbeinschwarz, JU	Kremer Pigmente GmbH & Co. KG (Aichstetten, Germany)
Histoacryl®	B. Braun Surgical, S.A. (Rubí, Spain)
Loctite 401 Prism Instant Adhesive	Henkel AG & Co. KGaA (Düsseldorf, Germany)
Paladur®	Heraeus Kulzer GmbH (Hanau, Germany)
Pattex® Ultra Gel	Henkel AG & Co. KGaA (Düsseldorf, Germany)
Renew-Duster	Tech Spray, L.P. (Hoofddorp, The Netherlands)
Silver Conductive paint	Structure Probe, Inc. (West Chester, PA, USA)
Ultraschall Gel	P.J. Dahlhausen & Co. GmbH (Köln, Germany)

2.1.10 Materials and Instruments

Material/instrument	**Supplier**
Gene Gun	
Emmi-5 Ultraschall-Reiniger	EMAG AG (Mörfelden-Walldorf, Germany)
Helios® Gene Gun System	Bio-Rad Laboratories Inc. (Hercules, CA, USA)
Tefzel Tubing, 3.175 mm OD, 2.36 mm ID	Bio-Rad Laboratories Inc. (Hercules, CA, USA)
Tubing Cutter	Bio-Rad Laboratories Inc. (Hercules, CA, USA)
Tubing Prep Station, Helios gene gun sample preparation station	Bio-Rad Laboratories Inc. (Hercules, CA, USA)
Organotypic slice cultures	
6-well Tissue Culture Test Plates	Techno Plastic Products AG (Trasadingen, Switzerland)
Heracell™ 150 CO_2 Incubator	Thermo Fischer Scientific (Waltham, MA, USA)
McIlwain tissue chopper	Mickle Lab Engineering Co. Ltd./Cavey Laboratory Engineering Co. Ltd.
Millicell® Cell Culture Inserts, 0.4 µm, 30 mm Diameter	Merck Chemicals GmbH/Merck Millipore (Darmstadt, Germany)
martor® Bügelklinge Nr. 44	H. Dummer (Munich, Germany)
Perfusion	
Discofix®-3, Dreiwegehahn, PVC- und Latexfrei	B. Braun Melsungen AG (Melsungen, Germany)

Dumont #4 Forceps – Dumoxel	Fine Science Tools GmbH (Heidelberg, Germany)
Fine Scissors – Sharp	Fine Science Tools GmbH (Heidelberg, Germany)
Footswitch w/3.5 mm Phone Jack	Hugo Sachs Elektronik – Harvard Apparatus GmbH
neoLab Verbinder, LL weiblich- Olive 4,0-5,0 mm, PP	neoLab® Migge GmbH (Heidelberg, Germany)
neoLab Verbinder, LL männlich- Olive 4,0-5,0 mm, PP	neoLab® Migge GmbH (Heidelberg, Germany)
Omnifix Luer Lock Latexfrei (60ml)	neoLab® Migge GmbH (Heidelberg, Germany)
Perfusion table for mice, metal	Max Planck Institute machine shop (Martinsried, Germany)
Student Fine Scissors	Fine Science Tools GmbH (Heidelberg, Germany)
Syringe Pump PhD Ultra infuse	Hugo Sachs Elektronik – Harvard Apparatus GmbH
Terumo Agani Canules, Luer-Lock, 0,60x32 mm	Terumo Corp. (Shibuya, Japan)
Tygon Labor Schlauch Sh-Härte 55, 4,8 x 6,4 mm, 15 m	neoLab® Migge GmbH (Heidelberg, Germany)

Surgical equipment	
Cotton tips, 15cm	Medical care & serve® (Wurmlingen, Germany)
Cover slips, round, 4 mm	Glaswarenfabrik Karl Hecht GmbH & Co. KG (Sondheim, Germany)
Disposable Biopsy Punch, 4 mm	Kai Europe GmbH (Solingen Germany)/pfm medical AG (Köln, Germany)
Drill bits HP 310 104 001 001 004	Hager & Meisinger GmbH (Neuss, Germany)
Dumont #5/45 Cover Slip Forceps – Dumoxel	Fine Science Tools GmbH (Heidelberg, Germany)
Dumont #3 Forceps – Dumoxel	Fine Science Tools GmbH (Heidelberg, Germany)
Dumont #5 Forceps – Inox	Fine Science Tools GmbH (Heidelberg, Germany)
Dumont #5/45C Forceps – Dumoxel	Fine Science Tools GmbH (Heidelberg, Germany)
Glass capillaries made of Borosilicate glass 3.3, ends cut (length: 100 mm, OD: 0.8 mm, wall thickness: 0.28 mm)	Hilgenberg GmbH (Malsfeld, Germany)
Headplate (chamber type, 46 x 14 mm, metal)	Max Planck Institute machine shop (Martinsried, Germany)
Homeothermic blanket with rectal probe	Harvard Apparatus (Holliston, MA, USA)
Hydraulic Micromanipulator M 0102 R	NARISHIGE International Ltd. (London, UK)
Infra-red lamp	Glamox Luxo GmbH (Bremen, Germany)
K.1070 High Speed Rotary Micromotor Kit, 2.35 mm	Foredom Electric Co. (Bethel, CT, USA)
Motorized Stereotaxic	Neurostar (Tübingen, Germany)
Nanofil 10 µm syringe, Sub-Microliter Injection System	World Precision Instruments Inc. (Berlin, Germany)

NanoFil Needles, beveled, 36G	World Precision Instruments Inc. (Berlin, Germany)
Omnican® 50	B. Braun Melsungen AG (Melsungen, Germany)
Omnifix®-F	B. Braun Melsungen AG (Melsungen, Germany)
Operationsmikroskop SOM-62	Karl Kaps GmbH (Asslar, Germany)
Picospritzer® III	INTRACEL (Shepreth, UK)/Parker Hannifin (Hollis, NH, USA)
P-97 Flaming/Brown Micropipette Puller	Sutter Instruments Co. (Novato, CA, USA)
Scalpel Blades #11	Fine Science Tools GmbH (Heidelberg, Germany)
Scalpel Handle #7 Short	Fine Science Tools GmbH (Heidelberg, Germany)
Standard Pattern Forceps	Fine Science Tools GmbH (Heidelberg, Germany)
StereoDrive Motorized Stereotaxic	Neurostar (Tübingen, Germany)
STERI 350 Sterilisator, dry beads	Simon Keller AG (Burgdorf, Switzerland)
Sterican® Gr. 1 Standardkanülen, 0.90 x 40 mm	B. Braun Melsungen AG (Melsungen, Germany)
Student Fine Scissors	Fine Science Tools GmbH (Heidelberg, Germany)
Stypro® Haemostypticum	Curasan AG (Kleinostheim, Germany)
Sugi® Sponge Points, triangular, 17 x 8 mm, sterile	Kettenbach Medical/Questalpha GmbH & Co. KG (Eschenburg, Germany)
EM staining & embedding	
Analytical Balance Cubis, Type MSE124S-100DA	Sartorius AG (Göttingen, Germany)
Magnetic stirrers with heating MR Hei-Standard	Heidolph Instruments GmbH & Co.KG (Schwabach, Germany)
Rotator SB 3	Stuart; Cole-Parmer Ltd (Staffordshire, UK)
SevenCompact™ S220 pH meter	Mettler-Toledo GmbH (Giessen, Germany)
UN30pa paraffin oven	Memmert GmbH + Co. KG (Schwabach, Germany)
Vapor pressure osmometer Vapro 5600	KREIENBAUM Wissenschaftliche Meßsysteme e.K. (Langenfeld, Germany)
VO 200 vacuum oven	Memmert GmbH + Co. KG (Schwabach, Germany)
Biopsy extraction	
Biopsy punch to toothbrush adapter, metal	Custom made: Thomas Olstinski, Mechanical Specialist, Max Planck Institute for Brain Research (Frankfurt am Main, Germany)
Braun Oral-B	Braun GmbH (Kronberg im Taunus, Germany)
Integra™ Miltex™ Standard Biopsy Punch, ID 1.5 mm	Integra York PA, Inc./Integra LifeSciences

Integra™ Miltex™ Standard Biopsy Punch, ID 2 mm	Integra York PA, Inc./Integra LifeSciences
Model 9800 Dual Stereotaxic	David Kopf Instruments (Tujunga, CA, USA)
Steinel HG350S, type 3509	Steinel Vertrieb GmbH (Herzebrock-Carholz, Germany)
Stereotaxe-to-headplate adapter, metal	Max Planck Institute machine shop (Martinsried, Germany)
Toothbrush to stereotaxic adapter, metal	Custom made: Thomas Olstinski, Mechanical Specialist, Max Planck Institute for Brain Research (Frankfurt am Main, Germany)
Vibratome Leica vt1200s	Leica Microsystems (Wetzlar, Germany)
Resin trimmer	
Fa.meyco Stirnfraeser	Anton Meyer & Co. AG (Port, Switzerland)
Leica EM TRIM2, Specimen trimming device	Leica Microsystems (Wetzlar, Germany)
Ultra Microtomy	
6" Siliziumscheibe, einseitig poliert, CZ, Durchmesser: 150 mm, Typ/Dotierung: p / Bor, Orientierung: (100), spez.Widerstand: 8,00-12,00 Ohmcm, Dicke: 525-675 µm	Science Services GmbH (Munich, Germany)
Conductive Double Carbon Tape, Width: 25 mm	Science Services GmbH (Munich, Germany)
DiATOME Diamantmesser, ultra 35° 4.0 mm	Diatome Ltd (Nidau, Switzerland)
Kapton tape for the ATUMtome, uncoated, 8 mm wide, 30 m long glow discharged	Science Services GmbH (Munich, Germany)
SEM Conductive Double sided Carbon Tape, Width: 8 mm	Science Services GmbH (Munich, Germany)
Microtomes & components	
Leica EM UC7, Ultramicrotome	Leica Microsystems (Wetzlar, Germany)
MANSON EP-925	Manson Engineering Industrial Ltd. (Kwai Chung, Hong Kong)
MICROM HM 400 R Manual Sliding Microtome	MICROM International Gmbh/Thermo Fischer Scientific (Walldorf, Germany)
Reusable microtome knife, length: 16 cm, Profile C, steel	Leica Biosystems Nussloch GmbH (Nussloch, Germany)

Microsocpes & components	
1500 MonoChrome Camera	Thorlabs (Dachau, Germany)
525/50-25 nm bandpass filter	Semrock (Rochester, USA)
562 nm longpass dichroic mirror 25.2 x 35.6 x 1.1 mm	Semrock (Rochester, USA)
607/70-25 nm bandpass filter	Semrock (Rochester, USA)
6210H galvanometer scanner, 6 mm mirror	Cambridge technology (Bedford, MA, USA)
Axio Imager M2	Carl Zeiss AG (Oberkochen, Germany)
B-Scope, rotating, translating multiphoton imaging microscope	Thorlabs (Dachau, Germany)
Canon EOS 1200D	Canon (Ōta, Japan)
CFI75 LWD 16x, 0.8 NA,	Nikon Corporation (Tokyo, Japan)
water-immersion objective	
Custom notched primary 2P dichroic, longpass 405/473-488/561/705-1600	Semrock (Rochester, USA)
Fibre Coupled LED, 470 nm	Thorlabs (Dachau, Germany)
Fibre Coupled LED, 530 nm	Thorlabs (Dachau, Germany)
Fibre Coupled LED, 735 nm	Thorlabs (Dachau, Germany)
First reflector 720/25 nm shortpass filter	Semrock (Rochester, USA)
GaAsP photomultiplier tubes, H7422P	Hamatsu (Toyooka, Japan)
GSI 8kHz resonant scanner	Cambridge technology (Bedford, MA, USA)
HXP 120 C	Carl Zeiss AG (Oberkochen, Germany)
Leica DFC450C	Leica Microsystems (Wetzlar, Germany)
Leica M80 Stereo Microscope with 8:1 Zoom	Leica Microsystems (Wetzlar, Germany)
Leica MDG41 Stereomicroscope	Leica Microsystems (Wetzlar, Germany)
MaiTai® HP DeepSee™ Laser	Spectra Physics/Newport (Santa Clara, CA, USA)
Olympus BX51WI	Olympus (Shinjuku, Japan)
Olympus Plan N 4x, 0.10 NA	Olympus (Shinjuku, Japan)
Operationsmikroskop SOM-62	Karl Kaps GmbH (Asslar, Germany)
PCI digitizer ATS9440, 14bit, 125 MS/s, 4 channels	Alazartech (Pointe-Claire, Canada)
Pockels cell 350-80LA-BK Electro-Optic Modulator	Conoptics (Danbury, CT, USA)
Pockels cell controller 302RM	Conoptics (Danbury, CT, USA)
P-726 PIFOC® High-Load Objective Scanner	Physik Instrumente (Karlsruhe, Germany)
SMZ-2T Stereomicroscope	Nikon Corporation (Tokyo, Japan)

SteREO Lumar.V12	Carl Zeiss AG (Oberkochen, Germany)
TIA60 PMT Transimpedance Amplifier	Thorlabs (Dachau, Germany)
VS25 25 mm Optical Shutter	Vincent Associates® Uniblitz® (Rochester, NY, USA)
Xradia 520 Versa 3D X-Ray microscope	Carl Zeiss AG (Oberkochen, Germany)
X-Cite® Series 120	Olympus (Shinjuku, Japan)
Zeiss Ax10 Imager A2 Vario	Carl Zeiss AG (Oberkochen, Germany)
ZEISS Axioscope	Carl Zeiss AG (Oberkochen, Germany)
Zeiss MultiSEM 505	Carl Zeiss AG (Oberkochen, Germany)
ZEISS Plan 25x, 0.45 NA	Carl Zeiss AG (Oberkochen, Germany)

2.1.11 Software

Software	**Company**
ImageJ	Wayne Rasband, National Institutes of Health (Bethesda, MD, USA)
Matlab	The MathWorks (Natick, MA, USA)
Psychophysics Toolbox	David H Brainard, Department of Psychology, University of California (Santa Barbara, CA, USA)
ScanImage 4.2	Vidrio Technologies, LLC (Janelia Farm, VA, USA)
StereoDrive	Neurostar (Tübingen, Germany)
ZEISS Efficient Navigation (ZEN)	Carl Zeiss AG (Oberkochen, Germany)

2.2 Ethics

All experimental procedures were conducted in compliance with the institutional guidelines of the Max Planck Society and the local government (Regierung von Oberbayern). Mice were housed in a 12-hour light-dark cycle with food and water available *ad libitum*.

2.3 Molecular Cloning

In order to control transduction sparsity in dLGN of Cre-expressing *Scnn1a-Tg3-Cre* mice (Madisen et al., 2010), a recombinant adeno-associated virus (AAV) encoding for the FlpO-recombinase under the transcriptional control of Cre and several AAVs coding for GECIs under the transcriptional control of FlpO were created.

For restriction digestion, 10 µg DNA was restricted for 2 h at 37°C in 1x CutSmart® Buffer with 10 U of the respective New England Biolabs enzyme, unless stated otherwise. DNA was purified using the QIAquick Gel Extraction Kit. Blunted DNA was 5'-dephosphorylated using Calf Intestinal Phosphatase (CIP) in 1x CutSmart® Buffer for 1 h at 37°C and restriction overhangs were blunted using 100 µl of purified DNA in 100 µl of 2x iProof™ High-Fidelity MasterMix, unless stated otherwise. Ligations were performed using T4 DNA Ligase at a 7:1 and 1:1 insert to backbone ratio alongside a negative control with a 1:1 insert to H2O ratio, to exclude backbone relegation. Plasmids were transformed into chemically competent E.coli bacteria One Shot™ Stbl3™ (OSS3) due to their reduced frequency of homologous recombination of long terminal repeats. Plasmid DNA was extracted from OSS3 cultures using the QIAfilter Mini, Maxi or Giga kits according to the manufacturer's handbook, unless stated otherwise and the resulting purified Plasmid DNA pellets re-suspended in nuclease-free H_2O. The DNA concentration and purity was determined by spectrophotometry at 260/280 nm using a NanoDrop® ND1000 Spectrophotometer.

2.3.1 Cloning of Cre-dependent FlpO-recombinase

For Cre-dependent expression of FlpO-recombinase, the plasmid pAAV-CAG-Flex-FlpO-WPRE was generated, with the coding sequence of FlpO inserted in flipped orientation against the reading direction, flanked by two loxP sites (see Tab. S1 for DNA sequence). The FlpO coding sequence was extracted from the donor plasmid pAAV-hSyn-FlpO-WPRE with EcoRI-HF. ArchT-tdTomato was removed from the target vector pAAV-CAG-Flex-ArchT-tdTomato-WPRE by double-digestion with KpnI-HF and XhoI. Both restriction reactions were purified and the overhangs subsequently blunted for 15 min at 72°C. The 5'-ends of the blunted backbone from the target vector were CIP dephosphorylated for 1 h at 37°C to prevent re-ligation. Both, the dephosphorylated backbone of the target vector and the restriction of the donor were individually loaded into a 0.7% agarose gel and fragments separated by size using agarose gel electrophoresis. The bands of the empty target backbone (5027 bps) and the FlpO coding sequence (1333 bps) were excised and the DNA purified. The purified fragments were ligated for 2 h at 23°C and transformed into OSS3. Bacteria were plated and incubated on ampicillin containing agar plates overnight at 37°C. 24 bacterial colonies were picked and inoculated overnight on a shaker at 170 rpm at 37°C in 6 ml of Terrific Broth medium, respectively. The plasmid DNA extracted from 2 ml of the bacterial cultures using a modified QIAGEN Plasmid Mini Kit protocol, omitting the column filtration. Correct direction of insertion of FlpO into the backbone of the target vector was verified by control double-restrictions with either NheI and HindIII or NheI and NotI or NheI and XbaII. 250 ml of 3 inoculated cultures, each containing the correct plasmid, were re-inoculated overnight on a shaker at 170 rpm at 37°C in 200 ml of Terrific Broth medium and 864 µl

subsequently stored in 15% glycerol (200 µl 80% glycerol) at -80°C, respectively. The pAAV-CAG-Flex-FlpO-WPRE plasmid DNA was extracted using the QIAGEN Plasmid Maxi Kit.

2.3.2 Cloning of FlpO-dependent jGCaMP7b

For FlpO-dependent expression of GECIs, several plasmids containing the coding sequence of various calcium indicators inserted in flipped orientation against the reading direction, flanked by two Flp recognition target sites were generated. First, the pAAV-EF1α-F-Flex-jGCaMP7b-WPRE plasmid was cloned (see Tab. S1 for DNA sequence). The jGCaMP7b coding sequence was excised by first digesting the donor plasmid pGP-AAV-Syn-jGCaMP7b-WPRE with HindIII. The sequence coding for ArchT-tdTomato was removed from the target vector pAAV-CAG-Flex-ArchT-tdTomato-WPRE by restriction digestion with BsrGI. Both were purified, the overhangs blunted for 15 min at 72°C and the DNA subsequently re-purified. To complete the excision of both inserts, both the target and donor vectors were additionally restriction digested with BamHI for 3 h at 37°C. After 2 h, 2 µl of CIP was added into the restriction reaction of the target vector pAAV-CAG-Flex-ArchT-tdTomato-WPRE for 1 h at 37°C to prevent re-ligation. Both restriction reactions were subsequently individually loaded into a 0.7% agarose gel and fragments separated by size using AGE. The bands of the empty target backbone (5608 bps) and the jGCaMP7b coding sequence (1369 bps) were excised and the DNA purified. The purified fragments were ligated overnight at 13°C and transformed into chemically competent OSS3. Bacteria were plated and incubated on ampicillin containing agar plates overnight at 37°C. Four bacterial colonies were picked and inoculated overnight on a shaker at 170 rpm at 37°C in 6 ml of Terrific Broth medium, respectively. The plasmid DNA extracted from 2 ml of the bacterial cultures using a modified QIAGEN Plasmid Mini Kit protocol, omitting the column filtration. Correct direction of insertion of FlpO into the backbone of the target vector was verified by two control double-restrictions with either HpaI and BamHI or HpaI and EcoRV. 250 ml of 1 inoculated culture, containing the correct plasmid, was re-inoculated overnight on a shaker at 170 rpm at 37°C in 200 ml of Terrific Broth medium and 384 µl subsequently stored in 15% glycerol at -80°C, respectively. pAAV-EF1α-F-Flex-jGCaMP7b-WPRE plasmid DNA was extracted using the QIAGEN Plasmid Maxi Kit.

2.4 Organotypic rat hippocampal slice cultures

Organotypic rat hippocampal slice cultures were prepared from Wistar rats between postnatal days 5-6 as described previously (Stoppini et al., 1991). In brief, all surgical instruments, except the Teflon-cutting slab and razor blade, were disinfected in 80% EtOH and flamed using a Bunsen burner. Both, organotypic slice culture prep-medium (kept at 4°C) and Stoppini-Muller medium (warmed to 37°C) were prepared. Wistar rats were decapitated, their brain extracted from the skull and quickly submerged in the pre-cooled prep-medium. Both hippocampi were surgically dissected under a dissection microscope and subsequently cut into 300-400 µm thick transverse sections with a razor blade on a Teflon slab using a McIlwain tissue chopper. Slices were immediately submerged in pre-cooled prep-medium and separated. Tissue integrity was visually inspected under a dissection microscope and the best sections transferred into fresh pre-cooled prep-medium. Slices were incubated for 45-60 minutes at 4°C to remove debris and allow for tissue regeneration. Regenerated slices were carefully transferred onto Millicell cell culture insets, which were submerged in 6-well plates in 1 ml of pre-heated Stoppini-Muller medium. A maximum of 4 slices were placed on an individual inset. The preparation was conducted entirely in a laminar flow hood.

Slice cultures were transferred to and maintained in an incubator at 35°C at a 5% CO_2 atmosphere. The Stoppini-Muller medium was exchanged 3x/week.

2.5 Biolistic transfection and viral transduction in organotypic slice cultures

Exogenous expression of transgenes in organotypic rat hippocampal slice cultures was induced either using biolistic transfection, viral transduction or a combination of both. This allowed for rapid verification of custom designed DNA-plasmids and viral vectors.

For biolistic transfection, first DNA-coated gold microprojectiles were prepared similarly as decribed previously (McAllister, 2000). In brief, 8 µg of each DNA plasmid, coding for the transgene of interest, was diluted to a single 100 µL solution in nuclease free H_2O at room temperature (RT). 7 mg of 1.6 µm microcarrier gold particles were submerged in 20 µL of 250 mM spermidine, vortexed vigorously and sonicated for 5 minutes to separate the gold particles. The DNA mixture was added and mixed by manual shaking of the Eppendorf tube. The DNA was subsequently precipitated onto the gold particles by addition of 120 µL of 1M $CaCl_2$ to the walls. The solution was rapidly mixed and incubated for 10 minutes on ice with repeated mixing. DNA-associated gold particles were precipitated by centrifugation for 60 s at 4000 rotations per minute (rpm), the supernatant removed and the pellet resuspended in -20°C cold fresh 100% EtOH. This washing procedure was repeated 3 times. The pellet was finally resuspended and transferred into a mixture of 3 ml of cold fresh 100% EtOH 0.05 mg/ml Polyvinyl-Pyrrolidone.

The DNA-coated gold microprojectiles were subsequently loaded into biolistic cartridges. Specifically, the gold-associated DNA solution was transferred into a 75 cm long Tefzel Tubing, which was internally purged by nitrogen flow at 4 liters/min for 10 min in rotation at a Tubing Prep-station. The gold-associated DNA solution was gravitationally precipitated onto the inner tubing walls without rotation and without nitrogen flow for 15 min. The supernatant was removed from the tubing and the DNA-associated gold particles dried to the tubing walls by nitrogen flow at 4 liters/min for 10 min in rotation. The tubing was cut into 1 cm long cartridges by a razorblade using a tubing cutter, which were stored dry in silica-gel filled falcon tubes at 4°C.

Organotypic rat hippocampal slice cultures were biolistically transfected in sterile environment under laminar flow. A 5 cm x 5 cm nylon mesh (pore size: 100 µm), the Gene Gun cartridge barrel, barrel liner and laminar flow hood were sterilized with EtOH and surgical instruments additionally flamed using a Bunsen burner. The cartridge barrel was loaded with the respective cartridges holding the DNA-coated gold microprojectiles of interest and installed into the helium gas-pressurized Gene Gun together with the barrel liner. The latter was covered with the nylon mesh to diffuse and filter out clumped gold-particles. The DNA-coated gold microprojectiles were blasted onto hippocampal slice cultures using a helium-gas pressurized Helios Gene Gun at a pressure of 120 psi at a mesh-to-slice distance of about 1 cm. Transfected slice cultures were incubated for transgene expression for 3-5 days in an incubator at 35°C at a 5% CO_2 atmosphere before experimentation.

For viral transduction, borosilicate glass capillaries were pulled on a horizontal puller (parameters: heat: 626, pull: 150, velocity: 120, time: 100) and clipped under a surgical microscope using a sterile forceps resulting in an outer tip diameter of about 10-15 µm. The back end of the glass capillary was flame-sterilized and 2-3 µl of the virus mixture of interest back-filled using a handheld pipette. Large air-bubbles were surfaced by tapping. The glass capillary was connected to a Pneumatic Pico Pump and the tip briefly submerged into ethanol under positive pressure with timed, 100 ms pulses at a pressure of 20 psi to push out microbubbles and sterilize the capillary tip. The microscope injection chamber was sterilized thoroughly with 70% ethanol, dried and filled with 0.8 ml of pre-warmed 37°C Stoppini-Muller medium. The Millicell inset containing the organotypic rat hippocampal slice cultures

was placed into the injection chamber and fixed into position, with the slice cultures at the medium-air interface. The glass capillary was positioned above the hippocampal CA3 region using an Olympus BX51WI microscope with a 4x, numerical aperture (NA) 0.10 objective. The tip investigated for clogging with the Pneumatic Pico Pump using a single 100 ms pulse at a pressure of 20 psi. The pulse parameters were adjusted to produce a viral droplet of about 100 µm in diameter. The injection capillary was carefully guided obliquely into the *stratum pyramidale* using a micro manipulator and the virus injected via 3-4 pressure pulses at about 0.25 Hz. The injection capillary was carefully removed in the same angle to minimize tissue damage and 2-3 further locations in the *stratum pyramidale* of hippocampal regions of CA3 or CA2 were injected per organotypic slice culture. Transduced slice cultures were incubated for transgene expression for 5-10 days in an incubator at 35°C at a 5% CO_2 atmosphere before experimentation.

2.6 Epifluorescence imaging of organotypic slice cultures

Fluorescent transgene expression of virally transduced and/or biolistically transfected organotypic rat hippocampal slice cultures was monitored and evaluated directly in their 6-well plates every second day until experimentation with a ZEISS SteREO Lumar.V12 fluorescent microscope. Surfaces were sterilized beforehand using 80% EtOH and the slice cultures only imaged briefly with a closed 6-well plate lid to avoid tissue infection and hypothermia. Slice cultures were then placed back into the incubator at 35°C at a 5% CO_2 atmosphere.

During experimentation, the slice culture insets were transferred into individual petri-dish lids containing 0.8 ml of pre-warmed 37°C Stoppini-Muller medium for epifluorescent imaging with a ZEISS Axio Imager M2. The expression pattern and fluorescent dynamics were documented in images or time-lapses with a resolution of 1388 x 1040 pixels at different magnifications (using 5x NA 0.15, 10x NA 0.3 or 20x NA 0.5 air objectives). Slice were discarded after experimentation due to the un-sterile experimental conditions, resulting in a high likelihood of infection.

2.7 In vivo virus injection and chronic window implantation

Prior to surgery, borosilicate glass capillaries were pulled on a horizontal puller (parameters: heat: 626, pull: 150, velocity: 120, time: 100) and clipped under a surgical microscope using a sterile forceps resulting in an outer tip diameter of about 30 µm. The capillary tip was beveled at a 45° angle under positive internal pressure using a sterilized, custom diamond-dust coated rotating harddrive disk. The final tip diameter and beveling quality were verified under a transmission light microscope. Beveled borosilicate glass capillaries were front-filled under internal negative pressure with the virus of interest (thawed on ice) and stored at 4°C until immediately prior to cortical injection. For injection into dLGN, a Nanofil glass syringe connected to a beveled gauge 36 needle was front-filled with the virus of interest (thawed on ice) via negative internal pressure using an automated micro-injector. Both the borosilicate glass capillary and NanoFil needle were investigated for lack of clogging right before injection. If required, tips were unclogged by submerging the tip in sterile cortex buffer.

In vivo surgeries were performed on male and female *Scnn1a-Tg3-Cre* mice between postnatal days 45-55. Anesthesia was induced with an intraperitoneal injection of a mixture of Fentanyl (0.075 µg/g), Medetomidine (0.75 µg/g) and Midazolam (7.5 µg/g). Analgesia was provided both, globally with a subcutaneous injection of Carprofen (5 µg/g) prior to surgery, as well as on the first and second day of post-surgical recovery and locally by application of 10 % Lidocaine. An iodine solution was applied on top of the skin prior to the first incision to prevent wound sepsis. Both eyes were protected from dehydration by application of eye-cream and thermal homeostasis was ensured throughout the

surgery using a homeothermic blanket (37°C). The surgical procedure was performed under visual guidance using a SOM-62 surgical microscope.

Mice were fixed into a motorized stereotaxic using pointed ear-bars and a bite plate to ensure stable cranial positioning and prevent rotation. A patch of skin above the skull was abscised using scissors, connective tissue and hair removed with cotton tips. The skull surface around the determined location of the craniotomy was roughened using a scalpel and the cut skin was fixed with Histoacryl. A 4 mm wide circular biopsy punch was used to outline the cranionomy-position centered on the binocular part of primary visual cortex (bV1) of the right hemisphere, which was subsequently performed using a handheld micro-motor drill. The circular cranial bone was then carefully removed, to avoid puncturing meningeal blood vessels. Any meningeal bleedings were cleared away using Sugis without touching the brain surface. Brain dehydration was prevented by periodic application of sterile artificial cerebro-spinal fluid on top of the brain.

The exogenous expression of the GECIs jGCaMP7b in dLGN and jRGECO1a in L4 of bV1 was mediated by viral gene transfer using AAVs.

For thalamic viral injection, the position of both, bregma and lambda were precisely determined in 3D and registered to the brain atlas to compensate for cranial tilt and scale (using the stereotaxic StereoDrive software). The location of bregma was defined as the coordinate origin for precise positioning of the viral injection site in the dLGN (2.06 mm posterior and 2.05 mm lateral). If the injection location coincided with the position of a meningeal blood vessel, then the x-y position was adjusted manually with the lowest deviation possible to avoid bleeding. Cells in the dLGN were sparsely transduced by a single targeted injection of 50-70 nl of a mixture of AAV2/1-CAG-Flex-FlpO-WPRE (final titer: 6.90 x 10^{10} genome copies/ml) and AAV1-EF1α-F-Flex-jGCaMP7b-WPRE (final titer: 1.10 x 10^{13} genome copies/ml) via a Nanofil glass syringe connected to a beveled gauge 36 needle at a rate of 0.5 nl/s and a depth of 2.75-2.85 mm using an automated micro-injector, unless stated otherwise.

Cells in layer 4 of bV1 were transduced by 3-4 separate 75-150 nl injections 350-450 µm below the pial surface of the viral vector AAV2/1-Syn-Flex-NES-jRGECO1a-WPRE (final titer: 1.08 x 10^{13} genome copies/ml) at a rate of ~0.3 nl/s using beveled borosilicate glass capillaries (outer diameter: 30 µm) connected via a micromanipulator to a pressure microinjection system, unless stated otherwise. The injection sports were placed ~150-200 µm apart along the anterior-posterior axis of bV1.

After injections, the brain surface was thoroughly rinsed with artificial cerebro-spinal fluid and sealed with a round, 4 mm glass cover slip using external superglue gel application, to avoid direct contact of the glue with the brain. A custom-machined aluminum head-plate (including one 8 mm round opening in the middle and two screw notches on the sides) was mounted onto the skull centered on and parallel to the cranial window using dental cement to allow head-fixation for brain imaging. The dental cement was mixed with black pigment to reduce optical interference from extra-brain light reflections during *in vivo* two-photon microscopy.

After surgery, anesthesia was counteracted with a subcutaneous injection of a mixture of Naloxone (1.2 µg/g), Flumazenil (0.5 µg/g) and Atipamezol (2.5 µg/g). Thermal homeostasis was maintained over the period of monitored anesthetic recovery using an infrared lamp. GECIs were expressed for 4-5 weeks prior to experimentation.

2.8 Intrinsic optical signal imaging

Reflected light imaging of intrinsic optical signals (Bonhoeffer and Grinvald, 1991; Bonhoeffer and Hübener, 2016) of OD and retinotopy was performed under light anesthesia as described previously (Jaepel et al., 2017; La Chioma et al., 2019). In brief, initial anesthesia was induced by a single intraperitoneal injection of a mixture of Fentanyl (0.035 µg/g), Medetomidine (0.35 µg/g) and Midazolam (3.5 µg/g) and maintained during imaging by hourly re-injections of 25% of the induction level anesthetics. Mice were fixed under the microscope using a custom machined headplate adapter and the optical axis was orthogonally aligned to the cranial window. The blood vessel pattern was first acquired as a reference for cortical position by side-illumination of the brain surface with light from a 530 nm light-emitting diode (LED). For intrinsic optical signal (IOS) imaging, the brain surface was side-illuminated from two opposite sides with 735 nm LEDs. Intrinsic signals were measured as decreases in reflected light in response to visual stimulation. Reflections caused by the visual stimulation were blocked by placing a light-shield around the objective lens and cranial window. Intrinsic optic signals were band-pass filtered at 700/40 nm. For coarse localization of bV1 signals were collected through a 4x, NA 0.28 objective lens and recorded with a Thorlabs 1500 MonoChrome charged-coupled device camera at a dynamic range of 12 bit, a resolution of 260 x 348 pixels at a frame-rate of 40 Hz. For coarse retinotopic mapping of bV1 signals were collected with a tandem lens macroscope setup using a 135 mm f/2.0 and an inversed 50 mm f/1.2 objective lens ($magnification = \frac{135\ mm}{50\ mm} = 2.7$). Signals were recorded with a pco.edge 4.2 LT sCMOS camera at a dynamic range of 16 bit, a resolution of 512 x 512 pixels at a frame-rate of 35 Hz. The imaging plane was set to be 400-450 µm below the pial surface. Both, acquisition and analysis software were custom written in Matlab.

In mice that did not undergo subsequent two-photon imaging, anesthesia was counteracted by a subcutaneous injection of a mixture of Naloxone (1.2 µg/g), Flumazenil (0.5 µg/g) and Atipamezol (2.5 µg/g) and anesthetic recovery monitored.

2.9 In vivo two-photon calcium imaging

In vivo two-photon imaging of Calcium signals was performed under light anesthesia similar to as described previously (Rose et al., 2016; Jaepel et al., 2017). Briefly, initial anesthesia was induced by a single intraperitoneal injection of a mixture of Fentanyl (0.035 µg/g), Medetomidine (0.35 µg/g) and Midazolam (3.5 µg/g) and maintained during imaging by hourly re-injections of 25% of the induction level anesthetics. Thermal homeostasis was provided with a 37°C heated blanket and eyes protected from dehydration by hourly application of Oculotect® eye fluid. Mice were fixed under the microscope using the implanted headplate adapter and the optical axis was aligned orthogonally to the cranial window using a periscope-based rotating, translating multiphoton imaging microscope system (see Fig. 2.1). GECIs were excited by a wavelength-tunable Ti:Sapphire laser with a pre-chirp unit with a pulse-width of 100 fs at a repetition rate of 80 MHz. Specifically, jGCaMP7b was excited with the laser tuned to a wavelength of 940 nm and jRGECO1a to 1040 nm. Fluorescent signals were collected through a 16x NA 0.8 objective lens, immersed in an ultrasonic imaging gel (diluted 4:1 with H_2O), that was applied directly onto the cranial window. Emitted photons were directed through a 720/25 nm short-pass filter, a primary beam splitter and detected by GaAsP photomultiplier tubes with a 525/50-25 nm (for green emission from jGCaMP7b) or 607/70-25 nm (for red emission from jRGECO1a) bandpass filter, respectively. Light leaks from visual stimulation were blocked from entering the detection path by placing a light-shield around the objective lens and cranial window.

Images with a resolution of 512 x 512 pixels were acquired at 30 Hz for functional imaging or at 1024 x 1024 pixels at 15 Hz for structural imaging by bidirectional scanning using an 8 kHz resonant scanner. Beam turnarounds were blanked using a Pockels cell to avoid excess fluorophore bleaching and image distortions. For functional volumetric multiplane imaging the objective lens was rapidly moved along the optical imaging axis by a high-load piezoelectric stepper, resulting in a pseudo-simultaneous acquisition of 4 successive inclined planes at an effective frame rate of 7.5 Hz. For functional imaging of cells in L4 of bV1, the imaging planes (FOV: 325 µm x 250 µm) were separated in z by 20-25 µm each, whereas for functional imaging of dLGN axons in L4 of bV1 the imaging planes (FOV: 64 µm x 50 µm) were separated 10-15 µm each at a cortical depth of 280-450 µm. For structural imaging 50 subsequent frames were acquired per optical section for post-hoc frame averaging. For structural imaging of cells in L4 bV1, 180-250 optical sections with a FOV of 400 µm x 320 µm were acquired in the red channel, each separated by 2 µm in the z-axis. For structural imaging of dLGN axons in L4 bV1 65-85 optical sections with a FOV of 114.5 µm x 90 µm were acquired in both the red and green channel, each separated by 1.3 µm in the z-axis. The average power for imaging was less than 50 mW below the objective (measured and calibrated using a photodiode).

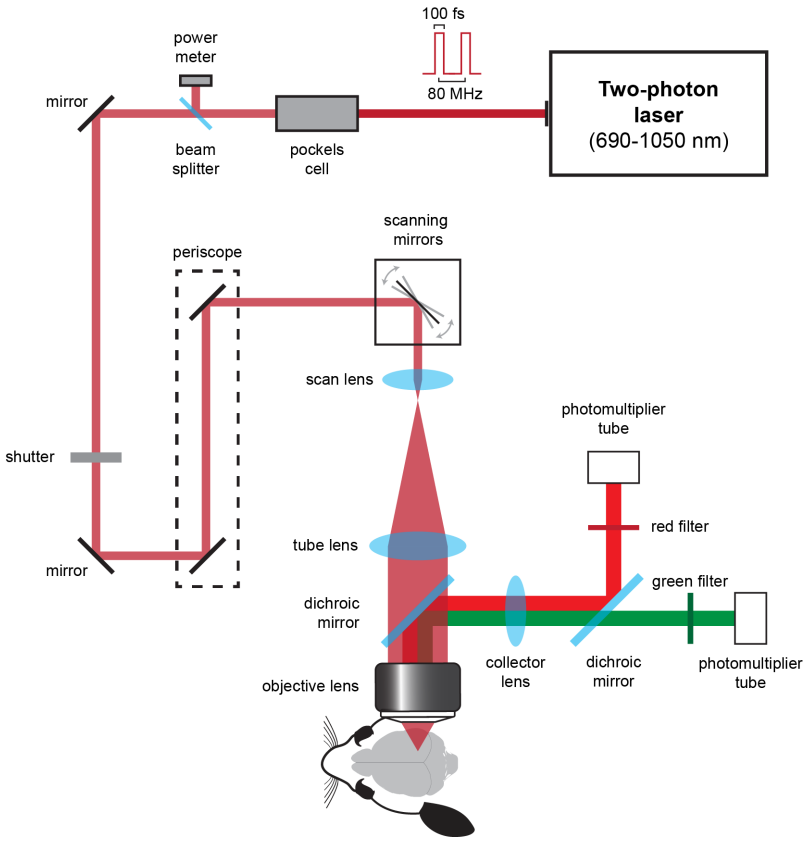

Figure 2.1: **Optical setup the custom-built rotating laser-scanning microscope used for two-photon calcium imaging.** A wavelength-tunable, pulsing Ti::Sapphire laser emitting 100 ns pulses at a repetition rate of 80 MHz acts as the light source. During excitation of jGCaMP7b, the laser is tuned to 940 nm, during excitation of jRGECO1a to 1040 nm. The beam is passed through a pockels cell, where the beam-intensity is regulated. 8% of the beam is subsequently re-directed by a beam-splitter into a power meter for measuring the laser-power. The residual 92% of the beam is redirected by mirrors through a stimulus-locked shutter (as a safeguard to only have the beam pass during imaging) to the scanning mirrors by a periscope. The periscope allows for rotation of the microscope body (and thereby the imaging angle) by keeping the beam centered without the need for re-alignment. The scanning mirrors consist of one 8 kHz resonant mirror and one galvanometric mirror and redirect the laser beam through a scan and tube-lens for beam expansion for filling the back aperture of the microscope objective. The expanded beam is then passed through a dichroic mirror into the objective lens, which focuses

the beam for two-photon excitation of the calcium indicators in the brain. Emitted photons are collected by the objective lens and re-directed by the dichroic mirror for detection. Re-directed photons are collected by a collector lens and directed through red or green filters into their respective photomultiplier-tubes using a dichroic mirror.

Data were acquired using ScanImage 4.2 (Pologruto et al., 2003) and custom written hardware drivers.

During two-photon imaging, the mouse including the stimulation screen and eye-shutters were imaged from behind using an infrared camera. Further, both eyes were imaged with an infrared video camera and their pupil position and diameter monitored online using custom-written software in LabVIEW as described previously (Sakatani and Isa, 2007).

In mice that were not subsequently perfused, anesthesia was counteracted was counteracted by a subcutaneous injection of a mixture of Naloxone (1.2 µg/g), Flumazenil (0.5 µg/g) and Atipamezol (2.5 µg/g) and anesthetic recovery monitored.

2.10 Visual stimulation

Visual stimulation was performed as described previously (Rose et al., 2016; Jaepel et al., 2017). In brief, all visual stimuli were generated using Matlab and the Psychophysics Toolbox extension (Brainard, 1997; Pelli, 1997) and presented on a gamma-corrected liquid-crystal display (resolution: 2560 x 1440 pixels, size: 27 inch, refresh rate: 60 Hz). The screen was positioned 16 cm in front of the mouse and the angle horizontally matched to the mouse's head tilt. All visual stimuli were warped using an OpenGL shader to correct for the representation of the spherical mouse visual space on a flat surface screen.

2.10.1 Visual stimulation for intrinsic optical signal imaging

For coarse localization of bV1 using IOS imaging (Rose et al., 2016; Jaepel et al., 2017) the screen was centered in the visual field of each mouse. Drifting square wave gratings (8 directions – changing every 0.6 s, SF: 0.04 cycles/°, temporal frequency (TF): 2 cycles/°) were presented monocularly in pseudo-random order in either the right of left 20° of the visual field azimuth as patches of 20° x 40° on grey background (50% contrast). Stimuli were presented to either the left or right eye for 7 s with an inter-trial interval of 8 s (number of stimulus trials: 7). Precise time-locked monocular presentation was ensured by using motorized eye-shutters.

For coarse retinotopic mapping of both V1 and bV1 using IOS imaging the screen was positioned in the right or left eye's hemifield, respectively, so that the binocular visual field (± 20° from midline) was still fully covered in azimuth (coverage azimuth: -20° to +100°, coverage elevation: -40° to +40°). Bars (width: 20°) consisting of a reversing checkerboard pattern (SF: 0.04 cycles/°, TF: 2 Hz) were periodically swept over a grey background (50% contrast) in both directions of each cardinal axis (Kalatsky and Stryker, 2003; Marshel et al., 2011; La Chioma et al., 2019) at a speed of 20 °/s. The stimuli were presented subsequently to either the right or left eye in 10 trials using locked eye-shutters.

2.10.2 Visual stimulation for two-photon Calcium-imaging

Additional to light shielding, the backlighting of the liquid crystal display was synchronized to the timing of beam-blanking by the Pockels cell during turnaround time of the resonant scanner to minimize the light leak of visual stimulation during two-photon image generation as described previously (Leinweber et al., 2014). Visual stimulation was always preceded by acquisition of 160 dark-frames, with laser excitation turned off.

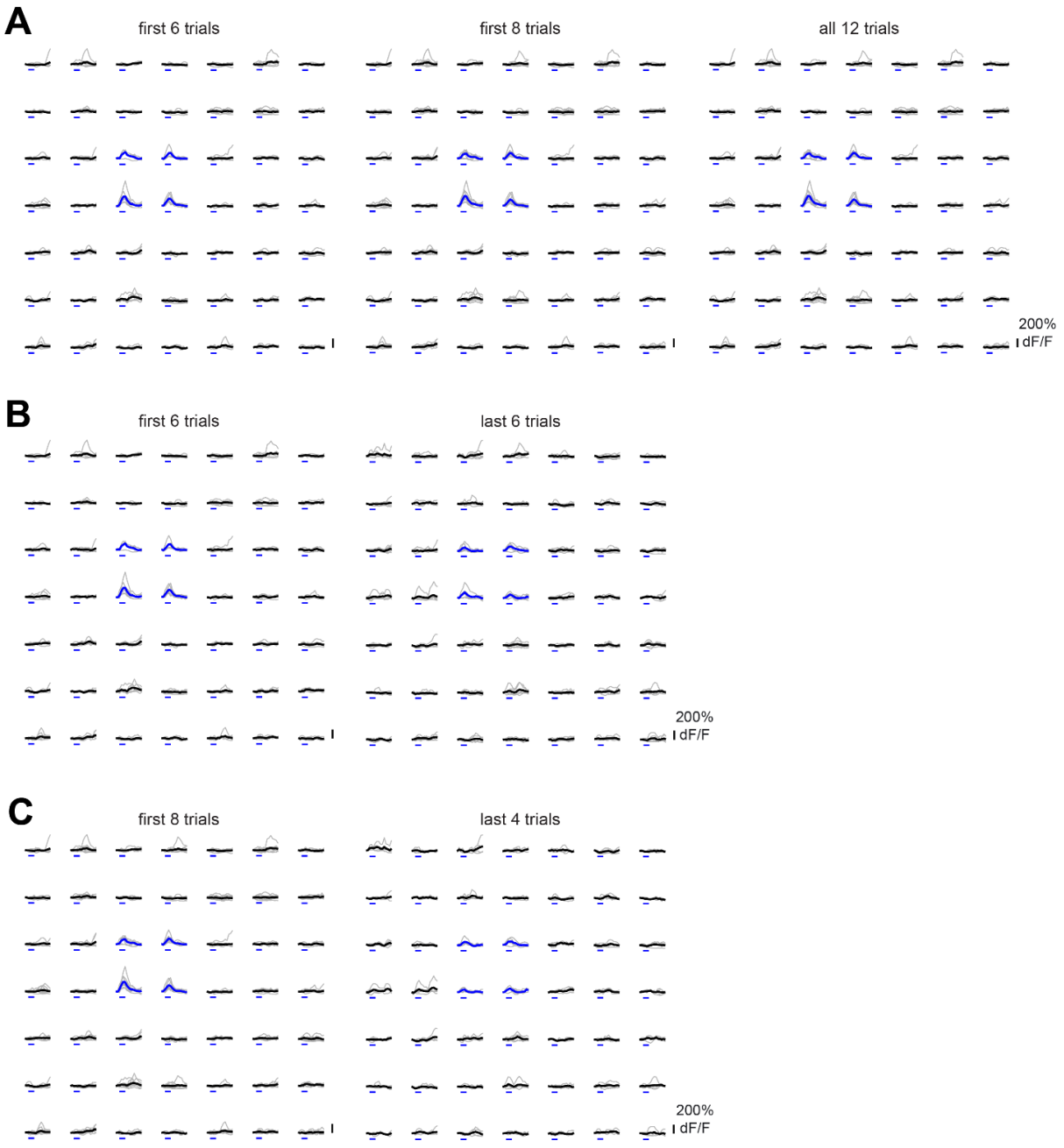

Figure 2.2: **Reliability of calcium transients of a dLGN bouton to sparse noise stimulation over trials. A-C|** RF calcium transients of the same bouton compared over different trial-numbers. Transients are shown in accordance to their relative sparse noise stimulus-patch positions for each trial (grey) and the trial average (black, bold). Trial averages of significant RF patches are illustrated in blue. Stimulation period is indicated as a blue bar below each transient. **A|** RF transients and averages taken from the first 6 (left), first 8 (middle) and all 12 sparse noise stimulation trials (right). **B|** RF transients and averages from the first 6 (left) compared to the last 6 sparse noise stimulation trials (right). **C|** RF transients and averages from the first 8 (left) compared to the last 4 sparse noise stimulation trials (right).

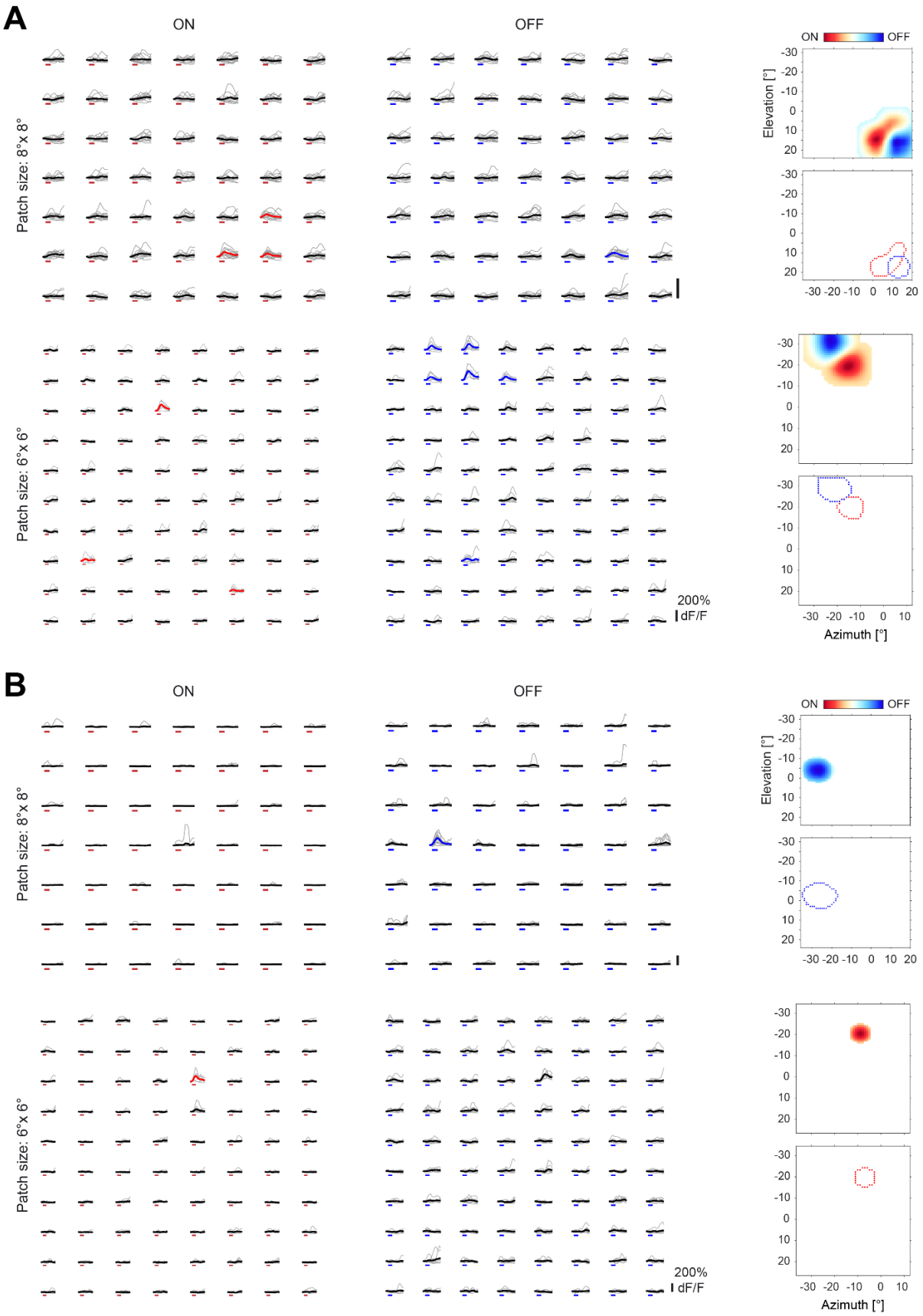

Figure 2.3: **Receptive fields of layer 4 cells and dLGN axons at different sparse noise resolutions. A-B|** Example RF-subfield calcium transients (left, middle). Transients are shown at their relative sparse noise stimulus-patch positions for each trial (grey) and the trial average (black, bold). Trial averages of significant RF patches are

illustrated in red for ON-subfields (left) and blue for OFF-subfields (middle). Timing of visual patch-presentation is indicated as a red bar for light-increments (ON) and blue for light decrements (OFF) below each transient. The corresponding RF (right, top) and subfield-outlines (right, bottom) are plotted in visual space. **A|** Example RFs of two cells imaged with a sparse noise patch size of 8°x8° (top) or once with 6°x6° (bottom). **B|** Example RFs of two boutons imaged with a sparse noise patch size of 8°x8° (top) or once with 6°x6° (bottom).

For determining OD, direction tuning and orientation tuning, the screen was centered in the visual field of each mouse. Square wave gratings drifting in 12 directions (SF: 0.04 cycles/°, TF: 3 cycles/s) were presented monocularly in pseudo-random order in the binocular visual field (coverage azimuth: -25° to +25°, coverage elevation: -15° to 35°, relative to midline) on a grey background (50% contrast). Stimuli were presented for 5 s, followed by 6 s of a full-screen grey background at 50% contrast to each eye using motorized eye-shutters (number of stimulus trials: 6).

Spatial RFs were mapped by monocular presentation of sparse noise using motorized eye shutters (number of trials: 8, unless stated otherwise; see Fig. 2.2 for responses to varying trial numbers). Sparse noise stimuli consisted of black and white patches (patch size: 6° x 6°, unless stated otherwise; see Fig. 2.3 for RFs mapped with different patch sizes) that were presented within an area of 48° in azimuth and 60° in elevation (-25° to 35° elevation and -36° to 12 azimuth, relative to midline) on a grey background. Patches were shown for 0.4 s with an inter-stimulus interval (ISI) of 0.2 s at 80 different positions in pseudo-random order, in which neighboring patches were never presented subsequently to avoid orientation-components in the RF responses.

2.11 Histology and Immunohistochemistry

Mice were anesthetized by an intraperitoneal injection of a mixture of Fentanyl (0.075 µg/g), Medetomidine (0.75 µg/g) and Midazolam (7.5 µg/g) and transcardially perfused with 15 ml of LM flushing perfusion solution followed by 45 ml of LM fixative solution at a flow-rate of 10 ml/min using a syringe pump. After perfusion, the brain was removed from the skull and submerged in fixative solution for post-fixation for about 7 days at 4°C. The brain was subsequently transferred into a 30% sucrose solution at 4°C until the brain sank to the bottom of the solution (about 3-4 days). During sucrose infiltration intracellular H_2O was exchanged to avoid membrane damage through crystallization of H_2O during subsequent sectioning on a freezing microtome.

Brains were sliced into 50 µm thick coronal sections using a sliding freezing microtome and transferred into PBS. Sections were either directly mounted on objective slides with Fluoro-Gel and sealed with a coverslip and transparent nailpolish, or first immunohistochemically stained.

For immunohistochemistry against GCaMP, brain slices were incubated in blocking buffer overnight at 4°C. Sections were then incubated in a primary anti-GFP antibody solution for 3 h at RT, followed by 4°C overnight. Sections were subsequently washed three times for 10 min in PBS, incubated in a secondary antibody solution for 2 h at RT and washed again three times for 10 min in PBS at RT, before being mounted on objective slides.

Both, direct fluorescent signals from exogenously expressed GCaMPs and/or jRGECO1a and immunohistochemically amplified fluorescent signals were acquired with a ZEISS Axio Imager M2 epifluorescent microscope. Images of 1388 x 1040 pixels were acquired with either a 5x NA 0.15, 10x NA 0.3 or 20x NA 0.5 air objective.

2.12 EM-grade transcardial perfusion

For functional connectomics experiments, mice were transcardially perfused immediately following completion of *in vivo* two-photon calcium imaging. Mice were transitioned from light anesthesia into deep anesthesia with an intraperitoneal injection of a mixture of Fentanyl (~0.06 µg/g), Medetomidine (~0.6 µg/g) and Midazolam (~6 µg/g). An about 1 cm long wooden shaft was placed between the jaws to allow for later stereotaxic fixation using a bite-plate. After 15-20 min mice were transcardially perfused through the left ventricle with 15 ml of EM flushing perfusion solution followed by 45 ml of EM fixative solution at a flow-rate of 10 ml/min using a syringe pump connected to a beveled cannula (length: 32 mm, diameter: 0.60 mm). Perfused animals were decapitated and the head fixed into a stereotaxic using ear-bars and a bite-plate. The dental cement and glue securing the cranial window were carefully removed using a handheld micro-motor drill under visual guidance through a SOM-62 surgical microscope. Drill-dust was cleared away and the cranial window removed. The head was immersed in EM fixative solution for approximately 24 h at 4°C for post-fixation through the craniotomy.

2.13 Stereotaxic biopsy extraction

Circular standard biopsy punch barrels (diameter: 2.0 mm, unless stated otherwise) were extracted from their plastic pens using a heat gun. The biopsy punch barrels were mounted to an electric, rotary toothbrush, which in turn was mounted to a stereotaxic micromanipulator using custom machined adapters. Adapter positioning was optimized under visual guidance using a Leica stereo microscope to minimize vibration of the biopsy punch in either axis during rotation, to ensure clean biopsy extraction and avoid tissue damage.

The fixed mouse head was mounted into a dual stereotaxic apparatus, using a bite-plate two custom machined stereotaxic earbar-to-headplate adapters. Stereotaxic headplate-mounting allowed for precise translation of the optical axis and cortical positioning of two-photon imaging for biopsy extraction. The z-axis angle of the stereotaxic micromanipulator was aligned parallel to the optical axis of two-photon imaging, using the angle information of the rotating, translating periscope two-photon microscope relative to the implanted headplate. The cortical position of the two-photon FOV in the exposed craniotomy was triangulated and re-confirmed by partial matching of meningeal blood-vessel patterns (stained in light blue by DiD from perfusion). The biopsy punch was centered on the two-photon FOV and carefully lowered 1-1.5 mm into the brain and retracted using the attached micromanipulator. The biopsy punch was in rotation by the electric toothbrush, to minimize tissue compression. After retraction, the headplate and the top of the skull were surgically removed to expose the brain. A control biopsy was analogously punched in the prefrontal cortex (PFC) on the same hemisphere. Here, the z-axis angle of the stereotaxic micromanipulator was manually aligned under visual guidance to be parallel to the cortical surface. The brain was carefully extracted from the skull and sectioned into 3 mm thick coronal slabs with a razor blade using an Adult Mouse Brain Matrix. Positioning of the coronal slabs was individually centered around the biopsy locations. Using a razor blade, the biopsies were extracted by a single cut angled parallel to the biopsy's cortical surface at the white matter border.

The resulting 1-1.5 mm deep cylindrical biopsies were sequentially glued to an angle-adjustable magnetic vibratome plate with the white matter facing down. Prior to experimentation, the positioning of the vibratome razorblade was optically verified and optimized using a Leica Vibrocheck™. Next, the vibratome plate was submerged into the cutting chamber containing 150 mM

Cacodylate Buffer and the biopsy surface, corresponding to the pial surface, was set parallel to the cutting direction and razor blade angle. To avoid heavy metal staining gradients in EM, the top 50 µm of the pial surface were sectioned off, unless stated otherwise, using a Leica VT1200 S Microtome. Due to the curvature of the cortical surface, the 50 µm were set from the peak of the cortical arch, located in the biopsy center. This resulted in about two thirds of the pial surface being cut, leaving enough meningeal blood-vessels on the sides of the biopsies for landmark-matching. Next, a 450-500 µm thick section was cut and incubated in 150 mM Cacodylate Buffer overnight, before subsequent *en bloc* heavy metal staining.

Both, biopsy extraction and vibratome cutting was performed under visual guidance using stereo microscopes. Brain dehydration was prevented by periodic application of 150 mM Cacodylate Buffer. Sample extraction was photographically documented using a Canon EOS 1200D.

2.14 En bloc heavy metal staining

Extracted biopsies were manually stained for 3D-EM in 2 ml eppendorf tubes using a protocol modified from Hua et al. 2015 at RT unless stated otherwise. All solutions were prepared fresh before their respective staining step. Samples carefully were transferred using one-time use plastic pipettes, to avoid tissue damage.

Samples were incubated in 150 mM cacodylate buffer for 30 min and subsequently transferred into 2% OsO4 in cacodylate buffer for 90 min. The samples were transferred into filtered 2.5% potassium-ferrocyanide in cacodylate buffer incubated for 90 min. Subsequently, the samples were submerged into 2% OsO_4 in cacodylate buffer for 45 min before being washed in 150 mM cacodylate buffer and ultrapure H_2O for 30 min each. The solution was exchanged with a filtered 1% thiocarbohydrazide solution and the samples incubated for 60 min at 40°C. The samples were washed twice in ultrapure H_2O for 30 min each and subsequently immersed in an unbuffered 2% OsO_4 solution for 90 min. After two washing steps in ultrapure H_2O for 30 min each the sample was incubated in a filtered 1% uranylacetate solution at 4°C overnight and subsequently for 120 min at 50°C. The samples were washed twice in ultrapure H_2O for 30 min each before being immersed a 20 mM lead aspartate solution for 120 min at 50°C. The samples were then washed twice in ultrapure H_2O for 30 min each.

2.15 En bloc embedding

To embed the heavy metal stained samples in resin *en bloc*, samples were first dehydrated. During these steps, samples were handled with extreme care, to avoid the induction of cracks. The stained biopsies were immersed at 4°C in pre-cooled 50% EtOH in ultrapure H_2O for 30 min, followed by pre-cooled 75% EtOH in ultrapure H_2O for 45 min. The solution was exchanged with fresh 100% EtOH (rinsed twice) and the tissue incubated at RT for 45 min, followed by 3 incubations in fresh 100% Acetone at RT for 45 min each. The tissue was then infiltrated by submersion in a 3:1 mixture of Epoxy resin and acetone for 4 h on a rotator at 2 rpm at RT. The biopsies were subsequently immersed in a 1:1 mixture of Epoxy resin and acetone overnight at 2 rpm at RT. The next day, samples were incubated in a 1:3 acetone and Epoxy resin mixture, followed by pure Epoxy resin for 4 h at RT, rotated 2 rpm respectively. The Epoxy resin was exchanged with fresh pure Epoxy resin and samples were incubated without rotation overnight at 4°C. The biopsies were then incubated at 2 rpm in fresh Epoxy resin for 4 h at RT. Infiltrated samples were then embedded in custom made molds on top of an aluminum-pin in fresh Epoxy resin and cured in a pre-heated oven at 60°C for 72 h. The molding base was prepared prior to embedding by curing Epoxy resin in the embedding molds onto the aluminum

pins for at least 24 h at 60°C. The hardened resin was then trimmed parallel to the pin surface with about 2 mm of excess epoxy resin covering the tip of the pin.

Both, dehydration and Epoxy resin solutions were freshly prepared prior to each step. Epoxy resin components were, stored at 4°C were pre-warmed at RT for 30-45 min before resin preparation and bubbles the Epoxy resin mixture were surfaced on a benchtop table-rocker.

2.16 Micro Computed Tomography

To investigate possible heavy metal staining gradients, sample orientation, sample localization and trimming verification in a non-invasive, non-destructive fashion, embedded biopsies were imaged using microCT using a Xradia 520 Versa 3D X-Ray microscope at 3.9615x optical magnification. Samples were rotated inside the imaging chamber directly on the embedded aluminum pin and the center-shift of the rotating sample determined prior to imaging. The distance of the sample to both, the x-ray source and detector were manually set for each sample.

To assess possible staining gradients each biopsy was first imaged with 801 angle-projections at a power of 80 kV at 88-89 µA and 2 s exposure per projection. Pixels were binned 4x resulting in an effective pixel size of ~7.8 µm.

Biopsies selected for further ultra-microtome sectioning, were additionally imaged with 1601 angle-projections at a power of 80 kV at 88 µA, 1 s exposure per projection and 2x pixel binning resulting in an effective pixel size of ~3.2 µm for more in-depth assessment of sample orientation and localization relative to the cortical surface. During sample trimming, correct orientation and positioning of trimmed edges were validated by imaging the trimmed samples at low resolution with 801 angle-projections at a power of 80 kV at 87-88 µA and 4x pixel binning resulting in an effective pixel size of ~7.4 µm. Exposure time was set to 0.12 s per projection to decrease sample-exposure to x-rays.

2.17 Sample trimming & smoothing

For all, single beam EM, ATUM and mSEM, embedded samples were trimmed using the rotating diamond head trimming machine Leica EM TRIM2. To prevent exposure to resin and heavy metal micro-dust, the trimmer was enclosed in a custom machined transparent enclosure connected to a vacuum and FFP3 masks were worn. Debris accumulating on the sample was periodically cleared using pressurized air. Sample surfaces were smoothed with a 4 mm wide DiATOME ultra 35° diamond knife inside a Leica EM UC7 ultra-microtome. Both trimming and smoothing were performed under visual guidance using Leica M80 Stereomicroscopes.

2.17.1 Trimming

Samples were first trimmed for investigation of the ultrastructure in a single beam EM. The aluminum-pin holding the embedded sample was mounted into the Leica EM TRIM2 using a custom-machined metal adapter. The sample surface was set parallel to the trimming direction using the 3D microCT reconstruction as reference. Excess Epoxy resin covering the sample was trimmed away and the entire surface carefully exposed, by removing the minimum amount of tissue necessary. Control biopsies were trimmed into the middle of the sample to expose the sample core. Next, the sample surface was aligned perpendicular to the trimming direction and the trimming depth adjusted with the tip of the trimmer head diamond about 100-300 µm below the lower sample edge. The triangulated ultra-microtome cutting direction was aligned parallel to the trimming direction using landmarks identified in microCT as reference. Most of the excess epoxy resin surrounding the sample was trimmed away, until the resin edge was about 200-400 µm outside the sample and the trimming angle verified using

low-resolution, low exposure microCT. The sample was rotated by 90 degrees and the resin trimmed until the resin edge was between 500-1000 µm outside the sample. The sample was rotated another 90 degrees and the previous to steps were repeated, resulting in an elongated resin rectangle, centered around the sample. The width of the minor axis was below 3.5 mm to not exceed the 4 mm wide diamond knife. Sample surfaces were subsequently smoothed using a Leica EM UC7 microtome, electrically connected to the aluminum pin using conductive silver paint. The resin rectangle and about 75% of the sample edges were manually painted with a thin hair brush and the paint dried for at least 30 min. Samples were subsequently screened using a single beam electron microscope.

Samples selected for ATUM cutting were further trimmed into a hexagonal shape. Excess silver-paint from screening was carefully trimmed away by removing the minimum amount of tissue and resin necessary. The sample was then iteratively trimmed into the symmetric, hexagonal shape designed on the basis of microCT. The final hexagon's inner rectangle was elongated along cutting direction at an aspect ratio of 1.1 and the upper and lower triangles trimmed at an angle of 30°, unless stated otherwise. The hexagon did not contain any excess resin on either side or corner with the exception of the upper tip in respect to cutting direction, to avoid introducing compression inhomogeneities during ultramicrotome cutting. The final hexagon shape was verified with low-resolution microCT at low exposure.

2.17.2 Smoothing

For smoothing, the major axis of the rectangle or hexagon was set to be parallel to cutting direction and centered on the 4 mm diamond knife. The knife edge was manually approached to about 1 mm from the sample surface. The sample surface was iteratively aligned parallel to both the knife edge and cutting axis, using bottom-lighting for visual guidance. Specifically, the light passing through the slit between the knife edge and sample surface was used at different positions along the cutting axis to guide exact alignment. During the final iteration the knife edge was about 1-2 µm from the sample surface.

The microtome arm movement was started and the sample approached to the knife edge at a cutting thickness of 200 nm and cutting speed of 600 µm/s. Once the entire rectangle or hexagon surface was cut, cutting thickness and cutting speed were reduced to 100 nm and 300 µm/s, respectively. The sample was cut for 1 to 2 µm and the cutting thickness sequentially reduced to 80 nm, 60 nm, 50 nm and 40 nm after cutting about 1 µm each. Finally, cutting thickness was reduced to 35 nm and the sample cut for another 1 to 2 µm. Sections were not collected and the accumulating debris on the knife edge was periodically removed using pressurized air along the knife edge and a vacuum. Debris removal and microtome adjustments in speed or cutting thickness were exclusively performed in the retraction phase of the microtome arm, to avoid introducing disturbances during cutting.

The surface of smoothed samples was visually investigated using light reflections.

2.18 Automated tape-collecting ultra-microtome

To remove impurities and contaminants from the tape surface, carbon-coated kapton tape was plasma cleaned at a sputtering current of 30 mA while tape-reeling using a Quorum Q150R ES Rotary Sputter Coater.

Biopsies were sectioned into ultra-thin serial sections using a Leica EM UC7 Ultramicrotome and a 4 mm wide DiATOME ultra 35° diamond knife as established by Meike Schurr (Sievers et al., unpublished) and further optimized by Lev Dadashev, Selina Horn and Smaro Soworka (MPI for Brain

Research). The knife edge was aligned to the sample surface analogous to during smoothing (see above).

2.18.1 ATUM experiments

Prior to experimentation, the sample was trimmed into an elongated hexagonal shape (length: 2.4 mm, width: 1.35 mm, aspect ratio of inner rectangle: 1.1) with the bV1 cortical surface parallel to the hexagonal surface. The sample was prepared with the upper 70-80 µm of cortical L5 (as evaluated with microCT) at the top and cortical L2/3 at the bottom, with the region of interest (ROI) in cortical layer 4 in between (sample depth: 360 µm) and the sample surface smoothed. The sample was then cut under continuous visual guidance into ultra-thin serial sections, which were collected on kapton tape using an ATUMtome (Schalek et al., 2011).

First, the sample rotation was set, by adjusting the lower edge of the interior rectangle within the hexagon to be parallel to the smoothing-knife edge, to avoid asymmetric compression during cutting. The sample surface was adjusted to be parallel to the knife edge. The knife chamber was filled with sterile H_2O and connected to the knife edge via surface tension using a single-hair brush. The tip of the ATUMtome arm guiding the kapton tape for section collection was minimally submerged into the water-bath and positioned about 2.5 mm from the knife edge, without touching the chamber or knife. The final position and height was micro-adjusted, so that the ATUMtome tape collection did not cause any disturbances on the water surface, to avoid disruptions to microtome sectioning and section collection. A water pump was connected to the water-bath behind the ATUMtome tip by a silicon tubing using a custom built magnetic adapter for remote water-level control.

The sample surface was visually set to be 2-4 µm from the knife edge and the sample surface approached at an ultramicrotome cutting speed of 600 µm/s at a step-size of 100 nm. When the sample was close to being cut (as evaluated under visual guidance using a connected stereomicroscope), the cutting speed was reduced to 300 µm/s. Once the entire sample surface was cut, the step size was sequentially reduced to 80 nm, 60 nm, 50 nm, 45 nm, 40 nm and 35 nm after 5-15 successful cuts, each. Cutting performance was assessed under visual guidance.

Next, the test-knife was exchanged with a new, unused diamond knife and the sample surface set parallel to the knife edge, the knife chamber filled with sterile H_2O, the ATUMtome set into position and the water pump connected analogous to the previous step. The sample surface was visually set to be ~2 µm from the knife edge and the sample surface approached at an ultramicrotome cutting speed of 600 µm/s at a step-size of 35 nm. Once the sample was close to being cut, the cutting speed was reduced to 300 µm/s and the ATUMtome was started for tape collection at an ATUM motor speed of 315 rpm for the upper and 300 rpm for the lower motor, to retain tape-tension. The first 20 full-cut sections were visually evaluated on-site for cutting quality and parameters adjusted in case of problems. The section count was started and from here on the cutting was continuously monitored remotely by a recorded camera-feed from the attached stereo-microscope, to prevent introduction of any disturbances to the experiment in form of vibrations. Furthermore, the water level was continuously monitored and remotely adjusted using the water pump. During problematic cutting regions, in which the variation in cutting thickness increased or compression artifacts occurred, the cutting step-size was temporarily increased from 35 nm to 40 nm, until cutting stabilized and the step size was set back to 35 nm.

Increased scratching of the slices during cutting and continuous degradation of cutting quality, likely caused by accumulation of micro-debris and/or blunting of the knife edge, was carefully monitored under visual guidance. Once scratches appeared repeatedly at the same position or before cutting quality degradation reached a detrimental point, cutting was stopped the knife was immediately exchanged or shifted, to avoid losing neurite continuity by artifacts. Both, knife shift and knife exchange were performed as precise and quick as possible to avoid losing sequential sections by e.g. inhomogeneous sample expansion. The microtome advance was reset and kapton tape tension in the ATUMtome evaluated and adjusted if required.

Knife shifts were performed if only one side of the knife has been used. The ATUMtome arm was removed from the knife chamber. Using an integrated micro-motor the knife was retracted 3-5 µm and the knife shifted parallel to the sample surface, so that the entire sample width was positioned on the uncut side of the knife edge and the ATUMtome arm was re-submerged into position. The parallel alignment of the knife edge to the sample was ensured and adjusted if necessary as described above. The sample surface was visually set to be ~1-2 µm from the knife edge and the sample surface approached at an ultramicrotome cutting speed of 300 µm/s at a step-size of 35 nm. Cutting performance of the first cuts was monitored on site and subsequently continued remotely as previously.

Knife exchanges were performed if both sides of the diamond knife have been used for cutting. The knife was retracted >20 µm from the sample and both, the ATUMtome arm and water pump were removed from the knife chamber. The diamond knife with the connected chamber were exchanged with a new knife, the knife edge was set parallel to the sample surface, the knife chamber filled with sterile H_2O, the ATUMtome set into position and the water pump connected as previously. The parallel alignment of the knife edge to the sample surface was re-confirmed and adjusted if necessary. The sample surface was visually set to be ~2 µm from the knife edge and the sample surface approached at an ultramicrotome cutting speed of 600 µm/s at a step-size of 35 nm. Cutting performance of the first cuts was monitored on site and subsequently continued remotely as previously. Once the sample was close to being cut, the cutting speed was reduced to 300 µm/s. Cutting performance of the first cuts was monitored on site and subsequently continued remotely as previously.

2.19 Multibeam Scanning Electron Microscopy

2.19.1 Mounting on silicon wafers

Silicon slabs were cut from their original 6 inch diameter into 10 cm x 9.5 cm rectangular wafers using a Fiber Laser Cutter at 1064 nm at 20 W. The polished side was covered without gaps edge to edge with a single layer of 25 mm wide double-sided conductive carbon tape. The ATUM kapton tape containing the hexagonal serial sections was sequentially cut between slices into 6-9 cm long stripes and mounted with the uncoated side on the double sided carbon tape to the wafer. The kapton tape was lowered with tweezers onto the sticky carbon tape parallel to the carbon tape or previous kapton stripe from the middle outwards. The stripe was carefully and slowly pushed onto the adhesive avoiding to trap bubbles in between and by minimal bending of the kapton tape to avoid micro-cracks. To avoid artifacts during mSEM imaging, the ATUM stripes were mounted at a minimum distance of 5 mm to the wafer edges and did not cross over the underlying carbon tape endings. Usually 10 kapton stripes containing 220-250 ATUM sections were mounted onto a single wafer with 2 stripes each on the top and bottom carbon tapes and 3 stripes each on the middle two carbon tapes.

Mounting was performed in a laminar flow hood to avoid contamination such as dust particles below the tape. Mounted silicon wafers were subsequently incubated for 24 h at RT and subsequently for at least 7 days in vacuum (~0.05 bar) at 40°C for outgassing, before being mounted on mSEM wafer holders.

2.19.2 Mounting on wafer holder

Wafers were removed from the vacuum oven and the ATUM tape inspected. In case of critical bubbles below the tape, the wafers were either directly further incubated in vacuum at 40°C, or the bubbles carefully punched with a pointed tweezer. Wafers were subsequently mounted onto an mSEM wafer holder. First, the wafer was positioned 1-2 mm adjacent to the wafer holder's calibration L-markers and fixed into position and electrically connected with a single drop of silver paint at each of the 3 carbon tape to carbon tape interfaces at the wafer edge. This was repeated at each of the two wafer sides with interfaces, resulting in total in 6 placed drops per wafer. Each drop was placed to connect to both respective carbon tapes as well as the wafer holder. Silver paint was dried for 10-15 min at RT. Next the wafer and ATUM kapton tape stripes were directly electrically connected to the wafer holder using SEM conductive double sided carbon tape. First, the 4 wafer edges were connected to the wafer holder, leaving a minimum distance of 2 mm to each L-marker. Next, each kapton tape was connected along both of its edges to the wafer holder with thin carbon tape stripes. To ensure tight fit, SEM carbon tape stripes were carefully swept with a bent tweezer without touching the kapton tape and ATUM sections. Each SEM carbon tape was placed at a minimum distance of 2 mm to the sections and the tape stripe widths was individually adjusted prior to placement using a razor blade. Mounted wafer holders were imaged in LM for section detection and subsequently incubated for a minimum of 24 h in vacuum at 40°C before mSEM imaging.

Successfully mSEM imaged wafers were unmounted from their wafer holders by removing the connecting carbon tape with tweezers without damaging the sections. The 6 silver paint connections were cut with a surgical razor and the wafer either stored in vacuum at 40°C or at RT and room pressure in a dust-free environment. The wafer surface was carefully cleared of tape glue and silver paint using 100% acetone and subsequently polished using 100% isopropanol, without touching the calibration L-markers. Empty wafer holders with contaminated calibration L-markers were plasma cleaned for 10-15 min inside the mSEM pre-chamber at a plasma pressure of 0.2 mBar at a plasma power of 20 Watt for 10 min.

Both mounting and unmounting of silicon wafers onto and from wafer holders was performed in a laminar flow hood, to reduce contamination with dust particles.

2.19.3 Wafer light microscopy and section definition

To define the exact position and orientation of each section for subsequent mSEM, wafer holders were imaged with light microscopy and section outlines defined. Mounted wafer holders were secured into a Zeiss AXIO Imager A2 Vario light microscope. First, all three L-markers ("L"-engraved plateaus in three of the for wafer holder corners) of the wafer holder were detected and defined, forming the wafer holder's internal coordinate system. Each marker was engraved with two "L"s of two sizes. The position of each marker was defined as the tip of the small L-engraving. Next, wafers were imaged with an EC Epiplan-NEOFLUAR 5x NA 0.13 HD DIC objective lens and stitched on the fly, using the Zeiss Efficient Navigation (ZEN) software.

Next, section positions and orientations were defined in ZEN. Each ATUM kapton tape was manually outlined with a rectangular ribbon each. A hexagon was manually drawn around the first section of the first imaged wafer, serving as the template for all sections. For subsequent wafers, the section template was copied and manually positioned and oriented around a section. Sections were then automatically detected within each ribbon based on the set template. Automatically detected section outlines were manually proofread, meticulously adjusted in both position and orientation to fit each section and numbered in ATUM cutting sequence with their respective section identifier (ID). Section outlines were triangulated as relative positions to the L-markers and were therefore transferable between microscopes, once calibrated. Results were saved and transferred to the mSEM.

2.19.4 Multibeam Scanning Electron Microscopy

Multibeam SEM was performed on a Zeiss mSEM 505 system (Eberle et al., 2015). Both, the imaging chamber and pre-chamber of the mSEM were regularly plasma cleaned to remove impurities and contaminants before imaging. The imaging chamber was plasma cleaned in vacuum for 25-30 min at 20 Watt at an ignition pressure of 0.27 mBar, prior to each imaging session. The pre-chamber was periodically plasma cleaned in vacuum for 10 min at 20 Watt at an ignition pressure of 0.27 mBar prior to imaging.

Wafers were transferred into the imaging chamber using a pre-chamber. Briefly, wafer holders were first attached to a metal rod in the pre-chamber, which was subsequently pumped to a negative pressure. Once the pressure was roughly equivalent to the vacuum of the imaging chamber, the wafer holder was secured into the wafer holder-holder inside the imaging chamber using the attached metal rod. The rod was retracted into the pre-chamber and the imaging chamber pumped to a negative pressure of $< 1 \times 10^{-6}$ mBar.

Both, the L-markers and the imaging system were calibrated prior to imaging. For the first section of the first wafer, a 1 x 1 mm^2 imaging EM FOV was set, centered on the two-photon imaging location as triangulated with 3D microCT. Further, 5 focus support points were distributed roughly equidistantly at the EM FOV border. Focus support points served as calibration of focus, stigmatism and centering of the 61 electron beams on the detectors prior to imaging of the respective EM FOV. Focus support points were automatically set for each ROI prior to imaging at a landing energy of 1.5 kV at a pixel dwell-time of 200 ns at a pixel-size of 10 nm x 10 nm. If more than 25% of the 5 focus support points failed in their procedure, that respective FOV was not imaged. These sections were later revisited and focus support point parameters manually determined for imaging. A focus-, stigmatism and beam on detector plane was fitted for each EM FOV using Delauney-interpolation to approximate the topological map and compensate for sections tilts. The EM FOV and focus support points were saved relative to the hexagonal section outline and applied to all sections. The SNRs from each beam readout were matched using detector equalization and focus distance minimized prior to imaging.

EM FOVs were imaged with a 61-beam Zeiss mSEM 505 at a landing energy of 1.5 kV and a pixel dwell-time of 50 ns at a pixel-size of 4 nm x 4 nm. Images within a 61-beam hexagon were imaged with a 1 µm overlap between individual beams. 61-beam hexagon tiles were imaged with a 6% overlap at a stage-settling time of 1 s. Sections were imaged on the wafer in snake sequence to minimize stage movement, but saved labeled according to their ATUM cutting ID. Images from each beam were acquired at 3128 x 2724 pixels and temporarily saved on a local copy buffer. Immediately subsequent to finishing the acquisition of a FOV, downsampled mosaics were automatically created by the mSEM ZEN software. Furthermore, 10 x 10 equidistant collage using a custom written Matlab script (Meike

Sievers, MPI for Brain Research). Each collage and mosaic was manually inspected for imaging quality (i.e. autofocus, stigmation, glitches, charging). Sections with artifacts were re-imaged. Subsequently, the raw and meta data was TAR-compressed and send via a 10 GBit fiber connection to a Max Planck Computing and Data Facility (MPCDF) server (gabaghi) and automatically backed up on a tape-system. After finishing the image-acquisition of an entire wafer, a list of the artifact-free raw-data sections was manually created and un-TARed onto a raw-data server gaba/conndata for further processing.

2.20 Image and data analysis

2.20.1 Intrinsic optical signal imaging – data analysis

Images of intrinsic optical signals were acquired and analyzed using custom written Matlab Software. For coarse localization of bV1, signals were processed as described previously (Rose et al., 2016). Briefly, intrinsic signal images were first clipped at 1.5%. Clipped images were high-pass filtered and blank-corrected to reduce background noise. Image averages were calculated for each stimulus condition and thresholded at each image background mean + 4x standard deviation, respectively. Finally, the largest object was extracted for each stimulus condition, color-coded for the ipsi- and contralateral half of the binocular visual field stimulation and overlaid on top of the cranial bloodvessel pattern. One map was created for both, ipsilateral and contralateral eye stimulation, respectively.

For coarse retinotopic mapping of bV1 retinotopic maps of azimuth and elevation were calculated applying a temporal phase method (Kalatsky and Stryker, 2003) as described previously (La Chioma et al., 2019). In brief, pixel time-courses were high-pass filtered using a moving averaging. The time-window of the moving window for averaging was set to the duration of the cycle of moving bar stimulation to compensate for potential drift in cranial illumination. Response strength and location of intrinsic signals at the drifting bar frequency was extracted by fourier-transformation. Hemodynamic delay was canceled out by subtraction of response times of intrinsic optical signals from conditions of opposing bar drifts, resulting in maps of absolute retinotopy. Further, equally spaced iso-azimuth and -elevation contour lines were extracted, color-coded and overlaid on top of the cranial bloodvessel pattern.

2.20.2 Two-photon imaging – pre processing

Images and data from *in vivo* two-photon calcium imaging were pre-processed and analyzed using custom written Matlab scripts. To correct for background detection noise, the dark-frames (first 160 frames, which were acquired without laser stimulation) in the beginning of each stimulation sequence were averaged and subtracted from all respective frames. To account for drifts and motion artefacts, the first 100 laser-stimulated frames were averaged and used as a template for translational registration of all frames.

Registered average fluorescent maps and average activity maps were calculated for each inclined piezo-plane and used as templates for ROI definition. Cellular and bouton ROIs were manually drawn using custom written Matlab code (Multiple ROI Predator, Pieter Goltstein). For functional connectomics experiments, only boutons were ROIed, whose axon could be followed for at least 15 µm within the respective piezo-plane. If applicable, both, boutons and cells of the same imaging FOV were manually matched over stimulation sessions.

The fluorescent time-course (F) for each ROI was extracted by averaging all pixel values of a given ROI per frame. F was neuropil corrected, by subtraction of the pixel-value averages of a circular annulus

around each respective ROI (L4 cells: 10 µm, dLGN boutons: 2 µm), excluding overlaps with neighboring ROIs or neuropil bands.

2.20.3 Two-photon imaging – baseline normalization and responsiveness

To determine whether cells or boutons were visually responsive to stimulation with moving gratings, first F_0 traces were calculated as a mean to compensate for fluorescent intensity drift. The raw fluorescent signals of pre-stimulation periods were low-pass filtered at a cutoff of 0.004 Hz and F_0 generated by linear extrapolation. Next, the raw fluorescent signals were normalized to global F_0, resulting in $\Delta F/F_0$ traces. Normalized fluorescence traces in response to visual stimulation were further corrected for local residual offsets by subtraction of their respective normalized, averaged pre-stimulation fluorescence ($\Delta F/F_{0(baseline)}$). Cells or boutons were defined as visually responsive, when peak $\Delta F/F_{0(stimulus)}$ was at least 8 * $\sigma\Delta F/F_{0(baseline)}$ in at least 50% of trials of the same stimulation condition of a specific eye.

2.20.4 Two-photon imaging – Preferred Orientation and Direction

The preferred stimulation direction (PsD) of cells and boutons were extracted as the mean $\Delta F/F_0$ across trials to the grating direction evoking the strongest response. Preferred stimulation orientation (PsO) was determined by first wrapping the 360° direction tuning curves into 180° orientation space. PO was defined as the peak of the trial-averaged orientation tuning curve. PsD and PsO were determined eye-specifically.

To compensate for under-sampling of directions and orientations in visual space (drifting gratings presented in 12 equidistant directions), the discrete tuning curves were fitted using a two-peaked 360° wrapped Gaussian function (Carandini and Ferster, 2000; Mazurek et al., 2014):

$$R_\theta = R_{BL} + R_{\theta(preferred)} * e^{-\frac{wrap(\theta-\theta_{preferred})^2}{2\sigma^2}} + R_{\theta(null)} * e^{-\frac{wrap(\theta+180°-\theta_{preferred})^2}{2\sigma^2}}$$

where R_{BL} is the baseline $\Delta F/F_0$ reponse, $R_{\theta(preferred)}$ is the $\Delta F/F_0$ response at PsD, $R_{\theta(null)}$ is the $\Delta F/F_0$ response to the direction opposite to PsD ($\theta(null) = PsD + 180°$) and σ is the standard deviation of the Gaussian function (tuning width). Wrap(θ) is a function wrapping angles into an interval between 0° and 180°.

PD was defined as the angle at the peak of the fitted tuning curve. PO was computed analogously, however on the fitted tuning curve, which was first transformed into orientation space.

2.20.5 Two-photon imaging – Ocular Dominance

OD of responsive cells and boutons were determined by using eye-specific responses to drifting gratings to calculate the ODI:

$$ODI = \frac{\frac{\Delta F}{F_0}\, contralateral_{PsD} - \frac{\Delta F}{F_0}\, ipsilateral_{PsD}}{\frac{\Delta F}{F_0}\, contralateral_{PsD} + \frac{\Delta F}{F_0}\, ipsilateral_{PsD}}$$

where $\Delta F/F_0$ is the mean $\Delta F/F_0$ across trials and PsD is the eye-specific PD. OD is expressed on a scale from -1 (ipsilateral dominance) to +1 (contralateral dominance).

Further, ODI based pixelmaps were generated analogously by calculating ODI for each 512 x 512 individual pixels per inclined piezo-plane instead. Pixels were then color-coded based on their ODI

with the hue coding for the OD and saturation for the mean of the summed ipsilateral and contralateral response amplitudes.

2.20.6 Two-photon imaging – Orientation & Direction Selectivity

Both, OS and DS were evaluated using eye-specific responses to drifting gratings via three methods. First, the DSI was determined:

$$DSI = \frac{\frac{\Delta F}{F_0}\,\theta_{preferred} - \frac{\Delta F}{F_0}\,\theta_{null}}{\frac{\Delta F}{F_0}\,\theta_{preferred} + \frac{\Delta F}{F_0}\,\theta_{null}}$$

where $\Delta F/F_0$ is the mean $\Delta F/F_0$ across trials, $\theta_{preferred}$ is the PsD and θ_{null} is the opposite direction of PsD (θ_{null} = PsD + 180°). Similarly, the OSI was calculated using tuning curved transformed into orientation space:

$$OSI = \frac{\frac{\Delta F}{F_0}\,\theta'_{preferred} - \frac{\Delta F}{F_0}\,\theta'_{orthogonal}}{\frac{\Delta F}{F_0}\,\theta'_{preferred} + \frac{\Delta F}{F_0}\,\theta'_{orthogonal}}$$

where $\Delta F/F_0$ is the mean, transformed $\Delta F/F_0$ across trials, $\theta'_{preferred}$ is the PsO and $\theta'_{orthogonal}$ is the opposite orientation of PsO ($\theta'_{orthogonal}$ = PsO + 90°). Both, DSI and OSI expressed on a scale from 0 (not selective) to 1 (selective to single direction/orientation).

Second, global orientation (gOSI) and direction selectivity indices (gDSI) were calculated as 1 – the circular variance of the mean tuning curves (Ringach et al., 2002):

$$gDSI = 1 - circular\ variance = \left|\frac{\sum R(\theta_k)e^{i\theta_k}}{\sum R(\theta_k)}\right|$$

$$gOSI = 1 - circular\ variance = \left|\frac{\sum R(\theta_k)e^{2i\theta_k}}{\sum R(\theta_k)}\right|$$

where $R(\theta_k)$ is the mean response to the direction θ_k for gDSI and the mean response to the orientation θ_k for gOSI. Both, gDSI and gOSI expressed on a scale from 0 (not selective) to 1 (selective to single direction/orientation).

Cells and boutons were defined as OS with an OSI > 0.3 and direction selective with a DSI > 0.3.

2.20.7 Two-photon imaging – Receptive fields

Spatial RFs were extracted from responses to sparse noise stimulation. Raw traces in response to stimulation were sorted according to stimulus position in visual space and their contrast polarity (white increment or black increment for ON- and OFF response regions, respectively). Sorted traces were normalized to pre-stimulus baseline (inter-trial interval + stimulus onset delay (0.1 s)) fluorescence ($\Delta F/F_{baseline}$).

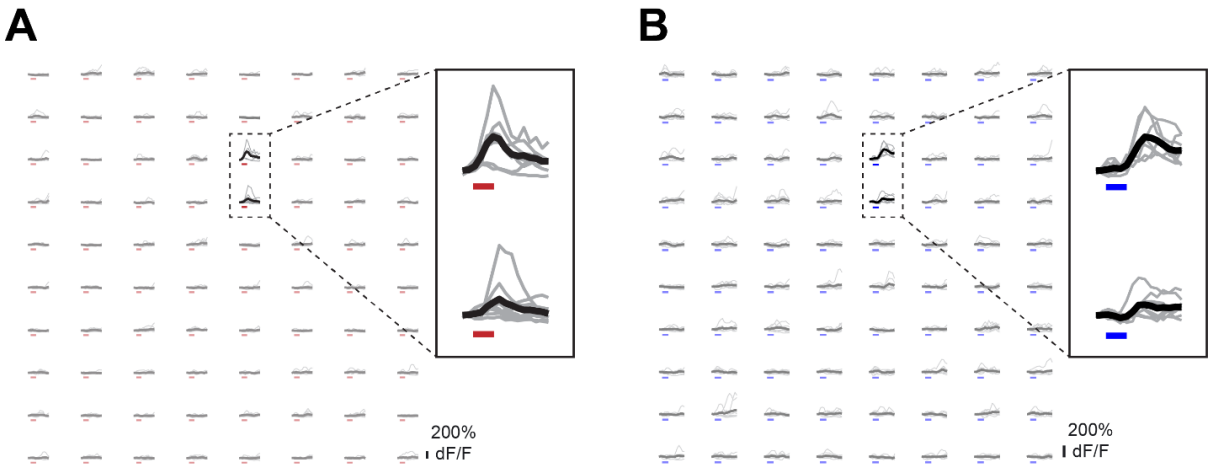

Figure 2.4: **Stimulus onset and stimulus offset responses during RF mapping using sparse noise stimulation. A-B|** Transients are shown in accordance to their relative sparse noise stimulus-patch positions for each trial (grey) and the trial average (black, bold). Zoom-ins of calcium transients of two patches (right) are indicated with dotted lines. **A|** RF calcium transients of a dLGN bouton to light increment sparse noise stimulation (ON). Zoom in highlights the response-timing locked to the stimulus onset. The visual stimulation period is indicated as red bars below each transient. **B|** RF calcium transients of a dLGN bouton to light decrement sparse noise stimulation (OFF). Zoom in highlights the response-timing of the same patches as in B locked to the stimulus offset (release of the light decrement patch to the grey-background, resulting in a light increment). The visual stimulation period is indicated as blue bars below each transient.

Receptive single polarity (ON or OFF) sub-Field (RsF) responses were tested for statistical significance similarly as previously described (de Vries et al., 2020), however, only taking frames of stimulus presentation into account to avoid averaging in stimulus-offset responses of opposite contrast polarity (see Fig. 2.4). Briefly, eye-specific subfield-responses were averaged over stimulation frames and significant stimulus positions extracted using ANOVA ($p < 0.05$) over stimulus positions and trials. Significant receptive subfields were z-scored:

$$zRF = \frac{RF_{mm} - RF_{mmm}}{\sigma}$$

where RF_{mm} is the RsF averaged over stimulation frames and trials, RF_{mmm} is the averaged RF_{mm} and σ is the standard deviation of RF_{mm}. For RFs with several disconnected subfields, only the subfield with the strongest average response was kept. RFs were thresholded (z-threshold = 2) and cubically upsampled to a resolution of 1° x 1° and re-thresholded (z-threshold = 2). If only a single polarity showed a significant response, then the RF was defined as the thresholded zRF of that respective polarity, else the RF was calculated by RsF subtraction:

$$RF = RsF_{ON} - RsF_{OFF}$$

where RsF_{ON} is the zRF to light increment stimulation and RsF_{OFF} is the zRF to light decrement stimulation of the same eye. Receptive fields were smoothed for display.

To determine the onset latency of significant RFs, each frame (Stimulation onset to end of subsequent inter-trial interval) was evaluated for response significance using ANOVA over trials and patch positions for each polarity, respectively. RsF onset latency was defined as the first frame to cross the $p < 0.05$ significance threshold and RF onset latency was defined as the shortest latency of its significant RsFs.

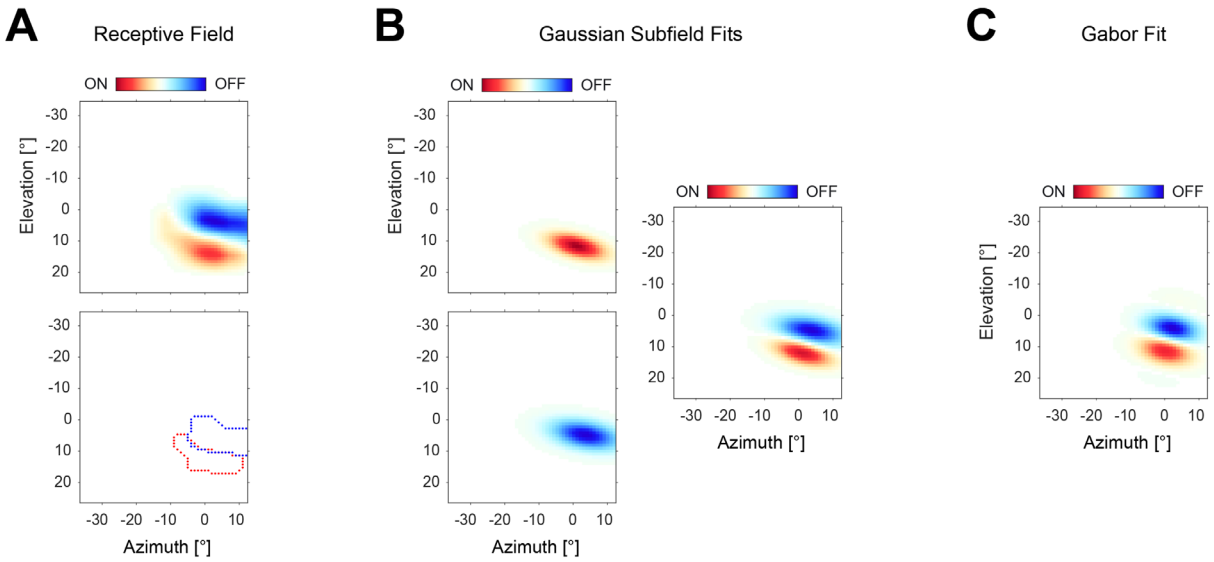

Figure 2.5: **Gaussian and Gabor-fitting of RFs. A|** The RF (right, top) and subfield-outlines (right, bottom) of a layer 4 cell are plotted in visual space. **B|** Gaussian fits of the ON-subfield (top left), OFF-subfield (bottom left) and the resulting full Gaussian RF (right; OFF-subfield subtracted from ON-subfield) of the cellular RF from panel A are plotted in visual space. **C|** Gabor fit of the cellular RF from panel A is plotted in visual space.

Next, using a standard non-linear least-squares solver algorithm (Matlab) significant RsFs were fitted with a 2D Gaussian (see Fig. 2.5A,B):

$$RsF_{Gauss} = A * e^{-\left(\frac{(x'-c_x')^2}{2\sigma_x^2} + \frac{(y'-c_x')^2}{2\sigma_y^2}\right)}$$

where A is the amplitude or maximum response of the RsF, σ_x and σ_y are the standard deviations of the Gaussian perpendicular and parallel to the Gaussian grating and x', y', c_x' and c_y' are obtained by translation and rotation of the original coordinate system by θ:

$$x' = x * \cos(\theta) - y * \sin(\theta)$$

$$y' = x * \sin(\theta) + y * \cos(\theta)$$

$$c_x' = c_x * \cos(\theta) - c_y * \sin(\theta)$$

$$c_y' = c_x * \sin(\theta) + c_y * \cos(\theta)$$

where x and y are linear 2D meshgrids of the size of the RsF, cx and cy are the center of the Gaussian and θ is the orientation. RsF centers, orientations, major and minor axes were extracted from their Gaussian fits.

RFs with both, significant eye-specific ON and OFF RsFs were further fitted by a Gabor wavelet using the Levenberg-Marquart algorithm as described previously (Jones and Palmer, 1987b; Lee et al., 2016a). In brief, RFs were fitted using a standard non-linear least-squares solver algorithm (Matlab) with a 2D Gabor function, which is an augmentation of the above described 2D Gaussian with a 2D cosine grating (see Fig. 2.5A,C):

$$RF_{Gabor} = A * e^{-\left(\frac{(x'-c_x')^2}{2\sigma_x^2} + \frac{(y'-c_x')^2}{2\sigma_y^2}\right)} * \cos(2\pi f_s(x' - c_x') + \varphi)$$

where f_s is the SF and ϕ the relative spatial phase of the 2D cosine grating. A, σ_x, and σ_y, x', y', c_x' and c_y' of the Gaussian envelope are obtained analogous to the above 2D Gaussian function.

2.20.8 mSEM Image Alignment

Individual images collected with mSEM were aligned in 3D using an alignment package (https://github.com/billkarsh/Alignment_Projects) originally developed for TEM data (Scheffer et al., 2013) using modified parameters and additional monitoring scripts (Matlab) for mSEM data developed by Meike Schurr (MPI Brain research, unpublished). The dataset was aligned on the Raven High Performance Supercomputing System of the MPCDF (Garching, Germany), using 80 computing nodes (384 GB memory and 96 Xeon CascadeLake-AP Platinum 9242 processors per node, interconnected by a 100 Gbits/s Mellanox HDR InfiniBand network). The C++ code of the alignment package was compiled by Meisam Farzalipour Tabriz (MPCDF). Distribution of compute workload was fine-tuned to maximize usage Raven computing resources during a small 5 section test-set with supervision of Klaus Reuter (MPCDF).

In brief, in-section overlaps between 8-bit normalized images within and between 61 beam hexagons were computed by point-pair cross-correlation using a least-squares solver. The initial image correlation-space was reduced using each image's respective mSEM stage coordinates to find overlapping image-pairs. Structures were linked across images using pairwise transformations. Image-pairs were placed into a global coordinate using affine transformations and warped by a deformable mesh algorithm to maximize matching using a least-squares solver.

In contrast, adjacent sections have to be aligned based on similar features (compared to identical for in-plane alignment), as the section-thickness of 35 nm is bigger than the smallest features. Furthermore, due to lack of inherent registration between slices in ATUM mSEM (similar to TEM), finding overlapping images cannot be solved by stage coordinates. Therefore, first, low-resolution in-plane montages were computed for a first coarse matching of position and angle between adjacent sections. Due to resolution downsampling, only prominent landmarks like bloodvessels and cell bodies were used to calculate a first rough positioning. To reduce computational workload, a centered vertical and horizontal montage strip of the width of 12 tiles was aligned. The best alignment to the adjacent section was found by iterative sweeping and rotation using normalized cross-correlation. Downsampled montages were subsequently rigidly transformed according the best found alignment, visualized for manual review and faulty section pairs re-aligned with tweaked parameters, if necessary. Next, using the rigid transforms from the coarse matching, adjacent sections are chopped into higher-resolution blocks for re-fined cross-layer matching. Blocks were aligned by normalized cross-correlation within to directly and up to 5 adjacent layers to circumvent imaging, tape and compression artifacts. The resulting affine transforms were then used to find cross-layer raw-image-pairs. Image-pairs were next aligned using the affine transforms as a starting guess via point-pair cross-correlation using a least squares solver. Image-pairs were placed into a global coordinate using affine transformations and warped by a deformable mesh algorithm to maximize matching using a least-squares solver. Finally a least-squares fit with regularization for scale and skew was iteratively used on those point-pairs to compute a global affine alignment over all blocks until the highest residual was below the threshold of 50 pixels.

For efficient online 3D access of the data, the image volume was partitioned into 1024x1024x1024 voxel blocks and transformed into webKnossos-wrapper format files (Boergens et al., 2017).

2.21 Statistics

All statistical analyses in this study were performed in Matlab. I report mean ± standard error of the mean (SE) for population data. In figures, I present the mean as bold lines for trial averages of calcium transients and bold dots for distribution histograms, as indicated in individual figures. For RF transients, the mean transients are further pseudo-colored red or blue if significant to visual stimulation to light increments (ON) or decrements (OFF). Significant RF patch-locations were determined using one-way ANOVA. Significant differences between both, biolistically transfected organotypic slice culture conditions and between functional representations of dLGN and L4 of bV1 were determined non-parametrically by the Mann-Whitney U test. In figures, significance values between distributions are indicated by asterisks: * $p < 0.05$, ** $p < 0.01$ and *** $p < 0.001$.

3 Results

How does orientation selectivity emerge in the geniculo-cortical pathway of mice? In this thesis, I establish and deploy a novel functional connectomics pipeline to address this question. By combining the readout of functional neuronal properties with the circuit's underlying connectome (see Fig. 3.1 for experimental pipeline), I aimed to produce a comprehensive dataset allowing for a precise dissection of the circuit's functional connectivity logic.

First, functional properties of both, presynaptic dLGN axon-terminals and postsynaptic L4 cells were mapped in anesthetized animals using *in vivo* two-photon calcium imaging. In this study, I focused specifically on OS, DS, RFs and OD. Both populations were imaged in the thalamo-recipient L4 of the same prep, using co-labeling with two GECIs of different color. Morphologies were mapped as 3D z-stacks for later re-finding. Mice were subsequently perfused, and BVs stained using DiD. A biopsy of the functionally imaged brain region was stereotaxically extracted using vascular landmarks as guidance. Membranes were subsequently stained with heavy metals. The location of the functionally imaged tissue was triangulated via vascular landmark matching using microCT. The biopsy was subsequently trimmed into a hexagonal shape, centered on the two-photon FOV and cut into ultra-thin serial sections using ATUM. The sections were subsequently imaged on silicon wafers using mSEM and aligned in 3D.

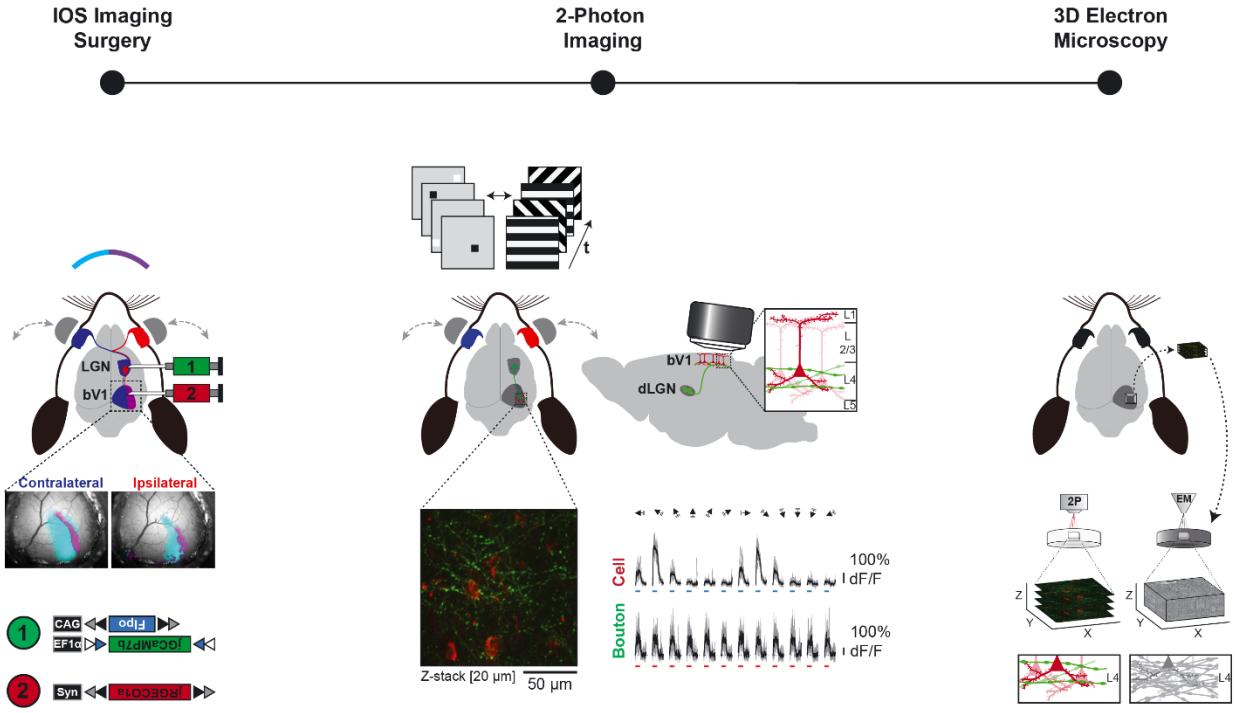

Figure 3.1: **Experimental pipeline for long-range functional connectomics of geniculo-cortical convergence.** Binocular primary visual cortex (bV1) is located using Intrinsic Optical Signal (IOS) imaging in Scnn1a-Tg3-Cre mice, expressing Cre-recombinase selectively in layer 4 of primary visual cortex and the dorso-lateral geniculate nucleus (dLGN), for subsequent viral injection, cranial window and headbar implantation (left). Sparse transfection of the dLGN is achieved by stereotactic injection of AAV2/1-CAG-Flex-FlpO-WPRE and AAV1-EF1a-F-Flex-jGCaMP7b-WPRE, while bV1 is transduced by injection of AAV2/1-Syn-Flex-NES-jRGECO1a-WPRE. After 4-5 weeks of expression, dLGN axons and their postsynaptic cells are functionally characterized with two-photon (2-Photon) microscopy in layer 4 of bV1 using sparse-noise and moving gratings as stimulation and their morphology mapped in high resolution (middle). Subsequently, the mouse is perfused, a biopsy of the functionally imaged region taken, membranes stained with heavy metals and embedded in resin. The imaged

region of interest is located en-bloc using micro computed tomography and subsequently imaged with 3D electron microscopy in high resolution (right).

3.1 Deep, dual-color in vivo two-photon imaging

3.1.1 Deep, in vivo two-photon axon imaging

Reading out functional information *in vivo* from dLGN neurons directly is challenging, as the thalamic nucleus is optically inaccessible due to its location deep in the brain. Therefore, in order to measure the response properties of dLGN cells *in vivo* using two-photon calcium imaging, I instead targeted their axons, which terminate in L4 of bV1. In order to maximize optical access (and therefore SNR) the correct choice of a reporter fluorophore is critical. The calcium indicator should further be able to act as a structural marker, as the second GECI color will subsequently be reserved for cellular imaging of L4 cells in bV1. I hence investigated these criteria on diverse GECIs in dLGN axon terminals using *in vivo* two-photon calcium imaging in L4 of bV1 (see Fig. 3.2 for representative examples). The mouse was placed under the microscope in front of a screen, displaying moving gratings. The red-shifted GECI jRGECO1a (Fig. 3.2A) exhibited a near undetectable baseline-fluorescence, hindering the reliable detection of inactive, expressing axons without visual stimulation. The low baseline fluorescence leads to less precise frame registration, in turn impairing the SNR of functional responses. While functional responses were extractable (Fig. 3.2A, right), it was difficult to follow axonal trajectories between boutons in cortical space (Fig. 3.2A, middle). In contrast, the high-baseline-fluorescence jGCaMP7b provided excellent access to axonal structure and function (Fig. 3.2B).

Both, the ability to follow axonal structure and to evaluate bouton function are tightly linked to sparseness of expression. To maximize axonal labeling without compromising quality of both the structural and functional readout, being able to control transduction is imperative. In order to avoid diluting the amount of transcript per cell, and instead affect the amount of transduced dLGN cells in a genetically specific manner, I developed a Cre-recombinase and FlpO-recombinase dependent sparsening approach. The mouseline *Scnn1a-Tg3-Cre*, expressing Cre-recombinase selectively in both dLGN and L4 of V1, was used for genetic targeting specificity. To be able to titrate the amount of labeled dLGN cells while retaining strong expression levels, I combined FlpO-recombinase expression under Cre-recombinase dependence and jGCaMP7b expression under FlpO-recombinase dependence. I first cloned the plasmid pAAV-CAG-Flex-FlpO-WPRE from pAAV-hSyn-FlpO-WPRE and pAAV-CAG-Flex-ArchT-tdTomato-WPRE (Fig. 3.3A, see methods for more detail). Next, I evaluated the leakiness of the plasmid using biolistic transfection of rat hippocampal organotypic slice cultures using a FlpO-recombinase dependent dsRed plasmid as a fluorescence readout. I imaged and quantified dsRed-expressing cell-counts without (Fig. 3.3B) and in the presence of Cre-recombinase (Fig. 3.3C) using epifluorescence microscopy. Expression without Cre-recombinase was almost absent (mean ± SE: 0.33 ± 0.21 cells/slice, N = 6 slice cultures) and significantly lower ($p = 0.0022$, Mann-Whitney U test, Fig. 3.3D) than with Cre-recombinase (mean ± SE: 31.67 ± 2.95 cells/slice, N = 6 slice cultures).

Next, I cloned the plasmid pAAV-EF1α-F-Flex-jGCaMP7b-WPRE from pAAV-hSyn-jGCaMP7b-WPRE and pAAV-EF1α-F-Flex-Kir2.1-T2A-tdTomato-WPRE (Fig. 3.3E, see methods for more detail). Analogous to before, I evaluated the leakiness of the plasmid using biolistic transfection of rat hippocampal organotypic slice cultures (Fig. 3.3F-G). Expression without FlpO-recombinase was almost absent (mean ± SE: 0.33 ± 0.33 cells/slice, N = 6 slice cultures) and significantly lower ($p = 0.0022$, Mann-Whitney U test, Fig. 3.3H) than with FlpO-recombinase (mean ± SE: 12.50 ± 3.21 cells/slice, N = 6 slice cultures). Both cloned constructs were subsequently packed into respective AAVs for *in vivo* experiments.

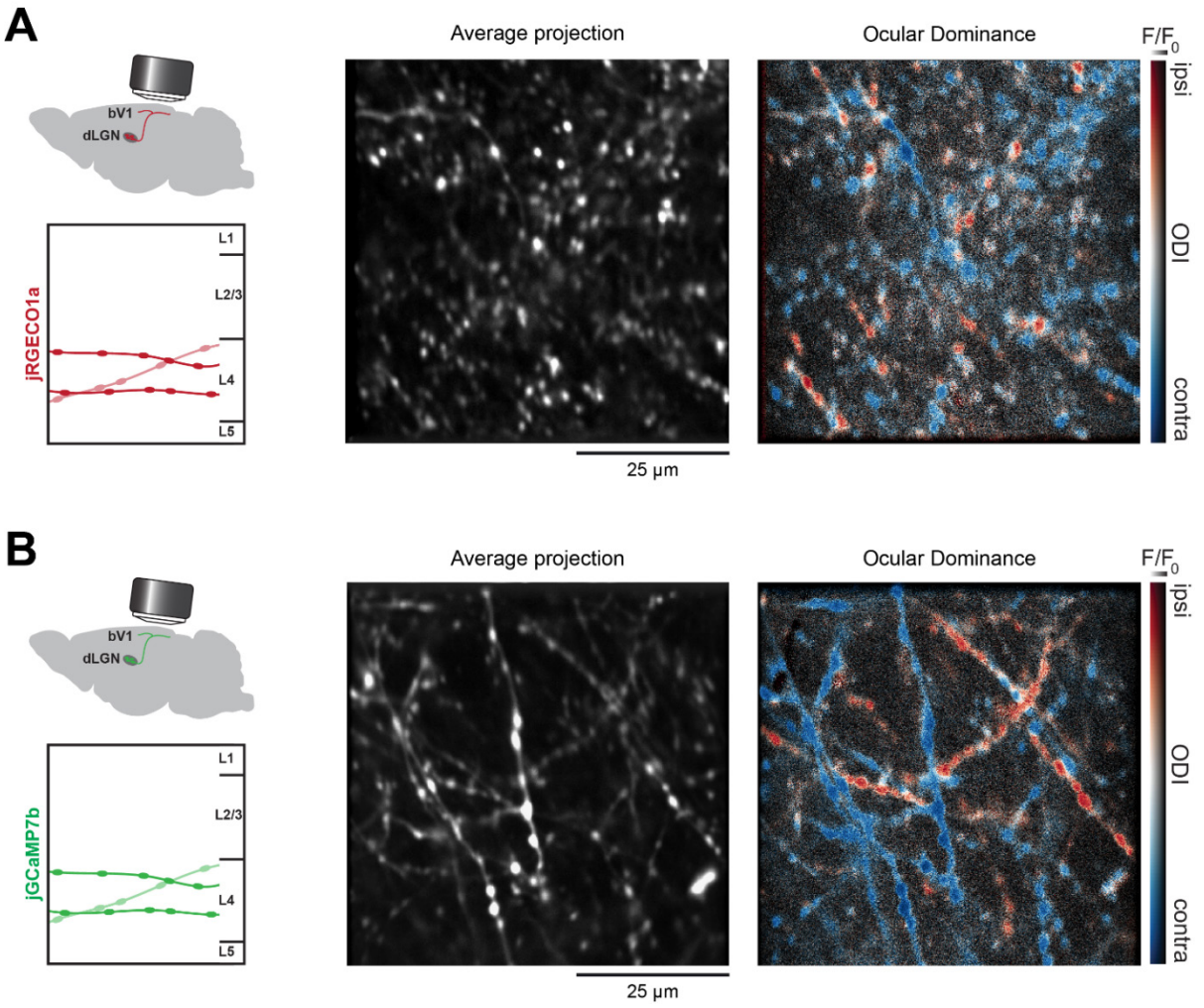

Figure 3.2: **Comparison between different calcium indicators for *in vivo* axon imaging. A|** Neurons in dLGN labeled with the red-shifted calcium indicator jRGECO1a, imaged at their axonal projections in layer 4 of bV1 (left) using visual stimulation with moving gratings. Axonal structure shown via an average fluorescence projection (middle) and functional responses illustrated by its respective pixelmap (right), color-coded for OD. **B|** Neurons in dLGN labeled with the green, high-baseline calcium indicator jGCaMP7b, imaged at their axonal projections in layer 4 of bV1 (left) using visual stimulation with moving gratings. Axonal structure shown via an average fluorescence projection (middle) and functional responses illustrated by its respective pixelmap (right), color-coded for OD.

The ideal sparsening range for *in vivo* expression of jGCaMP7b in dLGN was determined by several dilution series. The most promising results were achieved at a pAAV-CAG-Flex-FlpO-WPRE concentration of $1.38x10^{10}$ to $6.90x10^{10}$ genome copies/ml and a pAAV-EF1α-F-Flex-jGCaMP7b-WPRE concentration of $1.10x10^{13}$ genome copies/ml at an injection volume of 50-70 nl.

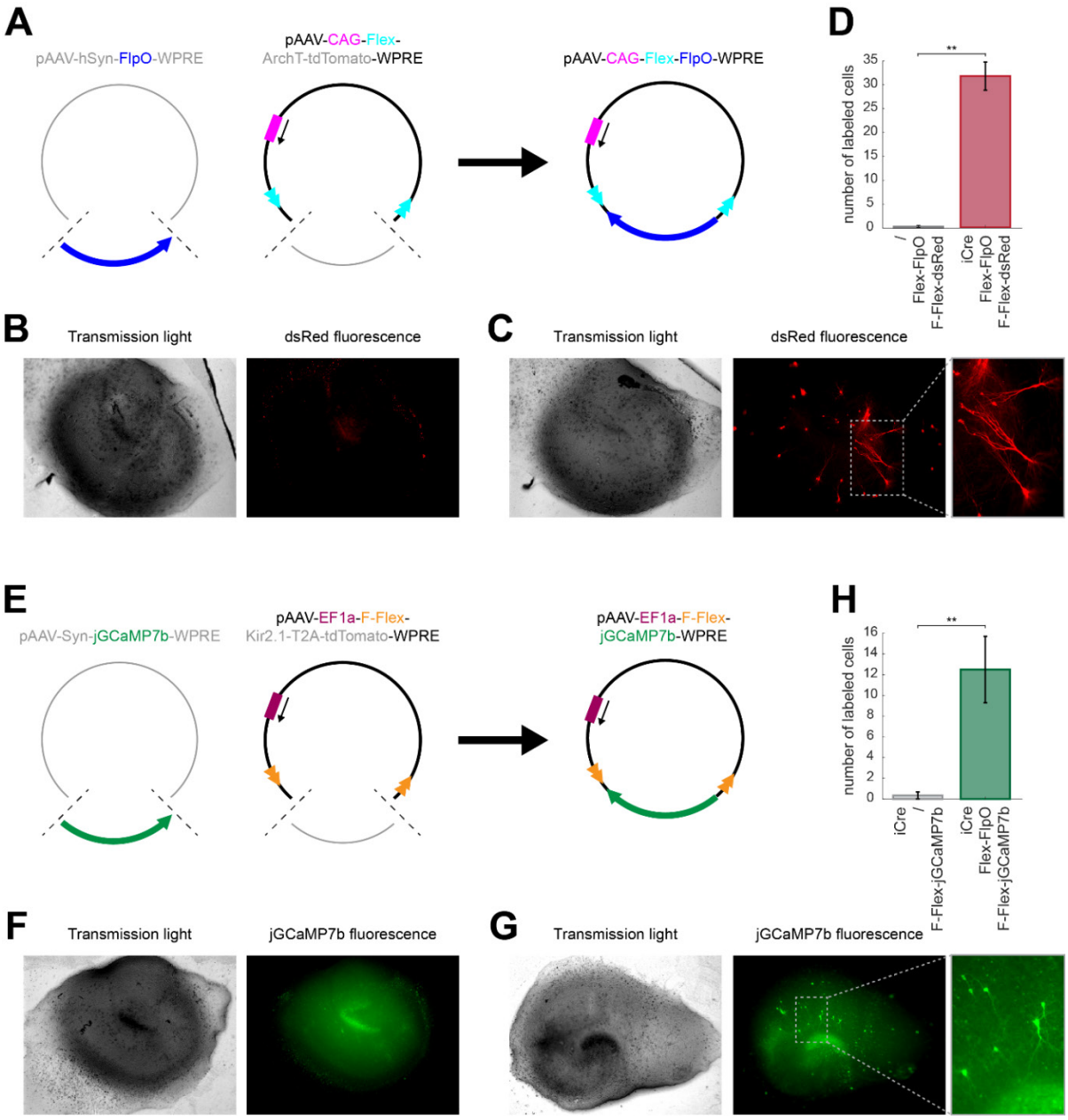

Figure 3.3: **Cloning and verification of Cre-dependent FlpO and FlpO-dependent jGCaMP7b expression in organotypic slice cultures. A|** Schematic illustrating the cloning of pAAV-CAG-Flex-FLpO-WPRE from pAAV-hSyn-FlpO-WPRE and pAAV-CAG-Flex-ArchT-tdTomato-WPRE using restriction digestion. **B|** Rat organotypic hippocampal slice culture biolistically transfected with pAAV-CAG-Flex-FlpO-WPRE and pCAFNF-dsRed shown in transmission light (left) and epifluorescent illumination (right, red channel). **C|** Rat organotypic hippocampal slice culture biolistically transfected with pPGK-iCre, pAAV-CAG-Flex-FlpO-WPRE and pCAFNF-dsRed shown in transmission light (left) and epifluorescent illumination (middle, red channel). Location of the zoom-in panel (right) illustrated with a dotted square in the original image. **D|** Quantification of Cre-dependent expression specificity of pAAV-CAG-Flex-FLpO-WPRE (Mann-Whitney U test, N = 4 slice cultures per condition, ** $p < 0.01$). **E|** Schematic illustrating the cloning of pAAV-EF1α-F-Flex-jGCaMP7b-WPRE from pAAV-Syn-jGCaMP7b-WPRE and pAAV-EF1α-F-Flex-Kir2.1-T2A-tdTomato-WPRE using restriction digestion. **F|** Rat organotypic hippocampal slice culture biolistically transfected with pPGK-iCre and pAAV-EF1α-F-Flex-jGCaMP7b-WPRE shown in transmission light (left) and epifluorescent illumination (right, green channel). **G|** Rat organotypic hippocampal slice culture biolistically transfected with pPGK-iCre, pAAV-CAG-Flex-FlpO-WPRE and pAAV-EF1α-F-Flex-jGCaMP7b-WPRE shown in transmission light (left) and epifluorescent illumination (middle, green channel). Location of the zoom-in panel (right) illustrated with a dotted square in the original image. **H|** Quantification of

FlpO-dependent expression specificity of pAAV-EF1α-F-Flex-jGCaMP7b-WPRE (Mann-Whitney U test N = 3 slice cultures per condition, ** p < 0.01).

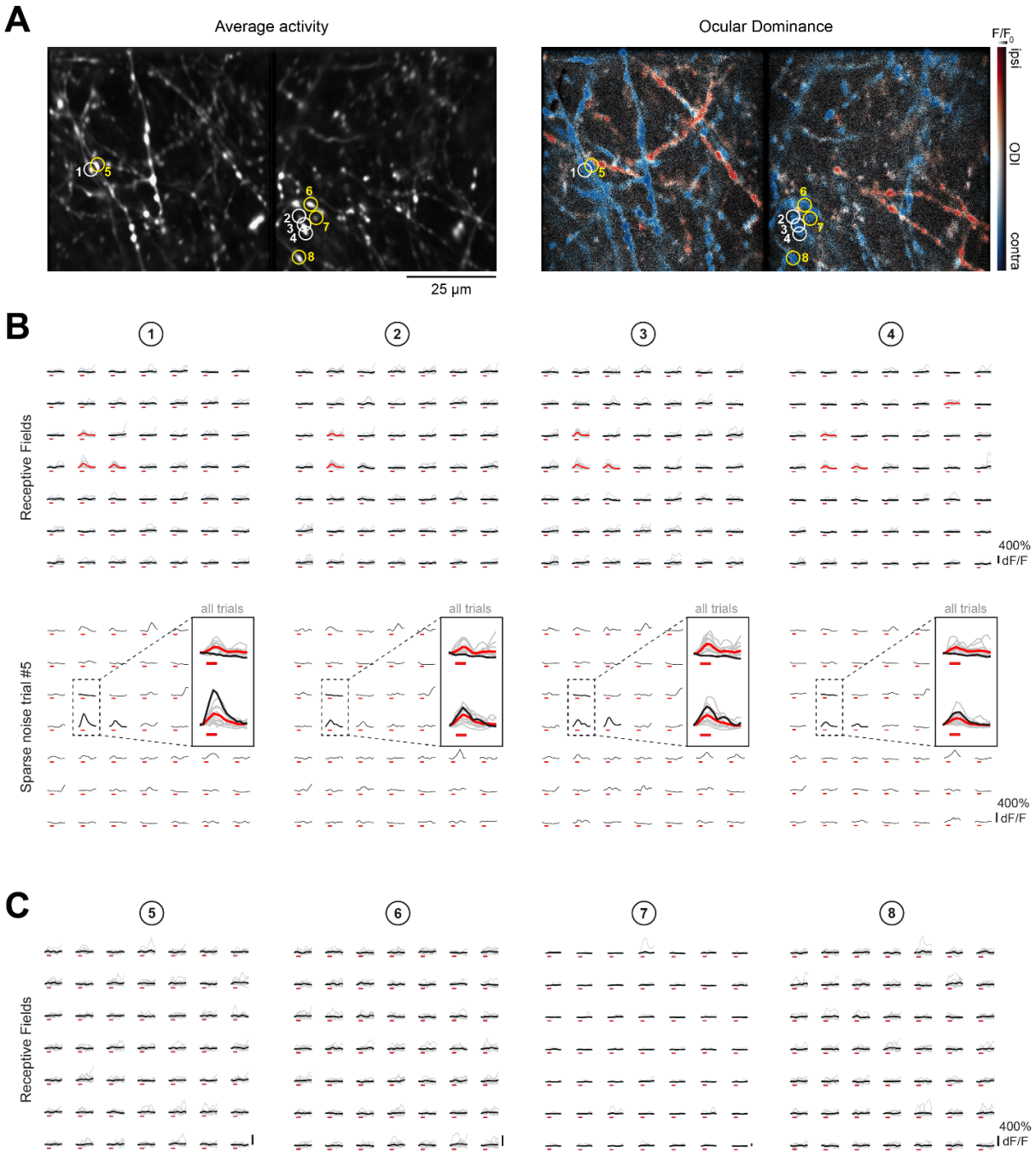

Figure 3.4: **Similarity of functional responses in boutons of the same axon. A|** Average fluorescence projection (left) and OD pixelmap (right) of dLGN axons labeled with jGCaMP7b acquired in L4 of bV1 using *in vivo* two-photon microscopy. Concatenated images represent two consecutive piezo-planes, separated by 15 µm in the z-direction. Circles and corresponding numbers indicate the boutons of origin of all traces shown in panels B and C. **B|** Calcium transients of RFs of four boutons from likely the same dLGN axon (top) and the corresponding sparse noise stimulation (patch size: 8°x8°) trial number 5 (bottom). Transients are shown in accordance to their relative sparse noise stimulus-patch positions for each trial (grey) and the trial average (black, bold). Trial averages of significant RF patches are illustrated in red. Stimulation is indicated as a red bar below each transient. Trial number 5 is indicated in black (bottom). Numbers indicate the corresponding bouton's ROI in panel A (white). **C|** Calcium transients of RFs of four boutons from likely different axons, but in spatial proximity to and

same OD as boutons shown in panel B. Colorcode and transient arrangement as in panel B. Numbers indicate the corresponding boutons ROI in panel A (yellow).

To assess the quality of functional signals extractable from dLGN terminals *in vivo*, I imaged dLGN axons expressing jGCaMP7b deep in L4 of bV1 in response to visual stimulation using two-photon calcium imaging. As boutons from the same axon report the output of their respective parent cell, they should exhibit the same functional properties. I therefore investigated the functional properties of boutons within and between axons. As neurons in the dLGN do not exhibit strong OS and DS, investigating responses to drifting gratings would yield too dense a population response with high probability of overlap. In contrast, due to their very small and restricted RFs, sparse noise stimulation induces much sparser responses with less chance of inter-neuron overlap, ideal for assessing bouton similarity. Therefore, I first used the average activity projection of two consecutive piezo-planes together with the ODI pixelmaps in response to moving gratings to morphologically identify potential boutons belonging to the same axon (Fig. 3.4A, white circles). In a second step, I then compared their RF response transients between single and all trials. Boutons from the same axon exhibited highly similar RFs overall (Fig. 3.4B, top) and within a given trial (see Fig. 3.4B, bottom for trial 5). Due to the intrinsic lower-potency of sparse noise stimulation in driving functional responses in dLGN, some trials exhibit response failures in individual neurons, even if stimulated at their RF location. Analogous to RF responses, trial failures were consistent between boutons of the same axon (Fig. 3.4B, bottom), even across piezo-planes (see bouton 1 vs. boutons 2/3/4). To ensure that bouton similarities did not result from spatial fluorescence bleed-through I further compared those boutons with their closest in-plane bouton of the same eye preference from a different axon (Fig. 3.4C). Inter-axon boutons showed distinctly different response patterns with no hint towards spatial bleed through.

3.1.2 Deep, simultaneous, dual-color in vivo two-photon calcium imaging of overlapping cells and axons

To read out activity in pre-synaptic dLGN axons as well as postsynaptic L4 cells in bV1, both populations need to be labeled with spectrally separate calcium-indicators to avoid fluorescence cross-contamination. The quality of spectral separation is, however, also dependent on the quality of the microscope components, specifically the spectral precision of the filters in the detection path. I sparsely labeled dLGN neurons with the green calcium indicator jGCaMP7b and densely labeled L4 neurons in bV1 with the red-shifted calcium indicator jRGECO1a at overlapping retinotopic locations. Both, L4 cells and dLGN axons were imaged in regions of fluorescence overlap in L4 of bV1. First, I imaged jRGECO1a-labeled L4 cells at 1040 nm (Fig. 3.5A) during sparse noise stimulation and investigated their RFs (Fig. 3.5B-D). Cellular RF transients did not show any signs of decreased quality or SNR in comparison to mice that had no jGCaMP7b co-expression. Excitation of jGCaMP7b labeled dLGN axons in non-jRGECO1a mice did not reveal any bleed-through in the red detection channel.

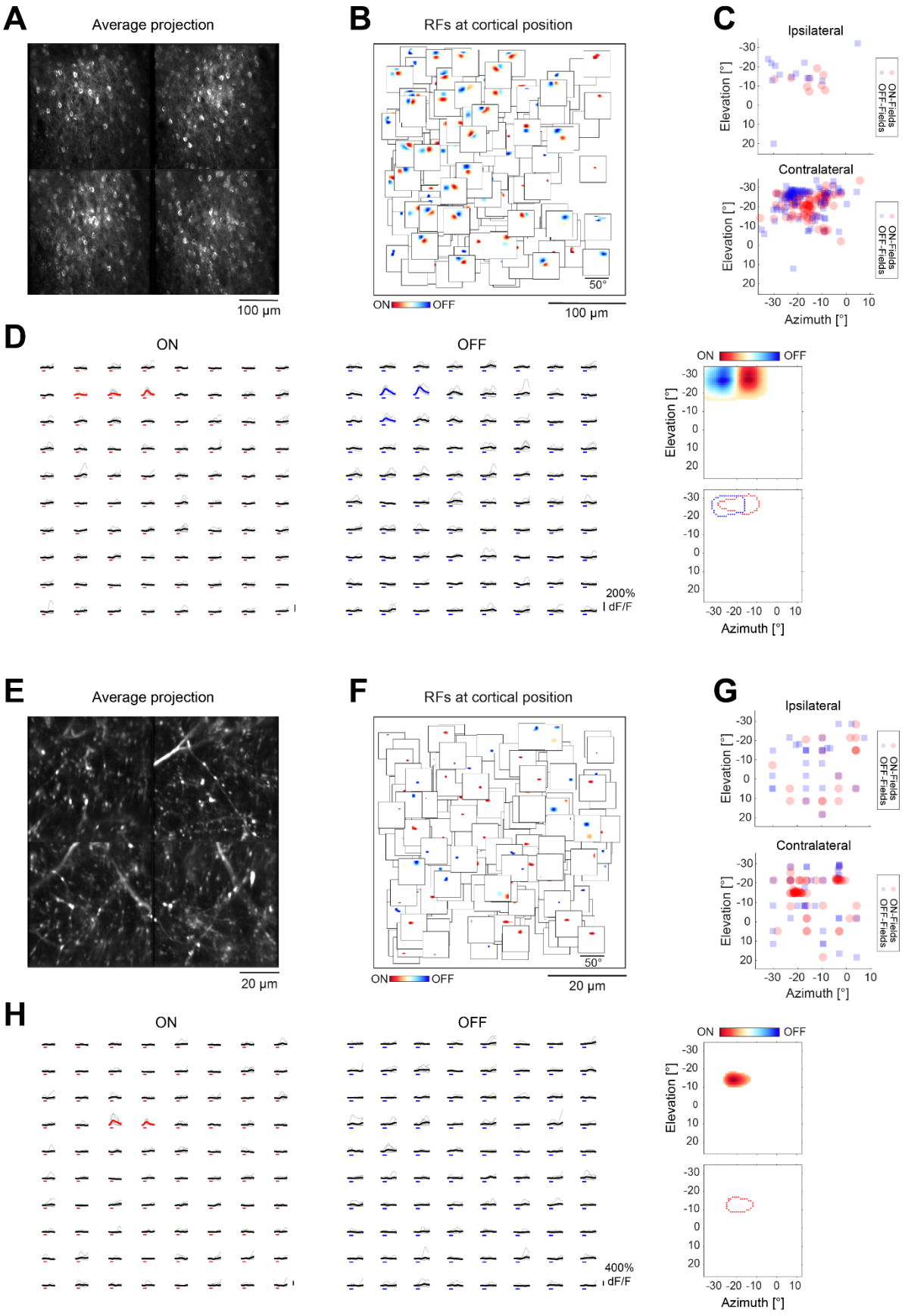

Figure 3.5: **Receptive fields of co-labeled L4 cells and dLGN axons in bV1. A|** Average fluorescence projection of L4 cells labeled with jRGECO1a acquired in L4 of bV1 using *in vivo* two-photon microscopy. Concatenated images represent four consecutive piezo-planes, separated by 25 µm in the z-direction each. **B|** Significant

cellular RFs plotted at their ROI position in cortical space. **C|** Center-positions of cellular RF sub-fields plotted in visual space for ipsilateral (top) and contralateral eye stimulation (bottom). **D|** Calcium transients of an example cellular RF (left and middle). Transients are shown at their relative sparse noise stimulus patch positions for each trial (grey) and the trial average (black, bold). Trial averages of significant RF patches are illustrated in red for ON-subfields (left) and blue for OFF-subfields (middle). Timing of visual patch-presentation is indicated as a red bar for light-increments (ON) and blue for light decrements (OFF) below each transient. The corresponding RF (right, top) and subfield-outlines (right, bottom) are plotted in visual space. **E|** Average fluorescence projection of dLGN axons labeled with jGCaMP7b acquired in L4 of bV1 using *in vivo* two-photon microscopy. Concatenated images represent four consecutive piezo-planes, separated by 15 µm in the z-direction each. **F|** Significant bouton RFs plotted at their ROI position in cortical space. **G|** Center-positions of bouton receptive sub-fields plotted in visual space for ipsilateral (top) and contralateral eye stimulation (bottom). **H|** Calcium transients of an example bouton RF (left and middle) with its corresponding RF and sub-field outlines plotted in visual space. Color code and arrangement as in panel D.

Analogously, I imaged jGCaMP7b-labeled dLGN axons at 940 nm (Fig. 3.5E) during sparse noise stimulation to investigate their RFs (Fig. 3.5F-H) was not affected by double-labeling. Despite significant fluorescence of jRGECO1a labeled cells in the red channel, bleed-through into the green channel was negligible. Importantly, jRGECO1a-induced fluorescence did not show any signs of activity induced intensity changes as compared to when excited at 1040 nm. Further, analysis of axonal RFs did not show signs of cellular RF contamination.

The ability to excite both jRGECO1a and jGCaMP7b at 940 nm while separately detecting their fluorescence in the red and green channels, respectively, enabled simultaneous readout of cellular and axonal morphologies. The clean separation into the two detection channels further enabled the clean functional readout of neuronal activity of either dLGN axonal boutons at 940 nm excitation in the green channel or L4 cells at 1040 nm excitation in the red channel in sequential fashion.

3.1.3 Deep in vivo two-photon calcium imaging of OS, DS and OD for functional connectomics

The first step towards investigating the functional logic of geniculo-cortical convergence is to map their pre- and post-synaptic OS and DS. In this study, I specifically looked at this in context of binocular convergence.

In mice with spatially overlapping dLGN axon and L4 cell labeling, bV1 boundaries and visuotopic arrangement were mapped using IOS imaging. The overlapping expression bolus located closest to the cortical representation of the center of the binocular visual field was selected for *in vivo* two-photon calcium imaging. Selected mice were presented with moving gratings in their binocular visual field to either eye using eye-shutters under anesthesia, and responses of L4 cells recorded (see Fig. 3.6A for data from the mouse that went through the entire functional connectomics pipeline (FC-mouse)). Calcium transients showed that cells were sharply tuned to certain orientations (see Fig. 3.6B, top, contralateral as a representative example) or directions of movement (see Fig. 3.6B, bottom, contralateral as a representative example) in visual space. To inspect the structural arrangement of cells in cortical space in terms of their response features to moving gratings, individual pixels of the average fluorescence projection (Fig. 3.6C, left) were pseudo-colored based on their ODI (Fig. 3.6C, middle left) and PO (Fig. 3.6C, middle right and right). Cells did not show a specific spatio-cortical ordering in terms of OD throughout all four piezo-planes (25 µm apart, covering L4) at the recording site. However, L4 cells were arranged in a salt-and-pepper like manner (Dräger, 1975; Antonini et al., 1999; Schuett et al., 2002; Ohki et al., 2005) when examining their PO for both, ipsilateral and contralateral stimulation. Analogously, I imaged dLGN axons (Fig. 3.6D) in upper L4 within the boundaries of the respective cellular FOV. Calcium transients of significantly responding boutons did

not show any selective tuning for orientations or directions (see Fig. 3.6E, top, contralateral as a representative example) in visual space. Few boutons exhibited a bias for the orientation of gratings (see Fig. 3.6E, bottom, ipsilateral as a representative example). As before, I pseudo-colored individual pixels of the average fluorescence projection (Fig. 3.6F, left column) based on their ODI (Fig. 3.6F, middle left column) and PO (Fig. 3.6F, middle right and right columns) for all three axonal FOVs (corresponding to rows in Fig. 3.6F). In contrast to L4 cells, ODI pixelmaps suggested a very monocular representation of dLGN axons projecting towards L4 of bV1. Geniculate axons did not show any structural arrangements for OD in cortical space throughout all piezo-planes of each FOV on that scale. Due to their broad tuning to orientations and directions in space, and smaller imaging FOV, pixelmaps did not reveal a spatial arrangement of dLGN axons in L4 of bV1 for PO.

To visualize both, the raw fluorescent timecourse and average tuning curves for all manually annotated (and matched across experiments) cells or boutons, I created so called activity matrices. Investigating the raw fluorescence can help in revealing potential drifts of the objective, and therefore the focal plane in z. Cases of drift will manifest themselves in gradual changes of fluorescence over timescales of minutes. The activity matrix of cellular raw fluorescence (Fig. 3.7A) showed overall stable fluorescence responses and no obvious signs of drift. The tuning curve matrix (Fig. 3.7B) revealed diverse degrees of tuning, hinting towards a wide spectrum of OSs, PDs and POs throughout L4 cells. Furthermore, most cells responded to both ipsilateral and contralateral stimulation with the majority, however, being dominated by the contralateral eye. Analogously, the activity matrix of raw bouton fluorescence pooled over all three axonal FOVs (Fig. 3.7C) showed similarly stable fluorescence responses and therefore no signs of drift. However, in stark contrast to cellular tuning, the tuning curve matrix of boutons (Fig. 3.7D) indicated overall flat tuning of dLGN axons in L4 of bV1, hinting towards lack of OS and DS. The great majority of boutons also seemed to be driven exclusively by either of the two eyes. Similar to L4 cells, responses of most dLGN boutons were driven by the contralateral eye.

To analyze these response features in more detail I first investigated which fractions of L4 cells and dLGN boutons responded significantly to visual stimulation with moving gratings (VR). Both, L4 cells and dLGN boutons were deemed as VR when their Calcium-response amplitudes were at least 8 times above the standard deviation of pre-stimulation baseline in at least 50% of trials for at least one grating direction of either eye-stimulation. Out of 267 L4 cells, I found 243 (91.01%) to be VR, with 24 (8.99%) being VR to ipsilateral stimulation only, 66 (24.72%) being VR to contralateral stimulation only and 153 (57.30%) being VR to both ipsilateral and contralateral stimulation (significantly binocularly responding). In contrast, out of 900 dLGN boutons only 456 (50.67%) were VR. Almost all responsive boutons were monocular, with 108 (12.00%) being VR to ipsilateral stimulation only and 345 (38.33%) being VR to contralateral stimulation only. Only a negligible number (3 boutons, 0.0033%) were significant binocular responders.

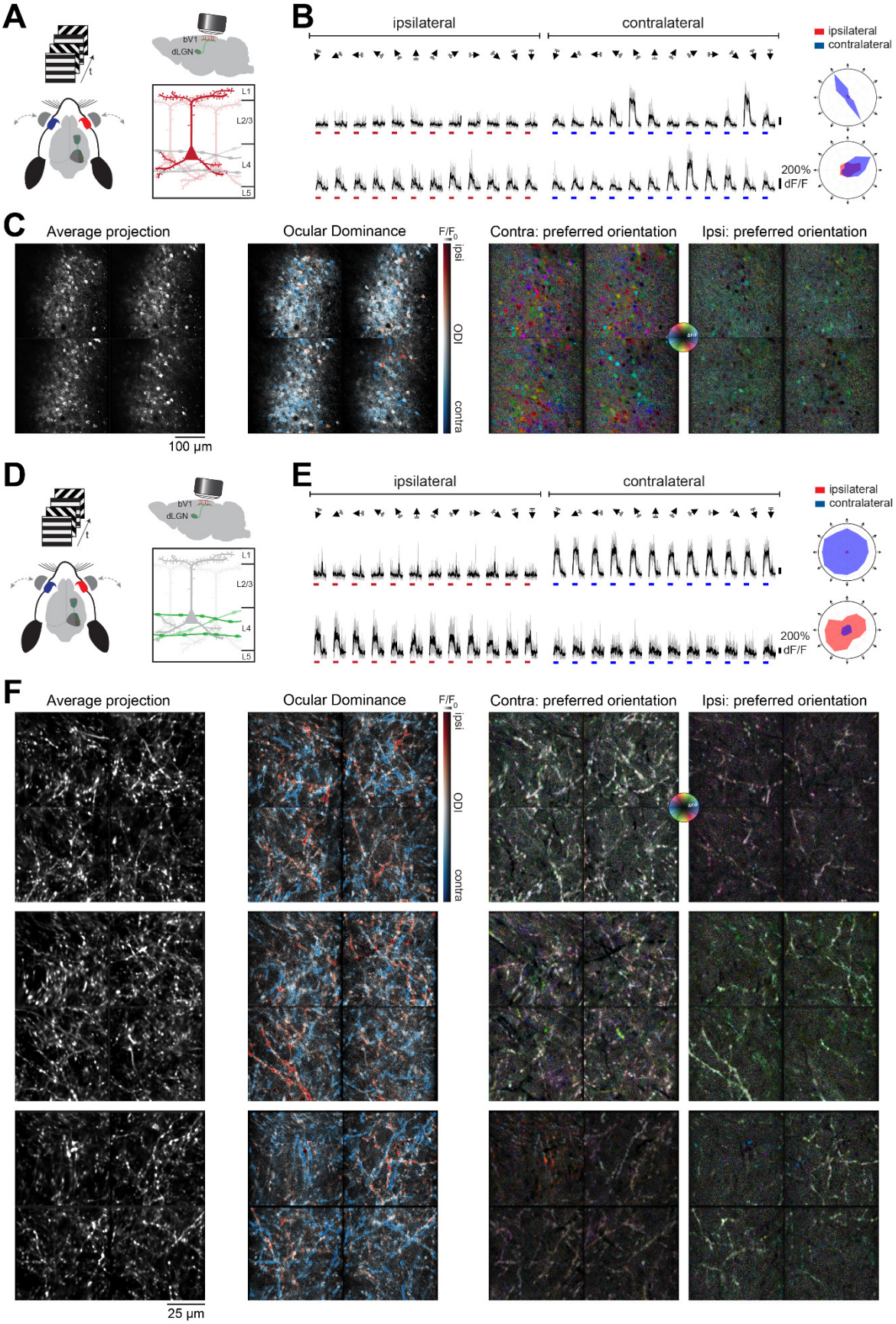

Figure 3.6: **Functional responses of cortical L4 cells and dLGN axons in L4 of bV1 in the FC-mouse to moving gratings. A|** Schematic illustrating visual stimulation (left) and cellular imaging (right) in L4 of bV1. **B|** Example calcium transients and radial tuning curves of two L4 cells (top and bottom row). Transients are shown with

respect to their respective moving grating stimulus (top) for each trial (grey) and the trial average (black, bold). Timing of visual patch-presentation is indicated as a red bar for ipsilateral and blue for contralateral eye stimulation below each transient. **C|** Average fluorescence projection (left), OD pixelmap (middle left) and PO pixelmaps for contralateral (middle right) and ipsilateral eye stimulation (right) of L4 cells labeled with jRGECO1a acquired in L4 of bV1 using *in vivo* two-photon microscopy. Concatenated images represent four consecutive piezo-planes, separated by 25 µm in z-direction each. **D|** Schematic illustrating visual stimulation (left) and imaging of dLGN axons (right) in L4 of bV1. **E|** Example calcium transients and radial tuning curves of two dLGN boutons in L4 of bV1 (top and bottom row). Arrangement and color-code as in panel B. **F|** Average fluorescence projection (left), OD pixelmap (middle left) and PO pixelmaps for contralateral (middle right) and ipsilateral (right) eye stimulation of three cortical FOVs (corresponding to rows) of dLGN axons labeled with jGCaMP7b acquired in L4 of bV1 using *in vivo* two-photon microscopy. Concatenated images represent four consecutive piezo-planes, separated by 15 µm in z-direction each.

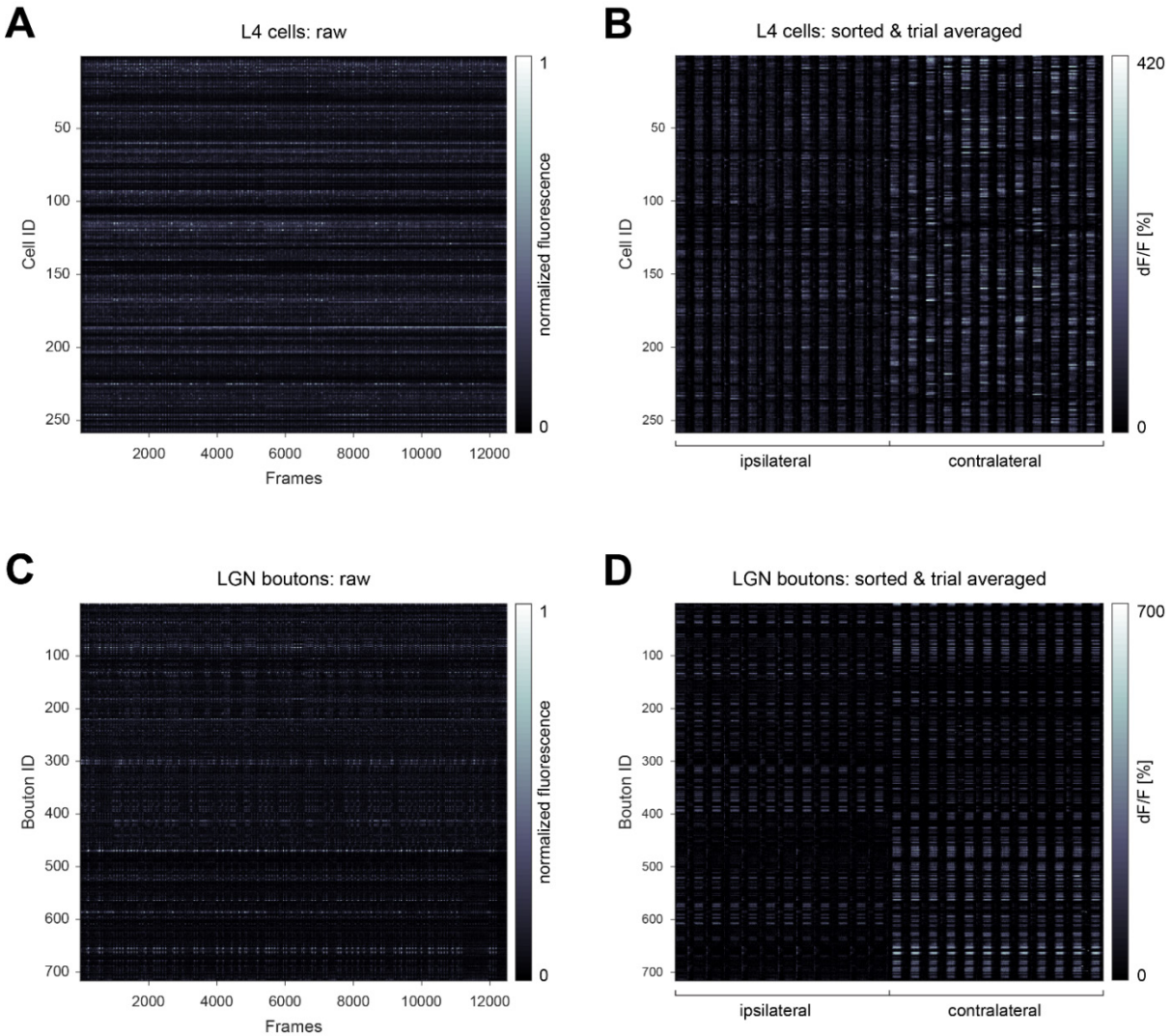

Figure 3.7: **Activity Matrices of cortical L4 cells and dLGN axons in L4 of bV1 of the FC-mouse in response to moving gratings. A|** Raw fluorescence activity matrix of jRGECO1a-labeled L4 cells. **B|** Average dF/F Tuning-Curve Matrix L4 cells, extracted from Activity Matrix in panel A. **C|** Raw fluorescence activity matrix of jGCaMP7b-labeled dLGN axons, pooled over all 3 FOVs. **D|** Average dF/F Tuning-Curve Matrix of all dLGN axons, extracted from Activity Matrix in panel C.

To investigate this discrepancy between the populations in finer detail, I compared the ODI distributions for VR L4 cells and dLGN boutons (Fig. 3.8A). While L4 cells exhibited a unimodal ODI distribution with a slight bias towards contralateral dominance (mean ODI: 0.27), the dLGN boutons

had a very bimodal distribution, with both peaks at the monocular ends of the ODI spectrum (mean ODI: 0.25).

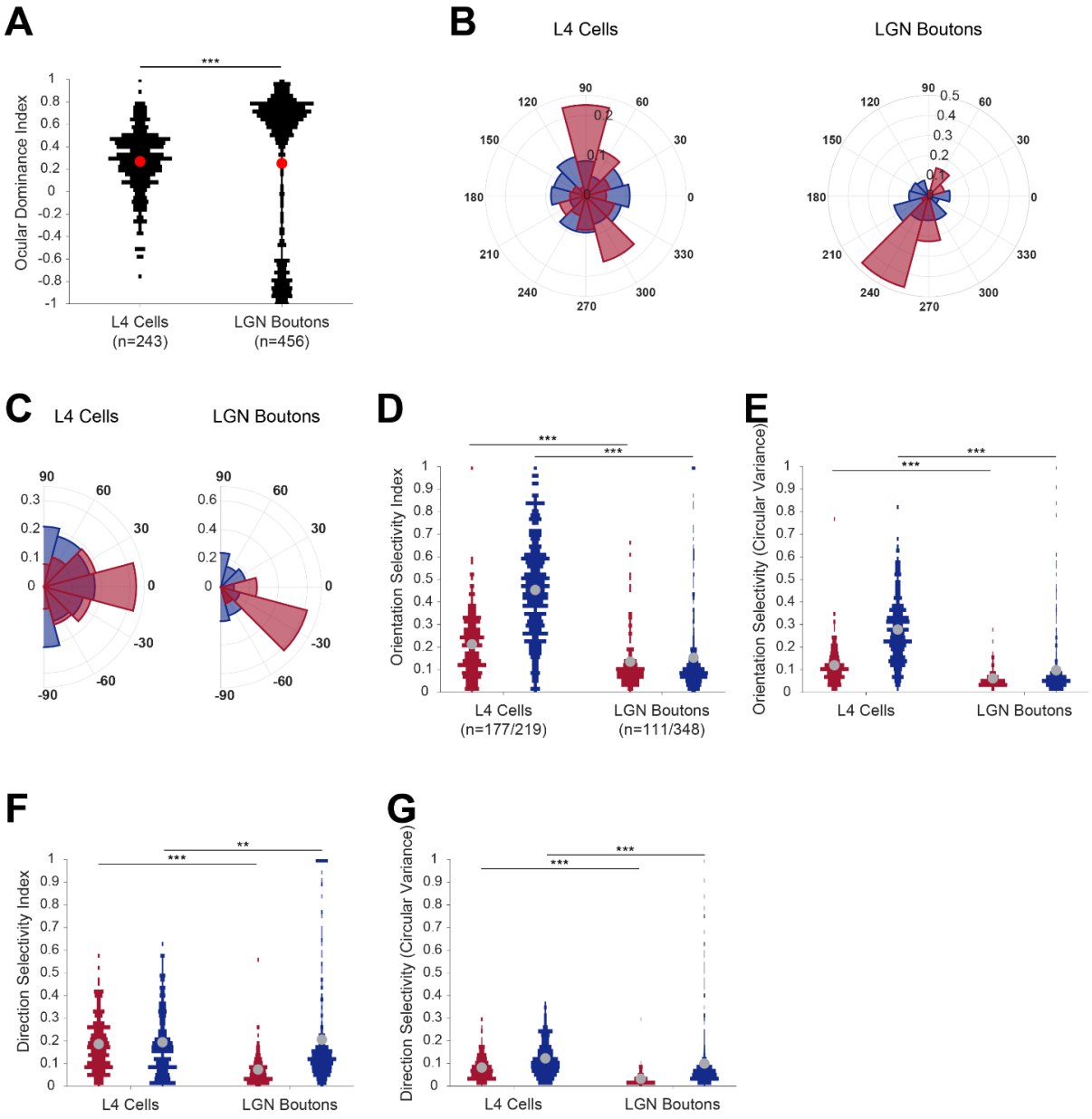

Figure 3.8: **Comparative response feature distributions between cortical L4 cells and dLGN axons in L4 of bV1 of the FC-mouse to moving gratings. A|** Normalized distributions (black histograms) and means (red dots) of Ocular Dominance Indices for VR L4 cells (left, n = 243) and dLGN axons (right, n = 456) (*** $p < 0.001$, Mann-Whitney U test). **B-F|** Ipsilateral eye stimulation shown in red and contralateral eye stimulation shown in blue. L4 cells: ipsilaterally (n = 177) and contralaterally (n = 219) responsive. dLGN boutons: ipsilaterally (n = 111) and contralaterally (n = 348) responsive. **B|** Normalized distributions of PDs of L4 cells (left) and dLGN axons (right). Radial heights corresponds to population fraction (thin black radial axis labels) and angles correspond to the stimulus movement direction (bold black angular axis labels). **C|** Normalized distributions of POs of L4 cells (left) and dLGN axons (right). Radial heights corresponds to population fraction (thin black radial axis labels) and angles correspond to the orientation of the grating stimulus (bold black angular axis labels). **D-G|** Distribution means (grey dots) (** $p < 0.01$, *** $p < 0.001$, Mann-Whitney U test). Normalized distributions of **D|** Orientation Selectivity Indices, **E|** Circular Variance Orientation Selectivity (gOSI), **F|** Direction Selectivity Indices and **G|** Circular Variance Direction Selectivity (gDSI) of L4 cells (left) and dLGN axons (right).

In other words, the majority of L4 cells showed strong binocular modulation, while dLGN bouton responses were mainly dominated by either of the two eyes, respectively. The difference between those neuronal populations was statistically significant ($p = 4.15*10^{-8}$, Mann-Whitney U test). Next, I calculated the PD, PO, OSI, global OSI, DSI and the global DSI for each VR L4 cell (177 ipsilaterally VR, 219 contralaterally VR) and VR dLGN bouton (111 ipsilaterally VR, 348 contralaterally VR). Overall, PDs of L4 cells covered all directions of movements in space, almost homogeneously during contralateral stimulation with a bias for movement in the directions of 90° and 300° (Fig. 3.8B, left). Analogously, PDs of dLGN boutons also covered all directions of movements in space, however with a more homogeneous coverage during contralateral compared to ipsilateral stimulation, which showed a bias towards 240° (Fig. 3.8B, right). These trends persisted after wrapping the tuning curves into orientation space and investigating PO (Fig. 3.8C), with L4 cells and dLGN boutons showing an overrepresentation of 0° and of -30°, respectively, in visual space during ipsilateral stimulation. During contralateral visual stimulation, orientations in space were represented more homogeneously for both neuronal populations. As PO does not represent the tuning bandwidth to orientations in space, I computed both, the traditional OSI (Fig. 3.8D) and the gOSI (Fig. 3.8E). Both metrics revealed a significant difference between the distributions of L4 cells and dLGN boutons during both, ipsilateral ($p(OSI) = 1.84*10^{-8}$, $p(gOSI) = 2.16*10^{-15}$; mean OSI/gOSI: L4 cells : 0.21/0.12, dLGN boutons: 0.14/0.06; Mann-Whitney U test) and contralateral stimulation ($p(OSI) = 2.84*10^{-50}$, $p(gOSI) = 4.03*10^{-53}$; mean OSI/gOSI: L4 cells : 0.45/0.28, dLGN boutons: 0.15/0.10; Mann-Whitney U test). Analogously, PD does not represent the tuning bandwidth to directions in space. Again, I computed both, the traditional DSI (Fig. 3.8F) and the gDSI (Fig. 3.8G). Both metrics revealed a significant difference between the distributions of L4 cells and dLGN boutons during both, ipsilateral ($p(DSI) = 1.13*10^{-19}$, $p(gDSI) = 3.25*10^{-22}$; mean DSI/gDSI: L4 cells : 0.19/0.08, dLGN boutons: 0.08/0.03; Mann-Whitney U test) and contralateral stimulation ($p(DSI) = 2.46*10^{-2}$, $p(gDSI) = 8.90*10^{-16}$; mean DSI/gDSI: L4 cells : 0.20/0.12, dLGN boutons: 0.21/0.10; Mann-Whitney U test). Taken together, dLGN boutons in L4 exhibited significantly more monocularly dominated responses and lower degrees of selectivity towards both, orientations and directions in visual space compared to postsynaptic L4 cells.

3.1.4 Deep in vivo two-photon calcium imaging for mapping of RFs for functional connectomics

To get a more complete picture of the encoded visual representations, I mapped the spatial RFs of the same L4 cells and dLGN axons in the same session. First, anesthetized mice were presented with sparse noise in their binocular visual field to either eye using eye-shutters and calcium responses recorded using two-photon imaging (Fig. 3.9A). RF calcium transients showed distinct, stimulus-locked responses (see Fig. 3.9B, left as a representative example) with elongated, retinotopically adjacent RF subfields (see Fig. 3.9B, right as a representative example). 169 L4 cells (57.68%) showed significant RF responses, with 30 (10.24%) responding to ipsilateral stimulation and 139 (47.44%) to contralateral stimulation. The cellular RFs were made up of 217 RF-subfields, with 14 ON-subfields and 17 OFF-subfields in response to ipsilateral, and 82 ON-subfields and 104 OFF-subfields in response to contralateral eye stimulation. 48 L4 cells (16.38%) exhibited both, significant ON and OFF-subfields (1 L4 cell to ipsilateral and 47 L4 cells to contralateral eye stimulation). Out of the 217 significant sub-fields, I excluded 27, as their RF centers were located outside the experimental visual sparse noise stimulation area (as determined by 2D Gaussian subfield fitting). To visualize the structural relationship between the cells in cortical space (Fig. 3.9C, left) and their retinotopic preference, I plotted each significant RF of L4 cells at their respective cell-body position in cortical space (Fig. 3.9C, right). Many RFs showed elongated shapes angled in diverse orientations in visual space. Although

several RFs showed significant responses to only a single subfield, many RFs had a Gabor-like shape. To provide a first approximation of the retinotopic RF spread, I computed the population RF in response to both, ipsilateral and contralateral stimulation, respectively (Fig. 3.9D). While L4 cell RFs at the recorded cortical position covered a range of visuotopic locations, the majority was visuotopically confined, centered in azimuth and below 0° in elevation. Analogously, I imaged dLGN axons (Fig. 3.9E) in upper L4 located within the cellular FOV. Similarly, RF calcium transients showed distinct, stimulus-locked responses (see Fig. 3.9F, left as a representative example).

In contrast to L4 cells, RFs of dLGN axons were smaller and round, with a single significantly responding subfield (see Fig. 3.9F, right as a representative example). To visualize the structural relationship between the dLGN axons in cortical space (Fig. 3.9G, average projections) and their boutons' retinotopic preference, I plotted each significant RF of dLGN boutons at their respective bouton position in cortical space (Fig. 3.9G, RFs at cortical position). 307 dLGN boutons (39.11%) showed significant RF responses, with 106 (13.50%) responding to ipsilateral stimulation and 201 (25.61%) to contralateral stimulation. The bouton RFs were made up of 332 RF-subfields, with 46 ON-subfields and 65 OFF-subfields in response to ipsilateral, and 88 ON-subfields and 133 OFF-subfields in response to contralateral eye stimulation. 25 dLGN boutons (3.19%) exhibited both, significant ON and OFF-subfields (5 dLGN boutons to ipsilateral and 20 dLGN boutons to contralateral eye stimulation). Out of the 332 significant sub-fields, I excluded 76, as their RF centers were located outside the experimental visual sparse noise stimulation area (as determined by 2D Gaussian subfield fitting). Contrary to L4 cells, dLGN bouton RFs were small and round, with no obvious elongation in visual space or Gabor-like subfield arrangement. Although RFs were more scattered in visual space (Fig. 3.9H), the majority of dLGN bouton RFs at the recorded FOVs seemed to be visuotopically confined, centered in azimuth and below 0° in elevation.

Analogous to moving grating stimulation, I visualized both, the raw fluorescence time-course and average tuning curves for all manually annotated (and matched across experiments) cells or boutons in response to sparse noise stimulation in activity matrices. I investigated gradual changes in fluorescence over time to find potential objective drifts during the experiments. The activity matrix of cellular raw fluorescence (Fig. 3.10A) showed no gradual change in fluorescence responses, and therefore no signs of drift. The tuning curve matrix (Fig. 3.10B) revealed sparse, but limited degrees of tuning, further hinting towards a restricted retinotopic diversity of RFs throughout L4 cells. Furthermore, most cells show responses to both ipsilateral and contralateral stimulation, however with the majority being dominated by contralateral eye stimulation. Analogously, the activity matrix of raw bouton fluorescence pooled over all three axonal FOVs (Fig. 3.10C) showed similar stable fluorescent responses over time – in other words, no signs of drift.

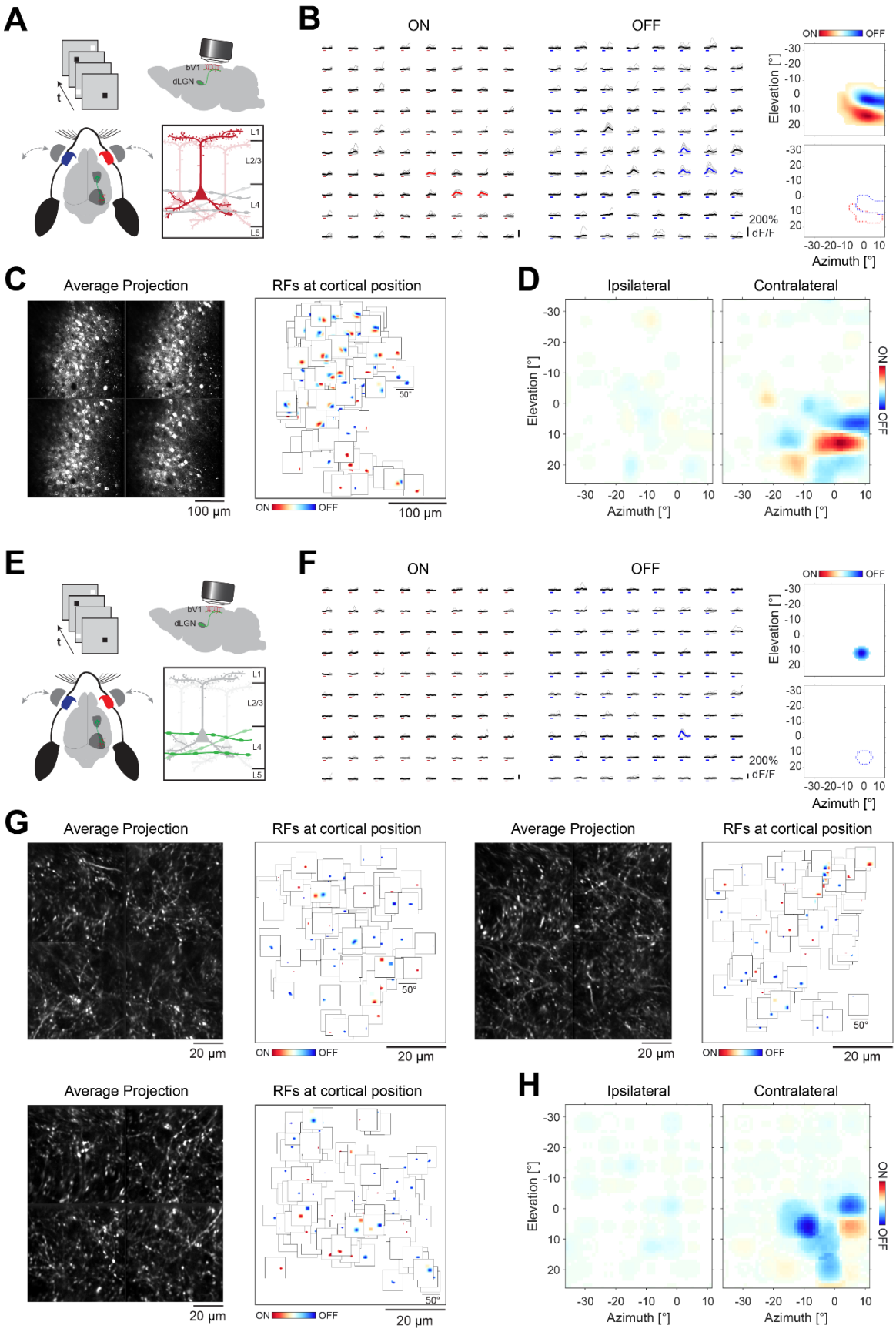

Figure 3.9: **Functional responses of cortical L4 cells and dLGN axons in L4 of bV1 in the FC-mouse to sparse noise. A|** Schematic illustrating visual stimulation (left) and cellular *in vivo* two-photon imaging (right) in L4 of bV1. **B|** Example RF-subfield calcium transients (left, middle). Transients are shown at their relative sparse noise

stimulus-patch positions for each trial (grey) and the trial average (black, bold). Trial averages of significant RF patches are illustrated in red for ON-subfields (left) and blue for OFF-subfields (middle). Timing of visual patch-presentation is indicated as a red bar for light-increments (ON) and blue for light decrements (OFF) below each transient. The corresponding RF (right, top) and subfield-outlines (right, bottom) are plotted in visual space. **C|** Average fluorescence projection of L4 cells (left). Concatenated images represent four consecutive piezo-planes, separated by 25 µm in z-direction each. Significant cellular RFs plotted at ROI position in cortical space (right). **D|** Cellular population RF of ipsilateral (left) and contralateral (right) eye stimulation plotted in visual space. **E|** Schematic illustrating visual stimulation (left) and axonal *in vivo* two-photon imaging (right) in L4 of bV1. **F|** Example RF-subfield calcium transients (left, middle), arranged and color-coded as in panel B. The corresponding RF (right, top) and subfield-outlines (right, bottom) are plotted in visual space. **G|** Average fluorescence projection of dLGN axons in L4 paired with respective significant bouton RFs plotted at ROI position in cortical space for all three axonal FOVs. Concatenated average fluorescence projection images represent four consecutive piezo-planes, separated by 15 µm in z-direction each. **H|** Axonal population RF (over all FOVs) of ipsilateral (left) and contralateral (right) eye stimulation plotted in visual space.

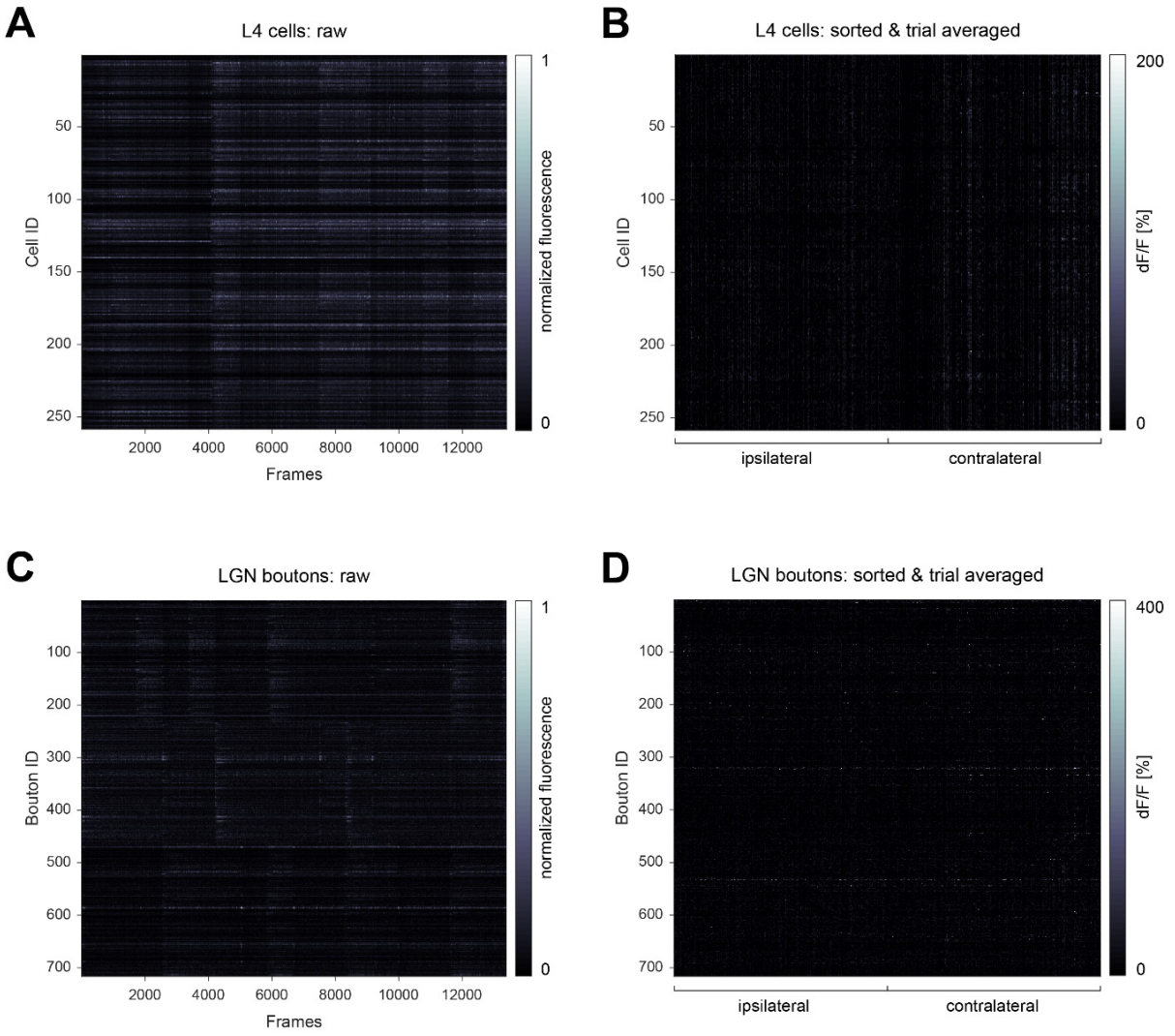

Figure 3.10: **Activity Matrices of cortical L4 cells and dLGN axons in L4 of bV1 of the FC-mouse in response to sparse noise. A|** Raw fluorescence activity matrix of jRGECO1a-labeled L4 cells. **B|** Average dF/F Tuning-Curve Matrix L4 cells, extracted from Activity Matrix in panel A. **C|** Raw fluorescence activity matrix of jGCaMP7b-labeled dLGN axons, pooled over all 3 FOVs. **D|** Average dF/F Tuning-Curve Matrix of all dLGN axons, extracted from Activity Matrix in panel C.

The tuning curve matrix of dLGN boutons (Fig. 3.10D) showed an even sparser response pattern, indicating a lower percentage of RFs with smaller size. The response locations were very diverse,

hinting towards more spread-out, less retinotopically constrained RFs. Furthermore, responses were less dominated by contralateral stimulation, compared to L4 cells.

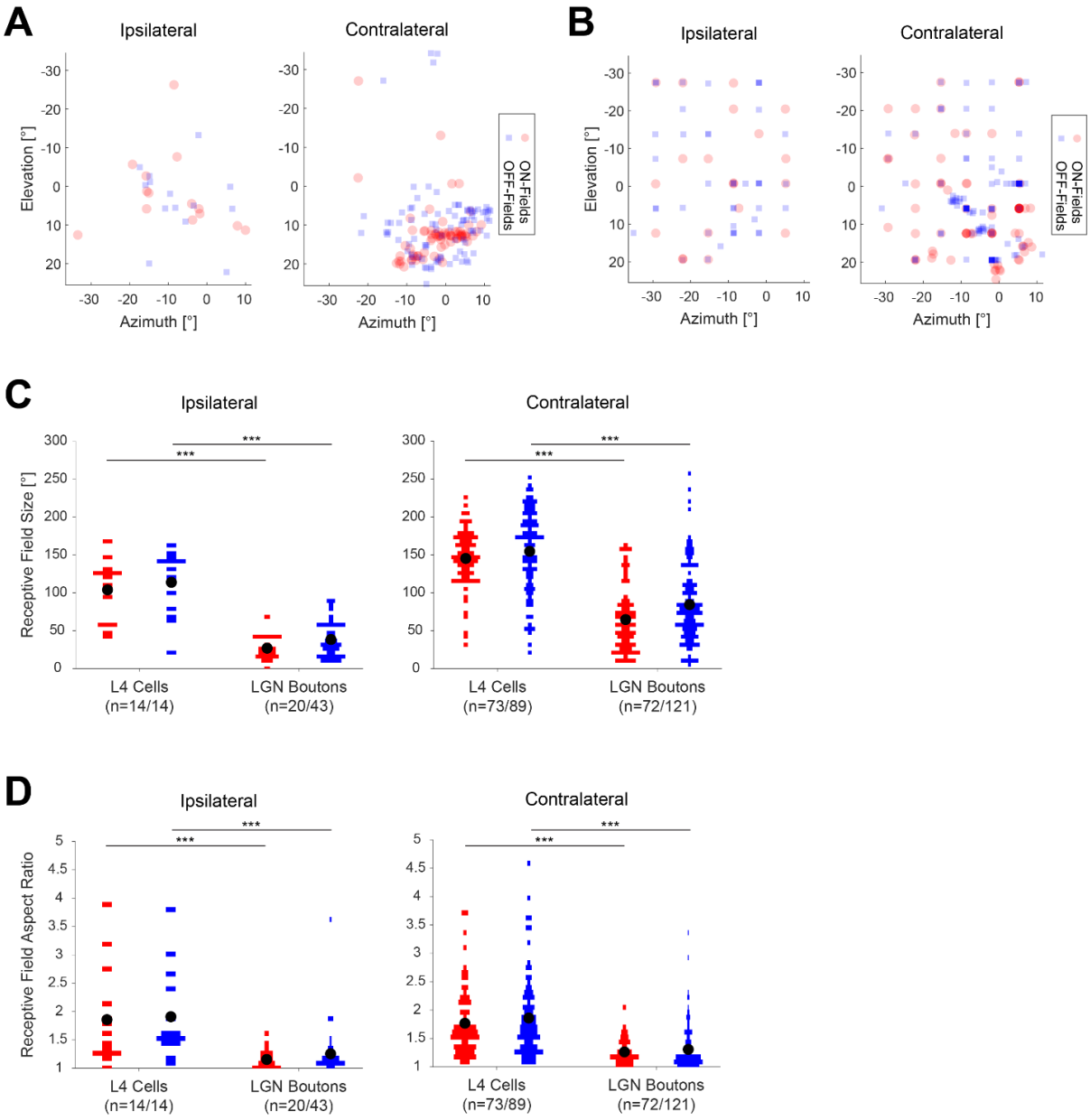

Figure 3.11: **Comparative response feature distributions between cortical L4 cells and dLGN axons in L4 of bV1 of the FC-mouse to sparse noise. A-D|** RF ON-subfields are plotted in red and OFF-subfields in blue. **A|** Center-positions of cellular RF sub-fields plotted in visual space for ipsilateral (left) and contralateral eye stimulation (right). **B|** Center-positions of bouton RF sub-fields plotted in visual space for ipsilateral (left) and contralateral eye stimulation (right). **C-D|** Distribution means (black dots) (*** $p < 0.001$, Mann-Whitney U test). L4 cells: significant ipsilateral ON (n = 14) and OFF-subfields (n = 14); significant contralateral ON (n = 73) and OFF-subfields (n = 89). dLGN boutons: significant ipsilateral ON (n = 20) and OFF-subfields (n = 43); significant contralateral ON (n = 72) and OFF-subfields (n = 121). **C|** Normalized distributions of RF sizes between L4 cells and dLGN boutons in L4 bV1 for ipsilateral (left) and contralateral eye stimulation (right). **D|** Normalized distributions of RF aspect ratios between L4 cells and dLGN boutons in L4 bV1 for ipsilateral (left) and contralateral eye stimulation (right).

To investigate the RF features and their discrepancies between L4 cells and dLGN axons in more detail, I looked into RF positions, RF sizes and RF aspect ratios. Population RFs (see Fig. 3.9D,H) provide only

a very limited picture of RF spread, especially since they conceal overlapping subfields of opposite polarity. Therefore, I instead examined the RF center locations of L4 cells (Fig. 3.11A) and dLGN axons (Fig. 3.11B). For both populations, the majority of RFs were visuotopically confined, centered in azimuth and below 0° in elevation. However, while L4 cells only showed a few outliers outside this retinotopically confined area, RFs from dLGN boutons exhibited a much stronger visuotopic spread, almost covering the entirety of the visual space mapped by the sparse noise stimulus, hinting at a retinotopically less refined cortical map. Differences in RFs between these neuronal populations were further substantiated by their distribution of RF sizes and aspect ratios. RF size differences were statistically significant during both, ipsilateral ($p(RF_{size\text{-}ON}) = 4.91*10^{-6}$, $p(RF_{size\text{-}OFF}) = 7.41*10^{-6}$; mean $RF_{size\text{-}ON}/RF_{size\text{-}OFF}$: L4 cells : 103.93°/113.86°, dLGN boutons: 26.90°/38.33°; Mann-Whitney U test) and contralateral stimulation ($p(RF_{size\text{-}ON}) = 5.56*10^{-17}$, $p(RF_{size\text{-}OFF}) = 4.03*10^{-16}$; mean $RF_{size\text{-}ON}/RF_{size\text{-}OFF}$: L4 cells : 145.25°/154.61°, dLGN boutons: 64.65°/84.35°; Mann-Whitney U test). Similarly, differences in RF aspect ratios (ARs) were statistically significant during both, ipsilateral ($p(RF_{AR\text{-}ON}) = 6.45*10^{-4}$, $p(RF_{AR\text{-}OFF}) = 2.65*10^{-5}$; mean $RF_{AR\text{-}ON}/RF_{AR\text{-}OFF}$: L4 cells : 1.86/1.91, dLGN boutons: 1.15/1.26; Mann-Whitney U test) and contralateral stimulation ($p(RF_{AR\text{-}ON}) = 2.07*10^{-11}$, $p(RF_{AR\text{-}OFF}) = 6.21*10^{-15}$; mean $RF_{AR\text{-}ON}/RF_{AR\text{-}OFF}$: L4 cells : 1.77/1.86, dLGN boutons: 1.26/1.31; Mann-Whitney U test). Taken together, dLGN boutons in L4 exhibited more visuotopic scatter and significantly smaller RF sizes and aspect ratios compared to postsynaptic L4 cells.

3.1.5 Alignment of RF orientation and PO in L4 cells

To investigate the connection of RF orientation with the PO of L4 cells, I fitted the Gabor-like RFs with a Gabor function (see methods section "2.20.7 Two-photon imaging – Receptive fields") and extracted their orientation. To visualize this relationship in the context of RF position, I plotted both, the RF orientation (Fig. 3.12A, left; measured using sparse noise stimulation) and the matched PO (Fig. 3.12A, right; as measured per moving grating stimulation) at their respective RF center positions as accordingly oriented and color-coded lines. While few L4 cells perfectly matched in orientation, the majority was roughly aligned with only a few cells exhibiting perpendicular PO and RF orientation. Overall, the RF-Gabor orientation of L4 cells positively correlated with their PO (Fig. 3.12B; $R^2 = 0.1551$, $p = 0.0089$).

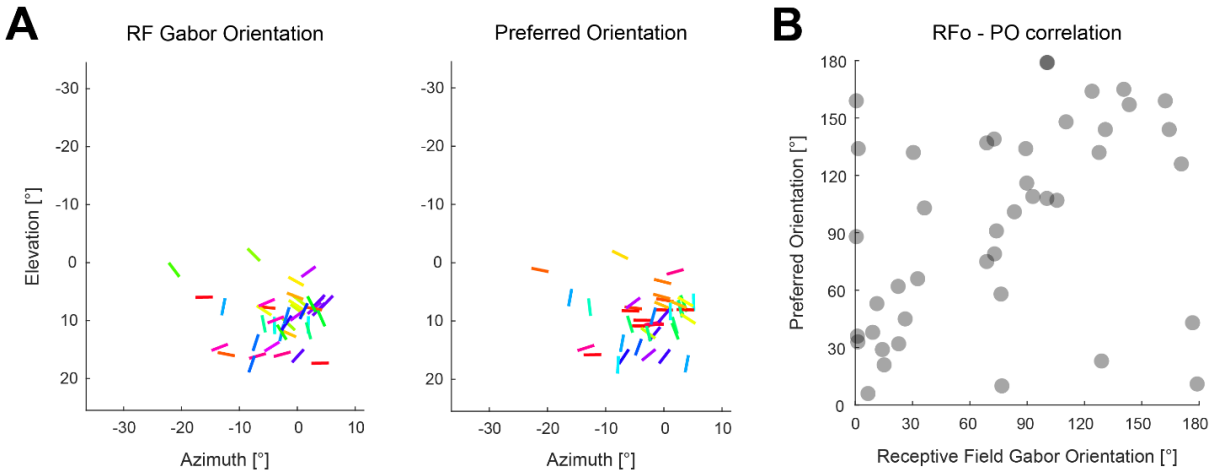

Figure 3.12: **Relationship of RF Gabor orientation and PO of L4 cells in bV1 of the FC-mouse. A|** Bars corresponding to RF Gabor orientations (left) and PO (right) plotted at their respective RF center positions in visual space. Bars are angled and pseudo-colored according to their respective orientation. **B|** Correlation of RF Gabor orientation and PO of L4 cells ($R^2 = 0.1551$, $p = 0.0089$).

3.1.6 Linking neuronal function to structure in L4 cells and dLGN axons in vivo

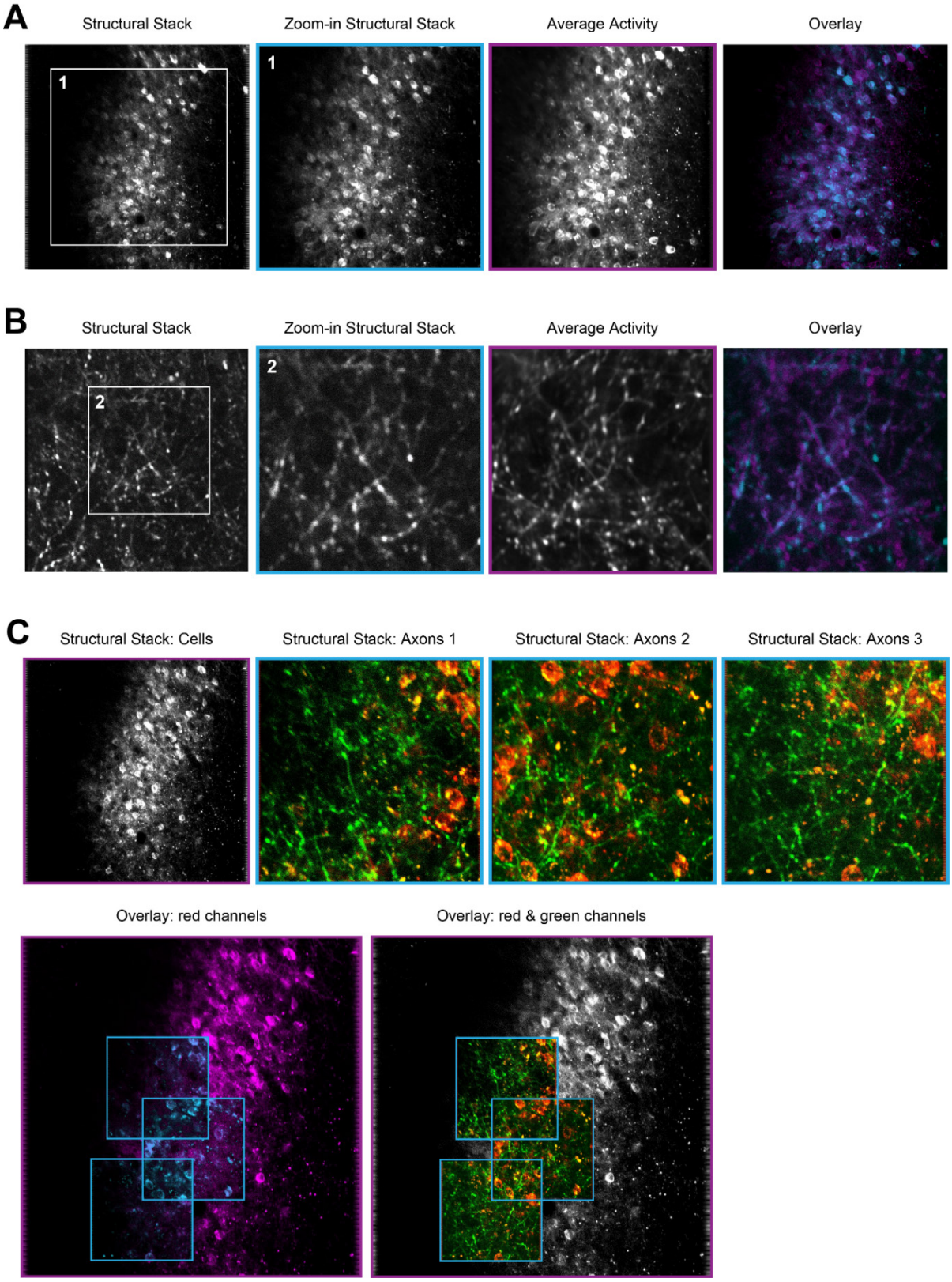

Figure 3.13: **Matching of functional and structural stacks from *in vivo* two-photon microscopy of the FC-mouse. A-B|** Exemplary matching of single average piezo-plane (middle right) of functional imaging to corresponding plane in structural stacks (left and middle left) for L4 cells in **A** and dLGN axons in L4 of bV1 in **B**. White box in structural stack (left) corresponds to functional imaging FOV. Outline colors of zoomed-in structural stack (middle left) and piezo-plane of functional imaging (middle right) correspond to colors in their overlay plot

(right). **C|** Matching of all three axonal structural stacks (top: middle left, middle right and right; both red (cellular jRGECO1a) and green (axonal jGCaMP7b) channels acquired) to structural stack of L4 cells (top, left). Outline colors of zoomed-in structural stacks (top) correspond to outline colors in their overlay plots (bottom). Matching was based on cellular red channel only (bottom left) and applied to both channels of the axonal structural stacks (bottom right).

For our functional connectomics approach, it is key to be able to link functionally imaged cells and axons to their underlying structure, to subsequently re-find them in the post-mortem 3D-EM volume. To address this, I acquired 3D structural stacks comprising all functionally imaged FOVs (structural x-y FOV was bigger than the functional one, see methods) and piezo-planes in the same session *in vivo*. Subsequently, all 4 functional cellular piezo-planes and all 12 axonal piezo-planes were re-found and matched to their respective 3D stack using the average fluorescence projections (see Fig12A for representative example of L4 cells and Fig12B for representative example of dLGN axons). To facilitate re-finding of small neurites like dLGN axons in 3D-EM space, I used both the red (jRGECO1a labeled L4 cells) and green channel (jGCaMP7b labeled dLGN axons) for all 3 structural stacks of dLGN axons to link the axonal to the cellular structure (Fig. 3.13C, top). I next used the red, cellular channel from these 3 FOVs for localizing them within the bigger cellular structural stack (Fig. 3.13C, bottom left) and thereby anchor the dLGN morphologies into the cellular stack (Fig. 3.13C, bottom right) as a framework.

3.2 Large-scale 3D multibeam electron microscopy

3.2.1 Homogeneous heavy metal staining for 3D-EM

Homogeneous tissue staining with heavy metals is imperative for high-quality SEM. Traditionally, to evaluate staining quality, the sample had to be smoothed and investigated directly in EM. As staining issues are mostly localized in the sample core, staining gradients often only become apparent in the middle of the 3D-EM experiment, several weeks into data acquisition. To circumvent this, I instead visualized staining gradients non-invasively using microCT (Fig. 3.14A).

For functional connectomics specifically, an important tradeoff is maximizing the biopsy volume to ensure correct targeting of previously functionally imaged regions, all while ensuring high-contrast staining throughout the sample. To tackle this challenge, I first extracted and stained cylindrical, 500 µm thick biopsies of either 1.5 mm or 2 mm diameter from V1 of non-functionally imaged perfused wildtype mice. While the 1.5 mm wide samples did not show any signs of staining gradients, some 2 mm wide samples had minor indications of slightly decreased staining quality in the sample core. To gain intuition on the impact of staining gradient strength on EM image acquisition, I trimmed all samples to the core (~250 µm) and imaged the entire surface with EM. While obvious staining gradients were not imageable in the sample core due to charging, minor staining gradient only had a minor effect on signal contrast, but did not inhibit imaging neuronal structures at high resolution.

For *Scnn1a-Tg3-Cre* mice previously functionally imaged using two-photon microscopy, I therefore extracted cylindrical biopsies of 2 mm diameter. Furthermore, to be able to assess the ultrastructure, I further extracted a sister sample from PFC of the same hemisphere to be stained with the same chemicals. Surprisingly, while the PFC samples consistently had near-perfect homogeneous staining, their sister bV1 biopsies showed strong staining gradients (see Fig. 3.14B for representative example). Interestingly, the area of low staining was not constrained to the sample core, but extended unilaterally to the edge of the sample, where pia was located. This hinted towards a diffusion barrier, possibly caused by dura-thickening below the chronic cranial window.

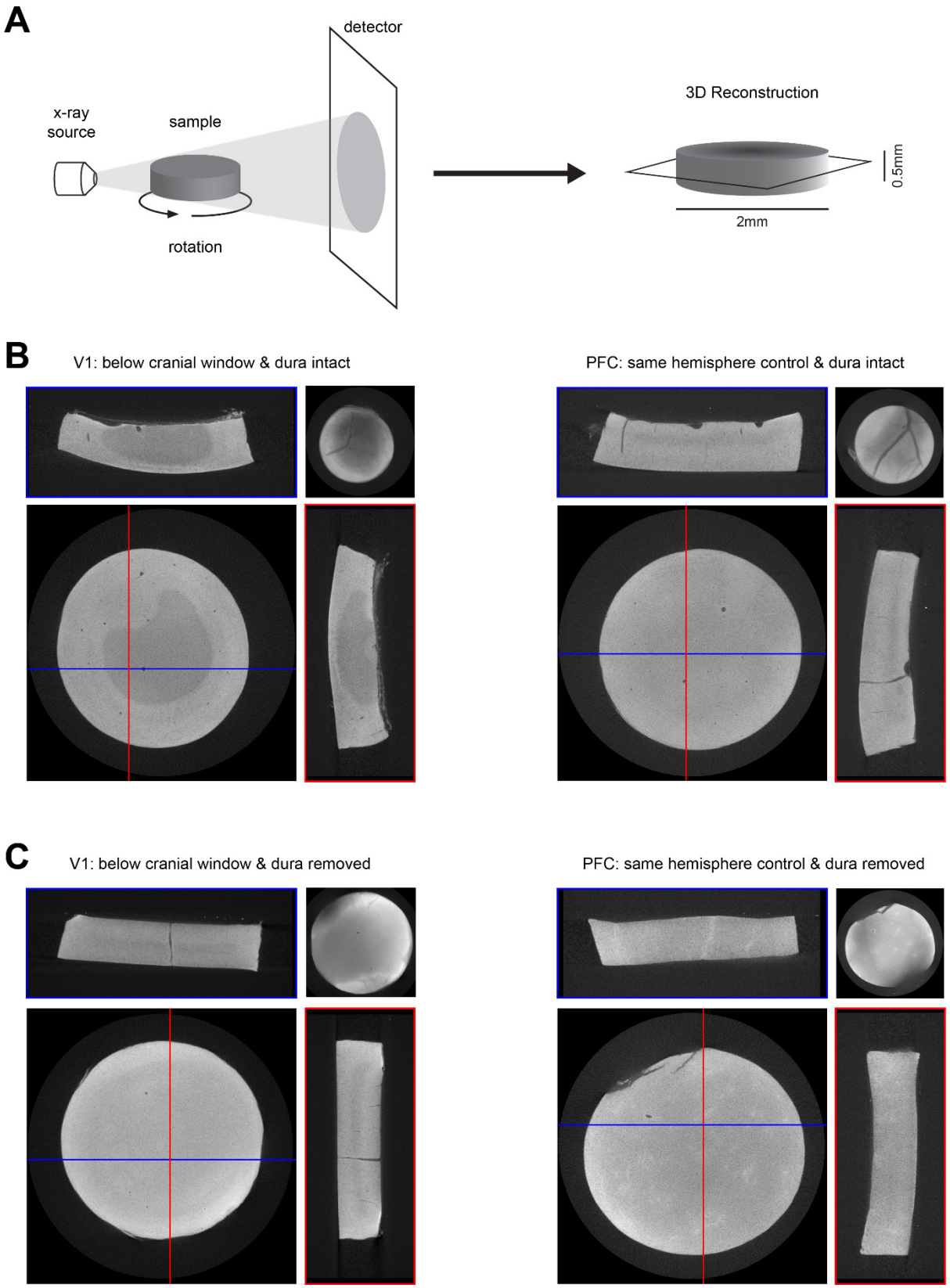

Figure 3.14: **Optimization of heavy metal staining homogeneity for EM assessed by microCT. A|** Schematic illustrating microCT imaging (left) of heavy metal stained tissue and subsequent reconstruction in 3D (right). **B-C|** Bottom left images show microCT cross-sections through the sample core (see black line in panel A, right) with red and blue lines indicating the positions of the microCT reslices of matching outline color. Small square images represent average projections of the biopsy surface (corresponding to dural/ pial surface). Biopsy

reconstructions taken from bV1 below the cranial window (left) and their respective same hemisphere control biopsies from PFC (right) are shown for samples with dura left intact in **B** and dura removed in **C**.

To circumvent this issue, I removed the top 50 µm of layer 1 in the middle of the biopsy with a vibratome to remove dura in subsequent attempts. Due to the curvature of bV1, only the surface in the middle was cut away to minimize tissue loss. All subsequent biopsies were prepared with the latter protocol and showed near-perfect homogeneous heavy metal staining in both biopsies (see Fig. 3.14C for representative example from the FC-mouse).

3.2.2 Targeted biopsy extraction via vascular triangulation for functional connectomics

To be able to image the same circuit both functionally *in vivo* using two-photon imaging and ultra-structurally post-mortem via 3D-EM, I developed an extensive, step-by-step pipeline for targeted biopsy extraction and tissue preparation for EM (see Fig. 3.15A for illustration, see methods for details). In brief, the location of the two-photon FOV was mapped onto the surface blood-vessel pattern of the cranial window (Fig. 3.15B). The mouse was perfused with the far-red lipophilic fluorophore DiD to stain blood vessels for post-mortem vascular re-identification. Post-perfusion the DiD-stained blood vessels in the cranial window were imaged using epifluorescence microscopy, allowing for re-identification of blood vessels from the *in vivo* imaging. The two-photon FOV was located using the re-identified vascular landmarks. A round, 2 mm in diameter biopsy, containing the two-photon FOV was stereotaxically extracted and cut into a 500 µm thick cylindrical slab using a vibratome (see methods for more details). The biopsy was subsequently stained with heavy metals and embedded into resin. To be able to center the EM FOV around the two-photon FOV, I imaged the stained biopsy with microCT and re-identified vascular landmarks from *in vivo* imaging (Fig. 3.15C). All re-identified blood vessels were further confirmed by cross-triangulation (see Fig. 3.15D as example). Next, the x-y location of the two-photon FOV was triangulated from re-identified vascular landmarks and a 1 mm^2 EM FOV was designed centered on it (Fig. 3.15E, left). A hexagon harboring the EM FOV was designed and trimmed for subsequent sectioning with ATUM. The localization of the designed 2P FOV and EM FOV were re-confirmed in the trimmed biopsy using microCT (Fig. 3.15E, right). As a final safeguard, the positioning of the EM FOV was confirmed in EM by vascular cross-triangulation (Fig. 3.15F). Specifically, I used blood vessels penetrating the cortical tissue perpendicular to the cortical surface for several hundreds of microns, to reduce the potential risk of pattern-matching caused by chance. Furthermore, I included the two biggest matched blood vessels within the biopsy, re-confirmed by their diameter. Although laborious, this biopsy extraction pipeline enabled me to image the FOV from two-photon microscopy in 3D-EM.

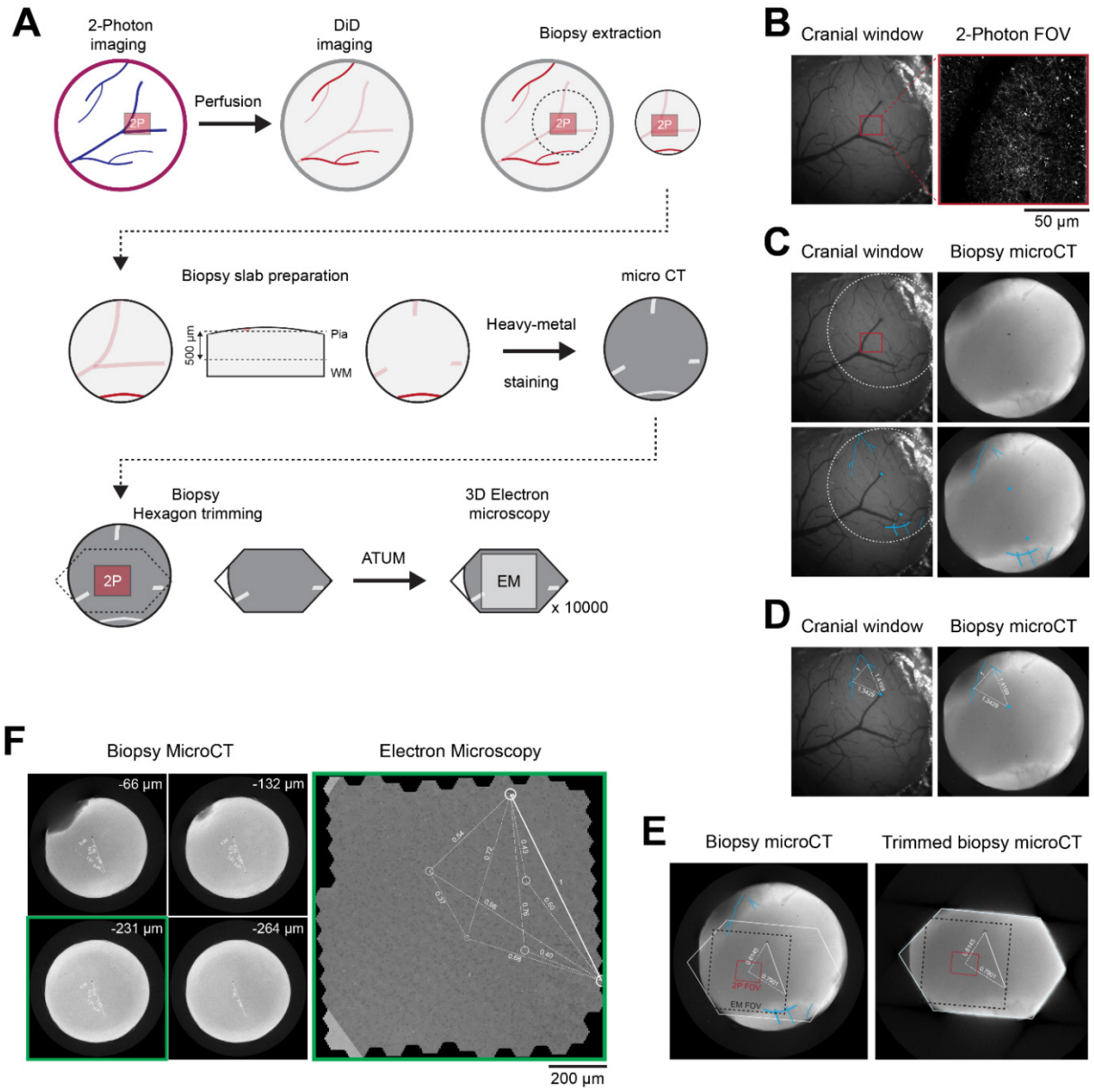

Figure 3.15: **Localization of the *in vivo* two-photon microscopy FOV in microCT and EM by triangulation from vascular landmarks. A|** Schematic illustrating the sequence and logic of targeted biopsy extraction of cortical tissue previously imaged using two-photon microscopy and subsequent hexagon preparation for ATUM mSEM. **B-C|** Two-photon FOV outline illustrated in cranial window overview as a red rectangle. **B|** Overview image of the bloodvessel-pattern below the cranial window (left). Two-photon microscopy cellular FOV illustrated via a structural z-stack of layer 4 cell dendrites in layer 1 of bV1 (right). **C|** Re-identification of vascular landmarks from *in vivo* imaging (left) in the heavy metal stained biopsy, imaged using microCT (right). Biopsy outline is indicated by a white dotted circle in the cranial window overview (left). Re-identified blood vessels are illustrated in cyan (bottom). **D-E|** Vascular landmarks are illustrated in cyan and triangulations as white dotted lines, with their respective normalized lengths as white numbers. **D|** Exemplary verification of re-identified blood vessel by vascular landmark triangulation. **E|** Design (left) and verification (right) of hexagonal biopsy shape for ATUM sectioning visualized using microCT. Two-photon FOV outlined as a red square with the mSEM FOV outlines as a black dotted square. **F|** Re-identification of vascular landmarks from microCT (left) in mSEM micrograph (right) and verification by triangulation. Vascular landmarks for triangulation were chosen based on their existence over different depths (left) to avoid stochastic vascular landmark pattern matching. Triangulations are shown as white dotted lines with their respective normalized lengths as white numbers. The depth of the section imaged by mSEM (right) is estimated to be located about -231 µm below the surface in the microCT reconstruction (bottom left) indicated by green rectangular outlines.

3.2.3 Optimizing ATUM for single-shot experiments

In order to efficiently acquire large-scale 3D-SEM volumes, the combination of ATUM mSEM has replaced the traditional SBEM. While separating the 3D-EM workflow into non-destructive microtome sectioning followed by mSEM offers great benefits (see introduction section "1.5.6 3D electron microscopy"), this technology still poses challenges that need to be optimized. Due to the multitude of experimental parameters, the workflow required multiple experimental attempts until successful. Given the length and complexity of this work's functional connectomics pipeline, such experimental uncertainty would be impractical. Furthermore, the localized targeting-requirements of the EM-volume to the two-photon FOV does not allow for several attempts in the same tissue.

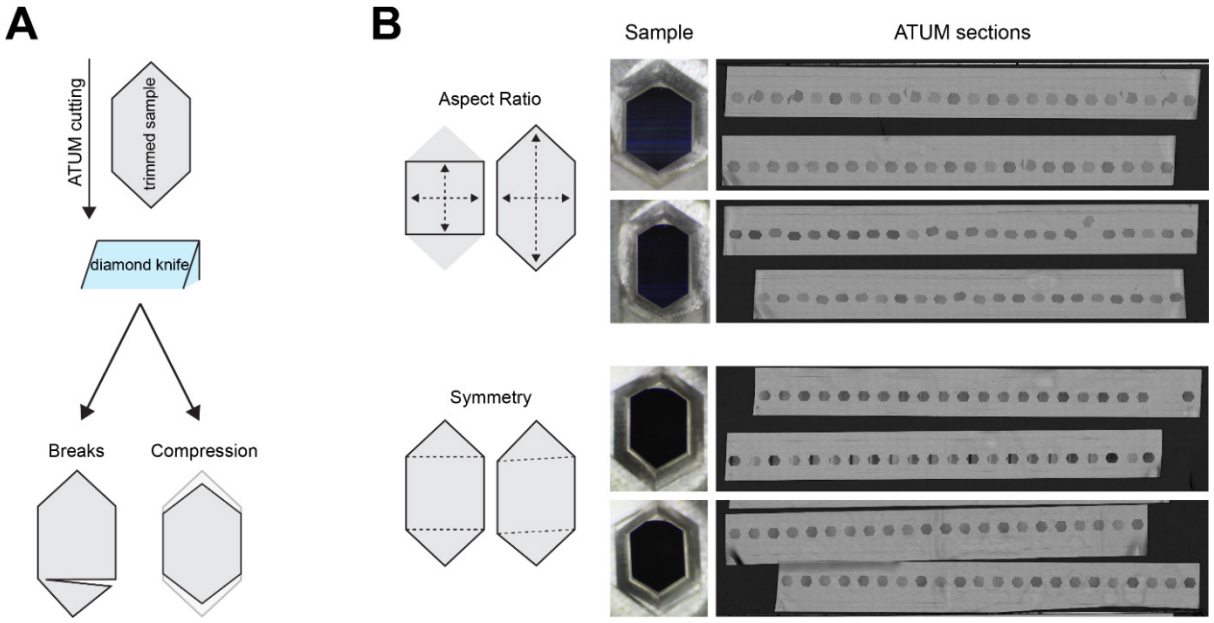

Figure 3.16: **Optimization of sample shape for continuous, homogeneous ATUM sectioning. A|** Schematic illustrating the sectioning of hexagonal samples using a diamond knife (top) and common cutting artifacts (bottom). **B|** Improvement in ATUM sectioning quality by elongated aspect ratio (top) and symmetric hexagon trimming (bottom) of biopsies. Trimmed sample pairs are shown in the middle with their respective 35 nm thin serial ATUM sections collected on Kapton tape on the right.

Therefore, I conducted a diverse set of pilot ATUM experiments to explore the experimental parameter space and tailor the experimental requirements towards a successful single-shot ATUM experiment with the FC-mouse. I specifically focused on solving the most common causes for loss of ultrastructural continuity in our hands: section breaks, inhomogeneous compression (see Fig. 3.16A for illustration) and loss of sections due to failures during collection on tape. I found that the latter was highly dependent on the distance of the tape-collecting arm to the knife edge. The ideal tape distance was at about the length of the hexagon in the cutting direction, so that the fully cut section hovered on the surface-tensioned water film on the tape-tip, prior to collection. The section was then pushed onto the collecting tape itself by the next cut section. If the tape was too far, the sections would float on the water surface and change angle, leading to the collection of sections in diverse angles, and sometimes to section loss by floating away from the tape collecting arm. If the tape was too close, the tape collection started before the entire section was cut, leading to pulling forces, that induced section ripping and inhomogeneous cutting.

To investigate the impact of sample shape on ATUM cutting, I iteratively changed shape parameters via sample-trimming and tracked resulting changes in cutting and tape-collection. I found that two

main factors influenced homogeneous ATUM sectioning the most: sample aspect ratio and symmetry. In my hands, an aspect ratio of the inner rectangle of the hexagon of 1.1 (elongated in the cutting direction) showed the least amount of compression and best collection. Wider aspect ratios increased the frequency of section breakages and compression artifacts at the triangle-rectangle border (Fig. 3.16B, top). On the other hand, while narrower aspect ratios did not exhibit any cutting artifacts, sections were collected in diverse angles due to unstable floating right before tape-collection. Furthermore, hexagon symmetry had a strong influence on the cutting homogeneity (Fig. 3.16B, bottom). Precise alignment of the hexagon tips along the cutting direction decreased rotation of floating sections, induced by asymmetric pushing onto the tape. Furthermore, alignment of the lower edge of the inner rectangle to the knife edge eliminated cutting and compression artifacts. Taken together, for samples prepared with all previously mentioned considerations in mind, I was able to achieve consistent successful cutting series without single section lossed and cutting artifacts. Being able to control these experimental parameters allowed us to move forward on preparing and ATUM sectioning the biopsy of the FC-mouse.

3.2.4 ATUM sectioning for functional connectomics

For ATUM sectioning of the previously functionally imaged FC-mouse, I first trimmed the sample into a hexagonal shape with the two-photon FOV included within the inner rectangle (see Fig. 3.15E). The hexagon was about 2.4 mm in length (tip-to-tip in cutting direction) and approximately 1.35 mm wide (measured using light microscopy) with an inner rectangle ratio of 1.1, elongated in the cutting direction. I next approximated the L4/L5 border at the two-photon FOV location with microCT, using the bigger L5 cell bodies as landmarks. The biopsy was smoothed from deep L5 up until 70-80 µm from the L4/L5 border, marking the start of the ATUM experiment.

The 355 µm thick biopsy was fully ATUM sectioned and collected on carbon-coated kapton tape in a 40 h continuous experiment without single section loss. The resulting sectioned z-depth was 353.015 µm, containing the top of L5, the entirety of L4 and the lower half of L2/3. Overall, the volume was cut into 10014 consecutive sections with an average section thickness of 35.25 nm. The majority of the tissue was cut at a section thickness of 35 nm, with a few regions of less stable cutting (mainly minor compression) sectioned at a thickness of 40 nm (see Tab. 3.1 for precise section thicknesses). The last 30 µm of the experiment were cut continuously at 40 nm, as the biopsy edges were retracting and therefore the hexagon edges were filled up increasingly with resin leading to inhomogeneous cutting at 35 nm. To combat premature loss of section continuity caused by possible blunting of- and debris accumulation on the diamond knife edge, I successfully performed one knife shift after 148.960 µm and one knife exchange after 255.010 µm. Both instances did not lead to a single section loss. After both, the knife shift and knife exchange, the knife edge was not perfectly parallel to the hexagonal surface anymore, leading to a few not fully cut sections. Specifically, for the knife shift the biopsy first started being cut from the left side, leading to 3 not fully cut hexagons. For the knife exchange, the knife was closer to the right, leading to 2 not fully cut sections.

Section #	Range [µm]	Section thickness [nm]	∑ [µm]
1-2966	103.810	35	103.810
2967-3044	3.120	40	106.930
3045-3071	0.945	35	107.875
3072-3154	3.280	40	111.155
3155-3159	0.175	35	111.330
3160-3370	8.440	40	119.770
3371-4055	23.975	35	143.745
4056-4140	3.400	40	147.145
4141-4185	1.575	35	148.720
4186-4291	0.240	40	148.960
Knife shift			
4292-7321	106.050	35	255.010
Knife exchange			
7322-9264	68.005	35	323.015
9265-10014	30.000	40	353.015

Table 3.1: **Section catalog from the ATUM experiment of the FC-mouse.** Table cataloging the section number (left), microtome step-size (middle right) and range (middle left) as well as summed cutting distance (right) of the last section per row respectively. The biopsy was cut from upper layer 5, through layer 4 and into the middle of layer 2/3 of bV1. The locations of the shift (3 non fully cut sections) and exchange (2 non fully cut sections) of the diamond knife during the experiment are indicated. The collection of each section was individually monitored. In total 10014 ultra-thin sections were cut and collected without a single section loss.

3.2.5 3D mSEM for functional connectomics

For 3D mSEM I successfully mounted the first 9643 of the 10014 ATUM sections onto 42 silicon wafers. Wafers were subsequently mounted on wafer holders and imaged with LM (see Fig. S1 for LM wafer gallery). Based on the hexagonal section outline, I triangulated a 1x1 mm^2 mSEM FOV (centered around the two-photon FOV) surrounded by 5 focus support points (Fig. 3.17A) to level height-differences. The support point positions (relative to the hexagonal outline) were saved and automatically applied to all subsequent hexagons. I successfully imaged the 9643 mounted sections with mSEM, resulting in a final volume of 1 x 1 x 0.33 mm^3, containing upper L5, all of L4 and about half of L2/3. Sections were imaged with 61 beams at a voxel-size of 4x4x35 nm. Each 1x1 mm^2 FOV was tiled into ~193 tiles of 61-beam hexagons (see Fig. 3.17B for representative example), resulting in ~11500 raw-data images/section and 112473935 images (excluding re-takes) for the entire 3D mSEM volume. This translated into >95.5 TB of raw-data/section, leading to a raw-data size of >0.92 PB for the entire 1 x 1 x 0.33 mm^3 volume. In total, the dataset was acquired within 132 days, including overheads and down-times (e.g. due to plasma-cleaning of the imaging chamber, maintenance, power-outages). This translated into ~59 days of continuous imaging at an average effective acquisition speed of 1.4 days per wafer (including re-takes).

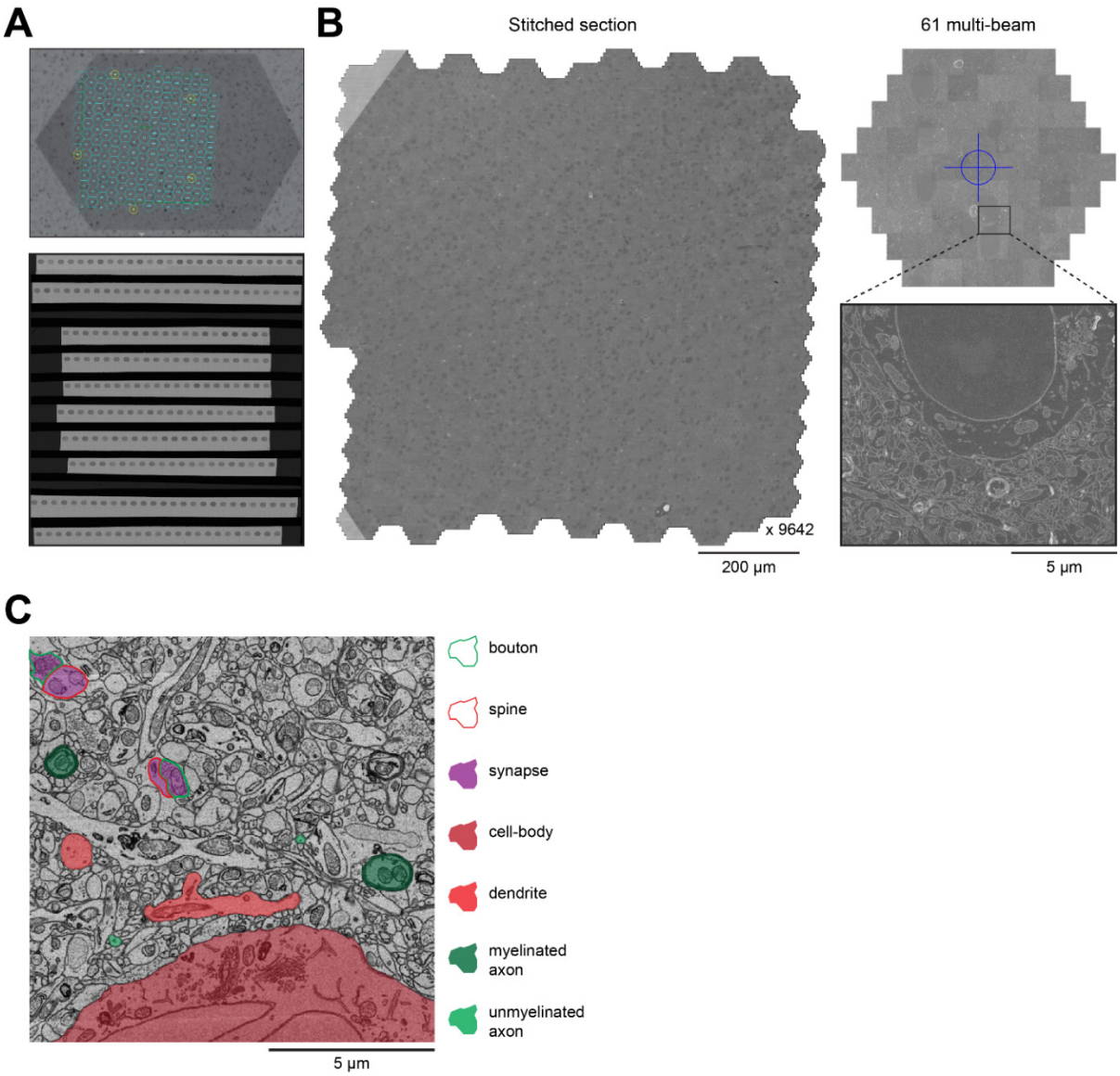

Figure 3.17: **Serial section mSEM of bV1 in the FC-mouse. A|** Silicon wafer mounted with ATUM-sections containing Kapton tape of the FC-mouse (bottom). mSEM scan tiling (cyan) and focus support points (yellow) overlaid on top of single ATUM section. **B|** mSEM FOV from a single ATUM section stitched together (left) from 193 61-EM-beam tiles (right top) translating 11773 single-beam images (bottom right). All images are shown non-inverted as acquired by the mSEM system. **C|** Inverted, contrast-adjusted, stitched and downsampled (1:8) EM image with selective neurite classes indicated color-coded overlays.

As the prior microCT of the biopsy revealed collapsed blood vessels, hinting towards a non-ideal perfusion, I inspected the neuronal ultrastructure for perfusion artifacts. While I did indeed find signs of collapsed blood vessels and infrequent erythrocytes trapped in major vessels, the neuronal ultrastructure was not affected. Specifically, I did not find any indications of membrane breakages, ripped neuropil surrounding vasculature or cell-death. On the contrary, diverse types of neuropil and intracellular organelles were clearly identifiable (Fig. 3.17C) and showed high quality of contrast and ultrastructure. Furthermore, during imaging I continuously manually monitored experimental artifacts and re-imaged all sections that did not pass our quality criteria (see methods). I occasionally encountered both, common mSEM imaging and ATUM related experimental artifacts. Specifically, low contrast of thin sections, mSEM scan glitches, cracking in the underlying carbon coating of the kapton tape, round kapton tape-artifacts, micro folds, warping of the top part of raw images and tissue

scratches from the diamond knife during cutting (see Fig. S2 for representative examples). However, these artifacts were stochastically distributed in the horizontal plane. Therefore, they did not occur at overlapping positions in subsequent sections. Charging artifacts exclusively occurred within big blood vessels. Consequently, ultrastructural continuity between serial sections was not hindered by experimental artifacts.

3.2.6 Alignment of mSEM raw-data in 3D

To enable further in-depth investigations of dense neuronal ultrastructure, I aligned the 2-dimensional mSEM-images into a 3D volume using point-cross correlation with a least squares solver algorithm (see methods for details). Overall, I excluded a single section (#1990) from alignment due to both, low SNR and cross-beam interaction artifacts caused by erroneous centering of the 61 electron beams onto their respective scintillators. I first solved in-plane overlaps within and between 61-beam tiles, then I performed a paired cross-plane alignment and in a final step I ran a global least squares to align all planes into one single coherent 3D volume. I stopped the global least squares optimization after 225000 iterations due to saturation at a final maximum root mean square (RMS) alignment error tolerance of 50.

The final RMS error of the 3D volume was low for both, in-plane (mean RMS error: 1.40) and cross-section alignment (mean RMS error: 3.50). The low RMS error SEM of 0.01 for both in-plane and cross-section alignment consolidated the overall homogeneous distribution of average RMS errors per section (Fig. 3.18A). However, several confined regions showed increased alignment errors. Two regions, approximately spanning sections 3700-4500 and sections 6900-7700, exhibited consecutively increased alignment errors. Visual inspection revealed a minor drift along the ATUM cutting direction over sections, although it retained membrane continuity of neurites in 3D. Furthermore, interspersed outliers with elevated average RMS errors (section of maximum average RMS error: in-plane: 11.14, cross-section: 13.24, section #6385) occurred between sections 5000 and 6500 as well as in the final sections. These outliers matched the sections with image warping artifacts caused by mSEM (see Fig. S2, bottom middle for representative example).

Overall, out of the 112473935 mSEM images 234273 (0.21%) did not meet the alignment quality criteria and were excluded in the final volume transform. In detail, 197960 images were removed due to insufficient point-pairs for solving the affine transformation, 34671 due to aberrant skew components and 1642 due to their lack of cross-layer connection. Visual inspection of the stitched whole-section montages revealed that the majority of excluded images was associated to resin in big blood vessels or at the FOV corners (see Fig. 3.18B, left, bottom left and top left corners for representative example).

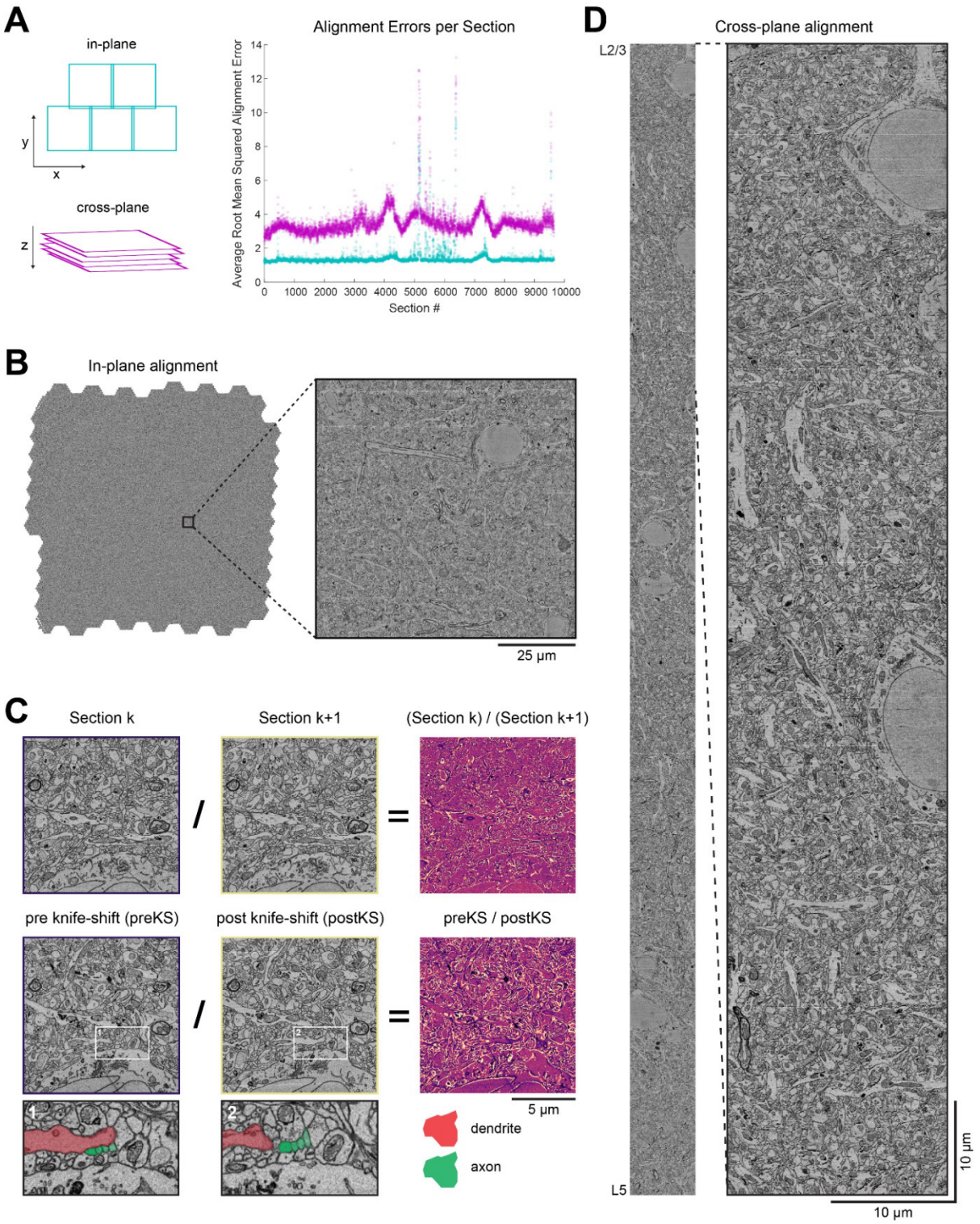

Figure 3.18: **Alignment quality of serial mSEM sections of the FC-mouse in 3D. A|** Final average RMS alignment error per mSEM-section (right) for in-plane (cyan) and cross-plane (magenta) alignment. **B-D|** In-plane pixel-resolution downscaled (1:8) with the exception of the overview in B. **B|** Overview of fully aligned single mSEM-section (left) with higher magnification zoom-in (right). Black square in overview indicates location of the zoom-in. **C|** Cross-section continuity for a sequential ATUM-section pair (top) and the pre and post knife-shift ATUM-section pair (bottom). First image of a section pair (left) was divided by the second section pair (middle) to result in a division image (right). Outline color of the section pairs correspond to the color-code in the division image. White squares in knife-shift image pairs indicate location of the respectively numbered zoom-ins (below, black outline). Zoom-ins are partly pseudo-colored for neurite type (see legend, bottom right). **D|** Re-slice through all

9642 sections of a single block in the middle (x-y) of the mSEM FOV (left) with the x-axis representing the original x-axis and the y-axis representing the z-axis (sections). Zoom-in from the upper third of the dataset shown on the right.

I next visually cross-checked the in-plane alignment for ultrastructural quality. I specifically assessed the impact of warping artifacts on the in-plane stitching and did not find obvious disruption in neurite continuity (see Fig. 3.18B for representative, down-sampled example). Furthermore, I examined the cross-section continuity at the critical knife-shift during the ATUM experiment. While the difference between the adjacent sections was higher compared to non-knife shift sections (Fig. 3.18C), neurites of all sizes were continuously traceable. To ensure the continuity of the smallest neurites, I explicitly assessed the continuity of cortical axons in the regions of largest ultrastructural jumps, e.g. adjacent, horizontally crossing dendrites (see Fig. 3.18C, bottom insets for representative, down-sampled example). However, even in these extreme cases, neurite continuity remained. I further manually inspected the cross-plane alignment through all sections in the middle and corners of the dataset. While I did find minor jumps at the very edges of the dataset, I did not find any in the middle at the approximated x-y location of the two-photon FOV (Fig. 3.18D).

3.3 Summary

In this study, I have developed an experimental pipeline for functional connectomics in the mouse, by combining *in vivo* two-photon calcium imaging with subsequent 3D-EM. I specifically applied this technique on the geniculo-cortical circuit in bV1, to produce a conclusive dataset for dissecting its functional wiring logic.

To overcome previous limitations, I first developed an experimental approach allowing for precise control of GECI expression sparseness in a genetically targeted manner. Creating viral constructs for Cre-recombinase dependent expression of FlpO-recombinase and FlpO-recombinase dependent expression of the GECI jGCaMP7b enabled me to precisely titrate their expression in dLGN cells in *Scnn1a-Tg3-Cre* mice (expressing Cre-recombinase in dLGN and L4 of V1). Specifically, by diluting only the virus coding for FlpO, I was able to achieve a high GECI-virus transduction in a low number of dLGN cells, preventing slow expression. Next, I established deep *in vivo* two-photon calcium imaging of dLGN axons in L4 of bV1. I was able to extract the OD, OS, DS and RFs of dLGN neurons from their boutons in high quality. Further, I showed that boutons of the same axon had highly similar calcium transients in response to visual stimulation. For functional readout of both, the pre-synaptic and postsynaptic neuronal populations in the same prep, I established simultaneous *in vivo* two-photon calcium imaging of dLGN axons and L4 cells in L4 of bV1 using calcium indicators of different color. To be able to dissect the connectome of previously functionally imaged mice with 3D-EM, I developed an experimental protocol for targeted biopsy extraction of the same circuit. Using epifluorescence imaging of DiD-stained blood vessels and microCT, the protocol enabled me to track the position of the functionally imaged circuit by triangulation from vascular landmarks, allowing for a targeted tissue preparation. I was able to stain cylindrical neuronal biopsies of 2 mm in diameter and 500 µm thickness. By partial removal of the superficial layers, I overcame major heavy metal staining gradients in previously functionally imaged samples. Furthermore, I characterized the impact of previously poorly understood experimental parameters such as hexagonal sample shape and tape positioning on the performance of ATUM sectioning. Using these insights, I optimized the ATUM protocol to allow for consistent, single-shot, long-range sectioning of brain tissue.

Finally, I applied the full experimental functional connectomics pipeline to acquire a dataset centered on the geniculo-cortical circuit, with the goal of deciphering its functional connectivity rules. Using deep *in vivo* two-photon calcium imaging, I mapped the OS, DS, OD and RFs of overlapping L4 cells and dLGN axons in thalamo-recipient L4 of bV1. Functional response properties significantly differed between both neuronal populations, with L4 cells having larger, more elongated and Gabor-shaped RFs compared to the small and round RFs of dLGN axons. Cellular RFs were in general more retinotopically confined compared to dLGN axons. Analogously, L4 cells were significantly sharper tuned to orientations and directions of movement in visual space. Interestingly, geniculate axons were strongly dominated by either eye respectively, while most L4 cells in contrast were strongly binocular, suggesting the geniculo-cortical synapse is also the first location of strong ocular convergence. For subsequent re-finding of functionally imaged neurites, I next linked the function of both cells and axons to their respective local morphologies using *in vivo* structural stacks. I extracted a targeted biopsy of the same circuit, stained with heavy metals and prepared it for later EM using microCT for vascular triangulation. I successfully cut the same tissue into ultra-thin sections and collected them on tape using ATUM without a single section loss. I subsequently imaged a volume of 1 x 1 x 0.33 mm^3 with 3D mSEM centered on the two-photon FOV at a voxel size of 4x4x35 nm^3 (see Fig. 3.19 for illustration of the microscopy datasets), resulting in > 0.92 PB of raw data. Lastly, I successfully aligned the >112 million EM images in 3D on the Raven supercomputer of the MPCDF. This will permit the

comprehensive investigation of the functional geniculo-cortical connectome underlying the generation of stimulus selectivity in layer 4 of mouse bV1.

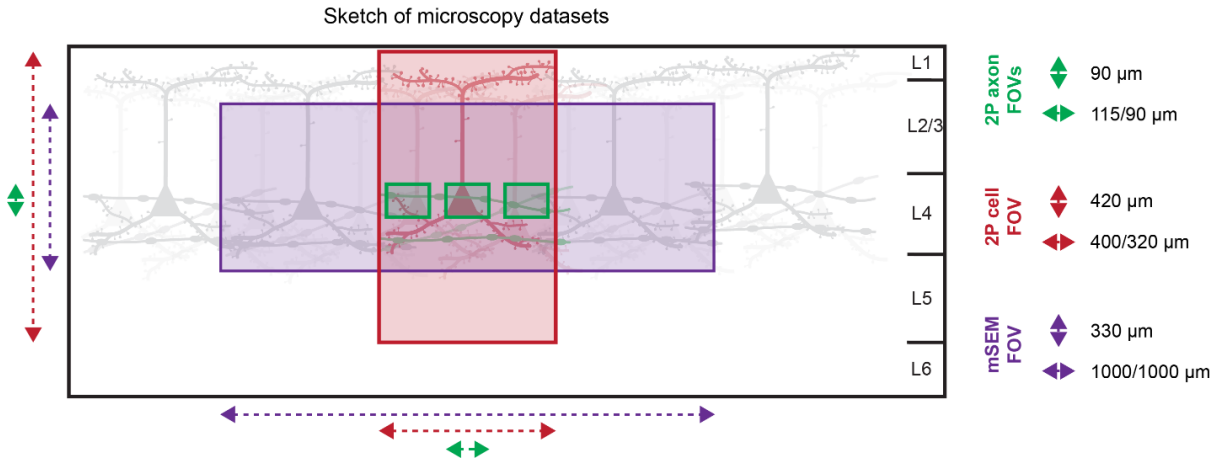

Figure 3.19: **Relative overview of microscopy datasets of the FC-mouse.** Sketch illustrating the relationship between the axonal FOVs (green rectangles) and cellular FOV (red rectangle) from two-photon (2P) microscopy and the mSEM FOV (magenta rectangle). Dimensions (see figure legend, right) not drawn to scale.

4 Discussion

In this thesis, I have successfully established and employed an experimental pipeline for long-range functional connectomics, tailored to enable investigating the functional logic of geniculo-cortical connectivity and its role in the generation of stimulus selectivity in L4 of V1, first proposed by David Hubel and Torsten Wiesel (Hubel and Wiesel, 1962). Although many studies have since been attempted to proof or disprove their feedforward prediction, conclusive evidence is still lacking today. Hence, I acquired a comprehensive dataset aimed to settle this question. In order to maximize the conclusiveness of the results, I combined the functional readout of *in vivo* two-photon microscopy with subsequent high resolution circuit mapping via 3D-EM in a novel pipeline. Before reviewing the quality of the acquired dataset, it is therefore worth first discussing the advantage of this experimental pipeline in the context of alternative approaches to investigate functional connectivity.

4.1 Alternative approaches to functional connectivity?

I believe that the presented experimental pipeline will enable conclusive statements about the functional logic of geniculo-cortical connectivity. While recent technological advances might promise to deliver experimentally less demanding roads to functional connectomics, their experimental shortcomings would – in the context of this circuit – either render them unfeasible or not allow conclusive statements about the underlying functional connectivity rule. In order to understand these intricacies, I will discuss the most popular and promising alternative approaches to testing functional connectivity with regards to investigating geniculo-cortical connectivity with single-cell resolution.

4.1.1 Paired/multi patch-clamp recordings

The most traditional approach to measuring functional connectivity has been patch clamp electrophysiology (Neher and Sakmann, 1976; Sigworth and Neher, 1980) – more specifically whole cell patch clamp recordings (Hamill et al., 1981). By recording from pairs of cells simultaneously, not only monosynaptic connectivity can be assessed, but also the functional strength of the synaptic connection. Specifically, by recording the presynaptic neuron in current-clamp mode and eliciting APs with current injections, connectivity can be determined by recording the postsynaptic response. The connection is considered monosynaptic, if the postsynaptic response occurs up to 2-3 ms after the presynaptic AP. Pre-synaptic strength can be evaluated by eliciting paired or multiple presynaptic APs and investigating the ratio of postsynaptic response amplitudes. This ratio can provide insights into release probability, the docked vesicle pool and recycling speed. However, when using multiple APs it is important to consider using protocols that do not induce synaptic plasticity. Postsynaptic responses can be recorded in both current and voltage clamp. While measuring currents can give indications about the postsynaptic receptor composition, voltage clamp has the advantage of clamping the membrane voltage, circumventing the impact of possible voltage-gated calcium channel responses by synaptic multi-hits in close dendritic proximity (e.g. Schmidt et al. 2017 in medial entorhinal cortex). This can be complemented with measurements of quantal release to investigate the post-synaptic strength by e.g. desynchronizing pre-synaptic vesicle release using Strontium (Goda and Stevens, 1994; Xu-Friedman and Regehr, 2000).

For investigating the geniculo-cortical functional connectivity, paired patch-clamp is, however, experimentally extremely challenging and it suffers from several pitfalls. As both, L4 and dLGN cells lie deep inside the brain, optically guided targeting of the patch pipettes would be near impossible, due to the opacity of brain tissue. While so called “shadow patching” can be performed by looking at the electrophysiological response for guidance, it is extremely challenging and throughput for successfully

patching connected pairs would be extremely low. Alternatively, one could split the interrogation of visual responses and connectivity into a two-step process. Visual responses could be measured *in vivo* using cellular calcium imaging and connectivity of selected geniculo-cortical pairs probed post-hoc via *in vitro* slice electrophysiology using established re-finding protocols (e.g. Weiler et al. 2018; Zhuang et al. 2021). As dLGN axons project in bundles to V1, they cannot reliably be traced to their cell of origin using fluorescence microscopy due to inherent resolution limits. Therefore, one would need to record dLGN activity directly at their cells' somata. As dLGN is optically inaccessible for *in vivo* multiphoton microscopy, one would need to opt for invasive workarounds such as GRIN lenses (Jung et al., 2004; Levene et al., 2004) or cortical aspiration (e.g. Mizrahi et al. 2004), which should be avoided as they likely impact brain physiology. However, more importantly, due to geniculo-cortical anatomy, slicing would not only truncate the dendrites of L4 cells but also very likely sever dLGN axonal projections, as dLGN is located more antero-medial and their axonal projections run as bundles around the hippocampus to reach V1. If no monosynaptic connectivity is detected, one could not directly conclude that the pair was indeed not synaptically connected *in vivo*. Hence, the throughput would be extremely low and results would be near impossible to interpret in the context of the role of geniculo-cortical convergence in generating OS.

4.1.2 In vivo dendritic spine imaging

One alternative approach to circumvent testing connectivity between pre- and postsynaptic neurons is to directly record presynaptic inputs postsynaptically in dendritic spines using *in vivo* calcium imaging. This is enabled by the strong compartmentalization of calcium responses by the thin and high-resistance spine necks (Yuste and Denk, 1995). One major caveat are backpropagating APs (bAPs, Stuart and Sakmann 1994; Schiller et al. 1995), which can propagate into spines and therefore mask incoming inputs. Despite being easily detectable in the dendritic shaft, subtracting bAPs proves difficult even to date (Kerlin et al., 2019). While trials with bAPs can in principle be excluded, it limits experimental investigations to conditions that do not strongly drive postsynaptic activity. Moreover, spine imaging does not provide any information on the input identity that induced the postsynaptic response. In the context of this thesis, dendritic spine imaging alone would therefore not be able to differentiate whether the input was of geniculate, cortical or other origin. Instead, presynaptic identity would need to be tested using chemical or genetic manipulations.

One widely used compound is muscimol (e.g. Chapman et al. 1991; Jaepel et al. 2017), which can be used to inactivate cortex by activating GABA-A receptors to suppress local excitatory activity. Usually applied by superfusion, potential differential biases in cortical silencing by diffusion extent and resulting concentration gradients should be considered. One additional major confounder is GABAergic co-innervation of dendritic spines (Tamás et al., 1997; Somogyi et al., 1998; Serwanski et al., 2006; Chen et al., 2012). Chronic GABAergic activation could therefore modulate geniculo-cortical transmission and mask the functional dLGN inputs. Muscimol would hence only provide a distorted readout of functional connectivity. More recently, optogenetic approaches have gained traction, due to their precise genetic targeting and temporal control. By expressing light-sensitive proteins, neuronal activity can be tightly controlled by either activation (see e.g. channelrhodopsin (Nagel et al., 2002, 2003; Boyden et al., 2005), Chronos or ChrimsonR (Klapoetke et al., 2014)) or suppression (see e.g. halorhodopsin (Oesterhelt et al., 1985; Kolbe et al., 2000; Han and Boyden, 2007; Zhang et al., 2007)) or ArchT (Ihara et al., 1999; Chow et al., 2010)). While optogenetically exciting inhibitory neurons could influence geniculate transmission in co-innervated synapses similar to muscimol, directly inhibiting excitation would be more promising. Expressing inhibitory opsins in excitatory

neurons in V1 would suppress cortical input, which in turn would result in mainly LGN-induced spine responses. Furthermore, bAPs would likely be suppressed in the imaged cell of interest, removing one of the major confounders of functional dendritic spine imaging. However, the scattering brain tissue would require high light intensities to sufficiently suppress activity throughout all cortical layers. Furthermore, cortical spiking needs to be suppressed during the entirety of visual stimulation, which would likely overheat the brain tissue and impact brain physiology. Moreover, integrating such a configuration would require clean spectral separation from two-photon excitation and detection, which is technically challenging. Instead, inhibitory step-function opsins (e.g. Berndt et al. 2016; Wietek et al. 2017) or chemogenetic methods such as Designer Receptors Exclusively Activated by Designer Drugs (Armbruster et al., 2007) can circumvent these issues. Excluding expression in dendritic spines by adding localization sequences to e.g. the soma or axon initial segment could prevent a direct effect on input signals by selectively suppressing the cell's output and in principle bAPs.

However, entire dendritic arbors of cells would need to be imaged. To ensure good SNR and avoid neuropil contamination, cells should only be labeled very sparsely, ideally with non-overlapping dendrites, further reducing throughput. While custom optics and 3D ROI scanning could improve imaging speed (Kerlin et al., 2019), building such a microscope requires extensive monetary and time investment as well as further optimization to be viable for imaging in L4. Nonetheless, even with such optical tools at hand, mapping the entire basal dendrites of few L4 cells with the full battery of visual stimuli would still require chronic imaging. The resulting functional connectome would therefore be integrated over time. Statements about how inputs relate to the cellular output would therefore be difficult to make, as the visual system is highly plastic (e.g. Rose et al. 2016; Jaepel et al. 2017) and neuronal representations drift over time (Montijn et al. 2016; Marks and Goard 2021; Deitch et al. 2021; but see Rose et al. 2016; Pérez-Ortega et al. 2021). Furthermore, visual cortex is not the only presynaptically connected brain area to bV1. Ensuring the silencing of all non-geniculate inputs is consequently nearly impossible. Lastly, functional manipulations of entire brain areas have been shown to result in acute functional off-target effects (Otchy et al., 2015; Hong et al., 2018; Andrei et al., 2021), which in turn might have unpredictable physiological influences on the neurons of interest, making the results challenging to interpret. Therefore, combining dendritic spine imaging with complementary approaches to verify connectivity would be necessary to make more conclusive statements about the role of functional geniculo-cortical convergence.

4.1.3 In vivo dendritic spine imaging and 3D-EM

One possibility could be to combine functional dendritic spine imaging with a high-resolution readout of neuronal structure and connectivity, to verify which spines have geniculate input. However, light microscopy in combination with the required selected neuronal labeling is not able to provide the resolution to assess connectivity between cells via structural overlap, as only about half of axons within dendritic reach form synapses (Mishchenko et al., 2010). Instead, 3D-EM can provide the necessary resolution and dense neuronal labeling. Synapses can be reliably detected (see e.g. Kreshuk et al. 2014; Dorkenwald et al. 2017; Staffler et al. 2017) and thalamic axons can be distinguished from cortico-cortical axons by their diameter, ultrastructural morphology and subcellular targeting (Motta et al., 2019) without targeted labeling. Functionally imaged L4 cells can be re-found in 3D-EM by either, subcellularly targeted electron-dense labeling (Shu et al., 2011; Martell et al., 2012; Atasoy et al., 2014; Lam et al., 2015; Joesch et al., 2016), or by morphology-based matching in combination with registration from labeled vascular landmarks (Bock et al., 2011; Briggman et al., 2011; Lee et al., 2016b; MICrONS Consortium et al., 2021).

To maximize the functional connectome, the entire basal dendritic tree of each functionally imaged L4 cell would need to be imaged and reconstructed with 3D-EM. To confirm the identity of dLGN innervated spines, thalamo-cortical axons could be ultrastructurally distinguished from cortico-cortical axons (Motta et al., 2019). Next, thalamic axons of dorsolateral geniculate origin can be distinguished from neighboring thalamic nuclei such as LP by their axonal tree morphology and laminar projection pattern (Harris and Shepherd, 2015). However, due to the requirement for sparse L4 cell labeling *in vivo*, multiple datasets across mice would have to be acquired. Such a pipeline is highly non-trivial and both experimentally and analytically extensive. Additionally, relating the functional responses acquired over multiple chronic imaging sessions to the snapshot post-hoc 3D-EM connectome would be complicated, as connectivity could rewire in between sessions due to e.g. plasticity (Rose et al. 2016; Jaepel et al. 2017; for representational drifts see: Montijn et al. 2016; Marks and Goard 2021; Deitch et al. 2021). Lastly, interpreting functional responses from multi-innervated spines would remain a big challenge, although their input origin could likely be reconstructed in 3D-EM. Taken together, while *in vivo* dendritic spine calcium imaging provides an exciting tool to read out neuronal input postsynaptically, it does not allow for the throughput, connectional specificity or statistical power crucial for the in-depth investigation of the functional logic of geniculo-cortical convergence.

4.1.4 In vivo two-photon microscopy and GRASPs

One group of tools for genetically encoded circuit tracing are fluorescent proximity markers, which are based on split-fluorophore technology. As the synaptic cleft is only very slim, this technology was adapted to express each split part selectively in genetically specified pre- and postsynaptic neurons, synaptically localized on the membrane surface. Hence, if two cells are synaptically connected, the complementary protein fragments should reconstitute and form a functional fluorophore, which can be detected using fluorescent microscopy. Specifically, GFP Reconstitution Across Synaptic Partners (GRASP; Feinberg et al. 2008), originally developed in *C.Elegans* and subsequently adapted to *Drosophila* (Gordon and Scott, 2009; Macpherson et al., 2015) has more recently been modified for mammalian use (mGRASP; Kim et al. 2012; Choi et al. 2018). Therefore, mGRASP could be combined with a functional readout from two-photon microscopy, such as dendritic spine imaging. By densely expressing pre-mGRASP in dLGN neurons, and post-mGRASP sparsely in L4 cells, dLGN-contacted spines could be identified. However, this method would not inform about potentially multi-innervated spines. Measured postsynaptic spine responses might therefore already represent modulated or processed information rather than the actual geniculate input.

Instead, the much cleaner option would be to extract functional response properties from presynaptic dLGN axons directly. In practice, one could therefore combine mGRASP technology with *in vivo* calcium imaging of sparse dLGN axons and L4 cells, similar to this thesis project. To be able to reliably assign mGRASP puncta, postsynaptic L4 cell expression would also require sparse expression. Hence, datasets from multiple animals would be needed to provide a representative sample size.

Although mGRASPs would significantly speed up the readout of geniculo-cortical connectivity in comparison to 3D-EM, they suffers from several confounders. As viral expression needs to ramp up over several weeks to reach detectable levels, the mGRASP-labeled connectome represents a maximum connectivity projection over time, rather than a snapshot of the connectivity at the time point of functional readout. Consequently, neuronal function would not be directly related to its underlying connectivity, due to the plasticity in the visual system. Furthermore, mGRASPs are primarily

proximity markers. Although synaptic localization can exclude most labeling via random touches, bouton-spine touches outnumber the actual amount of synapses in hippocampus by a factor of two (Mishchenko et al., 2010). While mGRASP expression does not seem to induce any obvious morphological artifacts (Kim et al., 2012), their impact on neuronal physiology remains to be determined. Structurally, long-term effects on connectivity by physically anchoring pre- and postsynaptic membranes remains a concern, limiting the value and interpretability of the extracted functional connectome.

4.1.5 In vivo two-photon microscopy and monosynaptic rabies virus tracing

The second category of genetically encoded circuit mapping tools are transsynaptic retrograde rabies viruses. When first adapted for circuit mapping (Ugolini, 1995), initial rabies variants were polysynaptic (Ugolini, 1995; Card and Enquist, 2001), as they carried their entire genome retrogradely, enabling them to jump monosynaptically repeatedly. The identification of the rabies glycoprotein as the driver for synaptic traversal and assembly of virus particles more than a decade later allowed limiting rabies tracing monosynaptically to a single step (Wickersham et al., 2007b). By deleting the glycoprotein coding sequence from the pseudo rabies virus genome, and instead supplying it in a separate vector, rabies could only traverse monosynaptically from the initially transduced starter cells to their presynaptic partners. Furthermore, the envelope glycoprotein was exchanged with that of the avian sarcoma and leucosis virus (EnvA; Wickersham et al. 2007a) instead. As their respective receptor does not have a homolog in mammalian cells (Bates et al., 1993; Young et al., 1993; Federspiel et al., 1994), the required ectopic expression allowed for a targeted genetic pre-selection of transduceable starter cells, preventing direct axonal uptake of free rabies virus. Cloning of fluorescent structural (e.g. Wickersham et al. 2007b) or functional markers (Granstedt et al., 2009; Osakada et al., 2011; Wertz et al., 2015; Rossi et al., 2020; Tang et al., 2020) into the rabies genome allowed for visualization of presynaptic partners.

To investigate geniculo-cortical functional convergence, L4 cells could be sparsely transduced (i.e., ideally a single cell) with a rabies vector coding for Cre-recombinase- or FlpO-recombinase-dependent expression of a calcium indicator. By expressing the respective recombinase specifically in dLGN, only presynaptic geniculate neurons would be labeled, negating the necessity for post-hoc identification. The L4 starter cell could be labeled in a rabies-independent manner and functionally mapped by a spectrally shifted calcium indicator in respect to the dLGN GECI. Presynaptic activity could be accessed in the dLGN directly using GRIN lenses (Jung et al., 2004; Levene et al., 2004) or cortical aspiration (e.g. Mizrahi et al. 2004). However, as discussed above, these techniques are highly invasive and are likely to disrupt brain physiology. Instead, activity of dLGN neurons can be recorded at their projections in L4 of V1 using deep in vivo axon imaging as established in this manuscript.

However, due to the requirement for sparse L4 labeling, throughput is a major challenge, as many postsynaptic simple cells with diverse features should be analyzed to provide a representative functional connectivity. Furthermore, the resulting connectome would be challenging to interpret due to inherent presynaptic subsampling of rabies tracing (Marshel et al. 2010; Miyamichi et al. 2011; Rancz et al. 2011; for review see Ginger et al. 2013). Whether this is caused by an underlying systematic bias, such as preferred traversal of synaptic subtypes, or completely random, remains to be determined. While known systematic biases can be accounted for in the analysis of the functional logic of connectomes, unknown biases cannot. Moreover, similar to GRASPs, the rabies virus needs several weeks of expression. Therefore, presynaptic labeling represents a cumulated connectome

over time instead of a snapshot at the timepoint of functional imaging, which makes the impact of geniculo-cortical connectivity on the generation of cortical OS challenging to interpret. Lastly, despite significant improvements of the recently developed N2c subtype (Reardon et al., 2016), toxicity of both, cell morphology (Wickersham et al., 2007a; Arenkiel et al., 2011) and physiology (Granstedt et al., 2009) could alter the connectivity and visual properties, further complicating the interpretation of the underlying functional connectivity logic.

Taken together, the advent and recent improvement of genetic circuit tracing tools add to an ever increasing palette of techniques for investigating neuronal circuits in bulk. Specifically, they can provide excellent screenings of interconnected brain areas to guide further studies. However, several drawbacks render them inconclusive for investigations of connectivity with single cell resolution, especially in the context of assessing the functional connectivity rules of geniculo-cortical convergence.

4.1.6 In vivo two-photon microscopy and 3D-EM

Altogether, despite the vast palette of existing experimental tools to investigate neuronal circuits, the majority of tools cannot provide the level of detail necessary for single-cell resolution functional connectomics. Particularly for this thesis' biological question, a more detailed experimental pipeline is key to be able to make conclusive statements about the functional logic of geniculo-cortical convergence.

To achieve the required level of detail, I instead opted to develop a novel experimental long-range functional connectomics pipeline, combining the two-photon microscope-mediated functional readout of both, L4 cells and dLGN axons with subsequent high-resolution ultrastructural reconstruction with 3D-EM. Mapping dLGN function in their axonal projections in L4 circumvents the issues related with inferring presynaptic activity from dendritic spines. Most prominently, it reduces the concern of reading out already pre-processed or modulated presynaptic signals by e.g. spine co-innervation. Owing to recently developed high baseline GECIs, such as jGCaMP7b (Dana et al., 2019), enabling a simultaneous readout of both neurite function and structure with the same fluorophore, both dLGN axons and L4 cells can be read out from spectrally separated labels in the same tissue. One major consideration, however, was the density of dLGN axons in L4. To avoid neuropil contamination of functional signals and enable crisp structural separation of axons for subsequent re-finding in EM, the axon sparsity needs to be optimally titrated. To maximize the functional connectome, dLGN axon expression should only be as sparse as functionally and structurally necessary, and L4 cells in contrast, labeled densely in bulk. Although dense functional imaging of dLGN somata would in principle be possible with GRIN lenses (Jung et al., 2004; Levene et al., 2004) or cortex aspiration (e.g. Mizrahi et al. 2004), extracting the connectome using 3D-EM would not be possible with the current technological *status quo*. Due to the dense dLGN axon bundles wrapping around the hippocampus to reach cortex, following their structure with fluorescence microscopy is not possible due to limitations in resolution. Hence, to compensate, the 3D-EM volume would need to include L4, dLGN and the entirety of dLGN axonal projections, exceeding the capabilities of even the most recent technological advancements in 3D-EM. Therefore, the combination of dLGN axon and L4 imaging in cortex presents the most promising approach. 3D-EM, albeit extremely time consuming both experimentally and analytically, allows for gold-standard synapse detection. One major upside is the recently described possibility of inferring synaptic strength from ultrastructural synaptic components (Holler et al., 2021), adding another important dimension to the analysis and interpretation of the functional connectome.

Moreover, the potential for fully dense reconstruction of the neuronal tissue, not only eliminates any biases in synapse detection but also enables the precise quantification of any potential bias in functional labeling in the context of all dLGN axons. Adding to that, analysis of geniculo-cortical convergence patterns are not merely limited to the functionally labeled axons, but can be augmented by convergence patterns of unlabeled thalamo-cortical axons and inter L4 cell connectivity, greatly enhancing the statistical power of the functional connectome. Lastly, owing to the superior resolution, patterns in ultrastructural features can be investigated, such as dendritic input clustering or spine co-innervation.

In conclusion, long-range functional connectomics combining two-photon microscopy with 3D-EM based connectomics bears the most promise to investigate the geniculo-cortical convergence rule in the most comprehensive and conclusive manner at last, almost 60 years after the initial proposal by David Hubel and Torsten Wiesel (Hubel and Wiesel, 1962). As presented above (see introduction section "1.4.4 Need for a comprehensive dataset"), despite the finding being reproduced in almost every neuroscience textbook and almost 60 years of follow up research, a conclusive proof of this claim is still lacking. I am convinced that the experimental developments and the acquired dataset presented in this thesis will provide conclusive evidence on the functional logic of this circuit. Although the dataset is not yet analyzed in full, the experimental pipeline, acquired and currently analyzed data as well as future avenues will be discussed in the following.

4.2 Towards a functional connectome underlying stimulus selectivity in bV1

4.2.1 Choice of GECIs

Investigating functional response properties via calcium imaging from somata is mostly considered routine, even in deep cortical layers. In contrast, axon imaging has mostly been restricted to the superficial layers due to SNR, especially for mapping spatial RFs (Roth et al., 2016; Jaepel et al., 2017). Functional dLGN axon imaging in L4 of V1 has been mainly performed using presentation of moving gratings (Sun et al., 2016; Broussard et al., 2018; Bauer et al., 2021), a stimulus that is optimized for driving neuronal activity in visual areas. In order to map spatial RFs, traditionally, sparse noise stimulation is used. While it is designed to avoid any local oriented patterns, allowing for precise mapping of the spatial structure of RFs, the small square patches elicit less reliable and smaller visual responses, as they often only partially cover RFs at a time. Moreover, axonal morphology needs to be reconstructable for at least 33 µm per individual axon to allow reliable re-identification of labeled axons in 3D-EM (Drawitsch et al., 2018). Therefore, the quality of axon imaging is imperative for driving the choice of fluorophore for labeling of dLGN and L4 in bV1.

Today's most efficient GECIs exist in two spectral variants: the original green GCaMPs and red-shifted variants such as jGCaMP1a or jRGECO1a. Although jGCaMP1a is closer to the well established GCaMPs, jRGECO1a provides higher SNR, faster temporal kinetics and less photobleaching (Dana et al., 2016). However, which of the variants would result in the best functional readout in cortical L4 was unclear. Specifically, due to the imaging depth, I set out to test whether the advantages in SNR by state of the art green GECIs (Dana et al., 2016, 2019) would be negated by the increased scattering of their shorter excitation and emission wavelengths in comparison to their red-shifted counterparts. I found that, *in vivo*, both GCaMP6m and jGCaMP7b yielded better functional responses in comparison to the red-shifted jRGECO1a (Fig. 3.2). Although the SNR in response to visual stimulation was good for the red-shifted variant, the overall fluorescence amplitude was very low. This strongly impeded initial investigation of expression and defining a FOV for functional imaging, as axonal structures were not

obviously visible, but instead manifested themselves as increased fluorescence noise during two-photon microscopy. The low overall fluorescence level was also challenging for frame-registration of functional imaging experiments, rendering the interpretation of calcium transients non-trivial. Overall, the reliability of achieving good quality axon imaging FOVs was low. Morphologically, exclusively the boutons of dLGN axons were visible even during the best imaging FOVs (Fig. 3.2A), making it near impossible to effectively trace axonal trajectories. In stark contrast, their green counterparts showed much improved fluorescence SNR, both functionally and structurally. This was especially true for the 7th generation high-baseline variant jGCaMP7b (Fig. 3.2B). The increased fluorescence in the calcium-unbound state greatly facilitated FOV screening and enabled easy morphological mapping of axonal arbors. Despite the high baseline-fluorescence, SNR compared to that of the calcium-bound state was high and consistently showed the highest amplitudes out of all three indicators. In summary, jGCaMP7b provided the best SNR both structurally and functionally for imaging dLGN axons in L4 of bV1, consequently dictating the labeling of L4 cells with jRGECO1a.

4.2.2 A system to titrate transduction sparsity in genetically modified, Cre-recombinase expressing mice

To maximize extraction quality, both, functional responses and axonal structure, it is crucial to control the transduction sparsity. As discussed above, to allow for reliable re-finding of labeled dLGN axons in EM (Drawitsch et al., 2018), being able to map their trajectories *in vivo* is indispensable. Due to the dense arborization of dLGN axons in L4 of V1 (Antonini et al., 1999), bulk labeling of retinotopically adjacent geniculate neurons would result in such high axonal density that individual axons would be indistinguishable by two-photon microscopy. Hence, to enable tracing of individual axons, expression needs to be sparse to reduce density and axonal overlap. Analogously, to obtain crisp measurements of functional response properties of geniculate axons, overlap of multiple boutons within the two-photon point-spead-function should be avoided. As bouton-activity is extracted by manual ROI selection, overlapping boutons would result in mixing of the activity of two axons. Further, fluorescent contamination emanating from the surrounding neuropil would increase masking, deteriorating the signal extraction. One workaround could be to image at the edge of the axonal bolus in L4, where axonal density will be sufficiently sparse. To ensure overlap with postsynaptically labeled L4 cells in bV1, this would require a retinotopically offset transduction of dLGN neurons. While this would provide a viable solution for the interrogation of morphology, it would miss the goal of investigating functional connectivity. In particular, due to the added spatial spread of L4 dendrites as well as retinotopic arrangement, the probability of connectivity would be low. Even if connected, the presynaptic dLGN neurons would be unlikely to have a large impact on driving L4 cell features due to the retinotopic displacement. This would also result in a strong deterioration of the power of the functional connectome for inferring a causal link between the emergence of stimulus selectivity and their geniculate inputs. Therefore, to avoid introducing any biases to the functional connectome extraction, sparse labeling of dLGN neurons is key for a retinotopically aligned circuit interrogation.

Ideally, sparsening would only affect the number of transduced neurons while at the same time ensuring strong expression. Hence, diluting the titer of the GECI expressing viral vectors for injection would not be effective as this would likely label the same number of cells, however with lower copy numbers, leading to weak expression levels that need to ramp up over a longer time period. This issue can be overcome by genetically-conditional expression of multiple inter-dependent constructs. The most widely employed system in mammals is the Cre-lox recombination system (Sternberg and Hamilton, 1981; Sauer and Henderson, 1988; Ventura et al., 2004). By e.g. inverting the genetic

sequence in the multiple cloning site coding for the GECI, the open reading frame is oriented opposing the reading direction, therefore not forming a sensible genomic strand. However, by flanking it with Cre-recombinase recognition sites, the insert will be inverted in the presence of Cre-recombinase and the GECI will be expressed. By transducing the same neurons with a second plasmid vector coding for Cre-recombinase, expression can be regulated. Specifically, by injecting the Cre-recombinase plasmid in low concentration and the GECI in high concentration, many neurons will be transduced with high copy numbers of the GECI plasmid, but only a few with the plasmid coding for Cre-recombinase. Consequently, only the few neurons, that have the Cre-recombinase plasmid will express the protein and subsequently be able to invert the GECI-fragment into the reading direction for expression. In other words, only a few neurons will express the GECI, but the few that do, will express the fluorophore at high levels.

One additional factor needs to be taken into consideration regarding the investigation of geniculo-cortical convergence: cell-specific labeling. For the interpretation of the functional connectome, it is critical to be certain about both, the dLGN axon and L4 cell origin. Transducing dLGN neurons and bV1 L4 cells in wild-type mice by viral injections leads to significant off-target labeling: cortical injections caused strong labeling of neurons in adjacent layers. Due to the depth of dLGN, geniculate injections caused significant labeling along the entire injection tract, including hippocampus, primary somatosensory cortex and higher visual areas. This is especially detrimental for axons, as their origin cannot be verified by tracing. Therefore, to abolish off-target labeling, I used the genetically modified mouse strain *Scnn1a-Tg3-Cre*, which expresses Cre-recombinase in specifically L4 of V1 and dLGN. However, owing to the intrinsic expression of Cre-recombinase, here Cre cannot be used for expression sparsening anymore. To overcome this limitation, I developed a sparsening strategy involving a separate recombinase: FlpO (Raymond and Soriano, 2007). Designing FlpO-recombinase expression in a Cre-dependent and jGCaMP7b expression in FlpO-dependent manner, allowed me to use FlpO for titrating sparseness of expression while retaining genetically specific targeting of the Cre-expressing mouseline (Bauer et al., 2021). To verify the genetic expression control, I tested the cloned DNA plasmids in organotypic hippocampal slice cultures using biolistic transfection (Fig. 3.3). Both constructs were highly selective with only minimal expression leaking (Fig. 3.3D,H). These stochastic breakthrough expression events can likely be attributed to impurities in the biolistic delivery system. While the cartridge barrel, barrel liner and mesh were sterilized prior to biolistic transfection, the Genegun barrel cannot be disassembled and sterilized. Therefore, gold-particles associated with various DNA fragments can accumulate over time and be released in subsequent shots. As Cre-recombinase containing plasmids are frequently used in experiments, breakthough expression in subsequent Cre-dependent experiments can easily be induced. Once packaged into AAVs, I employed the sparsening system *in vivo*. As expected, the tool allowed for precise titration of expression sparsity in dLGN. I next optimized the expression density to yield a high quality extraction of axonal morphologies using *in vivo* two-photon microscopy.

4.2.3 Intra-axonal bouton response similarity

For the final fine-tuning, I assessed the quality of functional responses of dLGN boutons in L4 of bV1. Geniculate bouton calcium transients in response to both moving gratings (Fig. 3.6-3.7) and sparse noise stimulation (Fig. 3.4-3.5, 3.9-3.10) allowed for high-quality extraction of OD, orientation tuning, direction tuning and spatial RFs. To ensure the quality of axon imaging, I tested whether boutons of the same axon showed similar tuning curves. As bouton calcium dynamics, especially within the same arbor, are driven by the same APs, I expected boutons from the same axon to show almost mirroring

tuning curves. Indeed, I found that dLGN boutons from the same axons exhibited analogous tuning to OD (Fig. 3.4A), orientation, direction and RFs (Fig. 3.4B). As orientation and direction tuning in dLGN neurons is overall weak (Roth et al. 2016; Sun et al. 2016; Jaepel et al. 2017; Fig. 3.6E, 3.7D), moving gratings elicit dense response patterns and are consequently not a good measure to assess similarity of response transients. Furthermore, moving gratings are such a strong driver of VR neurons that trial failures are seldom detected (see Fig. 3.6E for example transients). Hence, during moving grating stimulation, similarity can arise based on spuriously similar response tuning across the population, leading to frequent false-positives. In contrast, RFs are scattered throughout the population of dLGN boutons (see Fig. 3.9H, 3.10D, 3.11B), even taken into consideration the retinotopically biased readout of the limited FOV in L4 of bV1. Therefore, similarity of RFs between neurons is less likely. Adding to that, sparse noise stimulation drives activity with a lot less potency, resulting in variable amplitudes between trials and frequent trial response failures. Taken together, these features make sparse noise stimulation an excellent readout to assess bouton similarity of dLGN axons. Average RF transients revealed a striking similarity between boutons of the same axon (see Fig. 3.4B, top for representative example). This similarity became even more apparent when investigating single trials, specifically trial failures at significant RF patch locations. I consistently observed trial failures across all boutons of the same axon (see Fig. 3.4B, bottom for representative example), highlighting the high quality of the optimized deep axon imaging. Interestingly, for successful trials – although each bouton of the same axon consistently responded – amplitudes occasionally differed. While some differences might be caused by individual differences in neuropil subtraction and optical access, it has been previously shown that neighboring boutons of the same axons show surprising differences in release probabilities and response amplitudes (Rose et al., 2013; Dürst et al., 2019). To exclude that response similarity of nearby boutons is caused by spatial bleedthrough of calcium imaging, I investigated the RF responses of spatially close, in-plane boutons from a morphologically different axon of the same ocular preference. Response transients were highly dissimilar (see Fig. 3.4B-C), despite their immediate spatial proximity, which excludes spatial bleedthrough as a reason for the similarity of boutons in the same axon. These results further underscore the feasibility of deep dLGN axon imaging in L4 of bV1, providing the functional data quality required for a comprehensive assessment of the functional connectivity logic of geniculo-cortical convergence.

4.2.4 Extraction of functional responses in vivo in co-labeled dLGN axons and L4 cells in bV1

Towards the goal of assessing functional response transients of dLGN axons and L4 cells in co-labeled conditions, I first investigated fluorophore crosstalk. Specifically, I labeled dLGN neurons sparsely with jGCaMP7b and L4 cells densely with jRGECO1a in *Scnn1a-Tg3-Cre* mice. Although both fluorophores are spectrally shifted relative to each other, the tails of their absorption and emission spectra overlap (Dana et al., 2016, 2019). Therefore, multiple combinations of cross-talk could arise, such as co-excitation, co-emission and spectral crosstalk in the detection path of the two-photon microscopy. As expected (Dana et al., 2019) imaging jRGECO1a at 1040 nm did not excite jGCaMP7b, resulting in no detectable axonal signals in either the red or green channel, also in jGCaMP7b-only labeled mice. In contrast, imaging jGCaMP7b at 940 nm did also result in significant excitation and emission of the red-shifted fluorophore jRGECO1a, in line with the fluorophore's excitation and emission spectra (Dana et al., 2016). Nonetheless, the band-pass filters nicely separated the jGCaMP7b and jRGECO1a emissions into their respective detection channels. At very high excitation powers (beyond 65 mW), very faint jRGECO1a fluorescence noise could be detected in the green channel. However, the jRGECO1a signal in both channels did not show any detectable changes in fluorescence in response to visual

stimulation. This is in line with jRGECO1a's action cross section (Dana et al., 2016), where excitation at 940 nm is adjacent to the GECI's isosbestic point, rendering its emission near calcium-independent. Due to the excellent SNR and fluorescence intensity of jGCaMP7b at 940 nm, functional imaging was performed at a maximum of 50 mW in L4 to prevent ultrastructural damage. Taken together, spectral crosstalk between channels and fluorophores was negligible.

Nonetheless, in a final verification step, I investigated whether the quality of the extraction of functional response transients of dLGN axons and L4 cells could be maintained in co-labeled conditions. As expected, due to its potency in driving visual stimulation, moving gratings elicited high quality calcium transients in both, dLGN axons and L4 cells. As discussed above, more critical are the RF response transients during the much less potent sparse noise stimulation. Analogous to moving grating stimulation, I was able to consistently record high SNR RF calcium transients (Fig. 3.5). Significant RFs were reliably extracted with high precision by the analysis pipeline, and with RF features matching expectations (see section "4.2.6 Receptive Fields of dLGN axons and cells in L4 of bV1" for more in depth discussion) and uni-labeled experimental results. In summary, imaging of co-labeled dLGN axons with jGCaMP7b and L4 cells with jRGECO1a allowed for efficient, high-quality extraction of visual response properties in a spectrally separated manner. With this optimized labeling, imaging and extraction pipeline at hand, I moved forward and recorded from multiple mice to investigate the geniculo-cortical convergence using functional connectomics. The quality of the obtained datasets are discussed in detail in the following exemplified on the data obtained from one mouse that was selected for the full functional connectomics experimental pipeline.

4.2.5 Ocular dominance, orientation and direction tuning of dLGN axons and cells in L4 of bV1

For functional connectomics, I acquired 1 cellular and 3 dLGN axonal FOVs containing 4 successive piezo-planes each in L4 of mouse bV1. To map orientation tuning, direction tuning and OD, I presented moving gratings restricted to the binocular visual field to each eye in pseudorandom fashion and recorded their calcium response transients (Fig. 3.6-3.7). The response transients of both, jRGECO1a labeled cells and jGCaMP7b labeled dLGN axons in L4 were crisp (Fig. 3.6B,E) and SNR was consistently high throughout each neuronal population (Fig. 3.6-3.7), which displays the potency of the stimulus in driving visual responses. The high quality of imaging is clearly illustrated by the pixelmaps. Here, OD, PO and PD are calculated on a pixel-wise basis and pseudo-colored, and the consistent coloring of each pixel per cell and axon shows the high SNR and consistency of the deep *in vivo* imaging protocol developed in this work.

As expected, L4 cells showed significantly sharper tuning and hence higher selectivity to direction of movement and orientation in visual space compared to dLGN axons (Fig. 3.6-3.7). This matches not only the results of previous *in vivo* calcium imaging studies in mice (Kondo et al., 2016; Sun et al., 2016; Huh et al., 2020), but also the prediction about geniculo-cortical convergence by David Hubel and Torsten Wiesel (Hubel and Wiesel, 1962). Interestingly, both boutons and cells exhibited overall decreased OS and DS selectivity during ipsilateral compared to contralateral eye stimulation (Fig. 3.8D-G). Furthermore, PO and PD of L4 cells were cortically arranged in the previously described salt-and-pepper fashion (Fig. 3.6C; Dräger 1975; Antonini et al. 1999; Schuett et al. 2002; Ohki et al. 2005; Mrsic-Flogel et al. 2007; Ringach et al. 2016; Kondo et al. 2016; Maruoka et al. 2017). However, OSIs and DSIs were overall lower compared to previous reports for both, dLGN axons (Roth et al. 2016; Sun et al. 2016; Kondo et al. 2016; Durand et al. 2016; Huh et al. 2020; but see Scholl et al. 2013; Jaepel et al. 2017) and L4 cells (Niell and Stryker, 2008; Kondo et al., 2016; Sun et al., 2016; de Vries et al., 2020).

Although intuitively, for L4 cell imaging it could be argued that this discrepancy is caused by the inferior SNR of jRGECO1a (Dana et al., 2016), this does not apply to dLGN axons, which were imaged with the much improved jGCaMP7b (Dana et al., 2019) in comparison to said studies. Furthermore, despite my comparably conservative responsiveness criterion, the high fraction of VR neurons in L4 of over 90%, further highlights the SNR provided by jRGECO1a in L4 cells. The differences in responsiveness criteria and the non-linear affinities of calcium indicators used, such as GCaMP6s (Kondo et al., 2016; Sun et al., 2016; Huh et al., 2020), GCaMP6m (Roth et al., 2016; Jaepel et al., 2017), or GCaMP6f (Roth et al., 2016; de Vries et al., 2020; Huh et al., 2020) can affect tuning curves.

However, the choice of functional marker is only one of many experimental and analytical differences between these studies. Two studies (Sun et al., 2016; Huh et al., 2020) calculated OS and DS based on a fitted double-Gaussian, instead of the raw tuning curves. This function imposes pre-assumed equidistant bimodality onto the tuning curves, which can readily lead to an overestimation of tuning selectivity.

Furthermore, mice were either imaged under isofluorane anesthesia (Kondo et al., 2016; Roth et al., 2016), fentanyl based anesthesia (Jaepel et al., 2017) or awake (Sun et al., 2016; de Vries et al., 2020; Huh et al., 2020). Although response amplitudes are higher under awake conditions (see e.g. Niell and Stryker 2008; Lee et al. 2014; Reimer et al. 2014; Erisken et al. 2014; Vinck et al. 2015; Durand et al. 2016), it remains hard to control for how much they are purely visually driven, due to for example responses caused by general movement (Stringer and Pachitariu, 2019). Furthermore, mice move their eyes, which changes the representation of the visual stimuli on the retina and consequently the RF position of the imaged neurons. As visual stimulus selectivity is thought to be a RF property (Hubel and Wiesel, 1959, 1962), relating the recorded tuning curves to the stimulus is hence challenging. In case of anesthesia, it has been shown that anesthetics can differentially impact neuronal responses in visual cortex (Goltstein et al., 2015; Lee et al., 2021).

Moreover, different mouse-lines have been used for experimentation. While all four studies investigating L4 cells (Kondo et al., 2016; Sun et al., 2016; de Vries et al., 2020; Huh et al., 2020) used *Scnn1a-Tg3-Cre* mice for specific targeting of L4 in V1, the two studies also investigating dLGN axons (Sun et al., 2016; Huh et al., 2020) used *C57BL/6* wildtype mice for dLGN axon imaging, despite expression of Cre-recombinase in the dLGN in *Scnn1a-Tg3-Cre* mice. As the dLGN is located below the hippocampus, using wildtype animals will inevitably result in off-target labeling along the injection tract in hippocampus and cortical regions. As it is impossible to tell these axonal projections apart in *in vivo* two-photon microscopy, those axons can distort the measured distribution of axonal response features. Interestingly, only one of the studies investigated dLGN axons using genetically restricted labeling in *Scnn1a-Tg3-Cre* mice (Jaepel et al., 2017), whose distributions are the most similar to the results in this dataset. Furthermore, the retinotopic location of the cortical recording site differed, with most studies investigating the monocular part of visual cortex using contralateral eye stimulation (Kondo et al., 2016; Roth et al., 2016; Sun et al., 2016; de Vries et al., 2020), in comparison to bV1 using ipsi- and contralateral eye stimulation (Jaepel et al., 2017; Huh et al., 2020). This is essential in the context of the retinotopically confined location of, for example, direction selective ganglion cells in the dLGN shell (Piscopo et al., 2013), which would be expected to cause differences in dLGN bouton selectivities in cortex due to V1's retinotopic organization itself. Specifically, the data in Piscopo et al. would suggest lower selectivities in dLGN neurons projecting to the bV1, matching the discrepancies observed. Lastly, the spatial extent of moving gratings presented in visual space differed between

studies. While the vast majority of studies presented full-field drifting gratings (Kondo et al., 2016; Roth et al., 2016; Sun et al., 2016; de Vries et al., 2020; Huh et al., 2020), only a single study used visuotopically confined visual stimulation (Jaepel et al., 2017), analogous to this thesis. Although full field stimulation might intuitively be the desired choice to maximize the number of responding neurons, it bears the danger of introducing extra-RF responses into the calcium transients. In other words, due to, for example, cortical like-to-like connectivity and corticothalamic feedback loops, neurons from outside the retinotopically confined imaging FOV can influence the responses of the imaged neurons (Iacaruso et al., 2017). As outlined in the introduction (see section "1.4.3 Alternative and complementary models") cortex has been implicated in sharpening orientation tuning (Sillito, 1975; Ringach et al., 1997; Reinhold et al., 2015), which could explain the discrepancies in selectivity. Due to the limitation in imaging frame rate of two-photon microscopy, these differential inputs to the imaged cells cannot be temporally disambiguated. Taken together, the experimental and analytical differences in previous literature make it near impossible to compare distributions of visual stimulus selectivity. Further studies will be needed to elucidate the impact of each of the discussed differences onto the distribution of extracted response tuning.

In terms of OD, L4 cells were significantly more binocularly tuned compared to highly monocular dLGN axons (Fig. 3.6-3.7, 3.8A), adding another computational integration to the geniculo-cortical synapse, in line with previous reports (LGN: Howarth et al. 2014; Jaepel et al. 2017; Sommeijer et al. 2017; Huh et al. 2020; Bauer et al. 2021; L4 cells: Huh et al. 2020). However, the distribution of OD was substantially more binocular than expected for L4 cells (Huh et al., 2020), while LGN axons were slightly more monocular than in some previous reports (Howarth et al., 2014; Sommeijer et al., 2017). On the other hand, analogously to orientation and direction tuning above, comparing exact values to and between previous studies is complex, due to the variety of different experimental and analytical methodologies. These divergent approaches include inter alia recording techniques (electrophysiology: Howarth et al. 2014; Sommeijer et al. 2017; two-photon microscopy: Jaepel et al. 2017; Huh et al. 2020; Bauer et al. 2021), anesthesia (urethane: Howarth et al. 2014; Sommeijer et al. 2017; fentanyl: Jaepel et al. 2017; Bauer et al. 2021; awake: Huh et al. 2020) and visual stimulation (subfield drifting gratings: Jaepel et al. 2017; Bauer et al. 2021; fullfield drifting gratings: Huh et al. 2020; fullfield flash: Howarth et al. 2014; Sommeijer et al. 2017; Huh et al. 2020; Bauer et al. 2021). In a prior study I consolidated the majority of these differences for the dLGN, and found that variation in ODI is significantly influenced by stringency of visual response criteria and stimulus type (Bauer et al., 2021). Furthermore, the highly monocular response properties seen *in vivo* were confirmed *in vitro* using dual color optogenetic input mapping (Bauer et al., 2021), confirming the accuracy of functional responses extracted with the deep *in vivo* axon imaging pipeline I established.

Taken together, the divergence of previously reported metrics and experimental approaches makes it difficult to assess neuronal tuning in the context of current literature. This highlights the need for future studies to not only produce comprehensive datasets for ground-truth comparisons, but also set unified experimental standards in the neuroscience community. Nonetheless, response transients of jRGECO1a labeled L4 cells and jGCaMP7b labeled LGN axons in L4 of my dataset reliably showed clean responses of high SNR in response to drifting gratings.

4.2.6 Receptive Fields of dLGN axons and cells in L4 of bV1

Next, to map spatial RFs I recorded calcium transients in response to sparse noise stimulation (Fig. 3.9-3.10). The response transients of both, jRGECO1a labeled cells and jGCaMP7b labeled dLGN axons in

L4 were distinct (Fig. 3.9B,E), with a consistently high SNR throughout each population (Fig. 3.10). As expected, RFs of L4 cells were larger and more elongated in comparison to dLGN RFs (Fig. 3.9, 3.11C,D), matching the original model of geniculo-cortical convergence proposed by David Hubel and Torsten Wiesel (Hubel and Wiesel, 1962). The majority of dLGN RFs were circular and small, responding exclusively to a single sparse noise patch of single polarity (Fig. 3.9F-G), matching previous reports in mice (Dräger, 1975; Grubb and Thompson, 2003; Lien and Scanziani, 2013; Piscopo et al., 2013; Zhao et al., 2013; Durand et al., 2016; Roth et al., 2016; Tang et al., 2016; Jaepel et al., 2017). In contrast, L4 cell RFs were larger in size, more elongated and of Gabor shape, consisting of two adjacent subfields of opposite polarity (Fig. 3.9B-C), as reported in mice previously (Niell and Stryker, 2008; de Vries et al., 2020; van Beest et al., 2021). Interestingly, RF transients of dLGN boutons in response to patch presentation were more reliable and of higher amplitude (see Fig. 3.9B,F for representative examples). The faster rise- and decay times are in line with the reported improvements of jGCaMP7b in comparison to older GECI generations, and the red-shifted jRGECO1a (Dana et al., 2016, 2019). Furthermore, due to the small and circular RF shape, sparse noise patches of such a size efficiently cover the RFs of dLGN neurons – if retinotopically aligned – and therefore elicit strong responses. In the case of cortical L4 RFs, however, these patches only partially cover their RFs at any given time, therefore eliciting a decreased response. Nonetheless, calcium transients in response to sparse noise stimulation were clear and of high SNR, allowing for efficient extraction of RFs in high quality.

Overall, RF sizes of L4 cells and dLGN boutons were on the lower end of the previously reported spectrum. However, analogous to orientation and direction tuning, direct comparisons are problematic due to the scattered experimental and analysis approaches. The majority of studies used intracellular or extracellular electrophysiology to record visual responses (Grubb and Thompson, 2003; Niell and Stryker, 2008; Lien and Scanziani, 2013; Piscopo et al., 2013; Durand et al., 2016; Tang et al., 2016; van Beest et al., 2021) with only three studies using *in vivo* two-photon microscopy (Roth et al., 2016; Jaepel et al., 2017; de Vries et al., 2020) as in this thesis. In the latter studies, the calculation of significant RF responses differed, further complicating the interpretation and comparability. Due to the length in rise- and decay times of calcium-indicators, most two-photon studies determine response significance including several frames after stimulus offset, often including several subsequent patch presentations. Although responses to subsequent patches will be averaged out with enough trials due to the pseudorandom presentation of patches per trial, responses to the stimulus offset of the patch of interest will be integrated. As sparse noise patches are presented as light increments or decrements on a gray background, a disappearing white ON patch will result in a light decrement during stimulus offset. In other words, stimulus offset will mimic stimulus presentation of the opposite polarity. Therefore, stimulus onset responses and stimulus offset responses will be integrated and counted as the polarity of stimulus onset. Hence, ON and OFF subfields are not precisely mapped, which can lead to changes in RF size and shape. To counteract this issue (see Fig. 2.4 for representative example), I only considered frames during stimulus presentation for determining RF significance to improve precision. In turn, however, this inevitably results in several false negative RFs in my dataset, as significance is sometimes not determined at the fluorescence peak of the calcium transient due to the prolonged rise-time of especially the calcium-indicator jRGECO1a.

Visual stimulation protocols to map RFs differed between sweeping bars (Niell and Stryker, 2008), noise movies (Zhao et al., 2013; Tang et al., 2016), locally sparse noise (de Vries et al., 2020) and sparse noise stimulation (Grubb and Thompson, 2003; Lien and Scanziani, 2013; Piscopo et al., 2013; Durand et al., 2016; Roth et al., 2016; Jaepel et al., 2017; van Beest et al., 2021). Sparse noise stimulation

protocols further varied in their sampling-resolution in visual space, from 2 degrees all the way up to 11 degrees per patch. This has major implications on the precision and size of the RF readout. While small patches provide a higher resolution, they are also less potent in eliciting a neuronal response, even within the RF, as the stimulus only covers a small fraction of the RF area. Furthermore, throughput becomes a major concern. On the other hand, too large patches will not accurately capture the RFs shape, orientation and will additionally elicit decreased response amplitudes, as they are more likely to cover inhibitory subfields of the opposite polarity. Therefore, I first optimized the stimulus resolution to find the optimal RF patch size of 6 by 6 degrees to allow for efficient and representative RF mapping (Fig. 2.3) prior to the functional connectomics pipeline. In terms of RF size, reported metrics varied from RF subfield size (Lien and Scanziani, 2013) and RF size (Durand et al., 2016; Roth et al., 2016; Jaepel et al., 2017; de Vries et al., 2020) all the way to the RF radius or full width half maximum (Grubb and Thompson, 2003; Niell and Stryker, 2008; Piscopo et al., 2013; Tang et al., 2016; van Beest et al., 2021). This becomes especially hard to compare for RFs of L4 cells, due to the diversity of their shapes and subfield-combinations, which makes it impossible to align these metrics for comparison. Furthermore, various mouselines were used, with the majority *C57BL/6* (Grubb and Thompson, 2003; Niell and Stryker, 2008; Piscopo et al., 2013; Zhao et al., 2013; Durand et al., 2016; Roth et al., 2016; Tang et al., 2016), followed by *Scnn1a-Tg3-Cre* (Jaepel et al., 2017; de Vries et al., 2020), *PV-Cre* (Lien and Scanziani, 2013), *Thy1-GCaMP6f* (van Beest et al., 2021) and one study with several L4 specific Cre-expressing mice (de Vries et al., 2020). Taken together, future studies are necessary to produce more comprehensive RF datasets in mice, in order to both understand the impact of experimental and analytical differences on results, and provide a solid basis for comparison. Furthermore, the divergence in experimental and analytical methods highlights the need for more standardized protocols and metrics in the visual neuroscience community. Nonetheless, the RF distribution of shapes in this study lies within previously reported ranges, with elongated Gabor-like RF shapes in L4 and small circular RF shapes in dLGN.

To my knowledge, this is, however, the first study to compare RFs directly in the same volume from retinotopically matched dLGN projections and L4 cells. RFs of both populations overlapped in visual space (Fig. 3.9D,H; Fig. 3.11A,B). However, interestingly, dLGN RFs were more scattered throughout visual space in comparison to the retinotopically confined L4 cells, despite the smaller axonal two-photon FOV (Fig. 3.10B,D; Fig. 3.11 A,B). This observation aligns with the structural extent of geniculate arbors in cortical L4, spanning several hundred microns in diameter (Antonini et al., 1999). In the context of the millimeter-scale V1 in mouse, this will consequently result in lower overall retinotopic precision in cortical space. However, given the extent of basal dendrites of L4 pyramidal cells in V1, the retinotopic precision of L4 cells could be rectified by specific functional connectivity, which can be tested with this dataset. Nonetheless, despite the overall dLGN RF scatter, the vast majority of dLGN RFs was confined to the retinotopic position of L4 cell RFs (Fig. 3.11A,B). Interestingly, L4 cell RFs consistently segregated in visual space based on their subfield polarity (see Fig8D, Fig. 3.11A, right for representative example), as has been observed in L2/3 of mice (Smith and Häusser, 2010) and tree shrews (Lee et al., 2016a) as well as in L4 of cats (Kremkow et al., 2016). This observation might be a first hint towards the possibility of generation of cortical OS from receptive subfield segregation, although not yet conclusive.

4.2.7 Correlation of RF- and preferred orientation

So far, I have only discussed orientation tuning and RFs in isolation. However, David Hubel and Torsten Wiesel proposed an intrinsic connection. They observed that the PO of simple cells aligned with the

orientation of their RF in visual space (Hubel and Wiesel, 1959, 1962). Based on this correlation, they proposed OS to be an emergent feature of simple cell RF structure. Consequently, knowing the RF orientation in visual space would enable the prediction of the PO response. This correlation has since been shown in various species and cortical layers (see e.g. Lampl et al. 2001; Smyth et al. 2003; Niell and Stryker 2008; Yeh et al. 2009; Kremkow et al. 2016; Lee et al. 2016a; Iacaruso et al. 2017). Analogously, L4 cells in this thesis' dataset had their PO aligned to the orientation of the RF Gabor in visual space (Fig. 3.12). The variance and occasional outliers can most likely be attributed to the inherent biases introduced by subsampling visual space using square patches. The relationship of patch size to RF size thereby dictates the precision with which the true RF structure and orientation can be extracted. As some orientations can be better represented better by a checkerboard pattern than others, outliers and scatter in the correlation are to be expected. This can only be compensated for by RF fitting to a limited degree, depending on the degree of the subsampling bias. One intuitive workaround would be to oversample visual space instead. While possible in theory, smaller patches are also less potent in driving visual responses, as they cover less of the RF area at a time. Furthermore, the likelihood of subsequently placed patches being arranged along the elongation of the RF and eliciting an orientation response increases, which could however be compensated with extending the local exclusion settings. Hence, to efficiently map spatial RFs, the resolution of visual space sampling and potency of driving spatial RF responses represent an experimental tradeoff. Therefore, I initially optimized the sparse noise resolution (see Fig. 2.3 for representative example). Based on these results, I decided on a sparse noise patch resolution of 6 by 6 degrees extent in visual space, whereas most previous studies in mouse used 8 by 8 degrees (e.g Iacaruso et al. 2017; Jaepel et al. 2017). Taken together, the strength and precision of correlation between preferred and RF orientation in our data likely represents an underestimation.

4.2.8 Matching functional to structural imaging in vivo

To relate neuronal function to its underlying circuitry, the functionally imaged cells and neurites have to be ultimately re-identified in the 3D-EM volume. Therefore, the more of the *in vivo* neuronal structure that can be captured, the easier and more reliable matching will be. This holds true for matching of axons in particular (Drawitsch et al., 2018). However, functional *in vivo* calcium imaging is performed in 2D fashion, therefore only providing the spatial relationship of labeled somas and neurites laterally. Although both somata and neurites are not perfectly uniformly distributed, the chance of finding a spuriously matching, off-target 2D pattern in 3D is very high. To circumvent this issue and increase uniqueness of matching, I imaged *in vivo* structural stacks to map the morphology of L4 cells and dLGN axons in 3D. Combined with the possibility of vascular triangulation using microCT, this should provide enough structural uniqueness for re-identifying functionally imaged L4 cells in the 3D-EM volume. However, due to the density of geniculate axonal arbors in L4 of bV1, matching axonal structure directly might still be challenging. To circumvent this issue, I took advantage of the excitability of jRGECO1a at 940 nm and co-acquired images from both the red and green structural channels. This allowed me to anchor the axonal morphology to the somata of L4 cells and thereby both simplify and increase statistical confidence in axonal matching. Therefore, I first matched all functional imaging planes of both, L4 cells (see Fig. 3.13A for representative example) and dLGN axons (see Fig. 3.13B for representative example) with their respective structural stacks. In a second step, I successfully mapped the axonal stacks to the structural stacks of L4 cells, using the cellular morphologies in the red detection channel. In summary, I was able to match the functional readout

of both L4 cells and dLGN axons to their respective morphologies and anchored them into a single 3D structural volume for later matching in 3D-EM.

4.2.9 Single shot in vivo data acquisition and perfusion

The entirety of the aforementioned *in vivo* imaging of all 4 cellular and 12 axonal planes was performed as a single shot experiment. Due to the complexity and sheer difficulty of executing such an experimental pipeline, the interrogated functional connectome should be maximized. Therefore, adding further *in vivo* FOVs over several chronic experiments might seem a more intuitive approach. While this could strengthen the statistical power by increasing the investigated functional connectome, this approach has the potential to introduce several biases, which would ultimately complicate the interpretation of the dataset. First, both the dLGN and bV1 are highly plastic (see e.g. Rose et al. 2016; Jaepel et al. 2017). Paired with the presentation of moving grating stimuli, which are not naturalistic and have been optimized to maximize the drive of visual stimulus features, it is likely that plasticity would be modulated in chronic imaging sessions (see e.g. Zhuang et al. 2021 for LGN). Even in fully naturalistic conditions, changes in connectivity over time are likely (see e.g. Montijn et al. 2016; Marks and Goard 2021; Deitch et al. 2021). As the readout of connectivity using 3D-EM is, however, also a single shot post mortem experiment, relating neuronal function to underlying connectivity becomes problematic. Therefore, to ensure that the measured connectome is representative of the connectivity during functional interrogation, I extracted all functional and structural features *in vivo* in a single session and perfused the animal immediately afterwards.

4.2.10 Biopsy preparation and re-finding via vascular triangulation

Traditional 3D-EM without prior functional imaging has the great advantage that exact positioning (on the order of tens of microns) is not necessary, unless investigating very small brain structures. However, for functional connectomics, precision of both biopsy extraction and subsequent tissue preparation is key to ensure the EM volume is aligned to the functionally interrogated FOV. Specifically for this project, one critical step towards ensuring matching of functional connectivity is the correct positioning of the EM FOV centered on the volume imaged by two-photon imaging. This is especially challenging due to the cylindrical biopsy shape, as it is difficult to determine the exact rotational positioning of the heavy metal stained tissue using e.g. light microscopy, as the stained tissue appears black. One possible workaround would be to cut away a small part of tissue on one side as a unique identifier before staining. However, any unnecessary manual handling and compression of the tissue should be avoided in order to preserve ultrastructure.

Instead, I designed an experimental pipeline (Fig. 3.15A) that allowed me to track the exact positioning of the two-photon FOV using microCT. I specifically used microCT in order to re-identify vascular landmarks from *in vivo* imaging (Fig. 3.15B). However, due to the previously discussed staining gradients, I had to remove the cortical surface, therefore also removing distinctive cortical surface vasculature. To be able to retain partial cortical vasculature while at the same time ensuring homogeneous staining, I optimized the removal of the pial surface during biopsy extraction. As previous staining gradients were concentrated in the center of the cortical biopsy surface, I took advantage of the cortical curvature of V1 and only removed the central dural portion (Fig. 3.15A,C). This allowed for both homogeneous staining and retaining partial pial vasculature for efficient vascular matching (Fig. 3.15C). Next, I successfully confirmed the identity of re-identified blood vessels by cross-triangulation (see Fig. 3.15D for example). Using those matched blood vessels as vascular landmarks, I then triangulated the position of the FOV from *in vivo* two-photon imaging and designed

the EM FOV centered around it (Fig. 3.15E). Lastly, after trimming the sample into a hexagonal shape for ATUM cutting and re-confirming the correct positioning using microCT (Fig. 3.15E), several sections were cut and imaged with mSEM. This allowed me to successfully confirm the correct positioning of the EM FOV by vascular re-finding and confirmation via cross-triangulation (Fig. 3.15F). By introducing microCT as an intermediate imaging modality, I was therefore able to guide each biopsy preparation step with high precision and confidence. In conclusion, this careful stepwise matching pipeline allowed me to track the positioning of the functionally imaged *in vivo* FOV post-mortem throughout each biopsy preparation step.

4.2.11 Long-range ATUM ultra-sectioning for functional connectomics

With the knowledge gained from the ATUM optimization, I carefully prepared the FC-mouse hexagon accordingly. The hexagonal positioning relative to the biopsy was aligned centered on both the two-photon and EM FOVs. In order to ensure that possible ATUM compression artifacts, I trimmed the final hexagon with both microscopy FOVs biased towards the top as an additional safety measure (Fig. 3.15E). After a final confirmation and investigation of the hexagon symmetry and aspect ratio using microCT, I ultra-sectioned the biopsy using ATUM. The starting point was about 50-80 microns into upper L5, estimated by microCT based on the difference in soma size and density between L4 and L5 cells (Hattox and Nelson, 2007). As L4 in mouse V1 is between 100 and 150 µm thick (Smith et al., 2009; Ji et al., 2015; Durand et al., 2016; Sun et al., 2016; Scala et al., 2019), which matches the extent of L4-targeted expression I observed *in vivo* across *Scnn1a-Tg3-Cre* mice, the goal was to section about 250 microns to include the entirety of L4. I successfully cut and collected 10014 consecutive sections without a single section loss in a continuous 40 h long experiment. At an overall average section thickness of 35.25 nm, the final sectioned depth of 353.015 µm, therefore including an additional 120 to 200 microns of L2/3. Due to deterioration of cutting quality, likely caused by accumulation of debris or knife blunting (Kasthuri et al., 2015), one knife-shift and one knife exchange were performed. As both are manual interventions, the danger of breaking the neuronal section-to-section continuity, especially for small neurites, is high. After shift or exchange, the knife edge needs to be re-aligned to the tissue surface under visual guidance. As the ATUM cutting thickness is 35 nm, the required alignment precision lies well below the resolution limit of visible light. I minimized the effect of this resolution gap by shining light from below the tissue and knife edge, and visually inspecting the reflection color on the tissue surface. While the light slit passing through the knife edge and sample surface did not provide any more information in already well-aligned conditions, reflective color-gradients surprisingly provided us with enough additional information for improved alignment in less aligned conditions. However, one additional challenge is caused by inhomogeneous tissue expansion over time. While this does not affect sectioning during cutting, due to the fast enough cutting frequency, manual alignment needs to be performed as precise and as fast as possible to minimize this issue. As ATUM is still a rather novel technique, the reasons underlying these expansions remain elusive. One possibility could be the heating of the room during the procedure. As ATUM sectioning itself is controlled remotely to minimize perturbations such as vibrations, the temperature remains largely constant. However, knife shifts and knife exchanges are so far performed manually. Consequently, the room likely heats up slightly due to body temperature of the operator, which might have an effect on tissue expansion. In contrast, the lack of heat generated by the friction between the tissue and the knife might cool down the tissue surface. As the exact cause remains unknown, future investigations are needed to find the cause and possible solutions to improve reliability. Nonetheless, I was able to successfully shift and exchange the knife, without introducing detrimental cutting

artifacts. However, in both cases, the first sections were not fully cut over the entire tissue surface. Whether that was caused by imperfect alignment of the knife edge or tissue expansion is unclear. Despite the partial sectioning, all sections were successfully collected and exhibited constant thicknesses, as assessed by light microscopy. Although these initial assessments indicate these manual interventions did not cause any detrimental effects on sectioning, image quality in EM and small neurite continuity throughout these areas should be investigated for a final assessment (see section "4.2.13 3D-EM image alignment and neurite continuity"). This additional assessment of continuity is especially important in the context of the diameter of small neurites such as spine necks and cortico-cortical axons, which can be as thin as 50 nm in diameter (e.g. Motta et al. 2019). With an ATUM sectioning thickness of 35 nm, losing two consecutive sections can potentially result in a loss of continuity for those neurite segments. Although learned approaches have recently been implemented with the goal of overcoming missing consecutive sections or up to 38 partially cut sections (Macrina et al., 2021), relying on post-hoc augmentation for recovering continuity should be avoided.

Next, the first 9643 sections were manually mounted onto 42 silicon wafers (Fig. S1) from right to left and top to bottom. The three partially cut sections after the knife-shift and the two partially cut sections after knife exchange were mounted on wafers 20 (third tape from the bottom) and 33 (second tape from the bottom) respectively. Both knife handlings are a more than one order of magnitude improvement knife to surface alignment in comparison with recent state-of-the-art work, which resulted in 38 and 45 partially cut sections after knife handling (MICrONS Consortium et al., 2021; Macrina et al., 2021) or 30 and 62 partially cut sections after knife handling (Shapson-Coe et al., 2021). On few of my mounted tape stripes, larger gaps are visible. However, none of those represent lost sections. In brief, on the tape prior to the knife exchange the gap between sections was caused by the final section staying attached to the diamond knife edge after I stopped the microtome cutting. To avoid mechanical stress on the section by premature pulling of the ATUM tape before the entirety of the section was cut, I adjusted the distance, so that the section would not be collected automatically, but needed to be pushed onto the ATUM tape by the next section. Therefore, the final section was manually pushed onto the ATUM tape using a single-hair brush. An even longer gap is visible in the following stripe, which was caused by a brief stopping of sectioning to adjust camera focus for remote monitoring. Furthermore, in wafers 14, 19 and 20, a single section wide gap is visible. These are caused by ultra-thin LM-transparent sections, which were nonetheless imaged using mSEM. Overall collection was highly consistent and showed close to no obvious angle variations (Fig. S1), further illustrating the success of the prior optimization experiments.

In conclusion, I successfully ultra-sectioned and mounted a previously functionally imaged biopsy in high quality without a single section loss for subsequent 3D-EM. Diligent optimizations (see section "3.2.3 Optimizing ATUM for single-shot experiments") prior to the experiment enabled me to prevent common cutting and collection artifacts, such as breaks, cracks, folds and section losses (Turner et al., 2020; MICrONS Consortium et al., 2021; Macrina et al., 2021; Shapson-Coe et al., 2021). To my knowledge, this is the first time that a dataset of comparable size was sectioned without single section loss and major artifacts for functional connectomics, representing an important step towards establishing functional connectomics of relevant circuit volumes.

4.2.12 Multibeam Scanning Electron Microscopy

In the final experimental step of the functional connectomics pipeline, I imaged all 9643 mounted sections using 61-beam SEM (Eberle et al., 2015). In particular, I imaged a 1 mm by 1 mm FOV,

centered on the two-photon imaging FOV, acquired for each section (Fig. 3.17A,B), resulting in a total volume of 1 mm by 1 mm by 300 µm. The in-plane EM FOV was thereby parallel to the two-photon FOVs and, consequently, parallel to the cortical layers. Sample conductivity and SNR was overall excellent throughout the entire volume (see Fig. 3.17B for representative example), substantiating the homogeneous staining quality predicted by prior microCT (Fig. 3.14C). Moreover, the high quality of neuronal ultrastructure (Fig. 3.17C) re-affirmed both, good preservation via perfusion and high quality sectioning. However, as expected, I sporadically encountered several sectioning-, tape- and imaging-related artifacts (Fig. S2). While occasional thin sections resulted in lower contrast, the SNR remained sufficiently high to maintain ultrastructural membrane detail, with the exception of two non-consecutive sections. In both, the contrast was too low to effectively center each beam on the respective detector position on the scintillator, resulting in beam-crosstalk. This resulted in an overlap between the correct beam and neighboring beams, thereby deteriorating image quality. Both sections were therefore excluded from further processing and analysis.

I further identified two artifacts of different shape that were likely caused by underlying tape-artifacts. Sections at the ends of the tape stripes frequently showed oblique nano-stripes (Fig. S2, top right). These artifacts were exclusive to sections at tape stripe ends, and were also clearly visible on the tape surrounding those sections. These were therefore likely caused by cracks in the carbon coating of the ATUM tape, which might have been induced by the manual mounting procedure. During mounting, each tape edge was held with forceps, and the tape slowly lowered onto the double-sided carbon tape on the wafer. To avoid air bubbles below the tape, controlled pressure was applied by carefully bending the tape ends to increase tape tension. In the cases of sections with the line artifacts, the ATUM tape was likely bent too strongly, which caused the thin carbon coating to crack. The second type were of circular shape (Fig. S2, bottom left). These were observed throughout sections and were stochastically distributed. The frequency, size and distribution was consistent with spots visible on the naked ATUM tape and previous experiments (Sievers et al., unpublished, Schmidt et al., unpublished). As the tape was plasma-cleaned prior to ATUM cutting, and many of the artifacts have a diameter in the nanometer to micrometer range, they are unlikely to be caused by particle impurities such as dust grains. Moreover, particles below the sections would result in a local gradual focus deterioration due to the height-difference. However, the section was fully in focus even at the artifact core. Therefore, these artifacts are likely caused by minor imperfections during carbon coating.

One of the major reasons triggering the knife shift was an increase in the frequency of tissue scratches during ultra-sectioning caused by accumulation of debris in the diamond knife edge. The vast majority were, however, not visible in EM. Visible tissue scratches only occurred sporadically (Fig. S2, bottom right) and never at the same position in consecutive sections, therefore not affecting neurite continuity. Another sporadic artifact were localized nano-stripes (Fig. S2, bottom middle), although they occurred only extremely infrequently. Their exact cause remains unclear, with possible explanations being nano-folds or impurities in the underlying carbon coating of the ATUM tape. Lastly, a few sections in the middle of the dataset exhibited an increased frequency of image warping at the top (Fig. S2, bottom middle) and imaging glitches (Fig. S2, top right). The exact cause for the glitches remains unclear, even after several rounds of feedback with the manufacturer. Warping is usually caused by imperfect conductivity, leading to charge accumulation and beam deflection due to electrostatic repulsion. However, these artifacts were significantly reduced in frequency and strength after servicing of the mSEM by the manufacturer, indicating that the issue was hardware related

rather than caused by the tissue itself. I manually screened each section for both types of artifacts and re-imaged sections in which these artifacts were severely affecting the neuronal ultrastructure.

Overall, each artifact occurred stochastically. As the smallest neurites, such as cortico-cortical axons and spine necks, are larger than a single section thickness (e.g. Motta et al. 2019), local non-consecutive distortions will not affect continuity even in these smallest neurites. The frequency of artifacts is equal or even reduced compared to successfully segmented datasets from previous works (Sievers et al., unpublished). This groundwork by Meike Sievers shows that by training machine-learning based algorithms to detect these artifacts, the resulting data can be segmented using automated approaches (see introduction section "1.5.7 Towards automated data processing of petabyte-scale EM datasets" for more detail) in high quality without detrimental effects on neurite continuity.

4.2.13 3D-EM image alignment and neurite continuity

To evaluate the quality in the most critical parts of the EM dataset, I first aligned 10 sections before and after the knife shift with an RMS error tolerance of 500 (Fig. 3.18C). Although the jump between the last section prior to- and the first section after knife shift showed a slightly bigger difference in comparison to immediately adjacent sections, both sections were already well aligned despite the high error tolerance. As expected, neurite continuity was preserved, even in the smallest of neurites. As a final safeguard, I investigated locations, where the biggest displacements would be expected, such as in-plane moving dendrites (see Fig. 3.18C, bottom for representative example). As they move orthogonal to cutting direction, the change between sections is high at the tissue immediately surrounding those dendrites. Even in these extreme cases, continuity of the smallest neurites was preserved in the raw data itself, without the need for complex algorithmic data-augmentation to recover continuity.

In a final step I aligned the entire dataset in 3D. As the raw-data consisted of more than 112 million individual images adding up to almost 1 petabyte of raw-data, computation time becomes a major concern, even for alignment. This is further complicated by the lack of intrinsic EM image alignment between sections in comparison to SBEM. While in SBEM the tissue blockface does not move laterally relative to the electron microscope during sectioning, stage-coordinates are usually sufficient to find matching cross-section image pairs. However, using ATUM, each section is placed at a different relative position on the wafer. Although matching EM FOV positions are approximated by LM-based section-outline definition, this is not precise enough to reliably predict overlapping raw-images between sections. Furthermore, depending on the knife sharpness and section thickness, sections show slight variations in overall compression along the cutting direction. Consequently, the alignment procedure requires additional computational effort to find matching images for cross-correlation (Scheffer et al. 2013; see methods section "2.20.8 mSEM Image Alignment" for detailed alignment description). In other words, neither local nor standard server-based computing provides the viable computational capacity for aligning a dataset of this size in a reasonable amount of time. To overcome this bottleneck, I used the computational resources of the Raven Supercomputer from the Max Planck Computing and Data Facility, using 80 nodes, consisting of 96 compute cores each, 24/7 at full capacity for nearly 4 months. After optimizing the alignment code to use each core at full capacity, I successfully aligned the dataset in 3D at a final maximum RMS error tolerance of 50 with a negligible dropout rate of 0.21%. The vast majority of dropped out images were not localized in the neuronal tissue, but rather in the resin at the top and bottom left of the FOV (see e.g. Fig. 3.18B). The overall average RMS errors

of 1.4 for in-plane and 3.5 for cross-plane alignment reflect a high alignment quality for biological tissue (Scheffer et al., 2013) and are in line with prior ATUM dataset alignments that were already successfully segmented (Sievers et al., unpublished). Visualizing the average RMS error per section (Fig. 3.18A) revealed consistent high quality throughout the volume, with the exception of several outliers around the middle of the dataset. Visual inspection of the raw data revealed that these outlier correlated with warping artifacts produced during mSEM imaging, therefore likely causing the increased RMS error for both in-plane and cross-plane alignment. As this artifact is present in the raw data itself, increasing the amount of least squares solver iterations did not improve alignment further. Due to the lack of inherent alignment in ATUM, warping in consecutive sections was stochastically distributed, and hence did not affect continuity as determined by manual inspection. Lastly, I examined the quality of section alignment throughout all 9643 sections (Fig. 3.18D) in the middle and the edges of the FOV. While excellent alignment in the center is crucial for re-finding of neurites imaged prior by fluorescence microscopy (Drawitsch et al., 2018), it also inherently represents the region of best alignment due to the alignment procedure. To find image pairs for pixel cross-correlation, downsampled montages of each section are first approximately aligned based on large landmarks such as nuclei and blood vessels, which biases overall alignment to the FOV center. Due to minute section-to-section differences in compression along the ATUM cutting direction, the algorithm stretches or compresses pixels at the FOV edge along the cutting direction to optimize overlap. Manual inspection confirmed excellent alignment quality and did not reveal any detrimental discontinuities. In conclusion, each of the observed image artifacts (Fig. S2) was sparse and did not impede alignment of the image data into a continuous 3D volume (see (Shapson-Coe et al., 2021) for comparison).

These results are not only critical for the success of further automated processing, but also illustrate the overall paramount raw data quality of the presented long-range functional connectomics dataset in comparison to recent attempts at petabyte-scale local functional connectomics (MICrONS Consortium et al., 2021) or connectomics (Shapson-Coe et al., 2021).

4.3 Future directions

The goal of this thesis project was to develop and employ an experimental pipeline for long-range functional connectomics, and thereby to produce a dataset that allows for in depth investigations into the functional logic of geniculo-cortical connectivity, as originally proposed by David Hubel and Torsten Wiesel (Hubel and Wiesel, 1962). Above, I presented both the methodological advances and the successful acquisition of said dataset, laying the foundation for this multi-year project. Further complex and computationally intensive analyses are required on the path to extracting the functional geniculo-cortical connectome. Specifically, the extraction of the geniculo-cortical connectome from the acquired 3D-EM volume and matching to the functionally investigated cells and axons are important steps towards answering the biological question at hand. In the following, I will provide a brief overview over these next steps and challenges.

4.3.1 3D segmentation

After alignment, the first step required for the extraction of connectivity is to extract the neurite compartments in 3D. This step is called segmentation. Traditionally solved by manual contouring (White et al., 1986) for small volumes, this approach has become intractable due to the increasing 3D-EM volumes (see introduction section “1.5.7 Towards automated data processing of petabyte-scale EM datasets” for more detail). Instead, tremendous progress has been made towards automating this process using learned, convolutional neural network based approaches (Berning et al., 2015; Beier et

al., 2017; Dorkenwald et al., 2017; Wolf et al., 2017; Zung et al., 2017; Januszewski et al., 2018; Funke et al., 2019; Motta et al., 2019; Macrina et al., 2021). The Helmstaedter laboratory has developed state-of-the-art segmentation tools and pipelines (Berning et al., 2015; Motta et al., 2019), which have been successfully employed for dense reconstruction of a SBEM dataset (Motta et al., 2019). However, several key differences with previous datasets prevent the direct application of these algorithms to segment the dataset I acquired. Most importantly, the imaging modality differs, as those datasets were acquired using SBEM, in contrast to mSEM in this thesis' dataset. In particular, the differences include improved pixel resolution of 4 x 4 nm^2 (in comparison to 11.24 x 11.24 nm^2), different image contrast generation via secondary electrons (in comparison to backscattering electrons) and different artifacts generated by ATUM sectioning and the mSEM microscope (Fig. S2). Consequently, the segmentation pipeline requires re-training and fine-tuning for mSEM datasets. This includes e.g. automated artifact detection to minimize their impact on automatic segmentation performance. This work is currently being spearheaded in the Helmstaedter laboratory by Meike Sievers for mSEM-based petabyte scale 3D-EM volumes (Sievers et al., unpublished). This work is ongoing, therefore it would be inappropriate to disclose details here. However, combined with parallel in-house development of state-of-the-art improvements in both precision and automation of reconstruction and correct assignment of small neurite compartments by Martin Schmidt (RoboEM; Schmidt et al., unpublished), recent results have already produced excellent segmentations (Sievers et al., unpublished). As the quality of my dataset is directly comparable to the data used for development of said algorithms, I expect the segmentation pipeline to be immediately deployable with minimal re-training. Furthermore, as the geniculo-cortical circuit represents only a fraction of the acquired EM volume, dense reconstruction (Motta et al., 2019) is not required, which should aid the reconstruction process with the possibility for seeded segmentation.

4.3.2 LM-EM re-finding

One crucial step towards the extraction of the functional connectome is re-finding the functionally imaged cells and axons in the 3D-EM volume. Based on the 3D reconstruction of the heavy metal stained biopsy and hexagon by microCT, I was already able to match vascular landmarks to the *in vivo* tissue (Fig. 3.15). This in turn allowed me to estimate the expected position of the two-photon FOV in both microCT and mSEM in x-y using triangulation. This presents an important first step towards re-identification of functionally imaged neurites, as it allows me to significantly reduce the search-space for *in vivo* to EM matching. Furthermore, by acquiring *in vivo* 3D structural stacks of functionally investigated L4 cells and dLGN axons, I was not only able to link function to structure *in vivo*, but also importantly link axonal morphology itself to that of L4 cells (Fig. 3.13). This will allow for a high-precision matching of *in vivo* function to structure in a two-step process. First, the functionally imaged L4 cells will be matched by co-registration (Bock et al., 2011; Briggman et al., 2011; Lee et al., 2016b; MICrONS Consortium et al., 2021), as the search-space is significantly lower compared to axons, and their large size requires less alignment precision. Furthermore, together with bloodvessels, somata dominate electron micrographs, and can therefore be easily detected using e.g. convolutional neural networks trained for nucleus detection. In other words, in the first step, the sole pattern of *in vivo* somata of functionally imaged L4 cells would be used to match L4 cells in 3D-EM using nucleus or soma detection, which are already included in the segmentation pipeline (Motta et al. 2019, Sievers et al., unpublished). Together with triangulation of matched bloodvessels, the somatic search-space can already be dramatically reduced in x-y. As the used *Scnn1a-Tg3-Cre* mouseline allowed me to specifically label cells in L4 of V1 (Madisen et al., 2010), the searchspace can be further limited to L4

cells in the 3D-EM volume, as L4 is clearly detectable by an increased cell density (see e.g. MICrONS Consortium et al. 2021), and the distinct morphology of L5 cells further distinguishes them (Hattox and Nelson, 2007). Lastly, the *Scnn1a-Tg3-Cre* mouseline expresses Cre-recombinase in only excitatory neurons (Jäpel-Schael, 2017), further narrowing down the space of potential cell matches in the EM volume by excluding inhibitory neurons. However, it remains unclear whether Scnn1a targets all excitatory layer 4 cells, especially also considering the viral transduction, which leads to a Gaussian distribution of labeling density moving away from the center of the viral bolus during injection. Nonetheless, taken together with the previously described spatial confinement of the searchspace, I expect the soma-pattern to be unique enough for re-identification prior to the completed segmentation. While this presents a simple 3D point matching approach, the cellular *in vivo* 3D structural stack contains not only the somata but also their dendrites in high spatial detail. These cellular *in vivo* fluorescence morphologies can further be directly co-registered with e.g. a complete segmentation of L4 cells in the 3D-EM volume for a final, high confidence cellular co-registration based re-identification.

In the second step, dLGN axons will be re-identified using a previously established morphology-based axon matching logic (Drawitsch et al., 2018). However, due to several important differences in data-acquisition, some minor adaptions will be necessary. First, purely structural fluorophores such as GFP and tdTomato were used for labeling in the original work, in contrast to the functional calcium indicator jGCaMP7b from this study. Furthermore, the light-microscopy 3D stack was not acquired *in vivo*, but instead directly on the extracted biopsy after perfusion using confocal imaging, which is closer to the 3D-EM volume as both are acquired in the post-fixed tissue. Further, the 3D axonal morphologies are consequently directly linked to the stained blood vessel pattern. Taken together, the fluorescent axonal morphologies are of slightly superior resolution in comparison to scatter-prone deep *in vivo* two-photon axon imaging, which is why I spent considerable effort to optimize deep *in vivo* two-photon axon imaging as presented in this thesis. I therefore expect the excellent SNR of the acquired axonal fluorescence to result in only a minimally lower quality than the structural fluorophore data. In contrast, axonal matching should be improved in comparison to the original study, as *in vivo* axonal morphologies are linked to morphologies of surrounding L4 somata and their basal dendrites, which are unavailable in the dataset of Drawitsch et al. 2018. As the frequency of somata outnumber the frequency of blood vessels, local alignment should be more precise. This effect is further amplified by the fact that the labeled dendritic compartments are smaller in diameter, and form a much tighter 3D network compared to blood vessels. Therefore, using morphologies of L4 cells in contrast to blood vessels will greatly improve the precision of local co-registration. Furthermore, the network of dendrites will provide denser and more homogeneously distributed landmarks and anchor points to select bounding boxes for axon matching (Drawitsch et al., 2018), further improving the precision and statistical confidence for identifying the matching axons in 3D-EM using their morphologies and bouton pattern (Drawitsch et al., 2018). Each matched axon can then be segmented out, and consequently iteratively improve local registration precision. Using the original pipeline in L4 of primary somatosensory cortex revealed that fluorescent axon morphologies, including their bouton patterns, need to be reconstructable for at least 33 microns to be able to reliably match them in 3D-EM, given a registration precision of 5 microns using blood vessels (Drawitsch et al., 2018). In my dataset this minimum requirement is surpassed several-fold for axon trajectories. Lastly, as thalamo-cortical axons can be ultrastructurally distinguished from cortico-cortical axons due to their diameter, morphologies and synaptic pattern (see e.g. Motta et al. 2019), the search space for axonal matching

can be additionally constrained by disregarding all cortico-cortical axons in each bounding box. Taken together, with the expected improvement in landmark co-registration of L4 dendrites, I am confident that the axons imaged *in vivo* will be therefore reliably re-identifiable in the 3D-EM volume.

4.3.3 Connectome extraction

Once the functionally imaged L4 cells and dLGN axons are re-identified and fully segmented in the EM volume, synaptic connectivity can be extracted using SynEM, a convolutional neural network based synapse detector (Staffler et al., 2017), which has been successfully re-trained for mSEM data (Sievers et al., unpublished). The resulting functional synaptome can then be further condensed into a functional connectome by identifying axonal multi-hits. Although such a binary connectome or synaptome could already be used to investigate the logic of functional geniculo-cortical connectivity, it would not be an accurate representation, as this would assume equal weights per connection, which is non-physiological (see e.g. Román Rosón et al. 2019; Ringach 2021; Bauer et al. 2021). In reality, each geniculo-cortical synapse has a differential impact on driving postsynaptic activity. Therefore, geniculate inputs will have a wide distribution of functional impact to the postsynaptic tuning of L4 cells. This means that connectivity *per se* does not have to be a perfect representation of postsynaptic tuning but can rather be up or downregulated via synaptic weights. In this case, a binary connectome analysis would drown the specificity of functional connectivity and thereby mask the linear functional relationship between functional input and postsynaptic output. To overcome this issue, synaptic weights should be added as another connectome dimension. A recent study showed that synaptic strength can be readily extracted based on ultrastructural synaptic correlates (Holler et al., 2021). Although this readout cannot provide synaptic strength in absolute terms, it does give insights into the distribution of geniculo-cortical synaptic weights. Consequently, the synaptic strength of each input can be expressed in relative terms to each other, therefore refining the functional impact of synaptic inputs to the postsynaptic response.

4.3.4 Deciphering functional connectivity logic

Lastly, with such a functional connectome at hand, the connectivity pattern can be investigated in context of functional response properties, such as OD, orientation tuning, direction tuning, RF elongation and RF subfield segregation. The EM volume I acquired, with an in-layer extent of 1 x 1 mm^2 and a depth of 330 µm, reaching from upper layer 5 into the middle of layer 2/3, should be able to capture the vast majority of the functionally imaged geniculo-cortical axonal trees (see Antonini et al. 1999). Due to the retinotopic arrangement of dLGN axons, the likelihood of axons exiting and re-entering the EM volume should be minimal, as the two-photon FOV is located in the middle of the EM imaging region. Consequently, the majority of matched axons should have their axonal trees roughly centered in the middle of the dataset. Hence, all functionally imaged boutons should be assignable to their respective unique axonal, and therefore neuronal, identity. In turn, this dataset should therefore capture the full extent of geniculo-cortical synaptic divergence of the functionally interrogated axons and maximize the functional connectome. One notable exception is a minor fraction of dLGN axons projecting to L1 of V1, which could potentially connect to L4 apical dendrites, as L4 of V1 composed mostly of pyramidal neurons (Scala et al., 2019). These L1-projecting dLGN neurons have previously been thought to be located in the dLGN shell, which contains orientation and direction tuned cells (Cruz-Martín et al., 2014). However, recent *in vivo* axon imaging data did not show a difference in OS or DS between L1- and L4-projecting dLGN axons (Sun et al. 2016; Zhuang et al. 2021; but see Kondo and Ohki 2016). Moreover, we did not find any difference in OD between these two layers (Bauer et al., 2021). Taken together, these results render the differential layer-specific targeting of functional

subgroups of dLGN neurons unlikely. Lastly, to my knowledge, direct monosynaptic connectivity between these dLGN axons and L4 cells in L1 has not yet been shown. Although a contribution through L1-projecting dLGN axons cannot be excluded, I expect it to be minor. Taken together, the dataset I acquired should accurately capture the relevant functional geniculo-cortical connectivity and enable me to investigate the functional logic of geniculo-cortical convergence.

The analysis of geniculo-cortical convergence can be further substantiated by expanding the segmentation to all thalamo-cortical axons (Motta et al., 2019) in L4. However, apart from dLGN, LP also projects to lower L4 of V1 (Harris and Shepherd, 2015). Therefore, dLGN and LP axons would need to be morphologically disambiguated. Conveniently, the majority of LP axonal branching is confined to L1 and upper L5, and they will therefore be easily identifiable in EM by their distinct morphology. As a result, the full geniculo-cortical convergence or connectome can be extracted for all functionally imaged L4 cells. This allows not only to determine which percentage of the full structural feedforward connectome is covered by the acquired functional connectome, but also to estimate the relative functional impact of the functionally imaged axons on each L4 cell individually by assessing the ultrastructural correlates of synaptic strength (Holler et al., 2021). This enables to estimate the percentage of functional weight of the functionally imaged axons to, for example, the population RF of each L4 cells geniculate input. The resulting refinement in analysis of the functional connectome will further improve the precision of statistically relevant statements about the impact of the logic of functional connectivity in generating postsynaptic response properties.

Lastly, the statistical significance of the functional connectome can be further boosted by taking all geniculate axons connecting to the functionally imaged L4 cells and investigating their connectivity pattern. Since we know the postsynaptic response properties, the connectivity pattern can be investigated for clustering and specificity. For example, one can investigate whether the geniculate axons exclusively connect to other L4 cells with overlapping RF features. Combined with the approximation of synaptic strength, this connectivity pattern alone will most likely be able to infer the type of functional connectivity. Although motivated by the feedforward connectivity prediction by David Hubel and Torsten Wiesel (Hubel and Wiesel, 1962), the experimental design is not restricted to investigating this model alone, but instead contains the true underlying connectivity. Therefore, whether the logic of functional connectivity to generate cortical OS aligns with RF alignment in visual space (Hubel and Wiesel, 1962), RF subfield segregation (Kremkow et al., 2016; Lee et al., 2016a), a combination of the two or another model, the dataset provides hypothesis-independent data to be able to investigate the logic of geniculo-cortical connectivity in the mouse.

4.4 Conclusion

I have developed and employed a novel long-range functional connectomics pipeline to investigate the longstanding question about the functional connectivity rules of geniculo-cortical convergence proposed by David Hubel and Torsten Wiesel (Hubel and Wiesel, 1962) by combining two-photon calcium imaging with 3D-EM. Specifically, I used functional *in vivo* two-photon calcium imaging of both pre-synaptic dLGN and postsynaptic L4 neurons in bV1. As dLGN is situated so deep in the brain that it is optically inaccessible to non-invasive multiphoton microscopy, I first established deep *in vivo* two-photon axon imaging to functionally interrogate their axonal terminals in thalamorecipient L4. Next, I verified dual-color imaging of both structure and function of dLGN axons and L4 cells in the same tissue using spectrally separated calcium indicators. To enable controlled sparse expression in *Scnn1a-Tg3-Cre* mice, I further developed a sparsening approach using Cre-dependent FlpO-recombinase

expression and FlpO-dependent expression of jGCaMP7b in dLGN. To maximize the functional connectome extraction, postsynaptic cells were densely labeled with the red-shifted Cre-dependent calcium indicator jRGECO1a in *Scnn1a-Tg3-Cre* mice, which express Cre-recombinase in dLGN and specifically in L4 of V1. Both neuronal populations were transduced by retinotopically matched viral injections. The overall localization in bV1 was mapped using intrinsic optical signal imaging. Visual response properties were recorded under anesthesia by visual presentation of sparse noise and drifting gratings in a single session. Structural stacks of imaged neurites were acquired and the mouse subsequently perfused including a far-red lipophilic dye to label blood vessels. For targeted stereotaxically guided biopsy extraction of the functionally imaged tissue, I developed an extraction strategy involving vascular landmark matching via epifluorescence imaging of the lipophilic perfusion dye. For subsequent homogeneous heavy metal staining, I established a vibratome-based trimming protocol to remove the cranial window-induced thickened dura, which acts as a detrimental diffusion barrier. Next, the tissue was heavy metal stained, dehydrated and resin infiltrated. Subsequently, I imaged the stained biopsy with microCT and centered the 3D-EM FOV around the functionally imaged tissue using triangulation from matched vascular landmarks. After trimming the biopsy into a hexagonal shape, the tissue was ultra-sectioned by a diamond knife into continuous 35-40 nm thin slices and collected on tape using ATUM. Lastly, the EM FOV was verified by vascular landmark re-finding and the sections imaged with 3D mSEM. In a final step, I then aligned the almost 1 PB raw dataset, consisting of >112 million images in 3D using the MPCDF supercomputing facilities.

Although the connectome analysis is ongoing, I am convinced that the high quality of the presented dataset provides all means necessary to not only successfully complete these final analysis steps, but also to answer the functional logic of geniculo-cortical convergence as first proposed by David Hubel and Torsten Wiesel (Hubel and Wiesel, 1962). From an experimental standpoint, to my knowledge, this thesis work marks the first successful development and acquisition of a dataset for long-range functional connectomics. This represents a crucial step forward from prior local functional connectomics. With such an experimental pipeline at hand, the investigation of functional connectivity is not restricted anymore to local circuit motifs, but instead allows for the investigation of the functional logic of connectivity between any two connected pairs of brain-regions in mouse. In conclusion, I hope that the presented long-range functional connectomics pipeline will provide the neuroscience community with an important tool towards further transitioning from investigating “what” the brain is coding for to rather “how” the brain is computing neuronal representations.

5 Bibliography

Adelson EH, Bergen JR. (1985). Spatiotemporal energy models for the perception of motion. *Journal of the Optical Society of America A*, 2(2):284–299. doi: 10.1364/josaa.2.000284.

Adesnik H, Bruns W, Taniguchi H, Huang ZJ, Scanziani M. (2012). A neural circuit for spatial summation in visual cortex. *Nature*, 490(7419):226–231. doi: 10.1038/nature11526.

Ahmadlou M, Heimel JA. (2015). Preference for concentric orientations in the mouse superior colliculus. *Nature Communications*, 6:6773. doi: 10.1038/ncomms7773.

Almada RC, Genewsky AJ, Heinz DE, Kaplick PM, Coimbra NC, Wotjak CT. (2018). Stimulation of the Nigrotectal Pathway at the Level of the Superior Colliculus Reduces Threat Recognition and Causes a Shift From Avoidance to Approach Behavior. *Frontiers in Neural Circuits*, 12:36. doi: 10.3389/fncir.2018.00036.

Alonso J-M, Martinez LM. (1998). Functional connectivity between simple cells and complex cells in cat striate cortex. *Nature Neuroscience*, 1(5):395–403. doi: 10.1038/1609.

Alonso J-M, Usrey WM, Reid RC. (2001). Rules of Connectivity between Geniculate Cells and Simple Cells in Cat Primary Visual Cortex. *Journal of Neuroscience*, 21(11):4002–4015. doi: 10.1523/JNEUROSCI.21-11-04002.2001.

Andelin AK, Doyle Z, Laing RJ, Turecek J, Lin B, Olavarria JF. (2020). Influence of ocular dominance columns and patchy callosal connections on binocularity in lateral striate cortex: Long Evans versus albino rats. *Journal of Comparative Neurology*, 528(4):650–663. doi: 10.1002/cne.24786.

Anderson JC, Douglas RJ, Martin KAC, Nelson JC. (1994a). Map of the synapses formed with the dendrites of spiny stellate neurons of cat visual cortex. *Journal of Comparative Neurology*, 341(1):25–38. doi: 10.1002/cne.903410104.

Anderson JC, Douglas RJ, Martin KAC, Nelson JC. (1994b). Synaptic output of physiologically identified spiny stellate neurons in cat visual cortex. *Journal of Comparative Neurology*, 341(1):16–24. doi: 10.1002/cne.903410103.

Andrei AR, Debes S, Chelaru M, Liu X, Rodarte E, Spudich JL, Janz R, Dragoi V. (2021). Heterogeneous side-effects of cortical inactivation in behaving animals. *eLife*, 10:e66400. doi: 10.7554/eLife.66400.

Antonini A, Fagiolini M, Stryker MP. (1999). Anatomical Correlates of Functional Plasticity in Mouse Visual Cortex. *Journal of Neuroscience*, 19(11):4388–4406. doi: 10.1523/JNEUROSCI.19-11-04388.1999.

Arenkiel BR, Hasegawa H, Yi JJ, Larsen RS, Wallace ML, Philpot BD, Wang F, Ehlers MD. (2011). Activity-Induced Remodeling of Olfactory Bulb Microcircuits Revealed by Monosynaptic Tracing. *PLOS ONE*, 6(12):e29423. doi: 10.1371/journal.pone.0029423.

Armbruster BN, Li X, Pausch MH, Herlitze S, Roth BL. (2007). Evolving the lock to fit the key to create a family of G protein-coupled receptors potently activated by an inert ligand. *PNAS*, 104(12):5163–5168. doi: 10.1073/pnas.0700293104.

Atasoy D, Betley JN, Li W-P, Su HH, Sertel SM, Scheffer LK, Simpson JH, Fetter RD, Sternson SM. (2014). A genetically specified connectomics approach applied to long-range feeding regulatory circuits. *Nature Neuroscience*, 17(12):1830–1839. doi: 10.1038/nn.3854.

Baden T, Berens P, Franke K, Román Rosón M, Bethge M, Euler T. (2016). The functional diversity of retinal ganglion cells in the mouse. *Nature*, 529(7586):345–350. doi: 10.1038/nature16468.

Bang BG, Bang FB. (1957). Graphic reconstruction of the third dimension from serial electron microphotographs. *Journal of Ultrastructure Research*, 1(2):138–146. doi: 10.1016/s0022-5320(57)80002-1.

Barlow HB, Hill RM. (1963). Selective Sensitivity to Direction of Movement in Ganglion Cells of the Rabbit Retina. *Science*, 139(3553):412–414. doi: 10.1126/science.139.3553.412.

Barlow HB, Hill RM, Levick WR. (1964). Retinal ganglion cells responding selectively to direction and speed of image motion in the rabbit. *The Journal of Physiology*, 173(3):377–407. doi: 10.1113/jphysiol.1964.sp007463.

Bates P, Young JAT, Varmus HE. (1993). A receptor for subgroup A Rous sarcoma virus is related to the low density lipoprotein receptor. *Cell*, 74(6):1043–1051. doi: 10.1016/0092-8674(93)90726-7.

Bauer J, Weiler S, Fernholz MHP, Laubender D, Scheuss V, Hübener M, Bonhoeffer T, Rose T. (2021). Limited functional convergence of eye-specific inputs in the retinogeniculate pathway of the mouse. *Neuron*, 109(15):2457-2468.e12. doi: 10.1016/j.neuron.2021.05.036.

van Beest EH, Mukherjee S, Kirchberger L, Schnabel UH, van der Togt C, Teeuwen RRM, Barsegyan A, Meyer AF, Poort J, Roelfsema PR, Self MW. (2021). Mouse visual cortex contains a region of enhanced spatial resolution. *Nature Communications*, 12(1):4029. doi: 10.1038/s41467-021-24311-5.

Beier T, Pape C, Rahaman N, Prange T, Berg S, Bock DD, Cardona A, Knott GW, Plaza SM, Scheffer LK, Koethe U, Kreshuk A, Hamprecht FA. (2017). Multicut brings automated neurite segmentation closer to human performance. *Nature Methods*, 14(2):101–102. doi: 10.1038/nmeth.4151.

Berndt A, Lee SY, Wietek J, Ramakrishnan C, Steinberg EE, Rashid AJ, Kim H, Park S, Santoro A, Frankland PW, Iyer SM, Pak S, Ährlund-Richter S, Delp SL, Malenka RC, Josselyn SA, Carlén M, Hegemann P, Deisseroth K. (2016). Structural foundations of optogenetics: Determinants of channelrhodopsin ion selectivity. *PNAS*, 113(4):822–829. doi: 10.1073/pnas.1523341113.

Berning M, Boergens KM, Helmstaedter M. (2015). SegEM: Efficient Image Analysis for High-Resolution Connectomics. *Neuron*, 87(6):1193–1206. doi: 10.1016/j.neuron.2015.09.003.

Betzig E. (1995). Proposed method for molecular optical imaging. *Optics Letters*, OL 20(3):237–239. doi: 10.1364/ol.20.000237.

Betzig E, Patterson GH, Sougrat R, Lindwasser OW, Olenych S, Bonifacino JS, Davidson MW, Lippincott-Schwartz J, Hess HF. (2006). Imaging Intracellular Fluorescent Proteins at Nanometer Resolution. *Science*, 313(5793):1642–1645. doi: 10.1126/science.1127344.

Bickford ME, Zhou N, Krahe TE, Govindaiah G, Guido W. (2015). Retinal and Tectal "Driver-Like" Inputs Converge in the Shell of the Mouse Dorsal Lateral Geniculate Nucleus. *Journal of Neuroscience*, 35(29):10523–10534. doi: 10.1523/JNEUROSCI.3375-14.2015.

Birch-Andersen A. (1955). Reconstruction of the Nuclear Sites of Salmonella typhimurium from Electron Micrográphs of Serial Sections. *Journal of General Microbiology*, 13(2):327–329. doi: 10.1099/00221287-13-2-327.

Bishop D, Nikić I, Brinkoetter M, Knecht S, Potz S, Kerschensteiner M, Misgeld T. (2011). Near-infrared branding efficiently correlates light and electron microscopy. *Nature Methods*, 8(7):568–570. doi: 10.1038/nmeth.1622.

Blasdel GG, Salama G. (1986). Voltage-sensitive dyes reveal a modular organization in monkey striate cortex. *Nature*, 321(6070):579–585. doi: 10.1038/321579a0.

Bleckert A, Schwartz GW, Turner MH, Rieke F, Wong ROL. (2014). Visual Space Is Represented by Nonmatching Topographies of Distinct Mouse Retinal Ganglion Cell Types. *Current Biology*, 24(3):310–315. doi: 10.1016/j.cub.2013.12.020.

Bock DD, Lee W-CA, Kerlin AM, Andermann ML, Hood G, Wetzel AW, Yurgenson S, Soucy ER, Kim HS, Reid RC. (2011). Network anatomy and in vivo physiology of visual cortical neurons. *Nature*, 471(7337):177–182. doi: 10.1038/nature09802.

Boergens KM, Berning M, Bocklisch T, Bräunlein D, Drawitsch F, Frohnhofen J, Herold T, Otto P, Rzepka N, Werkmeister T, Werner D, Wiese G, Wissler H, Helmstaedter M. (2017). webKnossos: efficient online 3D data annotation for connectomics. *Nature Methods*, 14(7):691–694. doi: 10.1038/nmeth.4331.

Bonhoeffer T, Grinvald A. (1991). Iso-orientation domains in cat visual cortex are arranged in pinwheel-like patterns. *Nature*, 353(6343):429–431. doi: 10.1038/353429a0.

Bonhoeffer T, Hübener M. (2016). Intrinsic Optical Imaging of Functional Map Development in Mammalian Visual Cortex. *Cold Spring Harbor Protocols*, 2016(6). doi: 10.1101/pdb.top089383.

Bonhoeffer T, Kim D-S, Malonek D, Shoham D, Grinvald A. (1995). Optical Imaging of the Layout of Functional Domains in Area 17 and Across the Area 17/18 Border in Cat Visual Cortex. European *Journal of Neuroscience*, 7(9):1973–1988. doi: 10.1111/j.1460-9568.1995.tb00720.x.

Bonin V, Histed MH, Yurgenson S, Reid RC. (2011). Local Diversity and Fine-Scale Organization of Receptive Fields in Mouse Visual Cortex. *The Journal of Neuroscience*, 31(50):18506–18521. doi: 10.1523/JNEUROSCI.2974-11.2011.

Bourassa J, Deschenes M. (1995). Corticothalamic projections from the primary visual cortex in rats: a single fiber study using biocytin as an anterograde tracer. *Neuroscience*, 66(2):253–263. doi: 10.1016/0306-4522(95)00009-8.

Boyden ES, Zhang F, Bamberg E, Nagel G, Deisseroth K. (2005). Millisecond-timescale, genetically targeted optical control of neural activity. *Nature Neuroscience*, 8(9):1263–1268. doi: 10.1038/nn1525.

Brainard DH. (1997). The Psychophysics Toolbox. *Spatial Vision*, 10(4):433–436. doi: 10.1163/156856897X00357.

Briggman KL, Bock DD. (2012). Volume electron microscopy for neuronal circuit reconstruction. *Current Opinion in Neurobiology*, 22(1):154–161. doi: 10.1016/j.conb.2011.10.022.

Briggman KL, Helmstaedter M, Denk W. (2011). Wiring specificity in the direction-selectivity circuit of the retina. *Nature*, 471(7337):183–188. doi: 10.1038/nature09818.

Brodmann K. (1909). Vergleichende Lokalisationslehre der Grosshirnrinde in ihren Prinzipien dargestellt auf Grund des Zellenbaues. *Barth*.

Broussard GJ, Liang Y, Fridman M, Unger EK, Meng G, Xiao X, Ji N, Petreanu L, Tian L. (2018). In vivo measurement of afferent activity with axon-specific calcium imaging. *Nature Neuroscience*, 21(9):1272–1280. doi: 10.1038/s41593-018-0211-4.

Buhmann J, Sheridan A, Malin-Mayor C, Schlegel P, Gerhard S, Kazimiers T, Krause R, Nguyen TM, Heinrich L, Lee W-CA, Wilson R, Saalfeld S, Jefferis GSXE, Bock DD, Turaga SC, Cook M, Funke J. (2021). Automatic detection of synaptic partners in a whole-brain Drosophila electron microscopy data set. *Nature Methods*, 18(7):771–774. doi: 10.1038/s41592-021-01183-7.

Buniatyan D, Popovych S, Ih D, Macrina T, Zung J, Seung HS. (2020). Weakly Supervised Deep Metric Learning for Template Matching. *Advances in Computer Vision. CVC 2019. Advances in Intelligent Systems and Computing, vol 943. Springer Cham.*, 39–58. doi: 10.1007/978-3-030-17795-9_4.

Bussey TJ, Saksida LM, Rothblat LA. (2001). Discrimination of computer-graphic stimuli by mice: A method for the behavioral characterization of transgenic and gene-knockout models. *Behavioral Neuroscience*, 115(4):957-960. doi: 10.1037//0735-7044.115.4.957.

Cajal SR y. (1894). Die Retina der Wirbelthiere. *Bergmann*.

Campbell FW, Green DG. (1965). Monocular versus Binocular Visual Acuity. *Nature*, 208(5006):191–192. doi: 10.1038/208191a0.

Carandini M, Ferster D. (2000). Membrane Potential and Firing Rate in Cat Primary Visual Cortex. *The Journal of Neuroscience*, 20(1):470–484. doi: 10.1523/JNEUROSCI.20-01-00470.2000.

Card JP, Enquist LW. (2001). Transneuronal Circuit Analysis With Pseudorabies Viruses. *Current Protocols in Neuroscience*, 9:1.5.1-1.5.28. doi: 10.1002/0471142301.ns0105s09.

Carter-Dawson LD, Lavail MM. (1979). Rods and cones in the mouse retina. I. Structural analysis using light and electron microscopy. *Journal of Comparative Neurology*, 188(2):245–262. doi: 10.1002/cne.901880204.

Chapman B, Zahs KR, Stryker MP. (1991). Relation of cortical cell orientation selectivity to alignment of receptive fields of the geniculocortical afferents that arborize within a single orientation column in ferret visual cortex. *The Journal of Neuroscience*, 11(5):1347–1358. doi: 10.1523/JNEUROSCI.11-05-01347.1991.

Chen C, Regehr WG. (2000). Developmental Remodeling of the Retinogeniculate Synapse. *Neuron*, 28(3):955–966. doi: 10.1016/s0896-6273(00)00166-5.

Chen F, Tillberg PW, Boyden ES. (2015). Optical imaging. Expansion microscopy. *Science*, 347(6221):543-548. doi: 10.1126/science.1260088.

Chen JL, Villa KL, Cha JW, So PTC, Kubota Y, Nedivi E. (2012). Clustered Dynamics of Inhibitory Synapses and Dendritic Spines in the Adult Neocortex. *Neuron*, 74(2):361–373. doi: 10.1016/j.neuron.2012.02.030.

Chen T-W, Wardill TJ, Sun Y, Pulver SR, Renninger SL, Baohan A, Schreiter ER, Kerr RA, Orger MB, Jayaraman V, Looger LL, Svoboda K, Kim DS. (2013). Ultrasensitive fluorescent proteins for imaging neuronal activity. *Nature*, 499(7458):295–300. doi: 10.1038/nature12354.

Choi J-H, Sim S-E, Kim J, Choi DI, Oh J, Ye S, Lee J, Kim T, Ko H-G, Lim C-S, Kaang B-K. (2018). Interregional synaptic maps among engram cells underlie memory formation. *Science*, 360(6387):430-435. doi: 10.1126/science.aas9204.

Chow BY, Han X, Dobry AS, Qian X, Chuong AS, Li M, Henninger MA, Belfort GM, Lin Y, Monahan PE, Boyden ES. (2010). High-performance genetically targetable optical neural silencing by light-driven proton pumps. *Nature*, 463(7277):98–102. doi: 10.1038/nature08652.

Chung S, Ferster D. (1998). Strength and Orientation Tuning of the Thalamic Input to Simple Cells Revealed by Electrically Evoked Cortical Suppression. *Neuron*, 20(6):1177–1189. doi: 10.1016/s0896-6273(00)80498-5.

Cleland BG, Dubin MW, Levick WR. (1971). Simultaneous Recording of Input and Output of Lateral Geniculate Neurones. *Nature New Biology*, 231(23):191–192. doi: 10.1038/newbio231191a0.

Coleman JE, Law K, Bear MF. (2009). Anatomical origins of ocular dominance in mouse primary visual cortex. *Neuroscience*, 161(2):561–571. doi: 10.1016/j.neuroscience.2009.03.045.

Costa NM da, Martin KAC. (2011). How Thalamus Connects to Spiny Stellate Cells in the Cat's Visual Cortex. *The Journal of Neuroscience*, 31(8):2925–2937. doi: 10.1523/JNEUROSCI.5961-10.2011.

Cowey A. (1964). Projection of the retina on to striate and prestriate cortex in the squirrel monkey, saimiri sciureus. *Journal of Neurophysiology*, 27:366–393. doi: 10.1152/jn.1964.27.3.366.

Cowey A, Rolls ET. (1974). Human cortical magnification factor and its relation to visual acuity. *Experimental Brain Research*, 21(5):447–454. doi: 10.1007/BF00237163.

Crapse TB, Lau H, Basso MA. (2018). A Role for the Superior Colliculus in Decision Criteria. *Neuron*, 97(1):181-194.e6. doi: 10.1016/j.neuron.2017.12.006.

Creutzfeldt O, Sakmann B. (1969). Neurophysiology of Vision. *Annual Review of Physiology*, 31:499–544. doi: 10.1146/annurev.ph.31.030169.002435.

Crewe AV, Wall J, Langmore J. (1970). Visibility of Single Atoms. *Science*, 168(3937):1338-1340. doi: 10.1126/science.168.3937.1338.

Cruz-Martín A, El-Danaf RN, Osakada F, Sriram B, Dhande OS, Nguyen PL, Callaway EM, Ghosh A, Huberman AD. (2014). A dedicated circuit links direction-selective retinal ganglion cells to the primary visual cortex. *Nature*, 507(7492):358–361. doi: 10.1038/nature12989.

Cucchiaro JB, Uhlrich DJ, Sherman SM. (1991). Electron-microscopic analysis of synaptic input from the perigeniculate nucleus to the A-laminae of the lateral geniculate nucleus in cats. *Journal of Comparative Neurology*, 310(3):316–336. doi: 10.1002/cne.903100304.

Curcio CA, Sloan KR, Kalina RE, Hendrickson AE. (1990). Human photoreceptor topography. *Journal of Comparative Neurology*, 292(4):497–523. doi: 10.1002/cne.902920402.

Dacey DM, Petersen MR. (1992). Dendritic field size and morphology of midget and parasol ganglion cells of the human retina. *PNAS*, 89(20):9666–9670. doi: 10.1073/pnas.89.20.9666.

Dalangin R, Drobizhev M, Molina RS, Aggarwal A, Patel R, Abdelfattah AS, Zhao Y, Wu J, Podgorski K, Schreiter ER, Hughes TE, Campbell RE, Shen Y. (2020). Far-red fluorescent genetically encoded calcium ion indicators. *bioRxiv*, 380089. https://www.biorxiv.org/content/10.1101/2020.11.12.380089v1

Dana H, Mohar B, Sun Y, Narayan S, Gordus A, Hasseman JP, Tsegaye G, Holt GT, Hu A, Walpita D, Patel R, Macklin JJ, Bargmann CI, Ahrens MB, Schreiter ER, Jayaraman V, Looger LL, Svoboda K, Kim DS. (2016). Sensitive red protein calcium indicators for imaging neural activity. *eLife*, 5:e12727. doi: 10.7554/eLife.12727.

Dana H, Sun Y, Mohar B, Hulse BK, Kerlin AM, Hasseman JP, Tsegaye G, Tsang A, Wong A, Patel R, Macklin JJ, Chen Y, Konnerth A, Jayaraman V, Looger LL, Schreiter ER, Svoboda K, Kim DS. (2019). High-performance calcium sensors for imaging activity in neuronal populations and microcompartments. *Nature Methods*, 16(7):649–657. doi: 10.1038/s41592-019-0435-6.

Daniel PM, Whitteridge D. (1961). The representation of the visual field on the cerebral cortex in monkeys. *The Journal of Physiology*, 159(2):203–221. doi: 10.1113/jphysiol.1961.sp006803.

Deitch D, Rubin A, Ziv Y. (2021). Representational drift in the mouse visual cortex. *Current Biology*, 31(19):4327-4339.e6. doi: 10.1016/j.cub.2021.07.062.

Denk W, Delaney KR, Gelperin A, Kleinfeld D, Strowbridge BW, Tank DW, Yuste R. (1994). Anatomical and functional imaging of neurons using 2-photon laser scanning microscopy. *Journal of Neuroscience Methods*, 54(2):151–162. doi: 10.1016/0165-0270(94)90189-9.

Denk W, Horstmann H. (2004). Serial Block-Face Scanning Electron Microscopy to Reconstruct Three-Dimensional Tissue Nanostructure. *PLOS Biology*, 2(11):e329. doi: 10.1371/journal.pbio.0020329.

Denk W, Strickler JH, Webb WW. (1990). Two-Photon Laser Scanning Fluorescence Microscopy. *Science*, 248(4951):73-76. doi: 10.1126/science.2321027.

Denk W, Svoboda K. (1997). Photon Upmanship: Why Multiphoton Imaging Is More than a Gimmick. *Neuron*, 18(3):351–357. doi: 10.1016/s0896-6273(00)81237-4.

DeWeerdt S. (2019). How to map the brain. *Nature*, 571(7766):S6–S8. doi: 10.1038/d41586-019-02208-0.

Dhande OS, Hua EW, Guh E, Yeh J, Bhatt S, Zhang Y, Ruthazer ES, Feller MB, Crair MC. (2011). Development of Single Retinofugal Axon Arbors in Normal and β2 Knock-Out Mice. *The Journal of Neuroscience*, 31(9):3384–3399. doi: 10.1523/JNEUROSCI.4899-10.2011.

Dombeck DA, Harvey CD, Tian L, Looger LL, Tank DW. (2010). Functional imaging of hippocampal place cells at cellular resolution during virtual navigation. *Nature Neuroscience*, 13(11):1433–1440. doi: 10.1038/nn.2648.

Dorkenwald S, Schubert PJ, Killinger MF, Urban G, Mikula S, Svara F, Kornfeld J. (2017). Automated synaptic connectivity inference for volume electron microscopy. *Nature Methods*, 14(4):435–442. doi: 10.1038/nmeth.4206.

Douglas RJ, Martin KA. (1991). A functional microcircuit for cat visual cortex. *The Journal of Physiology*, 440:735–769. doi: 10.1113/jphysiol.1991.sp018733.

Douglas RJ, Martin KAC, Whitteridge D. (1989). A Canonical Microcircuit for Neocortex. *Neural Computation*, 1(4):480–488. doi: 10.1162/neco.1989.1.4.480.

Douglas RM, Alam NM, Silver BD, Mcgill TJ, Tschetter WW, Prusky GT. (2005). Independent visual threshold measurements in the two eyes of freely moving rats and mice using a virtual-reality optokinetic system. *Visual Neuroscience*, 22(5):677–684. doi: 10.1017/S0952523805225166.

Douglas RM, Neve A, Quittenbaum JP, Alam NM, Prusky GT. (2006). Perception of visual motion coherence by rats and mice. *Vision Research*, 46(18):2842–2847. doi: 10.1016/j.visres.2006.02.025.

Dow BM, Snyder AZ, Vautin RG, Bauer R. (1981). Magnification factor and receptive field size in foveal striate cortex of the monkey. *Experimental Brain Research*, 44(2):213–228. doi: 10.1007/BF00237343.

Dräger UC. (1975). Receptive fields of single cells and topography in mouse visual cortex. *Journal of Comparative Neurology*, 160(3):269–289. doi: 10.1002/cne.901600302.

Drager UC. (1978). Observations on monocular deprivation in mice. *Journal of Neurophysiology*, 41(1):28–42. doi: 10.1152/jn.1978.41.1.28.

Drager UC, Hubel DH. (1976). Topography of visual and somatosensory projections to mouse superior colliculus. *Journal of Neurophysiology*, 39(1):91–101. doi: 10.1152/jn.1976.39.1.91.

Dräger UC, Olsen JF. (1980). Origins of crossed and uncrossed retinal projections in pigmented and albino mice. *Journal of Comparative Neurology*, 191(3):383–412, doi: 10.1002/cne.901910306.

Drawitsch F, Karimi A, Boergens KM, Helmstaedter M. (2018). FluoEM, virtual labeling of axons in three-dimensional electron microscopy data for long-range connectomics. *eLife*, 7:e38976. doi: 10.7554/eLife.38976.

Durand S, Iyer R, Mizuseki K, Vries S de, Mihalas S, Reid RC. (2016). A Comparison of Visual Response Properties in the Lateral Geniculate Nucleus and Primary Visual Cortex of Awake and Anesthetized Mice. *The Journal of Neuroscience*, 36(48):12144–12156. doi: 10.1523/JNEUROSCI.1741-16.2016.

Dürst CD, Wiegert JS, Helassa N, Kerruth S, Coates C, Schulze C, Geeves MA, Török K, Oertner TG. (2019). High-speed imaging of glutamate release with genetically encoded sensors. *Nature Protocols*, 14(5):1401–1424. doi: 10.1038/s41596-019-0143-9.

Eberle AL, Mikula S, Schalek R, Lichtman J, Tate MLK, Zeidler D. (2015). High-resolution, high-throughput imaging with a multibeam scanning electron microscope. *Journal of Microscopy*, 259(2):114–120. doi: 10.1111/jmi.12224.

Ellis EM, Gauvain G, Sivyer B, Murphy GJ. (2016). Shared and distinct retinal input to the mouse superior colliculus and dorsal lateral geniculate nucleus. *Journal of Neurophysiology*, 116(2):602–610. doi: 10.1152/jn.00227.2016.

Erişir A, Van Horn SC, Sherman SM. (1997). Relative numbers of cortical and brainstem inputs to the lateral geniculate nucleus. *PNAS*, 94(4):1517–1520. doi: 10.1073/pnas.94.4.1517.

Erisken S, Vaiceliunaite A, Jurjut O, Fiorini M, Katzner S, Busse L. (2014). Effects of Locomotion Extend throughout the Mouse Early Visual System. *Current Biology*, 24(24):2899–2907. doi: 10.1016/j.cub.2014.10.045.

Evans DA, Stempel AV, Vale R, Ruehle S, Lefler Y, Branco T. (2018). A synaptic threshold mechanism for computing escape decisions. *Nature*, 558(7711):590–594. doi: 10.1038/s41586-018-0244-6.

Fahey PG, Muhammad T, Smith C, Froudarakis E, Cobos E, Fu J, Walker EY, Yatsenko D, Sinz FH, Reimer J, Tolias AS. (2019). A global map of orientation tuning in mouse visual cortex. *bioRxiv*, 745323. https://www.biorxiv.org/content/10.1101/745323v1

Fain GL, Dowling JE. (1973). Intracellular Recordings from Single Rods and Cones in the Mudpuppy Retina. *Science*, 180(4091):1178-1181. doi: 10.1126/science.180.4091.1178.

Farrell M, Recanatesi S, Reid RC, Mihalas S, Shea-Brown E. (2021). Autoencoder networks extract latent variables and encode these variables in their connectomes. *Neural Networks*, 141:330–343. doi: 10.1016/j.neunet.2021.03.010.

Faulk PW, Taylor MG. (1971). An immunocolloid method for the electron microscope. *Immunochemistry*, 8(11):1081–1083. doi: 10.1016/0019-2791(71)90496-4.

Federspiel MJ, Bates P, Young JA, Varmus HE, Hughes SH. (1994). A system for tissue-specific gene targeting: transgenic mice susceptible to subgroup A avian leukosis virus-based retroviral vectors. *PNAS*, 91(23):11241–11245. doi: 10.1073/pnas.91.23.11241.

Feinberg EH, Meister M. (2015). Orientation columns in the mouse superior colliculus. *Nature*, 519(7542):229–232. doi: 10.1038/nature14103.

Feinberg EH, VanHoven MK, Bendesky A, Wang G, Fetter RD, Shen K, Bargmann CI. (2008). GFP Reconstitution Across Synaptic Partners (GRASP) Defines Cell Contacts and Synapses in Living Nervous Systems. *Neuron*, 57(3):353–363. doi: 10.1016/j.neuron.2007.11.030.

Ferster D, Chung S, Wheat H. (1996). Orientation selectivity of thalamic input to simple cells of cat visual cortex. *Nature*, 380(6571):249–252. doi: 10.1038/380249a0.

Fiala JC. (2005). Reconstruct: a free editor for serial section microscopy. *Journal of Microscopy*, 218(Pt 1):52–61. doi: 10.1111/j.1365-2818.2005.01466.x.

Funke J, Tschopp F, Grisaitis W, Sheridan A, Singh C, Saalfeld S, Turaga SC. (2019). Large Scale Image Segmentation with Structured Loss Based Deep Learning for Connectome Reconstruction.

IEEE Transactions on Pattern Analysis and Machine Intelligence, 41(7):1669–1680. doi: 10.1109/TPAMI.2018.2835450.

Furigo IC, de Oliveira WF, de Oliveira AR, Comoli E, Baldo MVC, Mota-Ortiz SR, Canteras NS. (2010). The role of the superior colliculus in predatory hunting. *Neuroscience*, 165(1):1–15. doi: 10.1016/j.neuroscience.2009.10.004.

Gala R, Lebrecht D, Sahlender DA, Jorstad A, Knott G, Holtmaat A, Stepanyants A. (2017). Computer assisted detection of axonal bouton structural plasticity in in vivo time-lapse images. *eLife*, 6:e29315. doi: 10.7554/eLife.29315.

Gale SD, Murphy GJ. (2014). Distinct Representation and Distribution of Visual Information by Specific Cell Types in Mouse Superficial Superior Colliculus. *The Journal of Neuroscience*, 34(40):13458–13471. doi: 10.1523/JNEUROSCI.2768-14.2014.

Gao E, DeAngelis GC, Burkhalter A. (2010). Parallel Input Channels to Mouse Primary Visual Cortex. *The Journal of Neuroscience*, 30(17):5912–5926. doi: 10.1523/JNEUROSCI.6456-09.2010.

Garrett ME, Nauhaus I, Marshel JH, Callaway EM. (2014). Topography and Areal Organization of Mouse Visual Cortex. *The Journal of Neuroscience*, 34(37):12587–12600. doi: 10.1523/JNEUROSCI.1124-14.2014.

Ghose D, Maier A, Nidiffer A, Wallace MT. (2014). Multisensory Response Modulation in the Superficial Layers of the Superior Colliculus. *The Journal of Neuroscience*, 34(12):4332–4344. doi: 10.1523/JNEUROSCI.3004-13.2014.

Ghosh KK, Burns LD, Cocker ED, Nimmerjahn A, Ziv Y, Gamal AE, Schnitzer MJ. (2011). Miniaturized integration of a fluorescence microscope. *Nature Methods*, 8(10):871–878. doi: 10.1038/nmeth.1694.

Gilbert CD, Wiesel TN. (1989). Columnar specificity of intrinsic horizontal and corticocortical connections in cat visual cortex. *The Journal of Neuroscience*, 9(7):2432–2442. doi: 10.1523/JNEUROSCI.09-07-02432.1989.

Ginger M, Haberl M, Conzelmann K-K, Schwarz M, Frick A. (2013). Revealing the secrets of neuronal circuits with recombinant rabies virus technology. *Frontiers in Neural Circuits*, 7:2. doi: 10.3389/fncir.2013.00002.

Glas A, Hübener M, Bonhoeffer T, Goltstein PM. (2021). Spaced training enhances memory and prefrontal ensemble stability in mice. *Current Biology*, 31(18):4052-4061. doi: 10.1016/j.cub.2021.06.085.

Glickfeld LL, Andermann ML, Bonin V, Reid RC. (2013). Cortico-cortical projections in mouse visual cortex are functionally target specific. *Nature Neuroscience*, 16(2):219–226. doi: 10.1038/nn.3300.

Goda Y, Stevens CF. (1994). Two components of transmitter release at a central synapse. *PNAS*, 91(26):12942–12946. doi: 10.1073/pnas.91.26.12942.

Goltstein PM, Montijn JS, Pennartz CMA. (2015). Effects of Isoflurane Anesthesia on Ensemble Patterns of Ca2+ Activity in Mouse V1: Reduced Direction Selectivity Independent of Increased Correlations in Cellular Activity. *PLOS ONE*, 10(2):e0118277. doi: 10.1371/journal.pone.0118277.

Göppert-Mayer M. (1931). Über Elementarakte mit zwei Quantensprüngen. *Annalen der Physik*, 401:273–294. doi: 10.1002/andp.19314010303.

Gordon MD, Scott K. (2009). Motor Control in a Drosophila Taste Circuit. *Neuron*, 61(3):373–384. doi: 10.1016/j.neuron.2008.12.033.

Grabenbauer M, Geerts WJC, Fernadez-Rodriguez J, Hoenger A, Koster AJ, Nilsson T. (2005). Correlative microscopy and electron tomography of GFP through photooxidation. *Nature Methods*, 2(11):857–862. doi: 10.1038/nmeth806.

Graham J. (1977). An autoradiographic study of the efferent connections of the superior colliculus in the cat. *Journal of Comparative Neurology*, 173(4):629–654. doi: 10.1002/cne.901730403.

Granit R. (1947). Sensory mechanisms of the retina. *Oxford University Press*.

Granstedt AE, Szpara ML, Kuhn B, Wang SS-H, Enquist LW. (2009). Fluorescence-Based Monitoring of In Vivo Neural Activity Using a Circuit-Tracing Pseudorabies Virus. *PLOS ONE*, 4(9):e6923. doi: 10.1371/journal.pone.0006923.

Graybiel AM, Berson DM. (1980). Autoradiographic evidence for a projection from the pretectal nucleus of the optic tract to the dorsal lateral geniculate complex in the cat. *Brain Research*, 195(1):1–12. doi: 10.1016/0006-8993(80)90861-6.

Grubb MS, Thompson ID. (2003). Quantitative Characterization of Visual Response Properties in the Mouse Dorsal Lateral Geniculate Nucleus. *Journal of Neurophysiology*, 90(6):3594–3607. doi: 10.1152/jn.00699.2003.

Grubb MS, Thompson ID. (2004). Biochemical and anatomical subdivision of the dorsal lateral geniculate nucleus in normal mice and in mice lacking the β2 subunit of the nicotinic acetylcholine receptor. *Vision Research*, 44(28):3365–3376. doi: 10.1016/j.visres.2004.09.003.

Guillery RW. (1969). A quantitative study of synaptic interconnections in the dorsal lateral geniculate nucleus of the cat. *Zeitschrift für Zellforschung und Mikroskopische Anatomie*, 96:39–48. doi: 10.1007/BF00321475.

Hamill OP, Marty A, Neher E, Sakmann B, Sigworth FJ. (1981). Improved patch-clamp techniques for high-resolution current recording from cells and cell-free membrane patches. *Pflugers Archive: European Journal of Physiology*, 391(2):85–100. doi: 10.1007/BF00656997.

Hammer S, Monavarfeshani A, Lemon T, Su J, Fox MA. (2015). Multiple Retinal Axons Converge onto Relay Cells in the Adult Mouse Thalamus. *Cell Reports*, 12(10):1575–1583. doi: 10.1016/j.celrep.2015.08.003.

Hamos JE, Van Horn SC, Raczkowski D, Uhlrich DJ, Sherman SM. (1985). Synaptic connectivity of a local circuit neurone in lateral geniculate nucleus of the cat. *Nature*, 317(6038):618–621. doi: 10.1038/317618a0.

Han X, Boyden ES. (2007). Multiple-Color Optical Activation, Silencing, and Desynchronization of Neural Activity, with Single-Spike Temporal Resolution. *PLOS ONE*, 2(3):e299. doi: 10.1371/journal.pone.0000299.

Harris KD, Mrsic-Flogel TD. (2013). Cortical connectivity and sensory coding. *Nature*, 503(7474):51–58. doi: 10.1038/nature12654.

Harris KD, Shepherd GMG. (2015). The neocortical circuit: themes and variations. *Nature Neuroscience*, 18(2):170–181. doi: 10.1038/nn.3917.

Harris KM, Stevens JK. (1988). Dendritic spines of rat cerebellar Purkinje cells: serial electron microscopy with reference to their biophysical characteristics. *The Journal of Neuroscience*, 8(12):4455–4469. doi: 10.1523/JNEUROSCI.08-12-04455.1988.

Hartline HK. (1938). The response of single optic nerve fibers of the vertebrate eye to illumination of the retina. *American Journal of Physiology-Legacy Content*, 121(2):400–415. doi: 10.1152/ajplegacy.1938.121.2.400.

Hartline HK. (1969). Visual Receptors and Retinal Interaction. *Science*, 164(3877):270-278. doi: 10.1126/science.164.3877.270.

Hattox AM, Nelson SB. (2007). Layer V Neurons in Mouse Cortex Projecting to Different Targets Have Distinct Physiological Properties. *Journal of Neurophysiology*, 98(6):3330–3340. doi: 10.1152/jn.00397.2007.

Hayworth KJ, Kasthuri N, Schalek R, Lichtman JW. (2006). Automating the Collection of Ultrathin Serial Sections for Large Volume TEM Reconstructions. *Microscopy and Microanalysis*, 12(S02):86–87. doi: 10.1017/S1431927606066268.

Hayworth KJ, Morgan JL, Schalek R, Berger DR, Hildebrand DGC, Lichtman JW. (2014). Imaging ATUM ultrathin section libraries with WaferMapper: a multi-scale approach to EM reconstruction of neural circuits. *Frontiers in Neural Circuits*, 8:68. doi: 10.3389/fncir.2014.00068.

Hayworth KJ, Peale D, Januszewski M, Knott GW, Lu Z, Xu CS, Hess HF. (2020). Gas cluster ion beam SEM for imaging of large tissue samples with 10 nm isotropic resolution. *Nature Methods*, 17(1):68–71. doi: 10.1038/s41592-019-0641-2.

Hecht S, Shlaer S, Pirenne MH. (1942). ENERGY, QUANTA, AND VISION. *Journal of General Physiology*, 25(6):819–840. doi: 10.1085/jgp.25.6.819.

Heinrich Müller. (1856). Anatomisch-physiologische Untersuchungen über die Retina des Menschen und der Wirbelthiere. *Engelmann*.

Hell SW, Kroug M. (1995). Ground-state-depletion fluorscence microscopy: A concept for breaking the diffraction resolution limit. *Applied Physics B*, 60:495–497. doi: 10.1007/BF01081333.

Hell SW, Wichmann J. (1994). Breaking the diffraction resolution limit by stimulated emission: stimulated-emission-depletion fluorescence microscopy. *Optics Letters*, 19(11):780–782. doi: 10.1364/ol.19.000780.

Helmchen F, Denk W. (2005). Deep tissue two-photon microscopy. *Nature Methods*, 2(12):932–940. doi: 10.1038/nmeth818.

Helmstaedter M. (2013). Cellular-resolution connectomics: challenges of dense neural circuit reconstruction. *Nature Methods*, 10(6):501–507. doi: 10.1038/nmeth.2476.

Helmstaedter M, Briggman KL, Denk W. (2011). High-accuracy neurite reconstruction for high-throughput neuroanatomy. *Nature Neuroscience*, 14(8):1081–1088. doi: 10.1038/nn.2868.

Hennig P, Denk W. (2007). Point-spread functions for backscattered imaging in the scanning electron microscope. *Journal of Applied Physics*, 102:123101. doi: 10.1063/1.2817591.

Hersch SM, White EL. (1981). Thalamocortical synapses with corticothalamic projection neurons in mouse SmI cortex: Electron microscopic demonstration of a monosynaptic feedback loop. *Neuroscience Letters*, 24(3):207–210. doi: 10.1016/0304-3940(81)90157-9.

Heymann JAW, Hayles M, Gestmann I, Giannuzzi LA, Lich B, Subramaniam S. (2006). Site-specific 3D imaging of cells and tissues with a dual beam microscope. *Journal of Structural Biology*, 155(1):63–73. doi: 10.1016/j.jsb.2006.03.006.

Hofbauer A, Dräger UC. (1985). Depth segregation of retinal ganglion cells projecting to mouse superior colliculus. *Journal of Comparative Neurology*, 234(4):465–474. doi: 10.1002/cne.902340405.

Holler S, Köstinger G, Martin KAC, Schuhknecht GFP, Stratford KJ. (2021). Structure and function of a neocortical synapse. *Nature*, 591(7848):111–116. doi: 10.1038/s41586-020-03134-2.

Hong YK, Lacefield CO, Rodgers CC, Bruno RM. (2018). Sensation, movement and learning in the absence of barrel cortex. *Nature*, 561(7724):542–546. doi: 10.1038/s41586-018-0527-y.

Horikawa K, Armstrong WE. (1988). A versatile means of intracellular labeling: injection of biocytin and its detection with avidin conjugates. *Journal of Neuroscience Methods*, 25(1):1–11. doi: 10.1016/0165-0270(88)90114-8.

Horikawa K, Yamada Y, Matsuda T, Kobayashi K, Hashimoto M, Matsu-ura T, Miyawaki A, Michikawa T, Mikoshiba K, Nagai T. (2010). Spontaneous network activity visualized by ultrasensitive Ca2+ indicators, yellow Cameleon-Nano. *Nature Methods*, 7(9):729–732. doi: 10.1038/nmeth.1488.

Horton NG, Wang K, Kobat D, Clark CG, Wise FW, Schaffer CB, Xu C. (2013). In vivo three-photon microscopy of subcortical structures within an intact mouse brain. *Nature Photonics*, 7(3):205–209. doi: 10.1038/nphoton.2012.336.

Howarth M, Walmsley L, Brown TM. (2014). Binocular Integration in the Mouse Lateral Geniculate Nuclei. *Current Biology*, 24(11):1241–1247. doi: 10.1016/j.cub.2014.04.014.

Hoy JL, Bishop HI, Niell CM. (2019). Defined Cell Types in Superior Colliculus Make Distinct Contributions to Prey Capture Behavior in the Mouse. *Current Biology*, 29(23):4130-4138.e5. doi: 10.1016/j.cub.2019.10.017.

Hoy JL, Yavorska I, Wehr M, Niell CM. (2016). Vision Drives Accurate Approach Behavior during Prey Capture in Laboratory Mice. *Current Biology*, 26(22):3046–3052. doi: 10.1016/j.cub.2016.09.009.

Hua Y, Laserstein P, Helmstaedter M. (2015). Large-volume en-bloc staining for electron microscopy-based connectomics. *Nature Communications*, 6:7923. doi: 10.1038/ncomms8923.

Huang L, Ledochowitsch P, Knoblich U, Lecoq J, Murphy GJ, Reid RC, de Vries SE, Koch C, Zeng H, Buice MA, Waters J, Li L. (2021a). Relationship between simultaneously recorded spiking

activity and fluorescence signal in GCaMP6 transgenic mice. *eLife*, 10:e51675. doi: 10.7554/eLife.51675.

Huang M, Li D, Cheng X, Pei Q, Xie Z, Gu H, Zhang X, Chen Z, Liu A, Wang Y, Sun F, Li Y, Zhang J, He M, Xie Y, Zhang F, Qi X, Shang C, Cao P. (2021b). The tectonigral pathway regulates appetitive locomotion in predatory hunting in mice. *Nature Communications*, 12(1):4409. doi: 10.1038/s41467-021-24696-3.

Hubel DH, Wiesel TN. (1959). Receptive fields of single neurones in the cat's striate cortex. *The Journal of Physiology*, 148(3):574–591. doi: 10.1113/jphysiol.1959.sp006308.

Hubel DH, Wiesel TN. (1962). Receptive fields, binocular interaction and functional architecture in the cat's visual cortex. *The Journal of Physiology*, 160(1):106–154. doi: 10.1113/jphysiol.1962.sp006837.

Hubel DH, Wiesel TN. (1968). Receptive fields and functional architecture of monkey striate cortex. *The Journal of Physiology*, 195(1):215–243. doi: 10.1113/jphysiol.1968.sp008455.

Hubel DH, Wiesel TN. (1969). Anatomical Demonstration of Columns in the Monkey Striate Cortex. *Nature*, 221(5182):747–750. doi: 10.1038/221747a0.

Hubel DH, Wiesel TN. (1972). Laminar and columnar distribution of geniculo-cortical fibers in the macaque monkey. *Journal of Comparative Neurology*, 146(4):421–450. doi: 10.1002/cne.901460402.

Hubel DH, Wiesel TN. (1974a). Uniformity of monkey striate cortex: A parallel relationship between field size, scatter, and magnification factor. *Journal of Comparative Neurology*, 158(3):295–305. doi: 10.1002/cne.901580305.

Hubel DH, Wiesel TN. (1974b). Sequence regularity and geometry of orientation columns in the monkey striate cortex. *Journal of Comparative Neurology*, 158(3):267–293. doi: 10.1002/cne.901580304.

Hubel DH, Wiesel TN, Stryker MP. (1977). Orientation columns in macaque monkey visual cortex demonstrated by the 2-deoxyglucose autoradiographic technique. *Nature*, 269(5626):328–330. doi: 10.1038/269328a0.

Hübener M, Shoham D, Grinvald A, Bonhoeffer T. (1997). Spatial Relationships among Three Columnar Systems in Cat Area 17. *The Journal of Neuroscience*, 17(23):9270–9284. doi: 10.1523/JNEUROSCI.17-23-09270.1997.

Huberman AD, Feller MB, Chapman B. (2008). Mechanisms Underlying Development of Visual Maps and Receptive Fields. *Annual Review of Neuroscience*, 31:479–509. doi: 10.1146/annurev.neuro.31.060407.125533.

Huberman AD, Wei W, Elstrott J, Stafford BK, Feller MB, Barres BA. (2009). Genetic Identification of an On-Off Direction- Selective Retinal Ganglion Cell Subtype Reveals a Layer-Specific Subcortical Map of Posterior Motion. *Neuron*, 62(3):327–334. doi: 10.1016/j.neuron.2009.04.014.

Hughes HC, Mullikin WH. (1984). Brainstem afferents to the lateral geniculate nucleus of the cat. *Experimental Brain Research*, 54(2):253–258. doi: 10.1007/BF00236224.

Huh CYL, Abdelaal K, Salinas KJ, Gu D, Zeitoun J, Velez DXF, Peach JP, Fowlkes CC, Gandhi SP. (2020). Long-term Monocular Deprivation during Juvenile Critical Period Disrupts Binocular Integration in Mouse Visual Thalamus. *The Journal of Neuroscience*, 40(3):585–604. doi: 10.1523/JNEUROSCI.1626-19.2019.

Iacaruso MF, Gasler IT, Hofer SB. (2017). Synaptic organization of visual space in primary visual cortex. *Nature*, 547(7664):449–452. doi: 10.1038/nature23019.

Ihara K, Umemura T, Katagiri I, Kitajima-Ihara T, Sugiyama Y, Kimura Y, Mukohata Y. (1999). Evolution of the archaeal rhodopsins: evolution rate changes by gene duplication and functional differentiation. *Journal of Molecular Biology*, 285(1):163–174. doi: 10.1006/jmbi.1998.2286.

Jacobs GH, Neitz J, Deegan JF. (1991). Retinal receptors in rodents maximally sensitive to ultraviolet light. *Nature*, 353(6345):655–656. doi: 10.1038/353655a0.

Jaepel J, Hübener M, Bonhoeffer T, Rose T. (2017). Lateral geniculate neurons projecting to primary visual cortex show ocular dominance plasticity in adult mice. *Nature Neuroscience*, 20(12):1708–1714. doi: 10.1038/s41593-017-0021-0.

Januszewski M, Kornfeld J, Li PH, Pope A, Blakely T, Lindsey L, Maitin-Shepard J, Tyka M, Denk W, Jain V. (2018). High-precision automated reconstruction of neurons with flood-filling networks. *Nature Methods*, 15(8):605–610. doi: 10.1038/s41592-018-0049-4.

Jäpel-Schael J. (2017). Experience-dependent functional plasticity of thalamocortical axons. *Dissertation, LMU München: Fakultät für Biologie*. 22923. doi: 10.5282/edoc.22923.

Jeon C-J, Strettoi E, Masland RH. (1998). The Major Cell Populations of the Mouse Retina. *The Journal of Neuroscience*, 18(21):8936–8946. doi: 10.1523/JNEUROSCI.18-21-08936.1998.

Ji W, Gămănuţ R, Bista P, D'Souza RD, Wang Q, Burkhalter A. (2015). Modularity in the Organization of Mouse Primary Visual Cortex. *Neuron*, 87(3):632–643. doi: 10.1016/j.neuron.2015.07.004.

Jin J, Wang Y, Swadlow HA, Alonso JM. (2011). Population receptive fields of ON and OFF thalamic inputs to an orientation column in visual cortex. *Nature Neuroscience*, 14(2):232–238. doi: 10.1038/nn.2729.

Joesch M, Mankus D, Yamagata M, Shahbazi A, Schalek R, Suissa-Peleg A, Meister M, Lichtman JW, Scheirer WJ, Sanes JR. (2016). Reconstruction of genetically identified neurons imaged by serial-section electron microscopy. *eLife*, 5:e15015. doi: 10.7554/eLife.15015.

Jones JP, Palmer LA. (1987a). The two-dimensional spatial structure of simple receptive fields in cat striate cortex. *Journal of Neurophysiology*, 58(6):1187–1211. doi: 10.1152/jn.1987.58.6.1187.

Jones JP, Palmer LA. (1987b). An evaluation of the two-dimensional Gabor filter model of simple receptive fields in cat striate cortex. *Journal of Neurophysiology*, 58(6):1233–1258. doi: 10.1152/jn.1987.58.6.1233.

Jun JJ, Steinmetz NA, Siegle JH, Denman DJ, Bauza M, Barbarits B, Lee AK, Anastassiou CA, Andrei A, Aydın Ç, Barbic M, Blanche TJ, Bonin V, Couto J, Dutta B, Gratiy SL, Gutnisky DA, Häusser M, Karsh B, Ledochowitsch P, Lopez CM, Mitelut C, Musa S, Okun M, Pachitariu M, Putzeys J, Rich PD, Rossant C, Sun W, Svoboda K, Carandini M, Harris KD, Koch C, O'Keefe J, Harris TD.

(2017). Fully integrated silicon probes for high-density recording of neural activity. *Nature*, 551(7679):232–236. doi: 10.1038/nature24636.

Jung JC, Mehta AD, Aksay E, Stepnoski R, Schnitzer MJ. (2004). In Vivo Mammalian Brain Imaging Using One- and Two-Photon Fluorescence Microendoscopy. *Journal of Neurophysiology*, 92(5):3121–3133. doi: 10.1152/jn.00234.2004.

Jung JC, Schnitzer MJ. (2003). Multiphoton endoscopy. *Optics Letters*, 28(11):902–904. doi: 10.1364/ol.28.000902.

Kalatsky VA, Stryker MP. (2003). New Paradigm for Optical Imaging: Temporally Encoded Maps of Intrinsic Signal. *Neuron*, 38(4):529–545. doi: 10.1016/s0896-6273(03)00286-1.

Kandel ER, Mack S, Jessell TM, Schwartz JH, Siegelbaum SA, Hudspeth AJ. (2013). Principles of Neural Science, Fifth Edition. *McGraw Hill Professional*.

Kaschube M. (2014). Neural maps versus salt-and-pepper organization in visual cortex. *Current Opinion in Neurobiology*, 24(1):95–102. doi: 10.1016/j.conb.2013.08.017.

Kasthuri N, Hayworth KJ, Berger DR, Schalek RL, Conchello JA, Knowles-Barley S, Lee D, Vázquez-Reina A, Kaynig V, Jones TR, Roberts M, Morgan JL, Tapia JC, Seung HS, Roncal WG, Vogelstein JT, Burns R, Sussman DL, Priebe CE, Pfister H, Lichtman JW. (2015). Saturated Reconstruction of a Volume of Neocortex. *Cell*, 162(3):648–661. doi: 10.1016/j.cell.2015.06.054.

Kerlin A, Mohar B, Flickinger D, MacLennan BJ, Dean MB, Davis C, Spruston N, Svoboda K. (2019). Functional clustering of dendritic activity during decision-making. *eLife*, 8:e46966. doi: 10.7554/eLife.46966.

Kim I-J, Zhang Y, Meister M, Sanes JR. (2010). Laminar Restriction of Retinal Ganglion Cell Dendrites and Axons: Subtype-Specific Developmental Patterns Revealed with Transgenic Markers. *The Journal of Neuroscience*, 30(4):1452–1462. doi: 10.1523/JNEUROSCI.4779-09.2010.

Kim J, Zhao T, Petralia RS, Yu Y, Peng H, Myers E, Magee JC. (2012). mGRASP enables mapping mammalian synaptic connectivity with light microscopy. *Nature Methods*, 9(1):96–102. doi: 10.1038/nmeth.1784.

Klapoetke NC, Murata Y, Kim SS, Pulver SR, Birdsey-Benson A, Cho YK, Morimoto TK, Chuong AS, Carpenter EJ, Tian Z, Wang J, Xie Y, Yan Z, Zhang Y, Chow BY, Surek B, Melkonian M, Jayaraman V, Constantine-Paton M, Wong GK-S, Boyden ES. (2014). Independent optical excitation of distinct neural populations. *Nature Methods*, 11(3):338–346. doi: 10.1038/nmeth.2836.

Klar TA, Jakobs S, Dyba M, Egner A, Hell SW. (2000). Fluorescence microscopy with diffraction resolution barrier broken by stimulated emission. *PNAS*, 97(15):8206–8210. doi: 10.1073/pnas.97.15.8206.

Klinger E, Motta A, Marr C, Theis FJ, Helmstaedter M. (2021). Cellular connectomes as arbiters of local circuit models in the cerebral cortex. *Nature Communications*, 12(1):2785. doi: 10.1038/s41467-021-22856-z.

Knoll M, Ruska E. (1932). Das Elektronenmikroskop. *Zeitschrift für Physik*, 78:318–339. doi: 10.1007/BF01342199.

Knott G, Marchman H, Wall D, Lich B. (2008). Serial Section Scanning Electron Microscopy of Adult Brain Tissue Using Focused Ion Beam Milling. *The Journal of Neuroscience*, 28(12):2959–2964. doi: 10.1523/JNEUROSCI.3189-07.2008.

Knott GW, Holtmaat A, Trachtenberg JT, Svoboda K, Welker E. (2009). A protocol for preparing GFP-labeled neurons previously imaged in vivo and in slice preparations for light and electron microscopic analysis. *Nature Protocols*, 4(8):1145–1156. doi: 10.1038/nprot.2009.

Ko H, Cossell L, Baragli C, Antolik J, Clopath C, Hofer SB, Mrsic-Flogel TD. (2013). The emergence of functional microcircuits in visual cortex. *Nature*, 496(7443):96–100. doi: 10.1038/nature12015.

Ko H, Hofer SB, Pichler B, Buchanan KA, Sjöström PJ, Mrsic-Flogel TD. (2011). Functional specificity of local synaptic connections in neocortical networks. *Nature*, 473(7345):87–91. doi: 10.1038/nature09880.

Kolbe M, Besir H, Essen L-O, Oesterhelt D. (2000). Structure of the Light-Driven Chloride Pump Halorhodopsin at 1.8 Å Resolution. *Science*, 288(5470):1390–1396. doi: 10.1126/science.288.5470.1390.

Kondo S, Ohki K. (2016). Laminar differences in the orientation selectivity of geniculate afferents in mouse primary visual cortex. *Nature Neuroscience*, 19(2):316–319. doi: 10.1038/nn.4215.

Kondo S, Yoshida T, Ohki K. (2016). Mixed functional microarchitectures for orientation selectivity in the mouse primary visual cortex. *Nature Communications*, 7:13210. doi: 10.1038/ncomms13210.

Krauzlis RJ, Lovejoy LP, Zénon A. (2013). Superior Colliculus and Visual Spatial Attention. *Annual Review of Neuroscience*, 36:165–182. doi: 10.1146/annurev-neuro-062012-170249.

Kremkow J, Jin J, Wang Y, Alonso JM. (2016). Principles underlying sensory map topography in primary visual cortex. *Nature*, 533(7601):52–57. doi: 10.1038/nature17936.

Kreshuk A, Koethe U, Pax E, Bock DD, Hamprecht FA. (2014). Automated Detection of Synapses in Serial Section Transmission Electron Microscopy Image Stacks. *PLOS ONE*, 9(2):e87351. doi: 10.1371/journal.pone.0087351.

Kuan AT, Phelps JS, Thomas LA, Nguyen TM, Han J, Chen C-L, Azevedo AW, Tuthill JC, Funke J, Cloetens P, Pacureanu A, Lee W-CA. (2020). Dense neuronal reconstruction through X-ray holographic nano-tomography. *Nature Neuroscience*, 23(12):1637–1643. doi: 10.1038/s41593-020-0704-9.

Kuffler SW. (1953). Discharge patterns and functional organization of mammalian retina. *Journal of Neurophysiology*, 16(1):37–68. doi: 10.1152/jn.1953.16.1.37.

La Chioma A, Bonhoeffer T, Hübener M. (2019). Area-Specific Mapping of Binocular Disparity across Mouse Visual Cortex. *Current Biology*, 29(17):2954-2960.e5. doi: 10.1016/j.cub.2019.07.037.

La Chioma A, Bonhoeffer T, Hübener M. (2020). Disparity Sensitivity and Binocular Integration in Mouse Visual Cortex Areas. *The Journal of Neuroscience*, 40(46):8883–8899. doi: 10.1523/JNEUROSCI.1060-20.2020.

Laing RJ, Turecek J, Takahata T, Olavarria JF. (2015). Identification of Eye-Specific Domains and Their Relation to Callosal Connections in Primary Visual Cortex of Long Evans Rats. *Cerebral Cortex*, 25(10):3314–3329. doi: 10.1093/cercor/bhu128.

Lam SS, Martell JD, Kamer KJ, Deerinck TJ, Ellisman MH, Mootha VK, Ting AY. (2015). Directed evolution of APEX2 for electron microscopy and proximity labeling. *Nature Methods*, 12(1):51–54. doi: 10.1038/nmeth.3179.

Lampl I, Anderson JS, Gillespie DC, Ferster D. (2001). Prediction of Orientation Selectivity from Receptive Field Architecture in Simple Cells of Cat Visual Cortex. *Neuron*, 30(1):263–274. doi: 10.1016/s0896-6273(01)00278-1.

Lee AM, Hoy JL, Bonci A, Wilbrecht L, Stryker MP, Niell CM. (2014). Identification of a Brainstem Circuit Regulating Visual Cortical State in Parallel with Locomotion. *Neuron*, 83(2):455–466. doi: 10.1016/j.neuron.2014.06.031.

Lee BB, Virsu V, Creutzfeldt OD. (1983). Linear signal transmission from prepotentials to cells in the macaque lateral geniculate nucleus. *Experimental Brain Research*, 52(1):50–56. doi: 10.1007/BF00237148.

Lee H, Tanabe S, Wang S, Hudetz AG. (2021). Differential Effect of Anesthesia on Visual Cortex Neurons with Diverse Population Coupling. *Neuroscience*, 458:108–119. doi: 10.1016/j.neuroscience.2020.11.043.

Lee K, Zung J, Li P, Jain V, Seung HS. (2017). Superhuman Accuracy on the SNEMI3D Connectomics Challenge. *arXiv*, 170600120 [cs].

Lee K-S, Huang X, Fitzpatrick D. (2016a). Topology of ON and OFF inputs in visual cortex enables an invariant columnar architecture. *Nature*, 533(7601):90–94. doi: 10.1038/nature17941.

Lee W-CA, Bonin V, Reed M, Graham BJ, Hood G, Glattfelder K, Reid RC. (2016b). Anatomy and function of an excitatory network in the visual cortex. *Nature*, 532(7599):370–374. doi: 10.1038/nature17192.

Leighton SB. (1981). SEM images of block faces, cut by a miniature microtome within the SEM - a technical note. *Scanning Electron Microscopy*, (Pt 2):73–76.

Leinweber M, Zmarz P, Buchmann P, Argast P, Hübener M, Bonhoeffer T, Keller GB. (2014). Two-photon Calcium Imaging in Mice Navigating a Virtual Reality Environment. *Journal of Visualized Experiments*, (84):e50885. doi: 10.3791/50885.

LeVay S, Hubel DH, Wiesel TN. (1975). The pattern of ocular dominance columns in macaque visual cortex revealed by a reduced silver stain. *Journal of Comparative Neurology*, 159(4):559–575. doi: 10.1002/cne.901590408.

Levene MJ, Dombeck DA, Kasischke KA, Molloy RP, Webb WW. (2004). In Vivo Multiphoton Microscopy of Deep Brain Tissue. *Journal of Neurophysiology*, 91(4):1908–1912. doi: 10.1152/jn.01007.2003.

Liang L, Fratzl A, Goldey G, Ramesh RN, Sugden AU, Morgan JL, Chen C, Andermann ML. (2018). A Fine-Scale Functional Logic to Convergence from Retina to Thalamus. *Cell*, 173(6):1343-1355.e24. doi: 10.1016/j.cell.2018.04.041.

Lien AD, Scanziani M. (2013). Tuned thalamic excitation is amplified by visual cortical circuits. *Nature Neuroscience*, 16(9):1315–1323. doi: 10.1038/nn.3488.

Lin T-Y, Luo J, Shinomiya K, Ting C-Y, Lu Z, Meinertzhagen IA, Lee C-H. (2016). Mapping chromatic pathways in the Drosophila visual system. *Journal of Comparative Neurology*, 524(2):213–227. doi: 10.1002/cne.23857.

Lütcke H, Murayama M, Hahn T, Margolis D, Astori S, Meyer S, Göbel W, Yang Y, Tang W, Kügler S, Sprengel R, Nagai T, Miyawaki A, Larkum M, Helmchen F, Hasan M. (2010). Optical recording of neuronal activity with a genetically-encoded calcium indicator in anesthetized and freely moving mice. *Frontiers in Neural Circuits*, 4:9. doi: 10.3389/fncir.2010.00009.

Maco B, Holtmaat A, Cantoni M, Kreshuk A, Straehle CN, Hamprecht FA, Knott GW. (2013). Correlative In Vivo 2 Photon and Focused Ion Beam Scanning Electron Microscopy of Cortical Neurons. *PLOS ONE*, 8(2):e57405. doi: 10.1371/journal.pone.0057405.

Macpherson LJ, Zaharieva EE, Kearney PJ, Alpert MH, Lin T-Y, Turan Z, Lee C-H, Gallio M. (2015). Dynamic labelling of neural connections in multiple colours by trans-synaptic fluorescence complementation. *Nature Communications*, 6:10024. doi: 10.1038/ncomms10024.

Macrina T, Lee K, Lu R, Turner NL, Wu J, Popovych S, Silversmith W, Kemnitz N, Bae JA, Castro MA, Dorkenwald S, Halageri A, Jia Z, Jordan C, Li K, Mitchell E, Mondal SS, Mu S, Nehoran B, Wong W, Yu S, Bodor AL, Brittain D, Buchanan J, Bumbarger DJ, Cobos E, Collman F, Elabbady L, Fahey PG, Froudarakis E, Kapner D, Kinn S, Mahalingam G, Papadopoulos S, Patel S, Schneider-Mizell CM, Sinz FH, Takeno M, Torres R, Yin W, Pitkow X, Reimer J, Tolias AS, Reid RC, Costa NM da, Seung HS. (2021). Petascale neural circuit reconstruction: automated methods. *bioRxiv*, 445162. https://www.biorxiv.org/content/10.1101/2021.08.04.455162v1

Madisen L, Zwingman TA, Sunkin SM, Oh SW, Zariwala HA, Gu H, Ng LL, Palmiter RD, Hawrylycz MJ, Jones AR, Lein ES, Zeng H. (2010). A robust and high-throughput Cre reporting and characterization system for the whole mouse brain. *Nature Neuroscience*, 13(1):133–140. doi: 10.1038/nn.2467.

Mank M, Santos AF, Direnberger S, Mrsic-Flogel TD, Hofer SB, Stein V, Hendel T, Reiff DF, Levelt C, Borst A, Bonhoeffer T, Hübener M, Griesbeck O. (2008). A genetically encoded calcium indicator for chronic in vivo two-photon imaging. *Nature Methods*, 5(9):805–811. doi: 10.1038/nmeth.1243.

Maranto AR. (1982). Neuronal Mapping: A Photooxidation Reaction Makes Lucifer Yellow Useful for Electron Microscopy. *Science*, 217(4563):953-955. doi: 10.1126/science.7112109.

Markram H, Lübke J, Frotscher M, Roth A, Sakmann B. (1997). Physiology and anatomy of synaptic connections between thick tufted pyramidal neurones in the developing rat neocortex. *The Journal of Physiology*, 500(Pt 2):409–440. doi: 10.1113/jphysiol.1997.sp022031.

Marks TD, Goard MJ. (2021). Stimulus-dependent representational drift in primary visual cortex. *Nature Communications*, 12(1):5169. doi: 10.1038/s41467-021-25436-3.

Marshel JH, Garrett ME, Nauhaus I, Callaway EM. (2011). Functional Specialization of Seven Mouse Visual Cortical Areas. *Neuron*, 72(6):1040–1054. doi: 10.1016/j.neuron.2011.12.004.

Marshel JH, Kaye AP, Nauhaus I, Callaway EM. (2012). Anterior-Posterior Direction Opponency in the Superficial Mouse Lateral Geniculate Nucleus. *Neuron*, 76(4):713–720. doi: 10.1016/j.neuron.2012.09.021.

Marshel JH, Mori T, Nielsen KJ, Callaway EM. (2010). Targeting Single Neuronal Networks for Gene Expression and Cell Labeling In Vivo. *Neuron*, 67(4):562–574. doi: 10.1016/j.neuron.2010.08.001.

Martell JD, Deerinck TJ, Sancak Y, Poulos TL, Mootha VK, Sosinsky GE, Ellisman MH, Ting AY. (2012). Engineered ascorbate peroxidase as a genetically encoded reporter for electron microscopy. *Nature Biotechnology*, 30(11):1143–1148. doi: 10.1038/nbt.2375.

Martersteck EM, Hirokawa KE, Evarts M, Bernard A, Duan X, Li Y, Ng L, Oh SW, Ouellette B, Royall JJ, Stoecklin M, Wang Q, Zeng H, Sanes JR, Harris JA. (2017). Diverse Central Projection Patterns of Retinal Ganglion Cells. *Cell Reports*, 18(8):2058–2072. doi: 10.1016/j.celrep.2017.01.075.

Maruoka H, Nakagawa N, Tsuruno S, Sakai S, Yoneda T, Hosoya T. (2017). Lattice system of functionally distinct cell types in the neocortex. *Science*, 358(6363):610-615. doi: 10.1126/science.aam6125.

Matsuda T, Cepko CL. (2007). Controlled expression of transgenes introduced by in vivo electroporation. *PNAS*, 104(3):1027–1032. doi: 10.1073/pnas.0610155104.

Mazurek M, Kager M, Van Hooser SD. (2014). Robust quantification of orientation selectivity and direction selectivity. *Frontiers in Neural Circuits*, 8:92. doi: 10.3389/fncir.2014.00092.

McAllister AK. (2000). Biolistic Transfection of Neurons. *Science's STKE*, 2000:pl1. doi: 10.1126/stke.2000.51.pl1.

McLaughlin T, O'Leary DDM. (2005). Molecular gradients and development of retinotopic maps. *Annual Review of Neuroscience*, 28:327–355. doi: 10.1146/annurev.neuro.28.061604.135714.

Mechler F, Ringach DL. (2002). On the classification of simple and complex cells. *Vision Research*, 42(8):1017–1033. doi: 10.1016/s0042-6989(02)00025-1.

Métin C, Godement P, Imbert M. (1988). The primary visual cortex in the mouse: Receptive field properties and functional organization. *Experimental Brain Research*, 69(3):594–612. doi: 10.1007/BF00247312.

Michaelis GA. (1842). Über die Retina: besonders über die Macula lutea und das Foramen centrale.

MICrONS Consortium Mic, Bae JA, Baptiste M, Bodor AL, Brittain D, Buchanan J, Bumbarger DJ, Castro MA, Celii B, Cobos E, Collman F, Costa NM da, Dorkenwald S, Elabbady L, Fahey PG, Fliss T, Froudarakis E, Gager J, Gamlin C, Halageri A, Hebditch J, Jia Z, Jordan C, Kapner D, Kemnitz N, Kinn S, Koolman S, Kuehner K, Lee K, Li K, Lu R, Macrina T, Mahalingam G, McReynolds S, Miranda E, Mitchell E, Mondal SS, Moore M, Mu S, Muhammad T, Nehoran B, Ogedengbe O, Papadopoulos C, Papadopoulos S, Patel S, Pitkow X, Popovych S, Ramos A, Reid RC, Reimer J, Schneider-Mizell CM, Seung HS, Silverman B, Silversmith W, Sterling A, Sinz FH, Smith CL, Suckow S, Takeno M, Tan ZH, Tolias AS, Torres R, Turner NL, Walker EY, Wang T, Williams G, Williams S, Willie K, Willie R, Wong W, Wu J, Xu C, Yang R, Yatsenko D, Ye F, Yin W, Yu S. (2021). Functional connectomics spanning multiple areas of mouse visual cortex. *bioRxiv*, 454025. https://www.biorxiv.org/content/10.1101/2021.07.28.454025v2

Mikula S, Binding J, Denk W. (2012). Staining and embedding the whole mouse brain for electron microscopy. *Nature Methods*, 9(12):1198–1201. doi: 10.1038/nmeth.2213.

Mishchenko Y, Hu T, Spacek J, Mendenhall J, Harris KM, Chklovskii DB. (2010). Ultrastructural Analysis of Hippocampal Neuropil from the Connectomics Perspective. *Neuron*, 67(6):1009–1020. doi: 10.1016/j.neuron.2010.08.014.

Mitchell E, Keselj S, Popovych S, Buniatyan D, Seung HS. (2019). Siamese Encoding and Alignment by Multiscale Learning with Self-Supervision. *arXiv*, 190402643 [cs].

Miyamichi K, Amat F, Moussavi F, Wang C, Wickersham I, Wall NR, Taniguchi H, Tasic B, Huang ZJ, He Z, Callaway EM, Horowitz MA, Luo L. (2011). Cortical representations of olfactory input by trans-synaptic tracing. *Nature*, 472(7342):191–196. doi: 10.1038/nature09714.

Miyawaki A, Griesbeck O, Heim R, Tsien RY. (1999). Dynamic and quantitative Ca2+ measurements using improved cameleons. *PNAS*, 96(5):2135–2140. doi: 10.1073/pnas.96.5.2135.

Miyawaki A, Llopis J, Heim R, McCaffery JM, Adams JA, Ikura M, Tsien RY. (1997). Fluorescent indicators for Ca2+based on green fluorescent proteins and calmodulin. *Nature*, 388(6645):882–887. doi: 10.1038/42264.

Mizrahi A, Crowley JC, Shtoyerman E, Katz LC. (2004). High-Resolution In Vivo Imaging of Hippocampal Dendrites and Spines. *The Journal of Neuroscience*, 24(13):3147–3151. doi: 10.1523/JNEUROSCI.5218-03.2004.

Moerner WE, Kador L. (1989). Optical detection and spectroscopy of single molecules in a solid. *Physical Review Letters*, 62(21):2535–2538. doi: 10.1103/PhysRevLett.62.2535.

Montijn JS, Meijer GT, Lansink CS, Pennartz CMA. (2016). Population-Level Neural Codes Are Robust to Single-Neuron Variability from a Multidimensional Coding Perspective. *Cell Reports*, 16(9):2486–2498. doi: 10.1016/j.celrep.2016.07.065.

Morgan JL, Berger DR, Wetzel AW, Lichtman JW. (2016). The Fuzzy Logic of Network Connectivity in Mouse Visual Thalamus. *Cell*, 165(1):192–206. doi: 10.1016/j.cell.2016.02.033.

Morin LP, Studholme KM. (2014). Retinofugal projections in the mouse. *Journal of Comparative Neurology*, 522(16):3733–3753. doi: 10.1002/cne.23635.

Morris R. (1984). Developments of a water-maze procedure for studying spatial learning in the rat. *Journal of Neuroscience Methods*, 11(1):47–60. doi: 10.1016/0165-0270(84)90007-4.

Morton AJ, Skillings E, Bussey TJ, Saksida LM. (2006). Measuring cognitive deficits in disabled mice using an automated interactive touchscreen system. *Nature Methods*, 3(10):767–767. doi: 10.1038/nmeth1006-767.

Motta A, Berning M, Boergens KM, Staffler B, Beining M, Loomba S, Hennig P, Wissler H, Helmstaedter M. (2019). Dense connectomic reconstruction in layer 4 of the somatosensory cortex. *Science*, 366(6469):eaay3134. doi: 10.1126/science.aay3134.

Mrsic-Flogel TD, Hofer SB, Ohki K, Reid RC, Bonhoeffer T, Hübener M. (2007). Homeostatic Regulation of Eye-Specific Responses in Visual Cortex during Ocular Dominance Plasticity. *Neuron*, 54(6):961–972. doi: 10.1016/j.neuron.2007.05.028.

Murray TA, Levene MJ. (2012). Singlet gradient index lens for deep in vivo multiphoton microscopy. *Journal of Biomedical Optics*, 17(2):021106. doi: 10.1117/1.JBO.17.2.021106.

Nagel G, Ollig D, Fuhrmann M, Kateriya S, Musti AM, Bamberg E, Hegemann P. (2002). Channelrhodopsin-1: A Light-Gated Proton Channel in Green Algae. *Science*, 296(5577):2395–2398. doi: 10.1126/science.1072068.

Nagel G, Szellas T, Huhn W, Kateriya S, Adeishvili N, Berthold P, Ollig D, Hegemann P, Bamberg E. (2003). Channelrhodopsin-2, a directly light-gated cation-selective membrane channel. *PNAS*, 100(24):13940–13945. doi: 10.1073/pnas.1936192100.

Nakai J, Ohkura M, Imoto K. (2001). A high signal-to-noise Ca2+ probe composed of a single green fluorescent protein. *Nature Biotechnology*, 19(2):137–141. doi: 10.1038/84397.

Neher E, Sakmann B. (1976). Single-channel currents recorded from membrane of denervated frog muscle fibres. *Nature*, 260(5554):799–802. doi: 10.1038/260799a0.

Niell CM, Stryker MP. (2008). Highly Selective Receptive Fields in Mouse Visual Cortex. *The Journal of Neuroscience*, 28(30):7520–7536. doi: 10.1523/JNEUROSCI.0623-08.2008.

Oesterhelt D, Hegemann P, Tittor J. (1985). The photocycle of the chloride pump halorhodopsin. II: Quantum yields and a kinetic model. *The EMBO Journal*, 4(9):2351–2356. doi: 10.1002/j.1460-2075.1985.tb03938.x.

Ohki K, Chung S, Ch'ng YH, Kara P, Reid RC. (2005). Functional imaging with cellular resolution reveals precise micro-architecture in visual cortex. *Nature*, 433(7026):597–603. doi: 10.1038/nature03274.

Ohki K, Chung S, Kara P, Hübener M, Bonhoeffer T, Reid RC. (2006). Highly ordered arrangement of single neurons in orientation pinwheels. *Nature*, 442(7105):925–928. doi: 10.1038/nature05019.

Ohki K, Reid RC. (2007). Specificity and randomness in the visual cortex. *Current Opinion in Neurobiology*, 17(4):401–407. doi: 10.1016/j.conb.2007.07.007.

Olsen SR, Bortone DS, Adesnik H, Scanziani M. (2012). Gain control by layer six in cortical circuits of vision. *Nature*, 483(7387):47–52. doi: 10.1038/nature10835.

Oomen CA, Hvoslef-Eide M, Heath CJ, Mar AC, Horner AE, Bussey TJ, Saksida LM. (2013). The touchscreen operant platform for testing working memory and pattern separation in rats and mice. *Nature Protocols*, 8(10):2006–2021. doi: 10.1038/nprot.2013.124.

Osakada F, Mori T, Cetin AH, Marshel JH, Virgen B, Callaway EM. (2011). New Rabies Virus Variants for Monitoring and Manipulating Activity and Gene Expression in Defined Neural Circuits. *Neuron*, 71(4):617–631. doi: 10.1016/j.neuron.2011.07.005.

Osterberg GA. (1935). Topography of the layer of the rods and cones in the human retina. *Acta ophthalmoligica*, 13:1–102.

Otchy TM, Wolff SBE, Rhee JY, Pehlevan C, Kawai R, Kempf A, Gobes SMH, Ölveczky BP. (2015). Acute off-target effects of neural circuit manipulations. *Nature*, 528(7582):358–363. doi: 10.1038/nature16442.

Ouzounov DG, Wang T, Wang M, Feng DD, Horton NG, Cruz-Hernández JC, Cheng Y-T, Reimer J, Tolias AS, Nishimura N, Xu C. (2017). In vivo three-photon imaging of activity of GCaMP6-labeled neurons deep in intact mouse brain. *Nature Methods*, 14(4):388–390. doi: 10.1038/nmeth.4183.

Palade GE. (1952). A STUDY OF FIXATION FOR ELECTRON MICROSCOPY. *Journal of Experimental Medicine*, 95(3):285–298. doi: 10.1084/jem.95.3.285.

Pallotto M, Watkins PV, Fubara B, Singer JH, Briggman KL. (2015). Extracellular space preservation aids the connectomic analysis of neural circuits. *eLife*, 4:e08206. doi: 10.7554/eLife.08206.

Park S-G, Jeong Y-C, Kim D-G, Lee M-H, Shin A, Park G, Ryoo J, Hong J, Bae S, Kim C-H, Lee P-S, Kim D. (2018). Medial preoptic circuit induces hunting-like actions to target objects and prey. *Nature Neuroscience*, 21(3):364–372. doi: 10.1038/s41593-018-0072-x.

Payne BR, Berman N, Murphy EH. (1981). Organization of direction preferences in cat visual cortex. *Brain Research*, 211(2):445–450. doi: 10.1016/0006-8993(81)90971-9.

Pelli DG. (1997). The VideoToolbox software for visual psychophysics: transforming numbers into movies. *Spatial Vision*, 10:437–442.

Perez-Alvarez A, Fearey BC, O'Toole RJ, Yang W, Arganda-Carreras I, Lamothe-Molina PJ, Moeyaert B, Mohr MA, Panzera LC, Schulze C, Schreiter ER, Wiegert JS, Gee CE, Hoppa MB, Oertner TG. (2020). Freeze-frame imaging of synaptic activity using SynTagMA. *Nature Communications*, 11(1):2464. doi: 10.1038/s41467-020-16315-4.

Pérez-Ortega J, Alejandre-García T, Yuste R. (2021). Long-term stability of cortical ensembles. *eLife*, 10:e64449. doi: 10.7554/eLife.64449.

Perry VH, Cowey A. (1984). Retinal ganglion cells that project to the superior colliculus and pretectum in the macaque monkey. *Neuroscience*, 12(4):1125–1137. doi: 10.1016/0306-4522(84)90007-1.

Perry VH, Oehler R, Cowey A. (1984). Retinal ganglion cells that project to the dorsal lateral geniculate nucleus in the macaque monkey. *Neuroscience*, 12(4):1101–1123. doi: 10.1016/0306-4522(84)90006-x.

Peticolas WL, Rieckhoff KE. (1963). Double-Photon Excitation of Organic Molecules in Dilute Solution. *The Journal of Chemical Physics*, 39:1347–1348. doi: 10.1063/1.1734440.

Pilz G-A, Carta S, Stäuble A, Ayaz A, Jessberger S, Helmchen F. (2016). Functional Imaging of Dentate Granule Cells in the Adult Mouse Hippocampus. *The Journal of Neuroscience*, 36(28):7407–7414. doi: 10.1523/JNEUROSCI.3065-15.2016.

Piscopo DM, El-Danaf RN, Huberman AD, Niell CM. (2013). Diverse Visual Features Encoded in Mouse Lateral Geniculate Nucleus. *The Journal of Neuroscience*, 33(11):4642–4656. doi: 10.1523/JNEUROSCI.5187-12.2013.

Pologruto TA, Sabatini BL, Svoboda K. (2003). ScanImage: Flexible software for operating laser scanning microscopes. *BioMedical Engineering OnLine*, 2:13. doi: 10.1186/1475-925X-2-13.

Polyak SL. (1941). The retina. *Univ. Chicago Press.*

Preibisch S, Saalfeld S, Tomancak P. (2009). Globally optimal stitching of tiled 3D microscopic image acquisitions. *Bioinformatics*, 25(11):1463–1465. doi: 10.1093/bioinformatics/btp184.

Prusky GT, Alam NM, Beekman S, Douglas RM. (2004). Rapid Quantification of Adult and Developing Mouse Spatial Vision Using a Virtual Optomotor System. *Investigative Ophthalmology & Visual Science*, 45(12):4611–4616. doi: 10.1167/iovs.04-0541.

Prusky GT, Douglas RM. (2003). Developmental plasticity of mouse visual acuity. European Journal of *Neuroscience*, 17(1):167–173. doi: 10.1046/j.1460-9568.2003.02420.x.

Qian Y, Cosio DMO, Piatkevich KD, Aufmkolk S, Su W-C, Celiker OT, Schohl A, Murdock MH, Aggarwal A, Chang Y-F, Wiseman PW, Ruthazer ES, Boyden ES, Campbell RE. (2020). Improved genetically encoded near-infrared fluorescent calcium ion indicators for in vivo imaging. *PLOS Biology*, 18(11):e3000965. doi: 10.1371/journal.pbio.3000965.

Qian Y, Piatkevich KD, Mc Larney B, Abdelfattah AS, Mehta S, Murdock MH, Gottschalk S, Molina RS, Zhang W, Chen Y, Wu J, Drobizhev M, Hughes TE, Zhang J, Schreiter ER, Shoham S, Razansky D, Boyden ES, Campbell RE. (2019). A genetically encoded near-infrared fluorescent calcium ion indicator. *Nature Methods*, 16(2):171–174. doi: 10.1038/s41592-018-0294-6.

Rafols JA, Valverde F. (1973). The structure of the dorsal lateral geniculate nucleus in the mouse. A golgi and electron microscopic study. *Journal of Comparative Neurology*, 150(3):303–331. doi: 10.1002/cne.901500305.

Rancz EA, Franks KM, Schwarz MK, Pichler B, Schaefer AT, Margrie TW. (2011). Transfection via whole-cell recording in vivo: bridging single-cell physiology, genetics and connectomics. *Nature Neuroscience*, 14(4):527–532. doi: 10.1038/nn.2765.

Rapaport DH, Stone J. (1984). The area centralis of the retina in the cat and other mammals: Focal point for function and development of the visual system. *Neuroscience*, 11(2):289–301. doi: 10.1016/0306-4522(84)90024-1.

Raymond CS, Soriano P. (2007). High-Efficiency FLP and ΦC31 Site-Specific Recombination in Mammalian Cells. *PLOS ONE*, 2(1):e162. doi: 10.1371/journal.pone.0000162.

Reardon TR, Murray AJ, Turi GF, Wirblich C, Croce KR, Schnell MJ, Jessell TM, Losonczy A. (2016). Rabies Virus CVS-N2cΔG Strain Enhances Retrograde Synaptic Transfer and Neuronal Viability. *Neuron*, 89(4):711–724. doi: 10.1016/j.neuron.2016.01.004.

Reese BE. (1988). 'Hidden lamination' in the dorsal lateral geniculate nucleus: the functional organization of this thalamic region in the rat. *Brain Research Reviews*, 472(2):119-37. doi: 10.1016/0165-0173(88)90017-3.

Reese BE, Jeffery G. (1983). Crossed and uncrossed visual topography in dorsal lateral geniculate nucleus of the pigmented rat. *Journal of Neurophysiology*, 49(4):877–885. doi: 10.1152/jn.1983.49.4.877.

Reid RC. (2012). From Functional Architecture to Functional Connectomics. *Neuron*, 75(2):209–217. doi: 10.1016/j.neuron.2012.06.031.

Reid RC, Alonso J-M. (1995). Specificity of monosynaptic connections from thalamus to visual cortex. *Nature*, 378:281–284. doi: 10.1038/378281a0.

Reid RC, Soodak RE, Shapley RM. (1987). Linear mechanisms of directional selectivity in simple cells of cat striate cortex. *PNAS*, 84(23):8740–8744. doi: 10.1073/pnas.84.23.8740.

Reimer J, Froudarakis E, Cadwell CR, Yatsenko D, Denfield GH, Tolias AS. (2014). Pupil Fluctuations Track Fast Switching of Cortical States during Quiet Wakefulness. *Neuron*, 84(20:355–362. doi: 10.1016/j.neuron.2014.09.033.

Reinert S, Hübener M, Bonhoeffer T, Goltstein PM. (2021). Mouse prefrontal cortex represents learned rules for categorization. *Nature*, 593(7859):411–417. doi: 10.1038/s41586-021-03452-z.

Reinhold K, Lien AD, Scanziani M. (2015). Distinct recurrent versus afferent dynamics in cortical visual processing. *Nature Neuroscience*, 18(12):1789–1797. doi: 10.1038/nn.4153.

Rice DS, Williams RW, Goldowitz D. (1995). Genetic control of retinal projections in inbred strains of albino mice. *Journal of Comparative Neurology*, 354(3):459–469. doi: 10.1002/cne.903540312.

Ringach DL. (2021). Sparse thalamocortical convergence. *Current Biology*, 31(10):2199-2202.e2. doi: 10.1016/j.cub.2021.02.032.

Ringach DL, Hawken MJ, Shapley R. (1997). Dynamics of orientation tuning in macaque primary visual cortex. *Nature*, 387(6630):281–284. doi: 10.1038/387281a0.

Ringach DL, Mineault PJ, Tring E, Olivas ND, Garcia-Junco-Clemente P, Trachtenberg JT. (2016). Spatial clustering of tuning in mouse primary visual cortex. *Nature Communications*, 7:12270. doi: 10.1038/ncomms12270.

Ringach DL, Shapley RM, Hawken MJ. (2002). Orientation Selectivity in Macaque V1: Diversity and Laminar Dependence. *The Journal of Neuroscience*, 22(13):5639–5651. doi: 10.1523/JNEUROSCI.22-13-05639.2002.

Röhlich P, van Veen Th, Szél Á. (1994). Two different visual pigments in one retinal cone cell. *Neuron*, 13(5):1159–1166. doi: 10.1016/0896-6273(94)90053-1.

Rolls ET, Cowey A. (1970). Topography of the retina and striate cortex and its relationship to visual acuity in rhesus monkeys and squirrel monkeys. *Experimental Brain Research*, 10(3):298–310. doi: 10.1007/BF00235053.

Román Rosón M, Bauer Y, Kotkat AH, Berens P, Euler T, Busse L. (2019). Mouse dLGN Receives Functional Input from a Diverse Population of Retinal Ganglion Cells with Limited Convergence. *Neuron*, 102(2):462-476.e8. doi: 10.1016/j.neuron.2019.01.040.

Rompani SB, Müllner FE, Wanner A, Zhang C, Roth CN, Yonehara K, Roska B. (2017). Different Modes of Visual Integration in the Lateral Geniculate Nucleus Revealed by Single-Cell-Initiated Transsynaptic Tracing. *Neuron*, 93(4):767-776.e6. doi: 10.1016/j.neuron.2017.01.028.

Rose T, Goltstein PM, Portugues R, Griesbeck O. (2014). Putting a finishing touch on GECIs. *Frontiers in Molecular Neuroscience*, 7:88. doi: 10.3389/fnmol.2014.00088.

Rose T, Jaepel J, Hübener M, Bonhoeffer T. (2016). Cell-specific restoration of stimulus preference after monocular deprivation in the visual cortex. *Science*, 352(6291):1319-1322. doi: 10.1126/science.aad3358.

Rose T, Schoenenberger P, Jezek K, Oertner TG. (2013). Developmental Refinement of Vesicle Cycling at Schaffer Collateral Synapses. *Neuron*, 77(6):1109–1121. doi: 10.1016/j.neuron.2013.01.021.

Rossi LF, Harris KD, Carandini M. (2020). Spatial connectivity matches direction selectivity in visual cortex. *Nature*, 588(7839):648–652. doi: 10.1038/s41586-020-2894-4.

Roth MM, Dahmen JC, Muir DR, Imhof F, Martini FJ, Hofer SB. (2016). Thalamic nuclei convey diverse contextual information to layer 1 of visual cortex. *Nature Neuroscience*, 19(2):299–307. doi: 10.1038/nn.4197.

Sakatani T, Isa T. (2007). Quantitative analysis of spontaneous saccade-like rapid eye movements in C57BL/6 mice. *Neuroscience Research*, 58(3):324–331. doi: 10.1016/j.neures.2007.04.003.

Samonds JM, Choi V, Priebe NJ. (2019). Mice Discriminate Stereoscopic Surfaces Without Fixating in Depth. *The Journal of Neuroscience*, 39(41):8024–8037. doi: 10.1523/JNEUROSCI.0895-19.2019.

Sauer B, Henderson N. (1988). Site-specific DNA recombination in mammalian cells by the Cre recombinase of bacteriophage P1. *PNAS*, 85(14):5166–5170. doi: 10.1073/pnas.85.14.5166.

Scala F, Kobak D, Shan S, Bernaerts Y, Laturnus S, Cadwell CR, Hartmanis L, Froudarakis E, Castro JR, Tan ZH, Papadopoulos S, Patel SS, Sandberg R, Berens P, Jiang X, Tolias AS. (2019). Layer 4 of mouse neocortex differs in cell types and circuit organization between sensory areas. *Nature Communications*, 10(1):4174. doi: 10.1038/s41467-019-12058-z.

Schalek R, Kasthuri N, Hayworth K, Berger D, Tapia J, Morgan J, Turaga S, Fagerholm E, Seung H, Lichtman J. (2011). Development of High-Throughput, High-Resolution 3D Reconstruction of Large-Volume Biological Tissue Using Automated Tape Collection Ultramicrotomy and Scanning Electron Microscopy. *Microscopy and Microanalysis*, 17(S2):966–967. doi: 10.1017/S1431927611005708.

Scheffer LK, Karsh B, Vitaladevun S. (2013). Automated Alignment of Imperfect EM Images for Neural Reconstruction. *arXiv*, 13046034 [q-bio].

Schiller J, Helmchen F, Sakmann B. (1995). Spatial profile of dendritic calcium transients evoked by action potentials in rat neocortical pyramidal neurones. *The Journal of Physiology*, 487(Pt 3):583–600. doi: 10.1113/jphysiol.1995.sp020902.

Schmidt H, Gour A, Straehle J, Boergens KM, Brecht M, Helmstaedter M. (2017). Axonal synapse sorting in medial entorhinal cortex. *Nature*, 549(7673):469–475. doi: 10.1038/nature24005.

Scholl B, Tan AYY, Corey J, Priebe NJ. (2013). Emergence of Orientation Selectivity in the Mammalian Visual Pathway. *The Journal of Neuroscience*, 33(26):10616–10624. doi: 10.1523/JNEUROSCI.0404-13.2013.

Schubert PJ, Dorkenwald S, Januszewski M, Jain V, Kornfeld J. (2019). Learning cellular morphology with neural networks. *Nature Communications*, 10(1):2736. doi: 10.1038/s41467-019-10836-3.

Schuett S, Bonhoeffer T, Hübener M. (2002). Mapping Retinotopic Structure in Mouse Visual Cortex with Optical Imaging. *The Journal of Neuroscience*, 22(15):6549–6559. doi: 10.1523/JNEUROSCI.22-15-06549.2002.

Schultze M. (1866). Zur Anatomie und Physiologie der Retina. *Archiv für mikroskopische Anatomie*, 2:175–286.

Seabrook TA, Burbridge TJ, Crair MC, Huberman AD. (2017). Architecture, Function, and Assembly of the Mouse Visual System. *Annual Review of Neuroscience*, 40:499–538. doi: 10.1146/annurev-neuro-071714-033842.

Seligman AM, Wasserkrug HL, Hanker JS. (1966). A NEW STAINING METHOD (OTO) FOR ENHANCING CONTRAST OF LIPID-CONTAINING MEMBRANES AND DROPLETS IN OSMIUM TETROXIDE-FIXED TISSUE WITH OSMIOPHILIC THIOCARBOHYDRAZIDE (TCH). *Journal of Cell Biology*, 30(2):424–432. doi: 10.1083/jcb.30.2.424.

Serwanski DR, Miralles CP, Christie SB, Mehta AK, Li X, De Blas AL. (2006). Synaptic and nonsynaptic localization of GABAA receptors containing the α5 subunit in the rat brain. *Journal of Comparative Neurology*, 499(3):458–470. doi: 10.1002/cne.21115.

Shang C, Liu A, Li D, Xie Z, Chen Z, Huang M, Li Y, Wang Y, Shen WL, Cao P. (2019). A subcortical excitatory circuit for sensory-triggered predatory hunting in mice. *Nature Neuroscience*, 22(6):909–920. doi: 10.1038/s41593-019-0405-4.

Shang C, Liu Z, Chen Z, Shi Y, Wang Q, Liu S, Li D, Cao P. (2015). A parvalbumin-positive excitatory visual pathway to trigger fear responses in mice. *Science*, 348(6242):1472-1477. doi: 10.1126/science.aaa8694.

Shapson-Coe A, Januszewski M, Berger DR, Pope A, Wu Y, Blakely T, Schalek RL, Li PH, Wang S, Maitin-Shepard J, Karlupia N, Dorkenwald S, Sjostedt E, Leavitt L, Lee D, Bailey L, Fitzmaurice A, Kar R, Field B, Wu H, Wagner-Carena J, Aley D, Lau J, Lin Z, Wei D, Pfister H, Peleg A, Jain V, Lichtman JW. (2021). A connectomic study of a petascale fragment of human cerebral cortex. *bioRxiv*, 446289. https://www.biorxiv.org/content/10.1101/2021.05.29.446289v2

Shatz CJ, Lindström S, Wiesel TN. (1977). The distribution of afferents representing the right and left eyes in the cat's visual cortex. *Brain Research*, 131(1):103–116. doi: 10.1016/0006-8993(77)90031-2.

Sherman SM. (2004). Interneurons and triadic circuitry of the thalamus. *Trends in Neurosciences*, 27(11):670–675. doi: 10.1016/j.tins.2004.08.003.

Sherman SM, Guillery RW. (1998). On the actions that one nerve cell can have on another: Distinguishing "drivers" from "modulators." *PNAS*, 95(12):7121–7126. doi: 10.1073/pnas.95.12.7121.

Sherrington CS. (1906). The integrative action of the nervous system. *Yale University Press*. doi: 10.1037/13798-000.

Shi X, Barchini J, Ledesma HA, Koren D, Jin Y, Liu X, Wei W, Cang J. (2017). Retinal origin of direction selectivity in the superior colliculus. *Nature Neuroscience*, 20(4):550–558. doi: 10.1038/nn.4498.

Shu X, Lev-Ram V, Deerinck TJ, Qi Y, Ramko EB, Davidson MW, Jin Y, Ellisman MH, Tsien RY. (2011). A Genetically Encoded Tag for Correlated Light and Electron Microscopy of Intact Cells, Tissues, and Organisms. *PLOS Biology*, 9(40:e1001041. doi: 10.1371/journal.pbio.1001041.

Sigworth FJ, Neher E. (1980). Single Na+ channel currents observed in cultured rat muscle cells. *Nature*, 287(5781):447–449. doi: 10.1038/287447a0.

Sillito AM. (1975). The effectiveness of bicuculline as an antagonist of GABA and visually evoked inhibition in the cat's striate cortex. *The Journal of Physiology*, 250(2):287–304. doi: 10.1113/jphysiol.1975.sp011055.

Sjöstrand FS. (1948). The Ultrastructure of the Retinal Rods of the Guinea Pig Eye. *Journal of Applied Physics*, 19:1188–1188.

Sjöstrand FS. (1953). The ultrastructure of the inner segments of the retinal rods of the guinea pig eye as revealed by electron microscopy. *Journal of Cellular and Comparative Physiology*, 42(1):45–70. doi: 10.1002/jcp.1030420104.

Sjöstrand FS. (1958). Ultrastructure of retinal rod synapses of the guinea pig eye as revealed by three-dimensional reconstructions from serial sections. *Journal of Ultrastructure Research*, 2(1):122–170. doi: 10.1016/s0022-5320(58)90050-9.

Smith GB, Heynen AJ, Bear MF. (2009). Bidirectional synaptic mechanisms of ocular dominance plasticity in visual cortex. *Philosophical Transactions of the Royal Society B: Biological Sciences*, 364(1515):357–367. doi: 10.1098/rstb.2008.0198.

Smith SL, Häusser M. (2010). Parallel processing of visual space by neighboring neurons in mouse visual cortex. *Nature Neuroscience*, 13(9):1144–1149. doi: 10.1038/nn.2620.

Smyth D, Willmore B, Baker GE, Thompson ID, Tolhurst DJ. (2003). The Receptive-Field Organization of Simple Cells in Primary Visual Cortex of Ferrets under Natural Scene Stimulation. *The Journal of Neuroscience*, 23(11):4746–4759. doi: 10.1523/JNEUROSCI.23-11-04746.2003.

Sommeijer J-P, Ahmadlou M, Saiepour MH, Seignette K, Min R, Heimel JA, Levelt CN. (2017). Thalamic inhibition regulates critical-period plasticity in visual cortex and thalamus. *Nature Neuroscience*, 20(12):1715–1721. doi: 10.1038/s41593-017-0002-3.

Somogyi P, Tamás G, Lujan R, Buhl EH. (1998). Salient features of synaptic organisation in the cerebral cortex. *Brain Research Reviews*, 26(2-3):113–135. doi: 10.1016/s0165-0173(97)00061-1.

Staffler B, Berning M, Boergens KM, Gour A, Smagt P van der, Helmstaedter M. (2017). SynEM, automated synapse detection for connectomics. *eLife*, 6:e26414. doi: 10.7554/eLife.26414.

Stahl JS. (2004). Using eye movements to assess brain function in mice. *Vision Research*, 44(28):3401–3410. doi: 10.1016/j.visres.2004.09.011.

Steinmetz NA, Aydin C, Lebedeva A, Okun M, Pachitariu M, Bauza M, Beau M, Bhagat J, Böhm C, Broux M, Chen S, Colonell J, Gardner RJ, Karsh B, Kloosterman F, Kostadinov D, Mora-Lopez C, O'Callaghan J, Park J, Putzeys J, Sauerbrei B, Daal RJJ van, Vollan AZ, Wang S, Welkenhuysen M, Ye Z, Dudman JT, Dutta B, Hantman AW, Harris KD, Lee AK, Moser EI, O'Keefe J, Renart A, Svoboda K, Häusser M, Haesler S, Carandini M, Harris TD. (2021). Neuropixels 2.0: A miniaturized high-density probe for stable, long-term brain recordings. *Science*, 372(6539):abf4588. doi: 10.1126/science.abf4588.

Sternberg N, Hamilton D. (1981). Bacteriophage P1 site-specific recombination: I. Recombination between loxP sites. *Journal of Molecular Biology*, 150(4):467–486. doi: 10.1016/0022-2836(81)90375-2.

Sterratt DC, Lyngholm D, Willshaw DJ, Thompson ID. (2013). Standard Anatomical and Visual Space for the Mouse Retina: Computational Reconstruction and Transformation of Flattened Retinae with the Retistruct Package. *PLOS Computational Biology*, 9(2):e1002921. doi: 10.1371/journal.pcbi.1002921.

Stokes GG. (1852). XXX. On the change of refrangibility of light. *Philosophical Transactions of the Royal Society of London*, 142:463–562. doi: 10.1098/rstl.1852.0022.

Stoppini L, Buchs P-A, Muller D. (1991). A simple method for organotypic cultures of nervous tissue. *Journal of Neuroscience Methods*, 37(2):173–182. doi: 10.1016/0165-0270(91)90128-m.

Stosiek C, Garaschuk O, Holthoff K, Konnerth A. (2003). In vivo two-photon calcium imaging of neuronal networks. *PNAS*, 100(12):7319–7324. doi: 10.1073/pnas.1232232100.

Stringer C, Pachitariu M. (2019). Computational processing of neural recordings from calcium imaging data. *Current Opinion in Neurobiology*, 55:22–31. doi: 10.1016/j.conb.2018.11.005.

Stuart GJ, Sakmann B. (1994). Active propagation of somatic action potentials into neocortical pyramidal cell dendrites. *Nature*, 367(6458):69–72. doi: 10.1038/367069a0.

Sun W, Tan Z, Mensh BD, Ji N. (2016). Thalamus provides layer 4 of primary visual cortex with orientation- and direction-tuned inputs. *Nature Neuroscience*, 19(2):308–315. doi: 10.1038/nn.4196.

Svoboda K, Denk W, Kleinfeld D, Tank DW. (1997). In vivo dendritic calcium dynamics in neocortical pyramidal neurons. *Nature*, 385(6612):161–165. doi: 10.1038/385161a0.

Swindale NV, Matsubara JA, Cynader MS. (1987). Surface organization of orientation and direction selectivity in cat area 18. *The Journal of Neuroscience*, 7(5):1414–1427. doi: 10.1523/JNEUROSCI.07-05-01414.1987.

Swindale NV, Shoham D, Grinvald A, Bonhoeffer T, Hübener M. (2000). Visual cortex maps are optimized for uniform coverage. *Nature Neuroscience*, 3(8):822–826. doi: 10.1038/77731.

Szél Á, Röhlich P, Gaffé AR, Juliusson B, Aguirre G, Veen TV. (1992). Unique topographic separation of two spectral classes of cones in the mouse retina. *Journal of Comparative Neurology*, 325(3):327–342. doi: 10.1002/cne.903250302.

Talay M, Richman EB, Snell NJ, Hartmann GG, Fisher JD, Sorkaç A, Santoyo JF, Chou-Freed C, Nair N, Johnson M, Szymanski JR, Barnea G. (2017). Transsynaptic Mapping of Second-Order Taste Neurons in Flies by trans-Tango. *Neuron*, 96(4):783-795.e4. doi: 10.1016/j.neuron.2017.10.011.

Talbot SA, Marshall WH. (1941). Physiological Studies on Neural Mechanisms of Visual Localization and Discrimination. *American Journal of Ophthalmology*, 24(11):1255–1264. doi: 10.1016/S0002-9394(41)91363-6.

Tamás G, Buhl EH, Somogyi P. (1997). Fast IPSPs elicited via multiple synaptic release sites by different types of GABAergic neurone in the cat visual cortex. *The Journal of Physiology*, 500(Pt 3):715–738. doi: 10.1113/jphysiol.1997.sp022054.

Tanaka K. (1983). Cross-correlation analysis of geniculostriate neuronal relationships in cats. *Journal of Neurophysiology*, 49(6):1303–1318. doi: 10.1152/jn.1983.49.6.1303.

Tang J, Jimenez SCA, Chakraborty S, Schultz SR. (2016). Visual Receptive Field Properties of Neurons in the Mouse Lateral Geniculate Nucleus. *PLOS ONE*, 11(1):e0146017. doi: 10.1371/journal.pone.0146017.

Tang Y, Li L, Sun L, Yu J, Hu Z, Lian K, Cao G, Dai J. (2020). In Vivo Two-photon Calcium Imaging in Dendrites of Rabies Virus-labeled V1 Corticothalamic Neurons. *Neuroscience Bulletin*, 36:545–553. doi: 10.1007/s12264-019-00452-y.

Tartuferi F. (1887). Sulla anatomia della retina. *Vincenzo Bona*.

Thestrup T, Litzlbauer J, Bartholomäus I, Mues M, Russo L, Dana H, Kovalchuk Y, Liang Y, Kalamakis G, Laukat Y, Becker S, Witte G, Geiger A, Allen T, Rome LC, Chen T-W, Kim DS, Garaschuk O, Griesinger C, Griesbeck O. (2014). Optimized ratiometric calcium sensors for functional in vivo imaging of neurons and T lymphocytes. *Nature Methods*, 11(2):175–182. doi: 10.1038/nmeth.2773.

Thomson AM, West DC, Wang Y, Bannister AP. (2002). Synaptic Connections and Small Circuits Involving Excitatory and Inhibitory Neurons in Layers 2–5 of Adult Rat and Cat Neocortex: Triple Intracellular Recordings and Biocytin Labelling In Vitro. *Cerebral Cortex*, 12(9):936–953. doi: 10.1093/cercor/12.9.936.

Tian L, Hires SA, Mao T, Huber D, Chiappe ME, Chalasani SH, Petreanu L, Akerboom J, McKinney SA, Schreiter ER, Bargmann CI, Jayaraman V, Svoboda K, Looger LL. (2009). Imaging neural activity in worms, flies and mice with improved GCaMP calcium indicators. *Nature Methods*, 6(12):875–881. doi: 10.1038/nmeth.1398.

Tigges M, Tigges J. (1970). The retinofugal fibers and their terminal nuclei in Galago crassicaudatus (primates). *Journal of Comparative Neurology*, 138(1):87–101. doi: 10.1002/cne.901380107.

Tootell RB, Silverman MS, Valois RLD. (1981). Spatial Frequency Columns in Primary Visual Cortex. *Science*, 214(4522):813-815. doi: 10.1126/science.7292014.

Tsang TK, Bushong EA, Boassa D, Hu J, Romoli B, Phan S, Dulcis D, Su C-Y, Ellisman MH. (2018). High-quality ultrastructural preservation using cryofixation for 3D electron microscopy of genetically labeled tissues. *eLife*, 7:e35524. doi: 10.7554/eLife.35524.

Turner N, Lee K, Lu R, Wu J, Ih D, Seung HS. (2019). Synaptic Partner Assignment Using Attentional Voxel Association Networks. *arXiv*, 190409947 [cs].

Turner NL, Macrina T, Bae JA, Yang R, Wilson AM, Schneider-Mizell C, Lee K, Lu R, Wu J, Bodor AL, Bleckert AA, Brittain D, Froudarakis E, Dorkenwald S, Collman F, Kemnitz N, Ih D, Silversmith WM, Zung J, Zlateski A, Tartavull I, Yu S, Popovych S, Mu S, Wong W, Jordan CS, Castro M, Buchanan J, Bumbarger DJ, Takeno M, Torres R, Mahalingam G, Elabbady L, Li Y, Cobos E, Zhou P, Suckow S, Becker L, Paninski L, Polleux F, Reimer J, Tolias AS, Reid RC, Costa NM da, Seung HS. (2020). Multiscale and multimodal reconstruction of cortical structure and function. *bioRxiv*, 338681. https://www.biorxiv.org/content/10.1101/2020.10.14.338681v3

Tusa RJ, Palmer LA, Rosenquist AC. (1978). The retinotopic organization of area 17 (striate cortex) in the cat. *Journal of Comparative Neurology*, 177(2):213–235. doi: 10.1002/cne.901770204.

Ugolini G. (1995). Specificity of rabies virus as a transneuronal tracer of motor networks: Transfer from hypoglossal motoneurons to connected second-order and higher order central nervous system cell groups. *Journal of Comparative Neurology*, 356(3):457–480. doi: 10.1002/cne.903560312.

Usrey WM, Reppas JB, Reid RC. (1999). Specificity and Strength of Retinogeniculate Connections. *Journal of Neurophysiology*, 82(6):3527–3540. doi: 10.1152/jn.1999.82.6.3527.

Van Essen DC, Newsome WT, Maunsell JHR. (1984). The visual field representation in striate cortex of the macaque monkey: Asymmetries, anisotropies, and individual variability. *Vision Research*, 24(5):429–448. doi: 10.1016/0042-6989(84)90041-5.

Velden HA van der. (1946). The Number of Quanta Necessary for the Perception of Light of the Human Eye. *Ophthalmologica*, 111(6):321–331. doi: 10.1159/000300352.

Vélez-Fort M, Rousseau CV, Niedworok CJ, Wickersham IR, Rancz EA, Brown APY, Strom M, Margrie TW. (2014). The Stimulus Selectivity and Connectivity of Layer Six Principal Cells Reveals Cortical Microcircuits Underlying Visual Processing. *Neuron*, 83(6):1431–1443. doi: 10.1016/j.neuron.2014.08.001.

Venable JH, Coggeshall R. (1965). A SIMPLIFIED LEAD CITRATE STAIN FOR USE IN ELECTRON MICROSCOPY. *Journal of Cell Biology*, 25(2):407–408. doi: 10.1083/jcb.25.2.407.

Ventura A, Meissner A, Dillon CP, McManus M, Sharp PA, Parijs LV, Jaenisch R, Jacks T. (2004). Cre-lox-regulated conditional RNA interference from transgenes. *PNAS*, 101(28):10380–10385. doi: 10.1073/pnas.0403954101.

Vinck M, Batista-Brito R, Knoblich U, Cardin JA. (2015). Arousal and Locomotion Make Distinct Contributions to Cortical Activity Patterns and Visual Encoding. *Neuron*, 86(3):740–754. doi: 10.1016/j.neuron.2015.03.028.

Volland S, Esteve-Rudd J, Hoo J, Yee C, Williams DS. (2015). A Comparison of Some Organizational Characteristics of the Mouse Central Retina and the Human Macula. *PLOS ONE*, 10(4):e0125631. doi: 10.1371/journal.pone.0125631.

Von Ardenne M. (1938). Das elektronen-rastermikroskop. Praktische Ausführung. *Zeitschrift für technische Physik*, 19:407–416.

de Vries SEJ, Lecoq JA, Buice MA, Groblewski PA, Ocker GK, Oliver M, Feng D, Cain N, Ledochowitsch P, Millman D, Roll K, Garrett M, Keenan T, Kuan L, Mihalas S, Olsen S, Thompson C, Wakeman W, Waters J, Williams D, Barber C, Berbesque N, Blanchard B, Bowles N, Caldejon SD, Casal L, Cho A, Cross S, Dang C, Dolbeare T, Edwards M, Galbraith J, Gaudreault N, Gilbert TL, Griffin F, Hargrave P, Howard R, Huang L, Jewell S, Keller N, Knoblich U, Larkin JD, Larsen R, Lau C, Lee E, Lee F, Leon A, Li L, Long F, Luviano J, Mace K, Nguyen T, Perkins J, Robertson M, Seid S, Shea-Brown E, Shi J, Sjoquist N, Slaughterbeck C, Sullivan D, Valenza R, White C, Williford A, Witten DM, Zhuang J, Zeng H, Farrell C, Ng L, Bernard A, Phillips JW, Reid RC, Koch C. (2020). A large-scale standardized physiological survey reveals functional organization of the mouse visual cortex. *Nature Neuroscience*, 23(1):138–151. doi: 10.1038/s41593-019-0550-9.

Wagor E, Mangini NJ, Pearlman AL. (1980). Retinotopic organization of striate and extrastriate visual cortex in the mouse. *Journal of Comparative Neurology*, 193(1):187–202. doi: 10.1002/cne.901930113.

Walton J. (1979). Lead asparate, an en bloc contrast stain particularly useful for ultrastructural enzymology. *The Journal of Histochemistry and Cytochemistry*, 27(10):1337–1342. doi: 10.1177/27.10.512319.

Wang Q, Burkhalter A. (2007). Area map of mouse visual cortex. *Journal of Comparative Neurology*, 502(3):339–357. doi: 10.1002/cne.21286.

Wang Q, Gao E, Burkhalter A. (2011). Gateways of Ventral and Dorsal Streams in Mouse Visual Cortex. *The Journal of Neuroscience*, 31(5):1905–1918. doi: 10.1523/JNEUROSCI.3488-10.2011.

Wang Q, Sporns O, Burkhalter A. (2012). Network Analysis of Corticocortical Connections Reveals Ventral and Dorsal Processing Streams in Mouse Visual Cortex. *The Journal of Neuroscience*, 32(13):4386–4399. doi: 10.1523/JNEUROSCI.6063-11.2012.

Wang S, Bickford ME, Horn SC van, Erisir A, Godwin DW, Sherman SM. (2001). Synaptic targets of thalamic reticular nucleus terminals in the visual thalamus of the cat. *Journal of Comparative Neurology*, 440(4):321–341. doi: 10.1002/cne.1389.

Wässle H, Riemann HJ, Boycott BB. (1978). The mosaic of nerve cells in the mammalian retina. *Proceedings of the Royal Society of London Series B Biological Sciences*, 200(1141):441–461. doi: 10.1098/rspb.1978.0026.

Watson A, Ahumada A. (1983). A look at motion in the frequency domain.

Watson ML. (1958). Staining of Tissue Sections for Electron Microscopy with Heavy Metals. *The Journal of Biophysical and Biochemical Cytology*, 4(4):475–478. doi: 10.1083/jcb.4.4.475.

Wei P, Liu N, Zhang Z, Liu X, Tang Y, He X, Wu B, Zhou Z, Liu Y, Li J, Zhang Y, Zhou X, Xu L, Chen L, Bi G, Hu X, Xu F, Wang L. (2015). Processing of visually evoked innate fear by a non-canonical thalamic pathway. *Nature Communications*, 6:6756. doi: 10.1038/ncomms7756.

Weigand M, Sartori F, Cuntz H. (2017). Universal transition from unstructured to structured neural maps. *PNAS*, 114(20):E4057–E4064. doi: 10.1073/pnas.1616163114.

Weiler S, Bauer J, Hübener M, Bonhoeffer T, Rose T, Scheuss V. (2018). High-yield in vitro recordings from neurons functionally characterized in vivo. *Nature Protocols*, 13(6):1275–1293. doi: 10.1038/nprot.2018.026.

Weliky M, Bosking WH, Fitzpatrick D. (1996). A systematic map of direction preference in primary visual cortex. *Nature*, 379(6567):725–728. doi: 10.1038/379725a0.

Werblin FS, Dowling JE. (1969). Organization of the retina of the mudpuppy, Necturus maculosus. II. Intracellular recording. *Journal of Neurophysiology*, 32(3):339–355. doi: 10.1152/jn.1969.32.3.339.

Wertz A, Trenholm S, Yonehara K, Hillier D, Raics Z, Leinweber M, Szalay G, Ghanem A, Keller G, Rózsa B, Conzelmann K-K, Roska B. (2015). Single-cell–initiated monosynaptic tracing reveals

layer-specific cortical network modules. *Science*, 349(6243):70-74. doi: 10.1126/science.aab1687.

White EL, Hersch SM. (1982). A quantitative study of thalamocortical and other synapses involving the apical dendrites of corticothalamic projection cells in mouse SmI cortex. *Journal of Neurocytology*, 11(1):137–157. doi: 10.1007/BF01258009.

White JG, Southgate E, Thomson JN, Brenner S. (1986). The structure of the nervous system of the nematode Caenorhabditis elegans. *Philosophical Transactions of the Royal Society of London B, Biological Sciences*, 314(1165):1–340. doi: 10.1098/rstb.1986.0056.

Wickersham IR, Finke S, Conzelmann K-K, Callaway EM. (2007a). Retrograde neuronal tracing with a deletion-mutant rabies virus. *Nature Methods*, 4(1):47–49. doi: 10.1038/nmeth999.

Wickersham IR, Lyon DC, Barnard RJO, Mori T, Finke S, Conzelmann K-K, Young JAT, Callaway EM. (2007b). Monosynaptic Restriction of Transsynaptic Tracing from Single, Genetically Targeted Neurons. *Neuron*, 53(5):639–647. doi: 10.1016/j.neuron.2007.01.033.

Wiesel TN, Hubel DH, Lam DMK. (1974). Autoradiographic demonstration of ocular-dominance columns in the monkey striate cortex by means of transneuronal transport. *Brain Research*, 79(2):273–279. doi: 10.1016/0006-8993(74)90416-8.

Wietek J, Rodriguez-Rozada S, Tutas J, Tenedini F, Grimm C, Oertner TG, Soba P, Hegemann P, Wiegert JS. (2017). Anion-conducting channelrhodopsins with tuned spectra and modified kinetics engineered for optogenetic manipulation of behavior. *Scientific Reports*, 7(1):14957. doi: 10.1038/s41598-017-14330-y.

Wildenberg GA, Rosen MR, Lundell J, Paukner D, Freedman DJ, Kasthuri N. (2020). Primate neuronal connections are sparse as compared to mouse. *bioRxiv*, 311852. https://www.biorxiv.org/content/10.1101/2020.09.24.311852v2

Willingham MC, Rutherford AV. (1984). The use of osmium-thiocarbohydrazide-osmium (OTO) and ferrocyanide-reduced osmium methods to enhance membrane contrast and preservation in cultured cells. *The Journal of Histochemistry and Cytochemistry*, 32(4):455–460. doi: 10.1177/32.4.6323574.

Wolf S, Schott L, Köthe U, Hamprecht F. (2017). Learned Watershed: End-to-End Learning of Seeded Segmentation. *IEEE International Conference on Computer Vision (ICCV)*. p 2030–2038.

Wong AA, Brown RE. (2006). Visual detection, pattern discrimination and visual acuity in 14 strains of mice. *Genes, Brain and Behavior*, 5(5):389–403. doi: 10.1111/j.1601-183X.2005.00173.x.

Xue M, Atallah BV, Scanziani M. (2014). Equalizing excitation–inhibition ratios across visual cortical neurons. *Nature*, 511(7511):596–600. doi: 10.1038/nature13321.

Xu-Friedman MA, Regehr WG. (2000). Probing Fundamental Aspects of Synaptic Transmission with Strontium. *The Journal of Neuroscience*, 20(12):4414–4422. doi: 10.1523/JNEUROSCI.20-12-04414.2000.

Yamashita S, Kikkawa J, Yanagisawa K, Nagai T, Ishizuka K, Kimoto K. (2018). Atomic number dependence of Z contrast in scanning transmission electron microscopy. *Scientific Reports*, 8(1):12325. doi: 10.1038/s41598-018-30941-5.

Yeh C-I, Xing D, Williams PE, Shapley RM. (2009). Stimulus ensemble and cortical layer determine V1 spatial receptive fields. *PNAS*, 106(34):14652–14657. doi: 10.1073/pnas.0907406106.

Yilmaz M, Meister M. (2013). Rapid Innate Defensive Responses of Mice to Looming Visual Stimuli. *Current Biology*, 23(20):2011–2015. doi: 10.1016/j.cub.2013.08.015.

Yin W, Brittain D, Borseth J, Scott ME, Williams D, Perkins J, Own CS, Murfitt M, Torres RM, Kapner D, Mahalingam G, Bleckert A, Castelli D, Reid D, Lee W-CA, Graham BJ, Takeno M, Bumbarger DJ, Farrell C, Reid RC, da Costa NM. (2020). A petascale automated imaging pipeline for mapping neuronal circuits with high-throughput transmission electron microscopy. *Nature Communications*, 11(1):4949. doi: 10.1038/s41467-020-18659-3.

Young JA, Bates P, Varmus HE. (1993). Isolation of a chicken gene that confers susceptibility to infection by subgroup A avian leukosis and sarcoma viruses. *Journal of Virology*, 67(4):1811–1816. doi: 10.1128/JVI.67.4.1811-1816.1993.

Yuste R, Denk W. (1995). Dendritic spines as basic functional units of neuronal integration. *Nature*, 375(6533):682–684. doi: 10.1038/375682a0.

Zhang F, Wang L-P, Brauner M, Liewald JF, Kay K, Watzke N, Wood PG, Bamberg E, Nagel G, Gottschalk A, Deisseroth K. (2007). Multimodal fast optical interrogation of neural circuitry. *Nature*, 446(7136):633–639. doi: 10.1038/nature05744.

Zhang Y, Rózsa M, Bushey D, Zheng J, Reep D, Liang Y, Broussard GJ, Tsang A, Tsegaye G, Patel R, Narayan S, Lim J-X, Zhang R, Ahrens MB, Turner GC, Wang SS-H, Svoboda K, Korff W, Schreiter ER, Hasseman JP, Kolb I, Looger LL. (2020). jGCaMP8 Fast Genetically Encoded Calcium Indicators. *Janelia Research Campus*. https://doi.org/10.25378/janelia.13148243.v4

Zhao X, Chen H, Liu X, Cang J. (2013). Orientation-selective Responses in the Mouse Lateral Geniculate Nucleus. *The Journal of Neuroscience*, 33(31):12751–12763. doi: 10.1523/JNEUROSCI.0095-13.2013.

Zheng Z, Lauritzen JS, Perlman E, Robinson CG, Nichols M, Milkie D, Torrens O, Price J, Fisher CB, Sharifi N, Calle-Schuler SA, Kmecova L, Ali IJ, Karsh B, Trautman ET, Bogovic JA, Hanslovsky P, Jefferis GSXE, Kazhdan M, Khairy K, Saalfeld S, Fetter RD, Bock DD. (2018). A Complete Electron Microscopy Volume of the Brain of Adult Drosophila melanogaster. *Cell*, 174(3):730-743.e22. doi: 10.1016/j.cell.2018.06.019.

Zhuang J, Wang Y, Ouellette ND, Turschak E, Larsen RS, Takasaki KT, Daigle TL, Tasic B, Waters J, Zeng H, Reid RC. (2021). Motion/direction-sensitive thalamic neurons project extensively to the middle layers of primary visual cortex. *bioRxiv*, 451534. https://www.biorxiv.org/content/10.1101/2021.07.07.451534v1

Zung J, Tartavull I, Lee K, Seung HS. (2017). An Error Detection and Correction Framework for Connectomics. *Advances in Neural Information Processing Systems*, 30:3818-3829.

6 Supplement

pAAV-CAG-Flex-FlpO-WPRE (5' → 3')

CTTCCGCTTCCTCGCTCACTGACTCGCTGCGCTCGGTCGTTCGGCTGCGGCGAGCGGTATCAGCTCACTCAAAGGCGGTAA
TACGGTTATCCACAGAATCAGGGGATAACGCAGGAAAGAACATGTGAGCAAAAGGCCAGCAAAAGGCCAGGAACCGTA
AAAAGGCCGCGTTGCTGGCGTTTTTCCATAGGCTCCGCCCCCCTGACGAGCATCACAAAAATCGACGCTCAAGTCAGAGG
TGGCGAAACCCGACAGGACTATAAAGATACCAGGCGTTTCCCCCTGGAAGCTCCCTCGTGCGCTCTCCTGTTCCGACCCTG
CCGCTTACCGGATACCTGTCCGCCTTTCTCCCTTCGGGAAGCGTGGCGCTTTCTCATAGCTCACGCTGTAGGTATCTCAGTT
CGGTGTAGGTCGTTCGCTCCAAGCTGGGCTGTGTGCACGAACCCCCCGTTCAGCCCGACCGCTGCGCCTTATCCGGTAACT
ATCGTCTTGAGTCCAACCCGGTAAGACACGACTTATCGCCACTGGCAGCAGCCACTGGTAACAGGATTAGCAGAGCGAG
GTATGTAGGCGGTGCTACAGAGTTCTTGAAGTGGTGGCCTAACTACGGCTACACTAGAAGAACAGTATTTGGTATCTGCG
CTCTGCTGAAGCCAGTTACCTTCGGAAAAAGAGTTGGTAGCTCTTGATCCGGCAAACAAACCACCGCTGGTAGCGGTGGT
TTTTTTGTTTGCAAGCAGCAGATTACGCGCAGAAAAAAAGGATCTCAAGAAGATCCTTTGATCTTTTCTACGGGGTCTGAC
GCTCAGTGGAACGAAAACTCACGTTAAGGGATTTTGGTCATGAGATTATCAAAAAGGATCTTCACCTAGATCCTTTTAAAT
TAAAAATGAAGTTTTAAATCAATCTAAAGTATATATGAGTAAACTTGGTCTGACAGTTACCAATGCTTAATCAGTGAGGCA
CCTATCTCAGCGATCTGTCTATTTCGTTCATCCATAGTTGCCTGACTCCCCGTCGTGTAGATAACTACGATACGGGAGGGCT
TACCATCTGGCCCCAGTGCTGCAATGATACCGCGAGACCCACGCTCACCGGCTCCAGATTTATCAGCAATAAACCAGCCAG
CCGGAAGGGCCGAGCGCAGAAGTGGTCCTGCAACTTTATCCGCCTCCATCCAGTCTATTAATTGTTGCCGGGAAGCTAGA
GTAAGTAGTTCGCCAGTTAATAGTTTGCGCAACGTTGTTGCCATTGCTACAGGCATCGTGGTGTCACGCTCGTCGTTTGGT
ATGGCTTCATTCAGCTCCGGTTCCCAACGATCAAGGCGAGTTACATGATCCCCCATGTTGTGCAAAAAAGCGGTTAGCTCC
TTCGGTCCTCCGATCGTTGTCAGAAGTAAGTTGGCCGCAGTGTTATCACTCATGGTTATGGCAGCACTGCATAATTCTCTTA
CTGTCATGCCATCCGTAAGATGCTTTTCTGTGACTGGTGAGTACTCAACCAAGTCATTCTGAGAATAGTGTATGCGGCGAC
CGAGTTGCTCTTGCCCGGCGTCAATACGGGATAATACCGCGCCACATAGCAGAACTTTAAAAGTGCTCATCATTGGAAAA
CGTTCTTCGGGGCGAAAACTCTCAAGGATCTTACCGCTGTTGAGATCCAGTTCGATGTAACCCACTCGTGCACCCAACTGA
TCTTCAGCATCTTTTACTTTCACCAGCGTTTCTGGGTGAGCAAAAACAGGAAGGCAAAATGCCGCAAAAAAGGGAATAAG
GGCGACACGGAAATGTTGAATACTCATACTCTTCCTTTTTCAATATTATTGAAGCATTTATCAGGGTTATTGTCTCATGAGC
GGATACATATTTGAATGTATTTAGAAAAATAAACAAATAGGGGTTCCGCGCACATTTCCCCGAAAAGTGCCACCTAAATTG
TAAGCGTTAATATTTTGTTAAAATTCGCGTTAAATTTTTGTTAAATCAGCTCATTTTTTAACCAATAGGCCGAAATCGGCAA
AATCCCTTATAAATCAAAAGAATAGACCGAGATAGGGTTGAGTGTTGTTCCAGTTTGGAACAAGAGTCCACTATTAAAGA
ACGTGGACTCCAACGTCAAAGGGCGAAAAACCGTCTATCAGGGCGATGGCCCACTACGTGAACCATCACCCTAATCAAGT
TTTTTGGGGTCGAGGTGCCGTAAAGCACTAAATCGGAACCCTAAAGGGAGCCCCCGATTTAGAGCTTGACGGGGAAAGC
CGGCGAACGTGGCGAGAAAGGAAGGGAAGAAAGCGAAAGGAGCGGGCGCTAGGGCGCTGGCAAGTGTAGCGGTCAC
GCTGCGCGTAACCACCACACCCGCCGCGCTTAATGCGCCGCTACAGGGCGCGTCCCATTCGCCATTCAGGCTGCGCAACT
GTTGGGAAGGGCGATCGGTGCGGGCCTCTTCGCTATTACGCCAGCTGCGCGCTCGCTCGCTCACTGAGGCCGCCCGGGC
AAAGCCCGGGCGTCGGGCGACCTTTGGTCGCCCGGCCTCAGTGAGCGAGCGAGCGCGCAGAGAGGGAGTGGCCAACTC
CATCACTAGGGGTTCCTTGTAGTTAATGATTAACCCGCCATGCTACTTATCTACGTAGCCATGCTCTAGGAAGATCGTACC
ATTGACGTCAATAATGACGTATGTTCCCATAGTAACGCCAATAGGGACTTTCCATTGACGTCAATGGGTGGAGTATTTACG
GTAAACTGCCCACTTGGCAGTACATCAAGTGTATCATATGCCAAGTACGCCCCCTATTGACGTCAATGACGGTAAATGGCC
CGCCTGGCATTATGCCCAGTACATGACCTTATGGGACTTTCCTACTTGGCAGTACATCTACGTATTAGTCATCGCTATTACC
ATGGTCGAGGTGAGCCCCACGTTCTGCTTCACTCTCCCCATCTCCCCCCCCTCCCCACCCCCAATTTTGTATTTATTTATTTTT
TAATTATTTTGTGCAGCGATGGGGGCGGGGGGGGGGGGGGGCGCGCGCCAGGCGGGGCGGGGCGGGGCGAGGGGC
GGGGCGGGGCGAGGCGGAGAGGTGCGGCGGCAGCCAATCAGAGCGGCGCGCTCCGAAAGTTTCCTTTTATGGCGAGGC
GGCGGCGGCGGCGGCCCTATAAAAAGCGAAGCGCGCGGCGGGCGGGAGTCGCTGCGACGCTGCCTTCGCCCCGTGCCC
CGCTCCGCCGCCGCCTCGCGCCGCCCGCCCCGGCTCTGACTGACCGCGTTACTCCCACAGGTGAGCGGGCGGGACGGCCC
TTCTCCTCCGGGCTGTAATTAGCGCTTGGTTTAATGACGGCTTGTTTCTTTTCTGTGGCTGCGTGAAAGCCTTGAGGGGCT
CCGGGAGGGCCCTTTGTGCGGGGGGAGCGGCTCGGGGCTGTCCGCGGGGGGACGGCTGCCTTCGGGGGGGACGGGGC
AGGGCGGGGTTCGGCTTCTGGCGTGTGACCGGCGGCTCTAGAGCCTCTGCTAACCATGTTCATGCCTTCTTCTTTTTCCTA
CAGCTCCTGGGCAACGTGCTGGTTATTGTGCTGTCTCATCATTTTGGCAAAGAATTGGATCCCCATAACTTCGTATAAAGT
ATCCTATACGAAGTTATATCAAAATAGGAAGACCAATGCTTCACCATCGACCCGAATTGCCAAGCATCACCATCGACCCAT
AACTTCGTATAATGTATGCTATACGAAGTTATACTAGGATCCCCCCTCAGATCCGCCTGTTGATGTAGCTGCTCAGGTAGT
CCAGCACCTCCTGGCTGATGATGCCGTTCCAGGCGGGGTATCTGATGCTGCCCTCGGCGCTGCCCTTCAGCTGCTCGATGT
GCTGCCACTCCTCGATGGGGTTGGTCTCGTCCTTCAGGGCGATCATCTCCTTGCTGATGGGGTCGTAGGCGTAGTACCTG

GACACCAGGGCGAAGTAGTGGTCGGGGATGGCGGTGATCTGGTGGGTGTAGGTGGTCCTGGCCACGGCGGAGGCCCTC
TTGTCGCTCCAGTTGCCCACCACGTTTGTCAGCTCGGTCAGGCCCTTCATGCTCAGAAAGCTGGTCATCAGGTGCCTGCCG
ATGTGGCTCTTAGGGCCGTTCTTGATAGCGAAGATGGGGTAGGGGGCGTTCTTCTTCAGGGCCTTGTTGTAGCTGCGCAC
CAGGTTGTCCTTCAGCAGCTGGTACTCCTGCTTGTTGCTGCTGCTGTTGCCGGTCCTGTTCACTCTCTTCAGCACGGGCTCG
CTGTTCCTCAGGAACTCGTCCAGGTACACCAGGGGGTCGATCCTGCCTCTGGCGCTGAAAAAGTAGATGTGCCTGGACAC
GCTTGTCTTGGTCTCGGTCACCAGGCACTGAATGATCACGCCCAGGTACTTGTTCTGCACCAGCTTGAAGCTCTTGGGGTC
CACGTTCTTGATGTCGCTGAACCTGCCGCAGTTGATGAATGTGGCCAGGAACAGGAACTGGTACAGGGTCTTGGTCTTGG
TGAACCTGCTGGTGTACTCGAAGCTGTTCAGGATCTTCTCGGTGATCTCCCAGATGCTCTCGCCCTCGGACAGCAGGGCCT
TCAGCATCTTCTTGCTGTGGCTGTTGCCCTTGTCGGCCTCCTCGCTGCTCTCGAACTGCAGCTGCAGGCTGGACACGATGT
CGGTGATGTCGCTCTGGTGCTTCTGGCCGTTGTAAGGGATGATGGTGAACTCCCAGGCGGGGATCAGCTTCTTCAGGCTG
GCCTCCAGGATGGTGGCCTTCTGGGTCTTGTACTTGAACTGCAGGCTCTTGTTCACGATGTCGAAGCTCAGGCTGTTGCTG
ATGATGGTGTTGTAGCTCATGAAGGTGGCCCTCTTGATGGCGGTGCCGTTGTGGGTGATCATCCAGCACAGGTAGGTCAG
CTCGGCGGCACAGCTGGCGATCTTCTCGCCGCTGGGCCTCTCGAATCTCTCCACGAACTGCCGCACCAGCACCTTGGGGG
GGGTCTTGCACAGGATGTCGAACTGGCTCATCACCTTCCTCTTCTTCTTAGGAGCCATGGTGGCGGCGGATCCTTGCTAGC
AGCTTGCGAATTCTAGTATAACTTCGTATAGGATACTTTATACGAAGTTATCATTGGGATTCTTCCTATTTTGATCCAAGCA
TCACCATCGACCCTCTAGTCCAGATCTCACCATCGACCCATAACTTCGTATAGCATACATTATACGAAGTTATGTCCCTCGA
AGAGGTTCGAATTCGATATCAAGCTTATCGATAATCAACCTCTGGATTACAAAATTTGTGAAAGATTGACTGGTATTCTTA
ACTATGTTGCTCCTTTTACGCTATGTGGATACGCTGCTTTAATGCCTTTGTATCATGCTATTGCTTCCCGTATGGCTTTCATT
TTCTCCTCCTTGTATAAATCCTGGTTGCTGTCTCTTTATGAGGAGTTGTGGCCCGTTGTCAGGCAACGTGGCGTGGTGTGC
ACTGTGTTTGCTGACGCAACCCCCACTGGTTGGGGCATTGCCACCACCTGTCAGCTCCTTTCCGGGACTTTCGCTTTCCCCC
TCCCTATTGCCACGGCGGAACTCATCGCCGCCTGCCTTGCCCGCTGCTGGACAGGGGCTCGGCTGTTGGGCACTGACAAT
TCCGTGGTGTTGTCGGGGAAATCATCGTCCTTTCCTTGGCTGCTCGCCTGTGTTGCCACCTGGATTCTGCGCGGGACGTCC
TTCTGCTACGTCCCTTCGGCCCTCAATCCAGCGGACCTTCCTTCCCGCGGCCTGCTGCCGGCTCTGCGGCCTCTTCCGCGTC
TTCGCCTTCGCCCTCAGACGAGTCGGATCTCCCTTTGGGCCGCCTCCCCGCATCGATACCGTCGACCCGGGCGGCCGCTTC
GAGCAGACATGATAAGATACATTGATGAGTTTGGACAAACCACAACTAGAATGCAGTGAAAAAAATGCTTTATTTGTGAA
ATTTGTGATGCTATTGCTTTATTTGTAACCATTATAAGCTGCAATAAACAAGTTAACAACAACAATTGCATTCATTTTATGTT
TCAGGTTCAGGGGGAGATGTGGGAGGTTTTTTAAAGCAAGTAAAACCTCTACAAATGTGGTAAAATCGATAAGGATCTTC
CTAGAGCATGGCTACGTAGATAAGTAGCATGGCGGGTTAATCATTAACTACAAGGAACCCCTAGTGATGGAGTTGGCCAC
TCCCTCTCTGCGCGCTCGCTCGCTCACTGAGGCCGGGCGACCAAAGGTCGCCCGACGCCCGGGCTTTGCCCGGGCGGCCT
CAGTGAGCGAGCGAGCGCGCAGCTGCATTAATGAATCGGCCAACGCGCGGGGAGAGGCGGTTTGCGTATTGGGCGCT

pAAV-EF1α-F-Flex-jGCaMP7b-WPRE (5' → 3')

CCTGCAGGCAGCTGCGCGCTCGCTCGCTCACTGAGGCCGCCCGGGCAAAGCCCGGGCGTCGGGCGACCTTTGGTCGCCC
GGCCTCAGTGAGCGAGCGAGCGCGCAGAGAGGGAGTGGCCAACTCCATCACTAGGGGTTCCTGCGGCCGCACGCGTAA
GCTTTGCAAAGATGGATAAAGTTTTAAACAGAGAGGAATCTTTGCAGCTAATGGACCTTCTAGGTCTTGAAAGGAGTGGG
AATTGGCTCCGGTGCCCGTCAGTGGGCAGAGCGCACATCGCCCACAGTCCCCGAGAAGTTGGGGGGAGGGGTCGGCAA
TTGAACCGGTGCCTAGAGAAGGTGGCGCGGGGTAAACTGGGAAAGTGATGTCGTGTACTGGCTCCGCCTTTTTCCCGAG
GGTGGGGGAGAACCGTATATAAGTGCAGTAGTCGCCGTGAACGTTCTTTTTCGCAACGGGTTTGCCGCCAGAACACAGG
TAAGTGCCGTGTGTGGTTCCCGCGGGCCTGGCCTCTTTACGGGTTATGGCCCTTGCGTGCCTTGAATTACTTCCACTGGCT
GCAGTACGTGATTCTTGATCCCGAGCTTCGGGTTGGAAGTGGGTGGGAGAGTTCGAGGCCTTGCGCTTAAGGAGCCCCTT
CGCCTCGTGCTTGAGTTGAGGCCTGGCCTGGGCGCTGGGGCCGCCGCGTGCGAATCTGGTGGCACCTTCGCGCCTGTCTC
GCTGCTTTCGATAAGTCTCTAGCCATTTAAAATTTTTGATGACCTGCTGCGACGCTTTTTTTCTGGCAAGATAGTCTTGTAA
ATGCGGGCCAAGATCTGCACACTGGTATTTCGGTTTTTGGGGCCGCGGGCGGCGACGGGGCCCGTGCGTCCCAGCGCAC
ATGTTCGGCGAGGCGGGGCCTGCGAGCGCGGCCACCGAGAATCGGACGGGGGTAGTCTCAAGCTGGCCGGCCTGCTCT
GGTGCCTGGCCTCGCGCCGCCGTGTATCGCCCCGCCCTGGGCGGCAAGGCTGGCCCGGTCGGCACCAGTTGCGTGAGCG
GAAAGATGGCCGCTTCCCGGCCCTGCTGCAGGGAGCTCAAAATGGAGGACGCGGCGCTCGGGAGAGCGGGCGGGTGA
GTCACCCACACAAAGGAAAAGGGCCTTTCCGTCCTCAGCCGTCGCTTCATGTGACTCCACGGAGTACCGGGCGCCGTCCA
GGCACCTCGATTAGTTCTCGAGCTTTTGGAGTACGTCGTCTTTAGGTTGGGGGGAGGGGTTTTATGCGATGGAGTTTCCC
CACACTGAGTGGGTGGAGACTGAAGTTAGGCCAGCTTGGCACTTGATGTAATTCTCCTTGGAATTTGCCCTTTTTGAGTTT
GGATCTTGGTTCATTCTCAAGCCTCAGACAGTGGTTCAAAGTTTTTTTCTTCCATTTCAGGTGTCGTGAGGTACCGAAGTTC
CTATTCTATCAGAAGTATAGGAACTTCGCAGAATGGTAGCTGGATTGTAGCTGCTATTAGCAATATGAAACCTCTTAGAAG

TTCCTATTCTCTAGAAAGTATAGGAACTTCGAATTCTTACTTTTCACTTCGCTGTCATCATTTGTACAAACTCTTCGTAGTTTA
CCTGACCATCCCCATCGATGTCTGCTTCCCTGATCATTTCATCAACCTCTTCATCTGTTAACTTCTCTCCAAGGTTTGTCATCA
CGTGGCGAAGCTCTGCTGCACTGATGTAGCCATTGCCATCCTTATCAAACACACCGAACGCTTCTCTAATTTCTTCTTCCGT
GTCCCTGTATTTCATTTTTCTTGCGTACATTGTCAGGAACTCAGGGAAGTCGATTGTGCCGTCACCGTCGGCATCTACTTCA
TTGATCATGTCCTGCAGCTCTGCTTCTGTGGGGTTCTGCCCCAGAGACCGCATCACCGTCCCCAGCTCCTTGGTTGTTATTG
TCCCATCCCCGTCCTTGTCAAATAGGGAGAAAAGCTCTTTAAATTCTGCGATCTGCTCTTCAGTCAGTTGGTCAGGTGGGT
TGTACTCCAGCTTGTGCCCCAGGATGTTGCCGTCCTCCTTGAAGTCGATGCCCTTAAGCTCGATGCGGTTCACCAGGGTGT
CGCCCTCGAACTTCACCTCGGCGCGGGTCTTGTAGTTGCCGTCGTCCTTGAAGAAGATGGTGCGCTCCTGGATGTAGCCTT
CGGGCATGGCGGACTTGAAGAAGTCGTGCTGCTTCATGTGGTCGGGGTAGCGGCTGAAGCACTGCACGCCGTAGGTCAG
GGTGGTCACGAGGGTGGGCCAGGGCACGGGCAGCTTGCCGGTGGTGCAGATGAACTTCAGGGTCAGCTTGCCGTAGGT
GGCATCGCCCTCACCCTCGCCGGACACGCTGAACTTGTGGCCGTTTACGTCGCCGTCCAGCTCGACCAGGATGGGCACCA
CCCCGGTGAACAGCTCCTCGCCCTTGCTCACCATGCTCCCTCCGGTACCGCCCTTGTACAGCTCGTCCATGCCGAGAGTGA
TCCCGGCGGCGGTCACGAACTCCAGCAGGACCATGTGATCGCGCTTCTCGTTGGGGTCTTTCGAAAGTTTGGACTGCACG
CTCAGGTAGTGGTTGTCGGGCAGCAGCACGGGGCCGTCGCCGATGGGGGTGTTCTGCTGGTAGTGGTAGGCGAGCTGC
ACGCCGCCGTCCTCGATGTTGTGGCGGATCTTGAAGTTCGCCTTGATGCCGTTCTTCTGCTTGTCGGCCTTGATATAGACG
TTCTCGAGTGAGCTCAGCCGACCTATAGCTCTGACTGCGTGACCTGTCTTATTCCACTTACGACGTGATGAGTCGACCATG
GTGGCGAGATCCTTATCGTCATCGTCGTACAGATCCCGACCCATTTGCTGTCCACCAGTCATGCTAGCCATACCATGATGA
TGATGATGATGAGAACCCATGGTGGCGGGTGGATCCCGGCTAGCTACGTAGGCGCGCCTTAATTAAGAAGTTCCTATACT
TCTGATAGAATAGGAACTTCTTGCCTTAACCCAGAAATTATCACTGTTATTCTTTAGAATGGTGCAAAGAGAAGTTCCTATA
CTTTCTAGAGAATAGGAACTTCCAGAATTCGATATCAAGCTTATCGATAATCAACCTCTGGATTACAAAATTTGTGAAAGA
TTGACTGGTATTCTTAACTATGTTGCTCCTTTTACGCTATGTGGATACGCTGCTTTAATGCCTTTGTATCATGCTATTGCTTC
CCGTATGGCTTTCATTTTCTCCTCCTTGTATAAATCCTGGTTGCTGTCTCTTTATGAGGAGTTGTGGCCCGTTGTCAGGCAA
CGTGGCGTGGTGTGCACTGTGTTTGCTGACGCAACCCCCACTGGTTGGGGCATTGCCACCACCTGTCAGCTCCTTTCCGGG
ACTTTCGCTTTCCCCCTCCCTATTGCCACGGCGGAACTCATCGCCGCCTGCCTTGCCCGCTGCTGGACAGGGGCTCGGCTG
TTGGGCACTGACAATTCCGTGGTGTTGTCGGGGAAATCATCGTCCTTTCCTTGGCTGCTCGCCTATGTTGCCACCTGGATT
CTGCGCGGGACGTCCTTCTGCTACGTCCCTTCGGCCCTCAATCCAGCGGACCTTCCTTCCCGCGGCCTGCTGCCGGCTCTG
CGGCCTCTTCCGCGTCTTCGCCTTCGCCCTCAGACGAGTCGGATCTCCCTTTGGGCCGCCTCCCCGCATCGATACCGAGCG
CTGCTCGAGAGATCTACGGGTGGCATCCCTGTGACCCCTCCCCAGTGCCTCTCCTGGCCCTGGAAGTTGCCACTCCAGTGC
CCACCAGCCTTGTCCTAATAAAATTAAGTTGCATCATTTTGTCTGACTAGGTGTCCTTCTATAATATTATGGGGTGGAGGG
GGGTGGTATGGAGCAAGGGGCAAGTTGGGAAGACAACCTGTAGGGCCTGCGGGGTCTATTGGGAACCAAGCTGGAGTG
CAGTGGCACAATCTTGGCTCACTGCAATCTCCGCCTCCTGGGTTCAAGCGATTCTCCTGCCTCAGCCTCCCGAGTTGTTGG
GATTCCAGGCATGCATGACCAGGCTCAGCTAATTTTTGTTTTTTTGGTAGAGACGGGGTTTCACCATATTGGCCAGGCTGG
TCTCCAACTCCTAATCTCAGGTGATCTACCCACCTTGGCCTCCCAAATTGCTGGGATTACAGGCGTGAACCACTGCTCCCTT
CCCTGTCCTTCTGATTTTGTAGGTAACCACGTGCGGACCGAGCGGCCGCAGGAACCCCTAGTGATGGAGTTGGCCACTCC
CTCTCTGCGCGCTCGCTCGCTCACTGAGGCCGGGCGACCAAAGGTCGCCCGACGCCCGGGCTTTGCCCGGGCGGCCTCAG
TGAGCGAGCGAGCGCGCAGCTGCCTGCAGGGGCGCCTGATGCGGTATTTTCTCCTTACGCATCTGTGCGGTATTTCACAC
CGCATACGTCAAAGCAACCATAGTACGCGCCCTGTAGCGGCGCATTAAGCGCGGCGGGTGTGGTGGTTACGCGCAGCGT
GACCGCTACACTTGCCAGCGCCCTAGCGCCCGCTCCTTTCGCTTTCTTCCCTTCCTTTCTCGCCACGTTCGCCGGCTTTCCCC
GTCAAGCTCTAAATCGGGGGCTCCCTTTAGGGTTCCGATTTAGTGCTTTACGGCACCTCGACCCCAAAAAACTTGATTTGG
GTGATGGTTCACGTAGTGGGCCATCGCCCTGATAGACGGTTTTTCGCCCTTTGACGTTGGAGTCCACGTTCTTTAATAGTG
GACTCTTGTTCCAAACTGGAACAACACTCAACCCTATCTCGGGCTATTCTTTTGATTTATAAGGGATTTTGCCGATTTCGGC
CTATTGGTTAAAAAATGAGCTGATTTAACAAAAATTTAACGCGAATTTTAACAAAATATTAACGTTTACAATTTTATGGTGC
ACTCTCAGTACAATCTGCTCTGATGCCGCATAGTTAAGCCAGCCCCGACACCCGCCAACACCCGCTGACGCGCCCTGACGG
GCTTGTCTGCTCCCGGCATCCGCTTACAGACAAGCTGTGACCGTCTCCGGGAGCTGCATGTGTCAGAGGTTTTCACCGTCA
TCACCGAAACGCGCGAGACGAAAGGGCCTCGTGATACGCCTATTTTTATAGGTTAATGTCATGATAATAATGGTTTCTTAG
ACGTCAGGTGGCACTTTTCGGGGAAATGTGCGCGGAACCCCTATTTGTTTATTTTTCTAAATACATTCAAATATGTATCCGC
TCATGAGACAATAACCCTGATAAATGCTTCAATAATATTGAAAAAGGAAGAGTATGAGTATTCAACATTTCCGTGTCGCCC
TTATTCCCTTTTTTGCGGCATTTTGCCTTCCTGTTTTTGCTCACCCAGAAACGCTGGTGAAAGTAAAAGATGCTGAAGATCA
GTTGGGTGCACGAGTGGGTTACATCGAACTGGATCTCAACAGCGGTAAGATCCTTGAGAGTTTTCGCCCCGAAGAACGTT
TTCCAATGATGAGCACTTTTAAAGTTCTGCTATGTGGCGCGGTATTATCCCGTATTGACGCCGGGCAAGAGCAACTCGGTC
GCCGCATACACTATTCTCAGAATGACTTGGTTGAGTACTCACCAGTCACAGAAAAGCATCTTACGGATGGCATGACAGTA
AGAGAATTATGCAGTGCTGCCATAACCATGAGTGATAACACTGCGGCCAACTTACTTCTGACAACGATCGGAGGACCGAA
GGAGCTAACCGCTTTTTTGCACAACATGGGGGATCATGTAACTCGCCTTGATCGTTGGGAACCGGAGCTGAATGAAGCCA

TACCAAACGACGAGCGTGACACCACGATGCCTGTAGCAATGGCAACAACGTTGCGCAAACTATTAACTGGCGAACTACTT
ACTCTAGCTTCCCGGCAACAATTAATAGACTGGATGGAGGCGGATAAAGTTGCAGGACCACTTCTGCGCTCGGCCCTTCC
GGCTGGCTGGTTTATTGCTGATAAATCTGGAGCCGGTGAGCGTGGGTCTCGCGGTATCATTGCAGCACTGGGGCCAGAT
GGTAAGCCCTCCCGTATCGTAGTTATCTACACGACGGGGAGTCAGGCAACTATGGATGAACGAAATAGACAGATCGCTG
AGATAGGTGCCTCACTGATTAAGCATTGGTAACTGTCAGACCAAGTTTACTCATATATACTTTAGATTGATTTAAAACTTCA
TTTTTAATTTAAAAGGATCTAGGTGAAGATCCTTTTTGATAATCTCATGACCAAAATCCCTTAACGTGAGTTTTCGTTCCACT
GAGCGTCAGACCCCGTAGAAAAGATCAAAGGATCTTCTTGAGATCCTTTTTTTCTGCGCGTAATCTGCTGCTTGCAAACAA
AAAAACCACCGCTACCAGCGGTGGTTTGTTTGCCGGATCAAGAGCTACCAACTCTTTTTCCGAAGGTAACTGGCTTCAGCA
GAGCGCAGATACCAAATACTGTCCTTCTAGTGTAGCCGTAGTTAGGCCACCACTTCAAGAACTCTGTAGCACCGCCTACAT
ACCTCGCTCTGCTAATCCTGTTACCAGTGGCTGCTGCCAGTGGCGATAAGTCGTGTCTTACCGGGTTGGACTCAAGACGAT
AGTTACCGGATAAGGCGCAGCGGTCGGGCTGAACGGGGGGTTCGTGCACACAGCCCAGCTTGGAGCGAACGACCTACA
CCGAACTGAGATACCTACAGCGTGAGCTATGAGAAAGCGCCACGCTTCCCGAAGGGAGAAAGGCGGACAGGTATCCGGT
AAGCGGCAGGGTCGGAACAGGAGAGCGCACGAGGGAGCTTCCAGGGGGAAACGCCTGGTATCTTTATAGTCCTGTCGG
GTTTCGCCACCTCTGACTTGAGCGTCGATTTTTGTGATGCTCGTCAGGGGGGCGGAGCCTATGGAAAAACGCCAGCAACG
CGGCCTTTTTACGGTTCCTGGCCTTTTGCTGGCCTTTTGCTCACATGT

Table S1: **DNA-sequences of the cloned Plasmids pAAV-CAG-Flex-FlpO-WPRE and pAAV-EF1α-F-Flex-jGCaMP7b-WPRE.** Single-strand DNA-Sequences are written in 5’ to 3’ reading direction, starting at the origin of replication. Nucleobases are abbreviated as follows: A = adenine, T = thymine, C = cytosine and G = guanine.

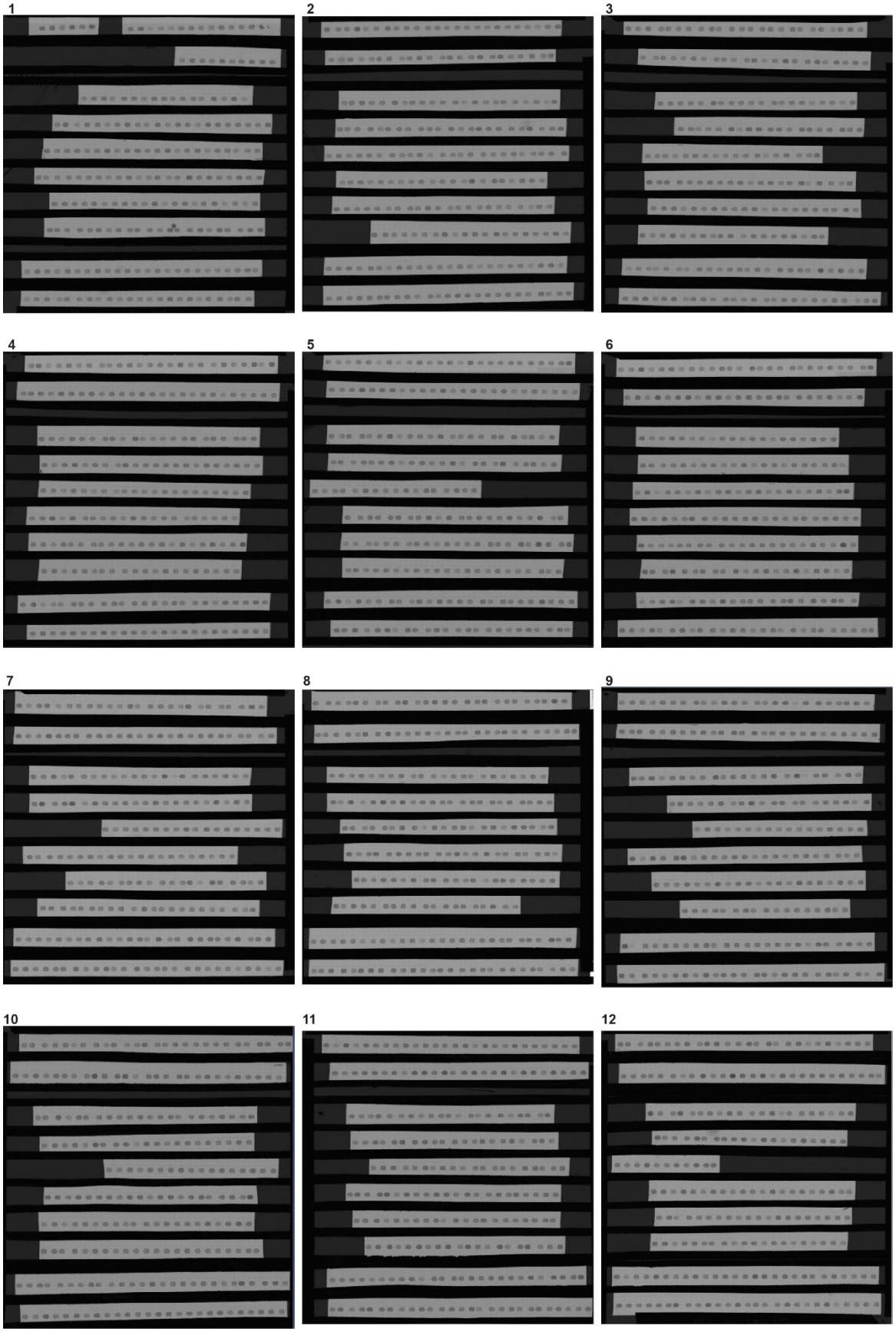
1
2
3
4
5
6
7
8
9
10
11
12

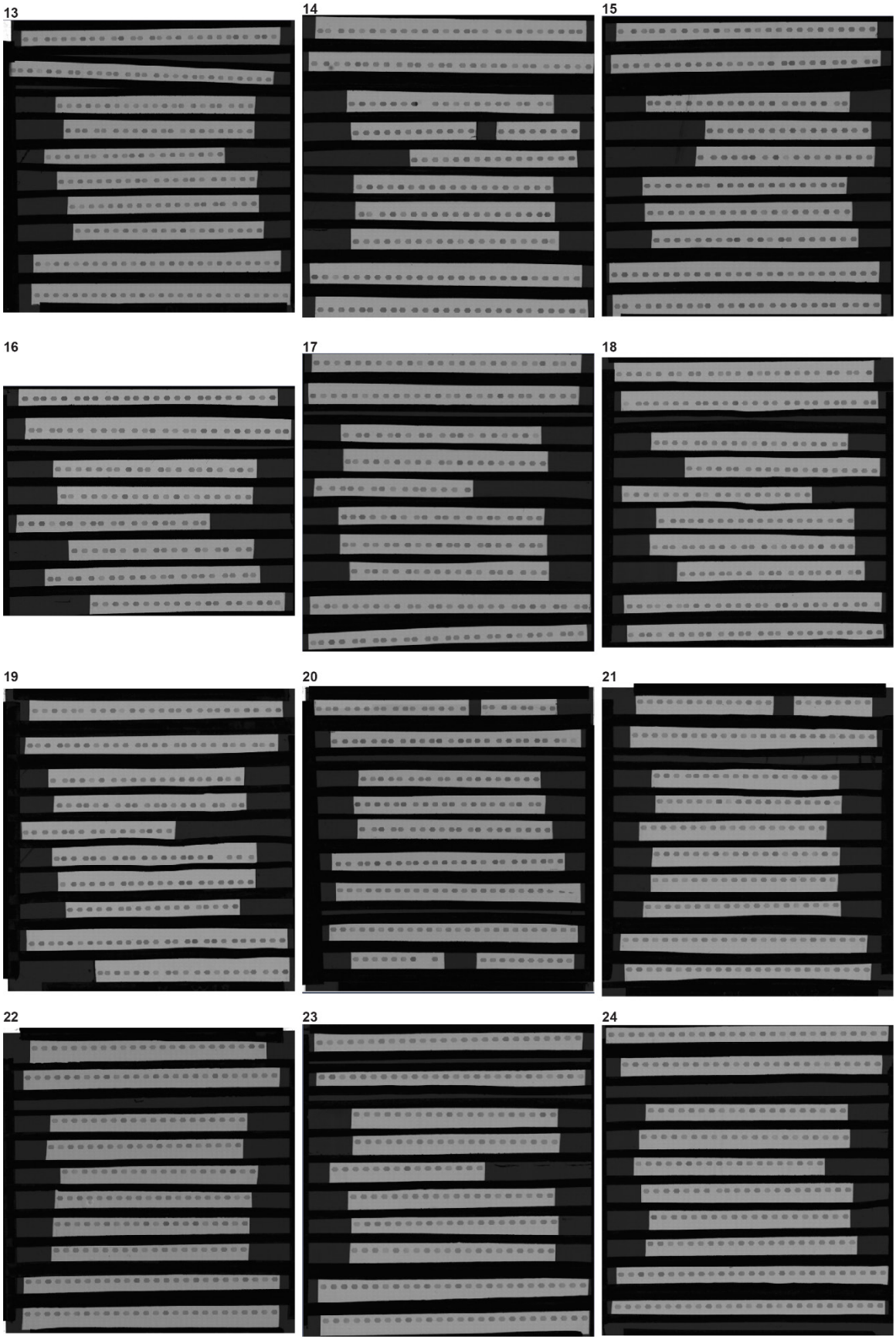
13
14
15
16
17
18
19
20
21
22
23
24

25

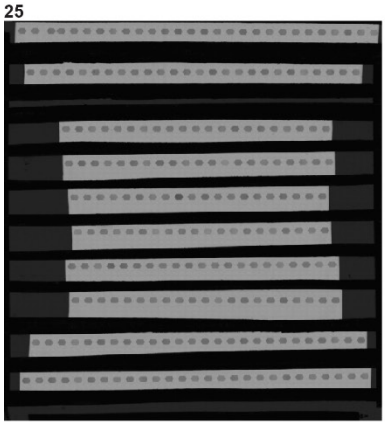

26

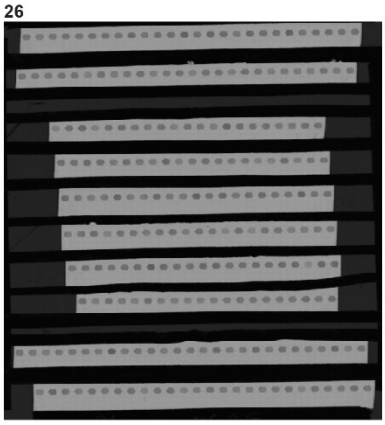

27

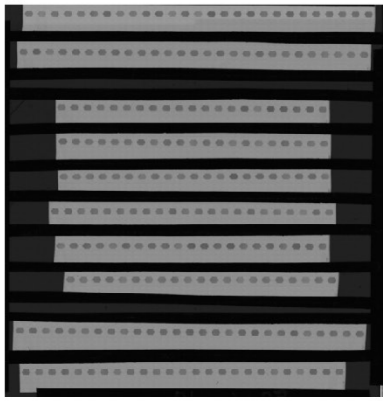

28

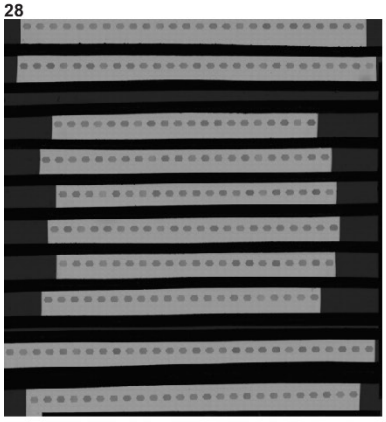

29

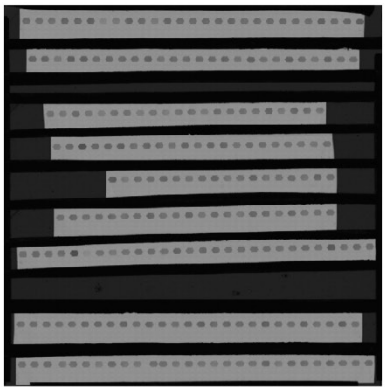

30

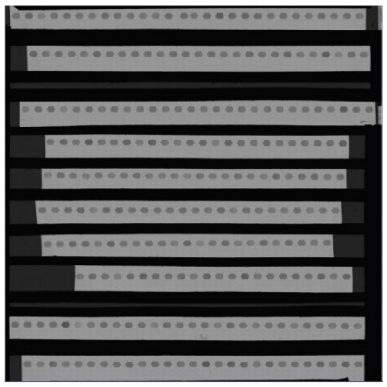

31

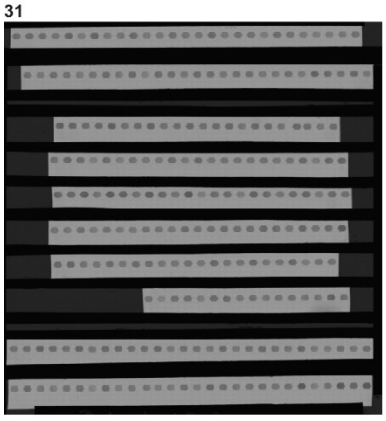

32

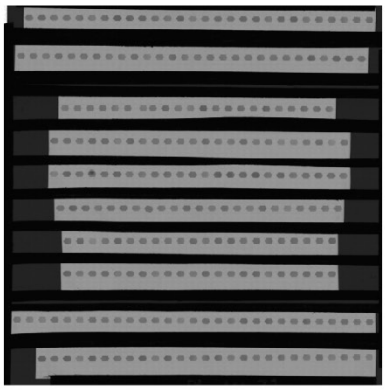

33

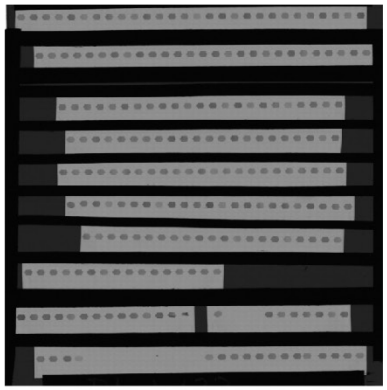

34

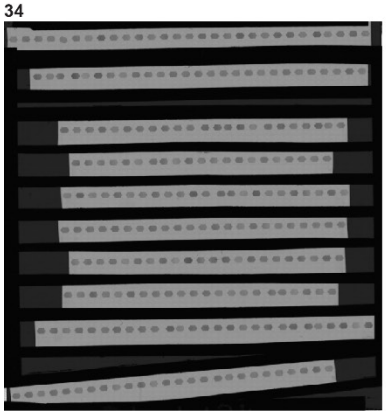

35

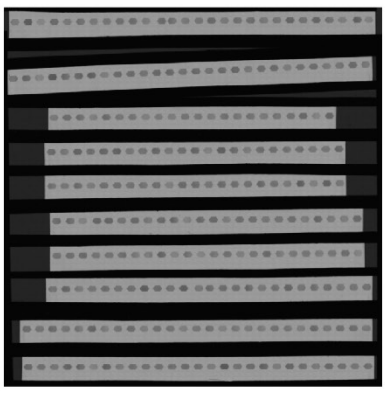

36

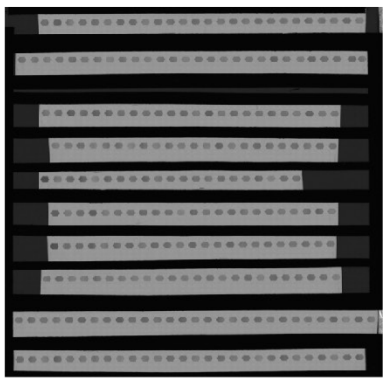

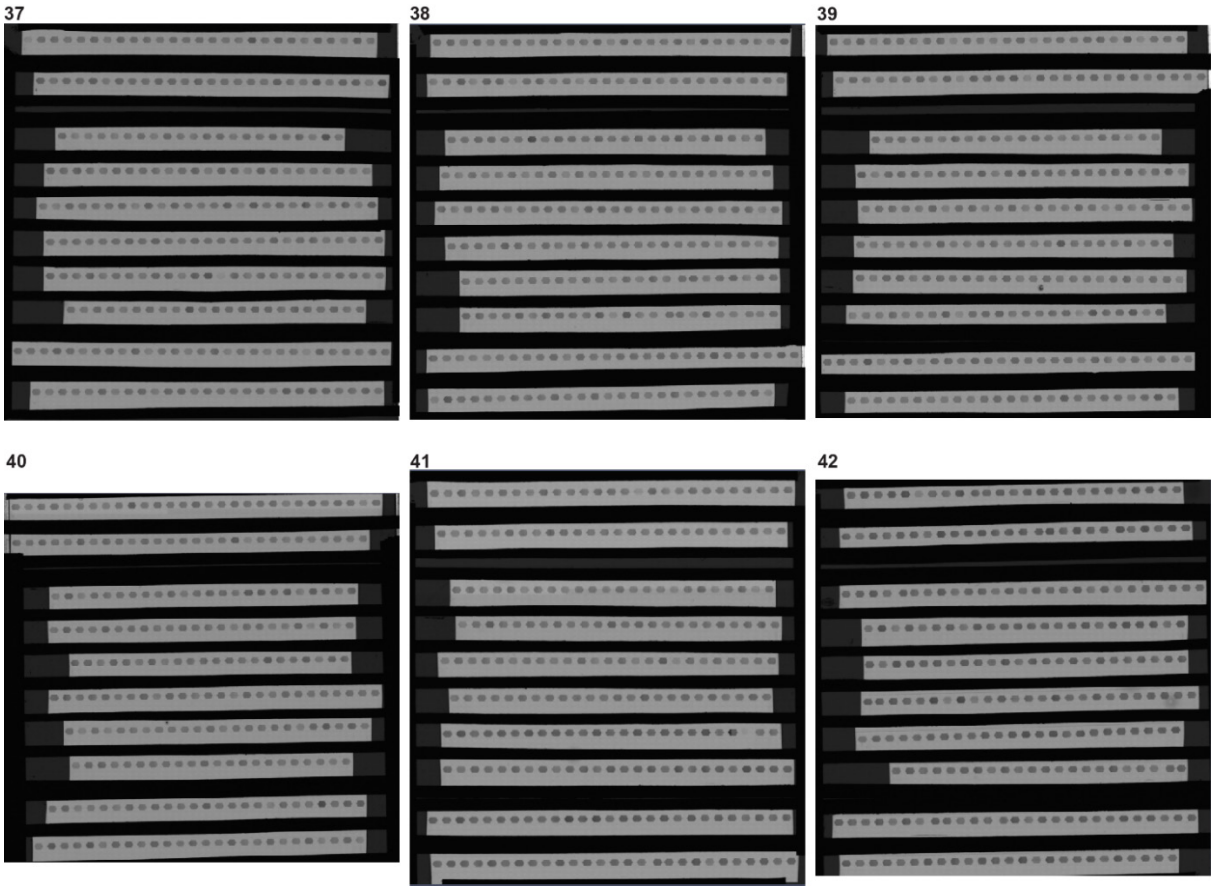

Figure S1: **Gallery of all ATUM-tape collected sections imaged with mSEM mounted on silicon-wafers from the FC-mouse.** Wafers are numbered in sequence on the top left in white letters. ATUM tapes were mounted onto silicon wafers via double-sided karbon tape in sequence from the top right to bottom left. Wafers were imaged via light-microscopy. ATUM tape appears as horizontal light-grey stripes with the ATUM-sections as dark-grey hexagons.

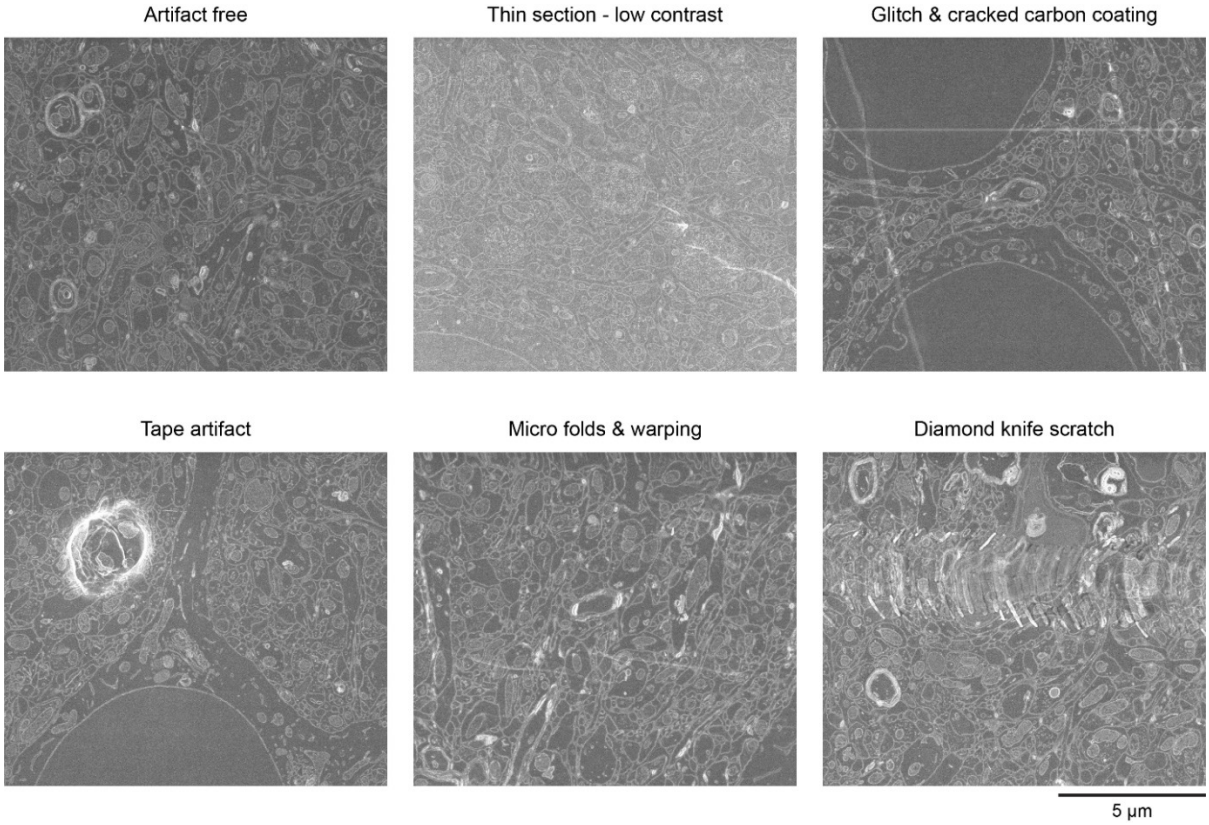

Figure S2: **Artifact gallery of the mSEM-dataset of the FC-mouse.** Example raw data, single beam mSEM-images of an artifact free region (top left), low contrast caused by a thin section (top middle), cracking of the underlying carbon coating of the ATUM kapton tape (top right), a mSEM glitch likely caused by an arching event (top right), an artifact on the underlying ATUM kapton tape (bottom left), micro folds of the ATUM section (bottom middle), warping on the top of the image likely caused by charging (bottom middle) and a scratch likely cause by the diamond knife during cutting (bottom right).

List of figures

Figure 1.1: **Models on the functional logic of retino-geniculate convergence.** 22
Figure 1.2: **3D Electron Microscopy techniques for reconstruction of neuronal ultrastructure.** 29

Figure 2.1: **Optical setup the custom-built rotating laser-scanning microscope used for two-photon calcium imaging.** 51
Figure 2.2: **Reliability of calcium transients of a dLGN bouton to sparse noise stimulation over trials.** 53
Figure 2.3 **Receptive fields of layer 4 cells and dLGN axons at different sparse noise resolutions.** .. 54
Figure 2.4: **Stimulus onset and stimulus offset responses during RF mapping using sparse noise stimulation.** 67
Figure 2.5: **Gaussian and Gabor-fitting of RFs.** 68

Figure 3.1: **Experimental pipeline for long-range functional connectomics of geniculo-cortical convergence.** 72
Figure 3.2: **Comparison between different calcium indicators for in vivo axon imaging.** 74
Figure 3.3: **Cloning and verification of Cre-dependent FlpO and FlpO-dependent jGCaMP7b expression in organotypic slice cultures.** 75
Figure 3.4: **Similarity of functional responses in boutons of the same axon.** 76
Figure 3.5: **Receptive fields of co-labeled L4 cells and dLGN axons in bV1.** 78
Figure 3.6: **Functional responses of cortical L4 cells and dLGN axons in L4 of bV1 in the FC-mouse to moving gratings.** 81
Figure 3.7: **Activity Matrices of cortical L4 cells and dLGN axons in L4 of bV1 of the FC-mouse in response to moving gratings.** 82
Figure 3.8: **Comparative response feature distributions between cortical L4 cells and dLGN axons in L4 of bV1 of the FC-mouse to moving gratings.** 83
Figure 3.9: **Functional responses of cortical L4 cells and dLGN axons in L4 of bV1 in the FC-mouse to sparse noise.** 86
Figure 3.10: **Activity Matrices of cortical L4 cells and dLGN axons in L4 of bV1 of the FC-mouse in response to sparse noise.** 87
Figure 3.11: **Comparative response feature distributions between cortical L4 cells and dLGN axons in L4 of bV1 of the FC-mouse to sparse noise.** 88
Figure 3.12: **Relationship of RF Gabor orientation and PO of L4 cells in bV1 of the FC-mouse.** 89
Figure 3.13: **Matching of functional and structural stacks from in vivo two-photon microscopy of the FC-mouse.** 90
Figure 3.14: **Optimization of heavy metal staining homogeneity for EM assessed by microCT.** 92
Figure 3.15: **Localization of the in vivo two-photon microscopy FOV in microCT and EM by triangulation from vascular landmarks.** 94
Figure 3.16: **Optimization of sample shape for continuous, homogeneous ATUM sectioning.** 95
Figure 3.17: **Serial section mSEM of bV1 in the FC-mouse.** 98
Figure 3.18: **Alignment quality of serial mSEM sections of the FC-mouse in 3D.** 100
Figure 3.19: **Relative overview of microscopy datasets of the FC-mouse.** 103

Figure S1: **Gallery of all ATUM-tape collected sections imaged with mSEM mounted on silicon-wafers from the FC-mouse.** 174
Figure S2: **Artifact gallery of the mSEM-dataset of the FC-mouse.** 175

List of tables

Table 3.1: **Section catalog from the ATUM experiment of the FC-mouse.** 97

Table S1: **DNA-sequences of the cloned Plasmids pAAV-CAG-Flex-FlpO-WPRE and pAAV-EF1α-F-Flex-jGCaMP7b-WPRE.** 170

List of abbreviations

2D	two-dimensional
3D	three-dimensional
3D-EM	three-dimensional electron microscopy
AAV	adeno-associated virus
APs	action potentials
ATUM	automated tape collecting ultra microtome
bAPs	backpropagating action potentials
bV1	binocular primary visual cortex
CIP	calf intestinal phosphatase
dLGN	dorsolateral geniculate nucleus
DNA	deoxyribonucleic acid
DiD	1,1'-Dioctadecyl-3,3,3',3'-Tetramethylindodicarbocyanine
DS	direction selectivity
DSI	direction selectivity index
EM	electron microscopy
FC-mouse	mouse that went through the entire functional connectomics pipeline
FOV	field-of-view
GABA	gamma-Aminobutyric acid
gDSI	direction selectivity index calculated via circular variance
GECIs	genetically encoded calcium indicators
GFP	green fluorescent protein
gOSI	orientation selectivity index calculated via circular variance
GRASP	Green fluorescent protein Reconstitution Across Synaptic Partners
ID	identifier
IOS	intrinsic optical signal
ISI	inter-stimulus-interval
L1	layer 1
L2/3	layer 2/3
L4	layer 4

L5	layer 5
L6	layer 6
L cones	long-wave cones
LED	light-emitting diode
LM	light microscopy
M cones	medium-wave cones
mGRASP	mammalian Green fluorescent protein Reconstitution Across Synaptic Partners
microCT	micro computed tomography
mSEM	multibeam scanning electron microscopy
MPCDF	Max Planck Computing and Data Facility
NA	numerical aperture
OD	ocular dominance
ODI	ocular dominance index
OFF	reacting to light decrements
ON	reacting to light increments
OS	orientation selectivity
OSI	orientation selectivity index
OSS3	One Shot™ Stbl3™
PO	preferred orientation
PD	preferred direction
PFC	prefrontal cortex
PR	photoreceptor
PsD	preferred stimulation direction
PsO	preferred stimulation orientation
RF	receptive field
RGC	retinal ganglion cell
RMS	root mean square
ROI	region of interest
Rpm	rotations per minute
RsF	receptive field subfield

RT	room temperature
SBEM	serial blockface electron microscopy
S cones	short-wave cones
SC	superior colliculus
SE	standard error of the mean
SEM	scanning electron microscopy
SF	spatial frequency
SNR	signal-to-noise ratio
TEM	transmission electron microscopy
TF	temporal frequency
V1	primary visual cortex
VR	significantly visually responsive to visual stimulation with moving gratings
ZEN	Zeiss Efficient Navigation

Acknowledgements

This thesis work would have not been possible without the personal and scientific support and the groundwork, laid by fellow colleagues, friends and family, who I would like to acknowledge in the following.

Primarily, I would like to express my gratitude to my four mentors Tobias Bonhoeffer, Mark Hübener, Tobias Rose and Moritz Helmstaedter for their guidance throughout my PhD, both scientifically and personally. I especially appreciate the faith they put in me for being able to find a way to pull off this project. Further, I would like to thank them for finding just the right balance between being patient in the start of my PhD and challenging me scientifically with great attention to detail. Without, I would not have acquired the multidisciplinary skills and meticulous mindset vital for the success of this project, which has been the biggest challenge in my life so far. Moreover, I would like to acknowledge them for recognizing the timing and impact of recent technological advancements that brought the realization of this project into the realm of possibility. I appreciate that Tobias Bonhoeffer and Moritz Helmstaedter consistently provided me with all means necessary for the development of this experimental pipeline and the acquisition of the dataset. I am thankful to Tobias Rose for sharing his technical expertise, without which the development of deep *in vivo* axon imaging would not have been completed in this timeframe. Finally, I am thankful to my TAC committee consisting of my four mentors and David Fitzpatrick for excellent scientific discussion, rigor and input throughout my PhD and personal support.

Special thanks goes to my fellow office mates Hiranmay Joag, Isa-Maria Gross and Annet Glas who started and shared this entire PhD journey with me, through the highs and the lows. I am grateful that I was always able to ask for their advice, both personal and scientifically. Without their cynicism, sarcasm, jokes and joyful attitude, the PhD would have been a lot harder. I am proud to be able to call them my friends and hope to do so for any more years to come. This extends to Martin Fernholz, Drago Guggiana Nilo, Joel Bauer, Sandra Reinert, Matt McCann, the TST group and the rest of the Bonhoeffer Department, which has been such a great environment to work in. I would like to specifically thank Juliane Jäpel, who established superficial layer *in vivo* axon calcium imaging in the lab and trained me on surgeries, Simon Weiler for initial training on two photon imaging, Joel Bauer for training me on the BScope2, especially on how to debug it and Pieter Goltstein sharing his ROI predator code. Last but not least, I would like to acknowledge both Martin Fernholz and Drago Guggiana Nilo for great scientific and personal feedback as well as a constant supply of excellent memes, which have kept my spirits up throughout my PhD.

Similarly, I would like to thank the lab members of the Helmstaedter department for their inclusivity despite me spending most of my time in Munich and for great scientific discussions. I would like to specifically acknowledge Meike Sievers, whose PhD work on ATUM mSEM has been instrumental by setting the groundwork for the successful acquisition of this dataset. Similarly, I am grateful for the excellent PhD work of Florian Drawitsch on re-finding light-microscopy imaged axons in 3D-EM. Without this pipeline, my project would have been significantly more difficult to pull off. I would like to thank both of the above for open sharing and discussing their own and my project with me to ensure a smooth knowledge-transfer. I would further like to thank the experimentalists Anjali Gour, Helene Schmidt-Helmstaedter, Kun Song and Natalie Heike, who have been of great scientific support regarding 3D EM and image alignment.

I am further grateful for all the technical assistance provided by the TA teams of both departments. Specifically, I would like to thank Claudia Huber for her help with molecular cloning and genotyping, Volker Staiger for technical assistance and discussions, Frank Voss for animal breeding, Lev Dadashev, Selina Horn, Smaro Soworka and Iris Wolf for teaching me heavy metal staining and their assistance during both the ATUM experiments and mSEM imaging. Further, I appreciate the expertise of Tomasz Garbowski, Robert Geissler and Dieter Lechner from Zeiss for their support in debugging the mSEM as well as Klaus Reuther and Meisam Tabriz from the MPCDF for compiling the alignment code on the Raven supercomputer system.

I am grateful to Tobias Bonhoeffer, Moritz Helmstaedter, the Max Planck Society, the International Max Planck Research School for Life Sciences (IMPRS-LS) and the Boehringer Ingelheim Fonds (BIF) for financial support. I would further like to thank both IMPRS-LS and BIF for the excellent skills training and for supporting me in my collaboration between both Max Planck Institutes. Finally, I am grateful to the MPCDF for providing generous supercomputing resources, without which alignment would have taken substantially longer.

Finally, I would like to thank my family and friends for their great understanding and personal support before and throughout my PhD. Without the unforgettable adventures with Ben Plitt, Thomas Fredenhagen, the Wurstgesichter-crew, the Burger-crew, Annika Sander, Andrea Holzer, Stefanie Kern and Tenna Mose I would not have become the person I am today. I am further grateful to my roommates Stephan Holtkamp and Leonie Kohlhammer for sharing the PhD journey with me and always brightening up my life. I am thankful to Philipp Schubert and Alf Hakon Lystad for great arctic adventures, that helped me reset. Lastly, I am deeply grateful to my family Thomas Laubender, Beatrix Laubender and Diana Laubender for their life-long support, patience, for always believing in me and having my back. Thank you for everything!

Affidavit

Eidesstattliche Erklärung

Ich versichere hiermit an Eides statt, dass die vorgelegte Dissertation von mir selbstständig und ohne unerlaubte Hilfe angefertigt ist.

München, den 12.01.2022

_____

David Laubender

Erklärung

Hiermit erkläre ich,

- dass die Dissertation nicht ganz oder in wesentlichen Teilen einer anderen Prüfungskomission vorgelegt worden ist.
- dass ich mich anderweitig einer Doktorprüfung ohne Erfolg nicht unterzogen habe.

München, den 12.01.2022

_____

David Laubender